UNIVERSITÀ
DEGLI STUDI
DI PADOVA

MICROSTRUCTURED POLYMERIC SUBSTRATES APPLIED TO HUMAN STEM CELLS STUDIES

ELEONORA GRESPAN

Chemistry and Physics of Interfaces
Department of Microsystems Engineering (IMTEK)
University of Freiburg

Ingegneria Chimica, dei Materiali e Meccanica
Dipartimento di Ingegneria Industriale
Universitá di Padova

SUPERVISORS:
Supervisor: Prof. Jürgen Rühe
Co-supervisor: Prof. Nicola Elvassore

Eleonora Grespan: *Microstructured polymeric substrates applied to human stem cells studies.*

ABSTRACT

Stem cells are undifferentiated cells that have the capability to differentiate into specialized cells and to subdivide indefinitely to produce more stem cells. Studies on human stem cells represent a powerful method to analyze biological and physiological processes specific of human cells, as well as for tissue engineering, regenerative medicine and cell therapies. When these studies are performed *in vitro* it is important to take in account that cellular processes such as adhesion, migration, growth, secretion, and gene expression are triggered, controlled, or influenced by the biomolecular three-dimensional organization of cell-surface contact. This organization cannot be straightforwardly reproduced in the laboratory; however modern methods in microtechnology enable researchers to generate complex environments at a biologically appropriate resolution.

In this work we employ microfabricated and photopatterned polymeric substrates to reproduce a 3D environment morphologically and chemically tuned to induce specific cell responses (from cell adhesion to cell shape) and to detect specific biological parameters relevant for human stem cells both at the pluripotent and at the differentiated stage.

In particular, at the pluripotent stage, we focus our attention on the response of the cell nucleus to specific microenvironments of the cells, as nuclear shape and structure are recognized to be deeply related with cell function during developmental, physiological and pathological changes which occur during the life time of the cells.

The aim of our investigations is to understand if nuclear morphological reorganization caused by the microenvironment of the cell could affect the further behavior of the cells, especially the gene expression. We employ micropillared substrates where the pillar to pillar distance is smaller than the cell size and in some cases even smaller than the cell nuleus to compare nuclear behavior of human pluripotent stem cells (hPSCs) and differentiated cells, especially to elucidate to what extent the microenvironment influences the shape of the nucleus. Nuclear deformability is quantified by analyzing the shape of fluorescent labeled nuclei on images acquired by fluorescent or confocal microscopy. It is observed that the cell geometry of human pluripotent stem cells seeded on microstructured substrates is strongly altered by through contact with the microstructured substrates. This includes even a strong deformation of the nucleus that

penetrates among the microstructures. In contrast to this, differentiated cells show much less deformable nuclei. To obtain information on a possible relationship between nuclear shape and cell function, we observe the nuclear shape and quantify nuclear deformability at the pluripotent stage and along the process of differentiation. In addition, we compare nuclear behavior and gene expression between cells seeded and differentiated on flat and on microstructured substrates. Our results show that pluripotency of hPSCs is maintained regardless whether the cells are seeded on flat or microstructured substrates. In contrast to this, gene expression analysis of endoderm, mesoderm and ectoderm germ layers, reveal that the morphological reorgaization of the nuclei, which is observed for cells seeded on microstructured substrates, can hinder the process of endoderm specification. Ectoderm and mesoderm early germ layer committment take place despite the highly deformed shape of the nuclei seeded on microstructured substrates, however ectoderm specification takes place along with a process of nuclear stiffening. Along ectoderm committment, cell nuclei raise up from micropillar interspaces and assume a round shape on top of the pillared surfaces. Such nuclear stiffening must be related to a structural and functional reorganization of cytoskeletal and nuclear envelope proteins. The use of a simple substrate fabrication approach combined with image analysis, allows to quantify variation in nuclear shape of hPSCs in a straightforward way. Thus, such approach can be combined in the future with a wider parallel analysis of protein expression to associate nuclear shape variation to specific changes in gene expression.

The developed platform consisting of microfabrication and image analysis is also used to study a second system. We realize here a platform that allows the quantification of physiological parameters of cells derived by differentiation of hPSCs, to evaluate the functional maturation of the investigated cells. In particular, we focus our attention on cardiomyocytes derived from hPSCs. These cells are of special interest since heart diseases are the leading cause of mortality in the Western Countries. In the last decades much effort was put in the research for new approaches in treatment of infarcted hearts as well as congenital heart diseases, spanning from pharmacological to cell therapies. Both need reliable representative study models at the cellular level, as close as possible to the human physiology.

To reach this goal we realize an *in vitro* set up that allows the simultaneous recording and analysis of calcium dynamics and contraction force of cardiomyocytes which have been directly derived from human pluripotent stem cells (hPSC-CMs). To tune cell response after seeding, we fabricate our substrates so that cell adhesion can be lo-

cally controlled. To this, we combine a cell-adhesive photopolymerizable elastomeric polymer, for the generation of a micropillared substrate obtained by replica molding, with a cell-repellent material. The cell-adhesive photoreactive polymer is a copolymer of n-butylacrylate and methacryloyl-4-oxy-benzophenone, P(nBA-co-%MABP). The cell-repellent polymer is polyacrylamide (PAA). To guide cell adhesion and shape, the cell-repellent PAA is attached and crosslinked to the rubber surface by UV light exposure through photolithography. The thus obtained substrate consists of elastomeric micropillars with cell attractive pillar heads onto which hPSC-CMs selectively grew and aligned assuming an elongated shape. Calcium dynamics is acquired through confocal analysis, where the transient of calcium is detected by intensity changes of the fluorescent probe Fluo-4, which serves as a calcium indicator. Micropillar deflection caused by cellular contraction and relaxation is quantified by analysis of confocal images. The deflection data are converted into (contraction) force values by using a finite element model. We apply the developed platform to compare calcium transient and contraction force of hPSC-CMs after 1 week and 5 weeks from seeding to study whether or not functional maturation of the cells occurrs in this time gap. This would be a crucial factor for their employment in drug testing and in the early pharmacological development pipeline. We report that hPSC-CMs cultured on our morpologically and chemically tuned substrates enhanced their functional properties from week 1 to week 5 of culture. In particular, the duration of the calcium transients was found to decrease, while the contraction force was found to increase on cells that were kept in culture for 5 weeks on microstructured and photopatterned substrates.
The use of microtechnology techniques to provide controlled microenvironments combined with stem cells, such as hPSCs and hPSC-CMs goes into the direction to realize *in vitro* biological assays of cells that are sensitive to the mechanical stimuli from the environment. The generation of soft, deformable matrices with local control of the surface chemistry mimics more closely the behavior of regular cells under physiological conditions. As the cells used in a 3D-microenvironment study are actually human cells, it could be possible to limit errors caused by the difference between human and animal physiology. The described approach can reduce the need of more expensive and often not satisfactory *in vivo* studies, i.e. animal testing, where ethical aspects are under strong debate. Such replacement of animal testing could be used for drug screening and for fundamental studies of the mechanisms triggered in cells in response to topographical, chemical or mechanical modifications of the cell microenvironment.

RIASSUNTO

Le cellule staminali sono cellule non specializzate che hanno la capacitá di differenziare dando origine a diversi tipi di linee cellulari presenti nel corpo umano. L'impiego di cellule staminali permette di effettuare studi biologici, fisiologici, di ingegneria tissutale e di medicina rigenerativa su cellule umane derivate dalle staminali stesse. Tali studi sono spesso svolti *in vitro*. Quando si realizzano test *in vitro* é di fondamentale importanza tenere conto che i fenomeni di adesione, migrazione, crescita ed espressione genica a livello cellulare sono controllati o influenzati anche dalla tipologia di interazione che intercorre tra cellula e ambiente circostante. L'ambiente cellulare non puó essere riprodotto totalmente in laboratorio, tuttavia la microtecnologia permette di progettare e realizzare ambienti di coltura cellulare complessi.

In questo lavoro vengono utilizzati substrati polimerici microstrutturati e fotopolimerizzati per realizzare un ambiente cellulare tridimensionale progettato dal punto di vista morfologico e chimico. La combinazione dell'aspetto morfologico e chimico inducono particolari risposte cellulari e permettono di individuare e analizzare determinati comportamenti cellulari in cellule staminali sia pluripotenti che differenziate.

In particolare, tali substrati vengono impiegati per studiare la deformabilitá del nucleo delle cellule sotto esame, dato il fondamentale ruolo del nucleo nel determinare la funzione, lo sviluppo e i possibili aspetti patologici a livello cellulare.

L'obiettivo del nostro studio sui nuclei é quello di determinare se variazioni della morfologia del nucleo (indotte dalla specifica struttura tridimensionale dei substrati utilizzati per svolgere gli esperimenti) in cellule staminali pluripotenti umane (hPSCs), possano influenzare il normale comportamento e sviluppo cellulare. Per indurre variazioni morfologiche a livello nucleare si utilizzano substrati caratterizzati da micropillars aventi una distanza da pillar a pillar inferiore alla dimensione media dei nuclei. La deformabilitá nucleare é quantificata a partire da immagini acquiaiti al microscopio confocale tramite utilizzo di semplici algoritmi che analizzano la forma dei nuclei. La nostra analisi mostra come la morfologia dei nuclei di hPSCs sia notevolmente alterata rispetto alla fisiologica forma rotondeggiante quando tali cellule vengono coltivate su sibstrati microstrutturati. Al contrario le cellule differenziate mostrano una de-

formabilitá molto piú bassa. Per ottenere informazioni relative ad una possibile relazione tra morfologia nucleare e funzione cellulare, la deformabilitá cellulare é stata quantificata nei diversi stadi di differenziamento. Inoltre, la morfologia cellulare e l'espressione di alcuni geni viene confrontata tra cellule differenziate su substrati microstrutturati e tra cellule differenziate su substrati piatti. I nostri dati mostrano che la pluripotenza cellulare Ãš mantenuta quando le cellule vengono coltivate su substrati microstrutturati cosí come quando vengono coltivate su substrati piatti. Al contrario, l'analisi dell'espressione genica realizzata su cellule dove é stato indotto il processo di sviluppo dei foglietti germinali (endoderma, ectoderma e mesoderma), rivela che la riorganizzazione morfologica dei nuceli osservata nel caso di cellule coltivate su substrati microstrutturati, puó ostacolare un normale processo di induzione del foglietto germinale endoderma. In particolare il normale sviluppo in endoderma sembra essere ostacolato dalla deformazione dei nuclei. Il processo di specializzazione cellulare in ectoderma e mesoderma avviene invece anche nel caso di cellule seminate su substrati microstrutturati dove i nuclei assumono forti deformazioni morfologiche. Tuttavia il processo di differenziamento in ectoderma avviene in concomitanza con un processo di irrigidimento del nucleo che assume forme tondeggianti e non é piú in grado di adattarsi alla geometria del substrato. Questo irrigidimento del nucleo deve essere correlato ad un processo di riorganizzazione strutturale e funzionale a livello della membrana cellulare e del citoscheletro. Il nostro studio mostra come combinando l'utilizzo di substrati microstrutturati ad un semplice processo di analisi delle immagini dei nuclei acquisite al confocale, si possono monitorare e quantificare facilmente e in maniera affidabile variazioni della deformabilitÃ nucleare. Questo approcio, se combinato ad una piú ampia analisi dell'espressione genica a livello cellulare, potrá permettere di correlare variazioni della morfologia nucleare a variazioni funzionali e di espressione genica a livello cellulare.

La combinazione di substrati microstrutturati con l'analisi di immagini acquisite al confocale é stata utilizzata anche per un secondo obiettivo. Abbiamo realizzzato una piattaforma in grado di quantificare importanti parametri fisiologici di cardiomiociti derivati dal differenziamento di cellule staminali pluripotenti umane (hPSC-CMs). Tale piattaforma é in grado di ottenere in maniera simultanea la dinamica del calcio e la forza di contrazione dei cardiomiociti. I cardiomiociti, grazie alla specifica chimica della superficie del substrato, assumono una forma allungata, simile a quella fisiologica, una volta seminati. Il substrato é stato realizzato in un elastomero fotopolimerizzabile, che promuove l'adesione cellulare. Tale polimero é costituito da n-

butilacrilato e da metacriloil-4-oxi-benzofenone P(n-BA-co-I nostri dati mostrano che quando gli hPS-CMs vengono mantenuti in coltura sui nostri substrati per 5 settimane la durata del transiente del calcio diminuisce mentre la forza di contrazione aumenta rispetto alle stesse cellule mantenute in coltura per 1 settimana. Tali dati suggeriscono che la combinazione di diversi fattori quali la morfologia della cellula, il tempo di coltura e lo stimolo meccanico dato dai micropillar elastici inducono un processo di maturazione funzionale a livello cellulare.
L'impiego della microtecnologia per realizzare un ambiente cellulare textitad hoc combinato con l'impiego di cellule staminali va nella direzione di realizzare test *in vitro* sempre piú complessi e che possano dare informazioni sempre piú specifiche e affidabili. Tale approccio puó permettere la riduzione di test *in vivo* che sono molto piú costosi, eticamente problematici e basati sul modello animale, che spesso presenta sostanziali differenze rispetto a quello umano.

CONTENTS

LIST OF FIGURES

LIST OF TABLES

E	Young's modulus
I	Moment of inertia
δ	Pillar deflection
r	Relative reactivity ratio
λ	Wavelength
T_g	glass transition temperature
σ	Stress
ϵ	Infinitesimal strain
G	Shear modulus
τ	Shear stress
γ	Shear strain
ϵ_c	Cauchy strain
Δl	Increase in length
L_0	Starting length
F	Force
A_0	Area
T	Shear force
ν	Poisson ratio
η	Viscosity
$E*$	Complex modulus
E'	Storage modulus
E''	Loss modulus
$\tan\delta$	Loss factor
F_t	Tangential force
Δx	Micropillar displacement
U	Energy functional
W	Work

ACRONYMS

3EBP	triethoxybenzophenone
AFM	atomic force microscopy
AFP	alpha fetoprotein
AIBN	azobisiobutyronitrile
ANEP	aminonaphthylethenylpyridinium
ANF	atrial natriuretic factor
ATR	attenuated total reflection
Beta-III Tub	Beta-III tubulin
BMP	bone morphogenic protein
Bra-T	brachyury-T
BP	benzophenone
CRR	calcium release rate
CUR	calcium uptake rate
CBMSCs	cord blood mesenchimal stem cells
CMs	cardiomyocytes
Cnx43	connexin 43
DAPI	4',6-diamidino-2-phenylindole
DCM	dichloromethane
DMTA	dynamic mechanical thermal analysis
cTnT	cardiac troponin-T
EB	embryoid bodies
ECC	excitation-contraction coupling
ECM	extracellular matrix
ESCs	embryonic stem cells

FEA finite element analysis

FEM finite element model

FGF fibroblast growth factor

GAPDH glyceraldehyde 3-phosphate dehydrogenase

GDF growth differentiation factor

GFP green fluorescent protein

hASCs human adult somatic cells

HEPES 4-(2-hydroxyethyl)-1-piperazineethanesulfonic acid)

hERCs human epithelial renal cells

hESCs human embryonic stem cells

hESC-CMs human embryonic stem cell derived-cardiomyocytes

HFF human foreskin fibroblasts

hiPSCs human induced pluripotent stem cells

hiPSC-CMs human induced pluripotent stem cell derived-cardiomyocytes

hMSCs human multipotent stem cells

hPSCs human pluripotent stem cells

hPSC-CMs human pluripotent stem cells derived cardiomyocytes

ICM inner cell mass

iPSCs induced pluripotent stem cells

IRM interference microscopy techniques

LINC Linker of the Nucleoskeleton and Cytoskeleton

MABP methacryloyl-4-oxy-benzophenone

MEFs mouse embryonic fibroblasts

n-BA n-butylacrylate

Oct-4 octamer-binding transcription factor 4

PAA polyacrylamide

PeT photo-induced electron transfer

PDMS polydimethylsiloxane

P(DMAA) poly(dimethyl acrylamide)

PMMA poly(methyl methacrylate)

PSCs pluripotent stem cells

PVC poly(vinyl chloride)

qRT-PCR quantitative real-time polymerase chain reaction

RIE reactive ion etching

RGD arginylglycylaspartic acid

SaOs-2 osteosarcoma cells

SEM scanning electron microscopy

SERCA-2a sarcoendoplasmic reticulum calcium-ATPase

SPR surface plasmon resonance spectrometry

SR sarcoplasmic reticulum

SSEA-4 stage-specific embryonic antigen-4

TAZ transcriptional coactivator with PDZ-binding

TGF-beta transforming growth factor-beta

TM transversal magnetic

VSDs voltage sensitive dies

YAP Yes-associated protein

TAZ transcriptional coactivator with PDZ-binding

1 INTRODUCTION

1.1 MECHANISMS OF CELL MECHANOSENSING

Cells perceive their microenvironment not only through signals acting up them from molecules present in their environment but also through physical and mechanical cues, such as the extracellular matrix (ECM) stiffness or local changes in the surface chemistry which lead to local variations in cell adhesion. Cells translate these stimuli through mechanotransduction systems into biochemical signals, which then control multiple aspects of cell behavior, including growth, differentiation and proliferation, but can also lead to cancer progression [1]. Numerous molecules and subcellular structures have been shown to mediate force sensation and mechanochemical conversion at the micro- and nano- meter scale, such as stretch-activated ion channels, integrins, cadherins, growth factor receptors, myosin motors, cytoskeletal filaments, nuclei, extracellular matrix (Figure 1) [2]. In particular, cell membrane molecules and cytoskeleton proteins play a major role in the process of interactions between cells and material surfaces.

1.1.1 *Cell structures involved in mechanosensing*

1.1.1.1 *Adhesion molecules in the cell membrane*

Cell-substrate adhesion and mutual interaction between cells is based on on certain transmembrane glykoproteins, namely cadherins, cell adhesion molecules (CAM), selectins and - as the most important class of adhesion molecules - integrins. Integrins are trans-membrane receptors consisting of non-covalently associated α and β subunits, that bind to specific amino acids sequences present in the ECM, such as the arginine-glycine-aspartic acid (RGD) recognition motif. Cell surfaces contain several different types of integrins, which vary in their protein sequence, but all allow to bind to collagen, fibronectin, laminin and other similar proteins present in the ECM. Integrins interact with the ECM through their extra-cellular domains and with components of cytoskeleton and also with signaling molecules through their intra-cellular domains, acting as an link between the intra- and extra-cellular components [3].

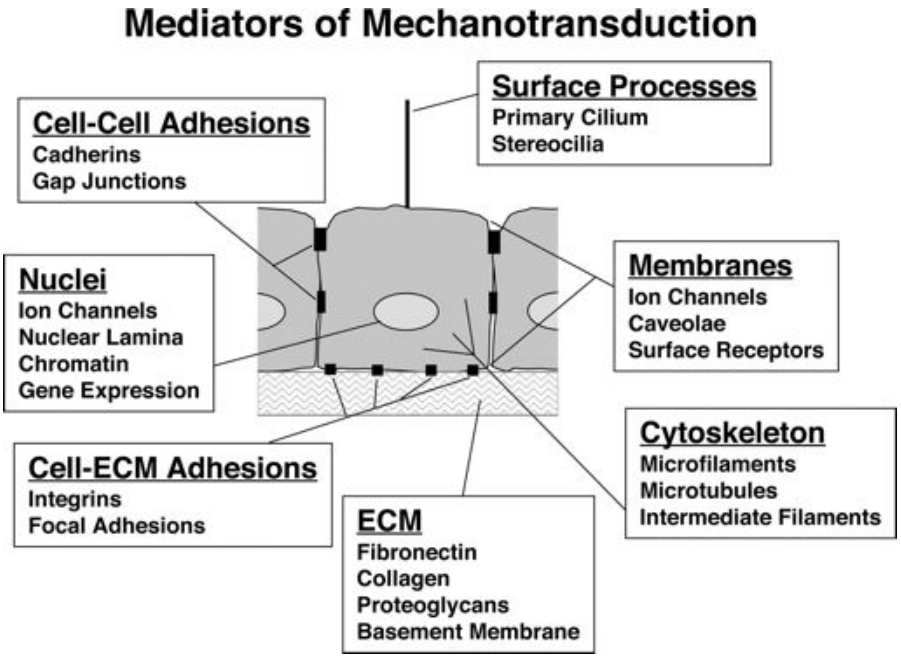

Figure 1: Mechanotransduction systems. Many molecules, cellular components, and extracellular structures have been shown to contribute to mechanochemical transduction. These transduction elements include ECM, cell-ECM, and cell-cell adhesions, membrane components, specialized surface processes, cytoskeletal filaments, and nuclear structures. (Adopted from Ingber, 2006 [2] with permission).

.

Cell-cell adhesions is also based on cadherins (calcium dependent adhesion proteins), which depend on the presense of calcium to form cell-cell junctions. Cadherins are, like the intergrins, transmembrane glycoproteins acting with intra-cellular partners: catenins. Catenins, which directly interact with intra-cellular proteins, receive cadherin signals that are transferred to the inner-cell and are involved in the process of cell response to the surrounding stimuli.

1.1.1.2 *Cytoskeleton proteins*

The cytoskeleton is the cell structure that provides structural integrity to the cell. It is composed of actin filaments, microtubules and intermediate filaments. The sites of adhesion that link the cytoskeleton to the material surface are called focal adhesions. Focal adhesions are large protein complexes, which are constantly formed, dissolved and altered, through which the cytoskeleton of a cell connects to the ECM. The stability of the complexes depends largely on whether the cell is sessile or moving along the surface.. Focal contacts are formed

by a polarized array of thin actin filaments that modify their size and thickness according to the external stimuli [4]. The focal adhesion sites are the points of attachment of the cell with the extracellular matrix and are the points of transfer of information from the outside of the cell to the interior of the cell. This transfer of information is two- fold: information is transmitted by the cytoskeleton to the focal adhesion sites and it is also transmitted to the cell from the focal adhesion sites. The external faces of focal contacts present integrins. On the internal face the interactions between actin filaments and integrins is mediated by some proteins like talin, paxillin, vinculin, tensin. Tubulin microtubules and vimentin, lamin or keratin microfilaments are also involved in the maintenance of cell architecture and undergo structural modification in respons to mechanical stimuli [3]. Essential proteins also involved in the process of mechanosensing are the myosins [5]. Myosins are motor proteins that translocate along actin, allowing cell shortening and therefore contraction and, thus, the maintenance of the cellular force balance. All the cytoskeleton molecules and the cell adhesion receptors act together in mechano-transduction and mechano-sensitivity and are represented in the schematic diagram of Figure 2.

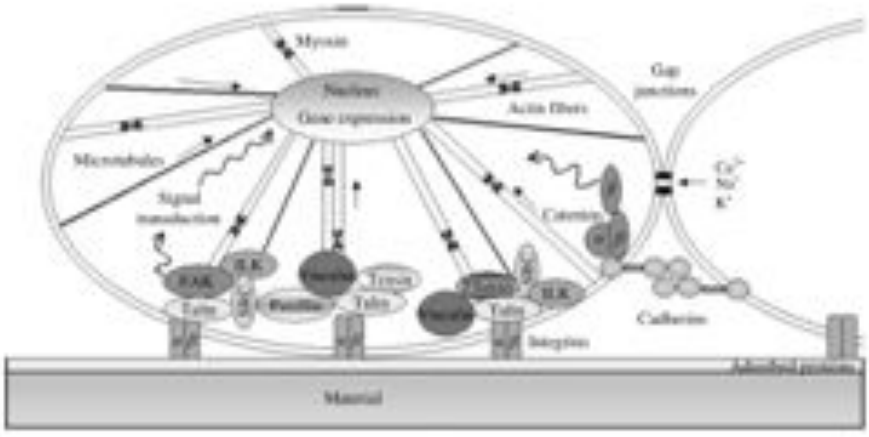

Figure 2: Schematic diagram of the proteins involved in cell adhesion and mechanotransduction. (Adopted from Anselme, 2010 [3] with permission).

1.1.1.3 *Nuclear membrane proteins*

The cell nucleus is the organelle that contains the genetic information of the cell: it is principally composed by DNA and a large variety of other proteins delimited by the nuclear membrane [6]. The nuclear membrane is connected to the cytoskeleton through several trans-

membrane proteins, such that belonging to the SUN (interior of the nuclear membrane) and KASH (exterior of the nuclear membrane) families of proteins. These proteins have been termed Linker of the Nucleoskeleton and Cytoskeleton (LINC) complex because they represent a link between the cytoskeleton and the nucleus' interior [7]. It has been demonstrated that they allow positioning of the nuclei as well as transmission of information to the nucleus, including displacement of chromosomes [8]. Though these complexes have been discovered only recently, nuclear membrane proteins have been described for each of the cytoskeletal fibres in the cell and it is well-established that there are direct links between the exterior of the cytoplasmic membrane and the nucleus [9]. In Figure 3 the interacting structures of the nuclear membrane and the cytoskeleton are depicted. Through this system, not only the biochemical signals produced by the cell but also the mechanical stimuli sensed by the cell at the focal adhesion sites, are transmitted to the nucleus through the cytoskeletal connections and can influence nuclear shape, structure and possibly nuclear function. The relevance of such cytoskeleton-nucleus connections is further discussed in Section 1.6.

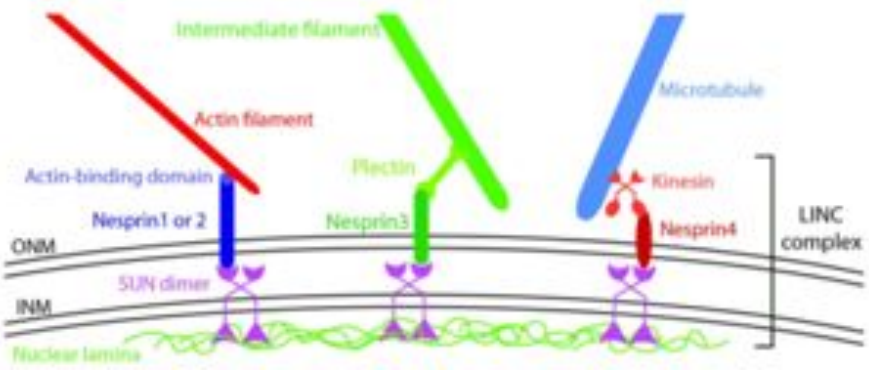

Figure 3: The interactions between the cytoskeleton and the nuclear membrane proteins. Each component of the cytoskeleton is able to connect directly to the nuclear lamina at the interior of the nucleus through the SUN and KASH proteins, which are present at the inner nuclear membrane and outer nuclear membrane, respectively. (Adapted from Davidson, 2011 [9]).

.

1.1.2 *Cell mechanoresponse to local geometry and forces*

Recent studies have determined that the crucial components of the cellular mechanoresponse are sensing of geometry at the sub-cellular level [10, 11] and physical forces acting onto the cells or developed by

the cells themselves [2, 12].
Local geometry influence cell morphology, which has been shown to regulate the signaling of different biological pathways [1, 13]. For example, Wada et al. [13] manipulated the morphology of single cells without cell-cell contact obtaining flat spread or round compact cells. They demonstrated the importance of cell morphology in the regulation of Hippo pathway. Hippo is a signaling pathway which plays an important role in regulating cell proliferation, apoptosis and stem cell self renewal. Dysregulation of the Hippo pathway contributes to cancer development. Core to the Hippo pathway is a kinase cascade which ends into phosphorylation and inhibition of the transcription co-activators Yes-associated protein (YAP) and transcriptional coactivator with PDZ-binding (TAZ) [14]. When dephosphorylated, YAP/TAZ translocate into the nucleus and interact with other transcription factors to induce expression of genes that promote cell proliferation and inhibit apoptosis promoting malignant cell behaviors [15]. According to Wada et al. [13], when cells are flat and spread, the formation of stress fibers is promoted, thereby reducing YAP phosphorylation, promoting nuclear YAP accumulation and cell proliferation. When cells are compact and tall, stress fibers are reduced and phosphorylation of YAP is promoted, reducing the presence of YAP in the nucleus and cell proliferation. Another example is when the adaptation of the cell to the geometry of the environment causes membrane curvature that modifies the spatial distribution of cytoplasmic adhesion proteins to conform to the curved membranes, thereby possibly affecting the adhesion complexes [12].
The conversion of external or internal forces into biochemical signals take place mainly through the following mechanisms: the force-induced exposure of otherwise cryptic peptide sequences, the alteration of enzyme activity and the opening of mechano- sensitive ion channels [16].
The primary cellular responses to mechanical signals occur in seconds to minutes, starting a cascade of events that can modify cell conformation, adhesion sites and finally protein expression in a timescale of a few days. In Figure 4 important factors which sense such modification, which are caused by a combination of extracellular and intracellular signals, are represented: initially, cells will sense the mechanical features of their environment, which will cause rapid signalling responses. As the cell pulls on the environment, it will modify the extracellular matrix and will create new signals. Intracellular signals will alter the expression pattern of the cell and, over time, the cellular forces and cell shape. The final step concerns adjustments of cell function through alteration of protein expression. Physical forces acting

onto the cells can modulate the kinetics of protein-protein or protein-ligand binding in living cells because of their effects on molecular conformation of the involved molecules. For example, mechanical distension of cell membranes modulates the cation-transporting activity of stress-sensitive ion channels by producing conformational changes that alter their opening or closing rates [2]. A further example is the application of a stalling force using optical tweezers to block the movement of molecular motors, such as myosin, that entails the inhibition of the activity of specific enzymes (such as RNA polymerase) [2].

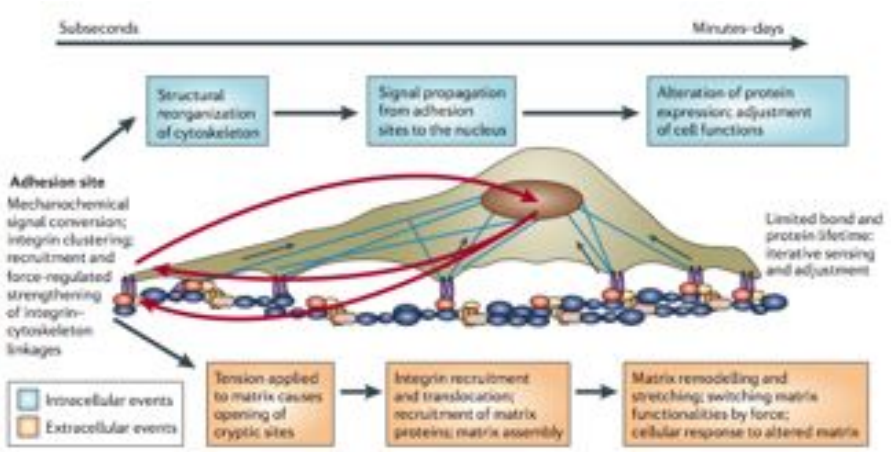

Figure 4: Cellular processes of mechanosensing and responses. The diagram shows the steps in mechanosensing over time that involve periodic testing of the substrate, substrate modification and changes in cellular protein content. (Adopted from Vogel et al., 2006 [16] with permission).

.

The application of a force directly to either the enzyme or its substrate, or to an activator/inhibitor of the enzyme can regulate enzyme activity [17]. Forces can influence chemical equilibria and molecular polymerization events as well. For example, application of tensional forces to cultured neurons or vascular smooth muscle cells results in increases in microtubule polymerization [2].
The forces that are developed by the cells themselves onto the ECM or that are caused by cellular contacts are also important. Cell-cell contacts are dynamic and change according to the environmental conditions. Cells evaluate the level of force exerted onto them and make adjustments to their structure, as the cytoskeleton filaments and their linkages to transmembrane proteins assemble, break down and reassemble [16]. Protein of the ECM as well as many proteins that link the integrins to the cytoskeleton present a tandem-repeat struc-

ture that can be modified by the exerted force, which results in alterations in molecular recognition sites, or in the exposure of peptide sequences that are otherwise hidden, which can elicit biological responses distinct from intact molecules [18].

Investigation of the effects of local forces (acting onto the cells or generated by the cells) is of paramount importance since the transduction of mechanosensing into biochemical processes activates many signalling pathways that interact to produce controlled functional responses: dysregulation of such mechanical responses contributes to major human diseases [19]. In the vascular system, for example, pressure and shear stress from pumping blood influence the morphology and pathology of the heart and vasculature. Stretch responses in cardiac myocytes, appear to involve stretch-activated ion channels and integrin/ECM-dependent signals [19]. Cardiac-muscle focal adhesion proteins, are also involved in cardiac mechanical responses. Knockout of specific focal adhesion proteins on mice show normal cardiac tissue architecture but under pressure-overload conditions, the cell response that leads to cardiac hypertrophy is impaired and cells develop an abnormal cardiac remodeling that evolves into contractile dysfunction [20]. Proteins of the cardiac myocyte Z disc, have also been proposed to participate in mechanotransduction, since mutations of these proteins increase susceptibility to dilated cardiac myopathy [19]. A better understanding of how external forces influence cardiac myocytes functions and of how the contractile forces of cardiac myocytes model their activity, can help to elucidate the pathophysiological mechanisms of heart failure and also facilitate development of novel therapeutic interventions.

It has also been postulated that cytoskeletal filaments can propagate stresses over long distances. Force on peripheral contacts can produce signaling molecules that could interact with the nucleus. It might be possible that physical factors and nuclear deformation could regulate gene expression through a still not completely elucidated mechanism. Transcription factors that are recruited to the adhesion sites could have an important role in translating the physical stimulus that is sensed at the periphery into biochemical signals that are transported to the nucleus and that could alter gene expression [12].

Microtechnologies and in particular microfabrication techniques will enable us to test the mechanisms of mechanosensing and transduction *in vitro*. Important questions include a further definition of the local responses to mechanical and geometrical forces and the effects of signal propagation within the cell, including within the nucleus, on functional parameters of the cells and possibly on gene expression. In particular, these questions will be addressed in the case of hu-

man stem cells, where physical properties of the ECM and mechanical forces are integral to morphogenetic processes in embryonic development, defining tissue architecture and driving specific cell differentiation programs. Thanks to a proper tuning of the morphological, mechanical and chemical properties of the substrates in which cells are cultured, the effects of force- and geometry- sensing on nuclei of human stem cells from the pluripotent to the differentiated stage is investigated. Human pluripotent stem cells are then differentiated into cadiomyocytes, and the consequences of the mechanical interaction between cells and substrates on the functional maturation of the cells is studied.

1.2 EFFECT OF SURFACE PROPERTIES ON CELL STRUCTURE AND FUNCTION

As described in Section 1.1, cells actively respond to stimuli present on their environment. Such interactions affect many aspects of cell function, including spreading, migration, proliferation and differentiation. In many examples, the cellular response is accompanied with changes in cellular and nuclear morphology [21]. A proper design of biointerfaces between cells and biomaterials, both for tissue-engineering applications and for biological *in vitro* studies needs to consider the topographical, chemical and mechanical properties of the surface, to meet the biochemical and biophysical requirements of the specific cell type under study.

1.2.1 *Cell response to surface topography*

Surface topography directly affects cell morphology, alignment, cytoskeletal arrangement, motility, proliferation, nuclear deformation, and gene regulation [21]. In many studies the surface was micro- and nano-structured with different topographies including grooves, pillars, holes and fibers, to investigate cellular responses for various cell types [22, 23, 24]. In general, on grooved patterns, a strong cellular alignment due to contact guidance is observed in the direction of the patterns [25]. The magnitude and presentation of patterns are also important: several studies have been concerned with the effects of depth and width of grooves on cell orientation [26, 27, 28], but the minimal depth and width needed for inducing cell orientation is strongly related to the cell types used.
Cell can sense variation of the roughness of the substrate at nanotopographical level as well [29]. For example, nanoscale disorder, is

shown to stimulate human mesenchimal stem cells to produce bone mineral in vitro [30]. It has also been found that cells adhere differently to surfaces that are structured with nanoposts compared with nanopit-covered surfaces [12]. Although nanoposts increased cell spreading, proliferation and cytoskeletal formation, a nanopitted pattern decreased adhesion relative to flat substrates. In fact, fibroblasts seem to endocytose nanocolumns.

It is important to remember that cell response to topographical cues is strictly related to cell phenotype. Kunzler et al. [31], developed surfaces with a roughness gradient in a range from 1 to 6 μm and they observed that rat calvaria osteoblast showed an increased proliferation rate with increasing roughness, whereas the human gingival fibroblasts showed the opposite behaviour.

These findings are not surprising, considering that the topographies from macro- to nanometer- scale that cells encounter in their native environment actively influence their process of growth and function development. As one example, cellular alignment is a critical process in musculoskeletal myogenesis, and musculoskeletal disorders are often associated with abnormalities in the muscle structure alignment [32, 33]. In cardiac tissue, the extracellular matrix is composed of a highly organized collagen scaffolding that maintains ventricular geometry and the spatial orientation of the fibers controls the distribution of stresses [34]. In failing hearts, cardiac muscle fiber alignment can be highly disorganized, and this is known to result in progressive fibrosis and ventricular dilatation [35]. Thus, it is of great interest to temporally and spatially manipulate surface topography *in vitro* to better understand and develop strategies to control biological processes.

Different mechanisms have been proposed to explain how cells sense the morphology of the surface. Curtis and Clark proposed the idea that cells react to discontinuities, where "a discontinuity has a radius of curvature less than the average length of a pseudopodium or of the distance part of the sensing elements that control movement" [25]. Cell response should involve focal adhesions and their linking to the cytoskeleton. Cells should firmly adhere to the substrate through focal adhesion points and would be able to stretch themselves on the substratum, and this would activate stretch receptors and cytoskeletal activity. This is related to the mechanism of mechano-sensitivity mediated by integrin-mediated cell-matrix adhesion, discussed in Section 1.1, and the cell's contractile machinery involving actin and myosin motors [3]. The process of adaptation of the cell to surface topography could also lead to the disruption or modification of normal focal adhesion formation and result in cell sig-

nalling transmission to the interior of the cell and the nucleus. This can evolve into changes in biochemical pathways. Acoording to other hypothesis, cells would sense the discontinuities of the surface due to thermodynamic reasons. The discontinuities would act as an energy barrier, where the size of the energy barrier is dependent on both the geometry and surface chemistry [36]. Thus, the cells would try to minimize contact with the high energy discontinuities and hence modify their orientation, adhesion or spreading. Despite several hypothesis have been proposed, the mechanism by which cells transduce changes in cell geometry into different biochemical responses is still under investigation.

1.2.2 *Cell response to surface chemistry*

The chemistry of the surface is a second important factor which guides the process of cell adhesion, cell growth and viability. In particular, surface energy plays a fundamental role in the process of cell adhesion [37]. In 1982 it was demonstrated by Baier and coworkers [38] that the higher is the surface energy of an implant, the stronger is the process of tissue adhesion *in vivo*. In 2005, Keselowsky et al. [39] reported that OH- and NH_2-terminated surfaces (hydrophilic surfaces) increased more osteoblasts specific gene expression, alkaline phosphatase enzymatic activity and matrix mineralization (all markers of osteoblastic differentiation) than surfaces presenting CH_3 groups (hydrophobic surfaces). Yanagisawa et al. [40] observed that when the surface had a water contact angle below 60^o, cell attachment rate and cell spreading were much pronounced than in the case of surfaces with higher contact angles. In 2004, Lim et al. [41] demonstrated that human fetal osteoblasts adhered and proliferated better on hydrophilic substrates than on hydrophobic ones. Linear gradients of surface energy were done by Lee et al. [42] using polyethylene substrates treated by corona discharge treatment. They investigated the behavior of different cell lineages, and reported that cell adhesion was increased on the areas with moderate hydrophilicity on the wettability gradient surface than onto the more hydrophobic or hydrophilic positions.

However, it is important to underline that cells practically never see a bare surface but a surface previously covered with proteins adsorbed from biological fluids. Cell adhesion takes place when cell adhesion receptors such as the integrin superfamily establish an anchorage with ECM proteins adsorbed to the surface. It is generally recognized that the proteins adsorb more and more rapidly on hy-

drophobic surfaces [43, 44, 45]. Hydrophilic substrates generally adsorb a lower quantity of proteins. Wörz et al. proposed a model for polymeric surfaces that is entirely based on thermodynamic considerations [46]. The interaction between proteins and polymeric surfaces is governed by the enthalpic and entropic components of the Gibbs free energy. The enthalpic term is stronger for hydrophobic or ionic interactions between surfaces and the respective components of the proteins. This condition promotes protein adsorption. In contrast to that, for neutral hydrogels no hydrophobic interactions are possible and the enthalpic contribution is considerably less or zero. Under this circumstance, there is low or no interaction between the polymer and the protein. Protein-repellency properties of hydrophilic surfaces are confirmed by several studies [47, 48, 49]. Therefore, when substrates are fabricated to be functionalized with specific proteins for subsequent cell culture, they should present an hydrophobic surface to promote cell adhesion or contain specific cell adhesion sites such as the arginylglycylaspartic acid (RGD) sequences.
Tuning surface chemistry it is possible to guide cells' adhesion and to study the influence of cell shape on their function. For example, Chen et al. [50], used micropatterned substrates that contained extracellular matrix-coated adhesive islands of decreasing size, which confined cell adhesion on areas going from 40 to 5 μm, to show that it was possible to switch endothelial cells response from growth to apoptosis. Cell shape was found to govern whether individual cells grow or die. Local geometric control of cell growth and viability, which can be obtained by a proper chemical functionalization of the surface, may therefore represent a fundamental mechanism for developmental regulation of the investigated cells.

1.2.3 *Cell response to surface mechanical properties*

A large number of cell types from many different tissues respond not only to biochemical signals but also to mechanical cues of their surrounding ECM. Cell mechanical behavior can be defined as viscoelastic, due to the co-existence of a liquid phase (water content of the cell) and a solid phase (structural proteins of the cell). While the latter allows for an elastic response to a mechanical stimulus, the liquid component allows for a viscous deformation. Such architecture allows cells to respond in a different way to mechanical stimuli exerted over short or long time scales, as described in Section 1.1.2 and sketched in Figure 4. Cells have a response that can be described as elastic when they react to sudden forces, while they undergo large deformations adapting in a viscous manner to forces applied over long time scales.

It has been demonstrated that cell mechanical stiffness is mainly determined by the cytoskeleton and it is a relevant parameter to evaluate the cytoskeletal structure, myosin activity and many other cellular processes [51]. Changes in cell mechanical properties are also often found to be closely associated with various disease conditions such as tumor formation and metastasis, therefore the investigation of cell response to the mechanical properties of their surrounding environment is of paramount importance.

The first study in which this interaction was investigated in a formal way was published by Pelham and Wang in 1997 [52]. In this work, they employed collagen-coated polyacrylamide gels with elastic moduli controlled by varying the amount of acrylamide monomer or bisacrylamide crosslinker used, and described changes in cellular properties including shape, spreading, and focal adhesion formation of both normal rat kidney epithelial cells and fibroblasts, setting a standard method for investigating cell response to substrate rigidity.

Another approach to vary substrate stiffness mantaining the same substrate chemistry is based on the use of arrays of elastomeric posts. The microposts act as springs to which the cells attach. By measuring the deflection of these microposts, it is possible to calculate and spatially map the local cellular traction forces. To control the substrate mechanics, microposts of different heights, corresponding to different spring constants can be employed [53].

Most cell types adhere and spread better on more rigid substrates [54]. For many cell types, increased substrate rigidity also leads to increased stress fiber organization and focal adhesion formation and increased proliferation [54]. Some groups have found a maximum in both fibroblast spreading and cell-substrate modulus matching on rigidities near 10 kPa, above which cells began to produce stress fibers [55, 56]. The 10 kPa modulus appears to be important for other cell types as well. Ventricular myocytes and C2C12 myoblasts demonstrated maximum striation around 10 kPa, which is, in both cases, near the stiffness of native tissue [57, 58]. Ventricular myocytes also showed highest axial force generation, calcium transients, and sarcoplasmic/endoplasmic reticular calcium ATPase expression on 10 kPa substrates [58].

Discher et al. [59] demonstrated that the stiffness of the substrate directed also stem cell differentiation. Soft matrices that mimic brain are neurogenic, stiffer matrices that mimic muscle are myogenic, and rigid matrices that mimic collagenous bone are osteogenic.

The mechanisms how cells feel their microenvironment, and particularly its elasticity, and how this affects cell structure and function is still under investigation and it was discussed already in Section 1.1.

The knowledge of cells' ability to sense and respond to the mechanical properties of the substrate is important for the understanding of basic cellular biology. Furthermore, an improved understanding of the relationship between cell function and substrate stiffness has a potential diagnostic and therapeutic value, since it may affect the study or treatment of diseases such as cancer or fibrosis, in which tissue mechanics are altered [54].

1.3 MICROTECHNOLOGIES APPLIED TO CELL STUDIES

As decsribed in Section 1.2, cellular processes are influenced by the interaction with neighboring surfaces [60]. Furthermore, cells respond to local concentrations of a variety of molecules that may be dissolved in the extracellular medium (e.g. enzymes, nutrients, and small ions) or present on the underlying surface (e.g. ECM proteins) or on the surfaces of adjacent cells (e.g. membrane receptors). In traditional cell culture, these factors are distributed homogeneously on the substrate. Recent works in three-dimensional culture systems have exposed significant limitation of the study of cells on flat (2D) surfaces [61]. Through microtechnology these limits can be overcome. First, microtechnology intrinsically enables control of the cellular environment at cellular resolution: this potentially enables researchers to replicate complex environments at a biologically appropriate resolution. Second, microtechnology facilitates high-throughput experimentation due to its ability to manipulate large numbers of small liquid volumes [62].

In this perspective, benefits from microscale technologies can derive from an accurate investigation of the following specific aspects: i) cell-substrate interactions; ii) cell-cell interactions; iii) cell-soluble environment interactions; iv) cell-electrical field coupling. In this work we will focus our attention on the investigation of cell-substrate interactions, meant as cell response to topological, chemical and mechanical properties of the substrates.

Microfabrication techniques allow to tune such properties, to create local cellular microenvironment to closely mimic the physiological and pathological environment.

A multiplicity of techniques have been applied in order to gain micrometric control over culture systems such as microtransfer molding, micromolding, selective chemical vapor deposition, wet or dry etching processes, bulk and surface micromachining [63, 64]. To date, lithographic techniques, and especially photolithography, are the most commonly used to fabricate microscale features on glass or silicon substrates to be subsequently used as masters for obtaining the final

devices. By photolitography, ultaviolet (UV) light is shone through a mask containing the pattern in an opaque material (usually chrome) on a transparent background (glass) and hits a layer of photosensitive polymer (photoresist). The polymer, or photoresist, either cross-links (negative resist) or deteriorates (positive resist) on action of exposure, allowing the copy to be formed after development. Another common method employed to obtain microstructured substrates is replica molding. This method is based on the realization of elastomeric substrates or stamps that take their shape from a master that it is usually fabricated through standard photolithography. The same master can be reused several time to fabricate the elastomeric (usually made in PDMS) negative replica.

To guide cell adhesion and process outgrowth, [65], chemical patterning techniques are commonly utilised as they allow fabricating surfaces which present two or more different types of chemcial moieties to the cells. In particular, microcontact printing and photopatterning are some of the most common microtechnology techniques used to modify the chemistry of surfaces. Microcontact printing is a method for patterning by printing material frequently using a PDMS stamp [66, 67, 68]. The general procedure for μCP is based on the use of a stamp inked with a solution of the substance to be printed. As the stamp is pressed on the surface, the liquid is transferred to the substrate and the solvent evaporates. As the adhesion of the liquid to the PDMS is usually rather weak, a large fraction of the solution is transferred to the substrate. This procedure has been most widely used in printing alkanethiolates onto gold and silver surfaces, but it is also used on glass and more recently on hydrogels [69]. By photopatterning, the substrate is coated with a light sensitive polymer and then irradiated through a master pattern presented on a semi-transparent mask. The polymer, cross-links on action of exposure. In this way only the irradiated areas of the surface will be modified. Photopatterning resolution is limited by the wavelength of light used during irradiation. The mechanical properties of the substrates can be tuned both varying the cross-linker density of the polymer used to fabricate the substrate or by creating surfaces with micropillars with different heights.

Microtechnology allows the fabrication of such surfaces and of substrates with micropatterned rigidity to examine effects of anisotropy and spatial differences in substrate modulus.

1.3.1 *Cell force measurements through microtechnology techniques*

The forces applied by cells onto their surrounding environment regulate several crucial processes as spreading, migration, attachment to a substrate and even differentiation [59, 70, 16, 71]. The cytoskeletal organization of the cell is also strongly related to the mechanical forces applied. Consequently they are associated with many phenomena occurring at the more regional or even global level of organisms such as immune response, wound healing and cancer metastasis. Cells sensitively respond to physical properties of the environment and even malignancy is promoted by an increase in stiffness of the cellular matrix [72].
Cells can locally apply up to several nanonewtons of force through nanometer-sized adhesion sites. The force is generated via the cytoskeletal motor protein myosin that pulls on actin filaments coupled to transmembrane integrins which anchor cells to the outside substrates. This process is mediated by several proteins that can act as mechanochemical signal converters [1, 73, 74].

In order to quantify cellular forces, several experimental methods have been employed such as AFM [75, 76, 77], micropipette technique [78], carbon fibre-based approaches [79], flat elastic substrates (traction force microscopy) [76, 80, 81], or elastic substrates with arrays of micro or nanoscopic pillars [82, 83, 84, 85].

The force measurements performed through the use of AFM are based on the evaluation of the vertical and lateral deflection (V_v and V_l respectively) of the cantilever, which is essentially a spring: knowing the spring constant k (mN/m and Nm/rad respectively) and the sensitivity s (nm/V and rad/V respectively) of the cantilever the conversion of the vertical signal into force and height and of the lateral signal into torque τ is possible [75]. Figure 5 displays how cell forces can be measured through AFM: when the height of the z-piezo of the AFM is kept constant, the vertical cantilever deflection is recorded and converted into force. Using such a setup Brunner et al. [75] have shown that a migrating keratocyte was able to generate, a signficant force (15 nN) in order to adjust its shape. This allowed it to successfully crawl under and ultimately past the obstacle represented by the AFM tip. A higher force (34 nN) exerted by the tip stopped the forward motion of the cell. If the force is fixed and the z-piezo of the AFM can move, the height of the cell can be measured as a function of force. In this way the authors were also able to record the maximum forces which were small enough to ensure that the cell morphology remained unchanged.

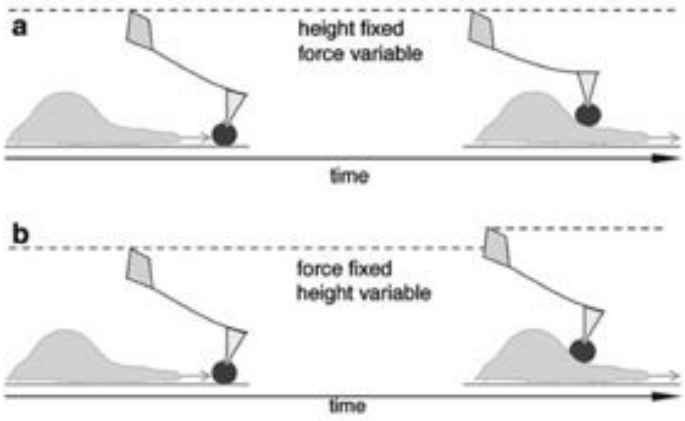

Figure 5: Cell force measured through AFM. A polystyrene bead (dark gray) glued to a cantilever-tip of an AFM was positioned on the substrate in front of a migrating cell. The cell moved toward the bead, crawled under it, and pushed the cantilever upwards. In constant height mode a), the z-piezo of the AFM was fixed, the vertical deflection of the cantilever was recorded, and calculated into force, whereas in constant force mode b), the piezo's z was not fixed and its movement was recorded. (Adopted from Brunner et al., 2006 [75] with permission).

.

The limits of this method are related to the complexity of the experimental set up: the velocity and the movements of the cells must be evaluated through the analysis of images recorded from the phase contrast image of the AFM or using the interference microscopy techniques (IRM) and they also are fundamental parameters in the determination of the force. In addition, the force distance curves of cells are not so straightforward to be interpreted, as cells are not hard balls with sharp boundaries, but are somewhat fuzzy and show non-linear compression behavior, which also depends on the rate of compression. The result is that the accuracy of the measurement is rather low and several groups begun to look for other possible methods.
In other works, two micropipettes integrated with a a force transducer have been used with mammalian cardiomyocytes (CMs) glued to the tips to measure active contraction force and passive tension force. In this technique, special adhesives for cell attachment are required and result in a low success rate of attachment [79, 86]. The carbon fiber-based technique in contrast to that, does not require adhesives and thus allows simpler cell handling. The attachment is likely caused by elctrostatic forces between the carbon fibre surface and the CMs surface, which has been demonstrated using a slight contact between the fibres and the cell surfaces [87, 88]. The force gen-

erated by or applied to a single myocyte can be measured by either connecting the fiber to a sensitive force transducer or monitoring the deflection of the fiber. However, the experiment is time-consuming and not amenable to quantitative measurements in a high throughput manner as certain parameters are not repeatable from measurement to measurement [78].
The first time in which the deformation of flat elastic substrates have been used to detect traction forces exerted by cells was in 1980 by Harris [89]. In his work he showed that the locomotion of fibroblasts on a soft elastomeric substrate leads to the formation of visible wrinkles. To overcome the complex problem of quantitatively link the size of the wrinkles and the amplitude of the generated force, other techniques have been developed in order to achieve a better spatial resolution, especially at individual adhesion sites [84, 90, 91].

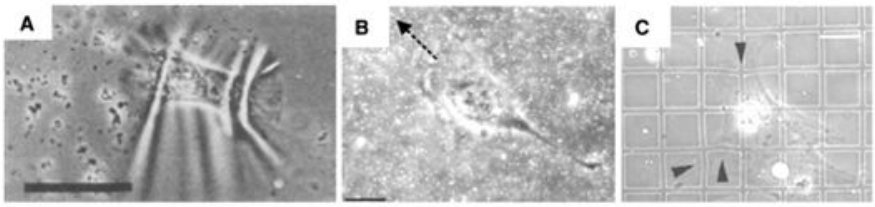

Figure 6: Forces exerted by cells on flexible continuous substrates. A) Wrinkles on a silicon sheet induced by fibroblast. Scale bar is 50 μm. B) Deformation of PAA gels visualized by embedded fluorescent beads induced by the migration of a 3T3 fibroblast. Scale bar is 20 μm. C) Traction forces exerted by a fibroblast on micropatterned flexible substrate. Scale bar is 30 μm. (Adopted from Le Digabel et al., 2010, [84] with permission).

All these methods are based on the conversion of the displacement of the substrate at the focal adhesion points to the force exerted thus the accuracy of the quantification of this displacement is crucial. For this reason, the most recent methods developed employ fluorescent beads that are used as markers for the deformation and that are embedded in transparent elastomers where the stiffness can be regulated and the surfaces can be functionalized in order to assure an optimal adhesion of the cell [84]. Figure 6 shows an example of cell forces measured by a flexible substrate with embedded fluorescent beads to better visualize surface deformations. Quantification of force can be made through complex computation methods that convert maps of substrate deformation into maps of traction stress. This inverse operation has the limit to require assumptions about the force distribution patterns and it does not lead to unique solutions. To simplify the measurement Polio et al. fabricated polyacrylamide (PAA) substrates with

an array in which 1µm fluoresecent markers are dispersed, which are tracked as a function of time, so that single particle trajectories are obtaineds and traction forces are modeled as discrete point forces [92].
A further possible strategy to detect cell forces in an high throughput manner has been developed based on the use of elastomeric microstructured substrates [82, 85, 93, 94, 95]. In this last approach, the force applied by cells is evaluated measuring the deflection that cells induce on substrates composed of flexible arrays of micropillars. These pillars are usually fabricated using polydimethylsiloxane (PDMS) poured on stamps made with silicon wafers. In the case of silicon wafers, the microfabrication process usually consists on a deposition of a thin layer of photoresist on a silicon wafer to create an etching mask, followed by the etching of the uncovered paths of the silicon wafer up to the desired length. The silicon wafer are then silanized to make them anti-adhesive and covered with PDMS that is peeled-off after curing it. PDMS is commonly used because it is transparent, elastic, and it has a Young's modulus that can be modulated in a certain range changing the ratio between elastomeric base material and cross-linker.

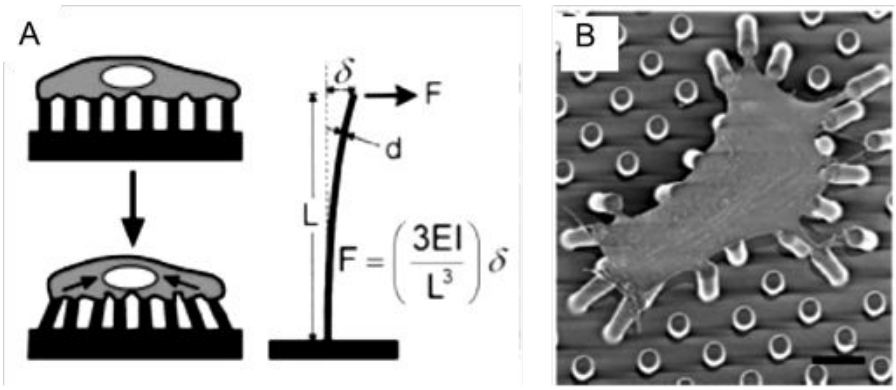

Figure 7: Cell force measured through arrays of posts. A) With the appropriate surface density of vertical posts positioned on a substrate, a cell should spread across multiple posts as depicted. Under the proper geometric constraints of post height and width, cells exerting traction forces would deflect the elastomeric posts. B) Fibroblast spread on the top of micropillars. Scale bar is 10 µm. (Adapted from Tan et al., 2003, [85] with permission).

The mechanical properties of the pillars can be modulated varying the aspect ratio of the posts and nano-Newton forces can be detected: the deflection of each pillar gives a direct measurement of the local force exerted by the attached cells independently of the forces acting on the neighboring posts. For small deflections, the posts behave like

simple springs. In this case the deflection is directly proportional to the force applied by the attached cell and Equation 1 can be used to determine the force:

$$F = \left(\frac{3EI}{L^3}\right)\delta \tag{1}$$

where F, E, I, L and δ are the bending force, Young's modulus, moment of inertia, length, and resulting deflection of the post [85]. In Figure 7 on the left a scheme of a cell adhering to the microstructured substrate and the method of calculation of the force are depicted; the right part of the image shows a fibroblast which spread on the substrate and that is bending some micropillars, deflecting them.

1.4 HUMAN PLURIPOTENT STEM CELLS

1.4.1 *Human embryonic stem cells and human induced pluripotent stem cells*

Stem cells are undifferentiated cells that have the capability to differentiate into specialized cells and to subdivide indefinetely to produce more stem cells. The self-maintenance capacity is given by the peculiar characteristics of cellular division which is regulated by two main mechanisms: symmetric proliferative division gives rise to two identical cells from the mother cells, while symmetric differentiative division generates two identical cells but more differentiated ones [96]. These two mechanisms maintain a constant percentage of stem cell in an organism. Stem cells allow tissues to maintain a proper architectural, cytological and biochemical structure in order to guarantee the correct functionality of the different organs. In mammals, there are two broad types of stem cells: embryonic stem cells, which are isolated from the inner cell mass of blastocysts, and adult stem cells, which are found in various tissues. Adult stem cells are multipotent cells which can give rise to all cell types within one particular lineage [97]. Embryonic stem cells ESCs are pluripotent cells: they can replicate indefinitely while maintaining an undifferentiated state and they can also differentiate into a wide range of cells, which maintain the original hereditary information but reduce the potential of their genome to specialize and acquire defined functions. The first report of human embryonic stem cells (hESCs) was given by Thomson et al in 1988. [98]. Pluripotent cells in the embryo have the capacity to give rise to differentiated progeny representative of all three embryonic germ layers, as well as the extraembryonic tissues that support development. Under certain conditions, pluripotent stem cells (PSCs) can be propagated indefinitely in vitro and still maintain the capacity for

differentiation into a wide variety of somatic and extraembryonic tissues [99]. Figure 8 describes the process of generation of hESCs: donor embryos are first obtained after in vitro fertilization and allowed to develop in vitro. Pluripotent cells are then isolated either from the inner cell mass of pre-implantation blastocysts or from 4, 8, or 16 - cell stage morulae. Finally, isolated cells are plated in defined hESCs medium with or without feeder cell layers to propagate and select for pluripotent cell populations. These processes have resulted in hESCs lines able to generate tissues from all three embryonic germ layers and the germline. Embryonic stem cells provide a unique resource for the functional analysis of early human development. For example, hESCs are used to identify polypeptide factors involved in differentiation and proliferation of committed embryonic progenitor cells [99]. Furthermore, because embryonic stem cells (ESCs) can in principle serve as an unlimited source of any cell type in the body, hESCs could yield highly effective in vitro models for use in drug discovery programs, and provide a renewable source of cells for use in transplantation therapy. Since their discovery, much attention has been devoted to the potential applications of stem cells in biology and medicine [96, 100]. The properties of pluripotentiality and immortality (correlated with telomerase expression) are unique to ESCs and enable investigators to approach many issues in human biology and medicine for the first time.

Embryonic stem cells potentially can address the shortage of donor tissue for use in transplantation procedures, particularly where no alternative culture system can support growth of the required committed stem cell. However a strong debate arose in the scientific community on whether the use of hESCs is ethical or not. In fact, they derive from the inner cell mass (ICM) of a 5-days fertilized blastocyst. When the clonal expansion begins, only cell colonies showing undifferentiated state, high clonal capacity, pluripotency and normal karyotype are kept and expanded.

The ethical issues centered on the use of embryos for the obtainment of human embryonic cells, have been a driving force towards the development of alternative strategies for obtaining similar and such powerful cells. Several different strategies such as nuclear transplantation, cellular fusion, and culture induced reprogramming have been tested to induce the conversion of differentiated cells into an embryonic state [101]. In 2007 Yamanaka found a way to overcome the ethical issues raised by hESCs, by reprogramming adult somatic cells to a pluripotent state. Mouse embryonic fibroblasts and adult fibroblasts were successfully reprogrammed to pluripotent ES-like cells after viral-mediated transduction of the four transcription factors Oct4,

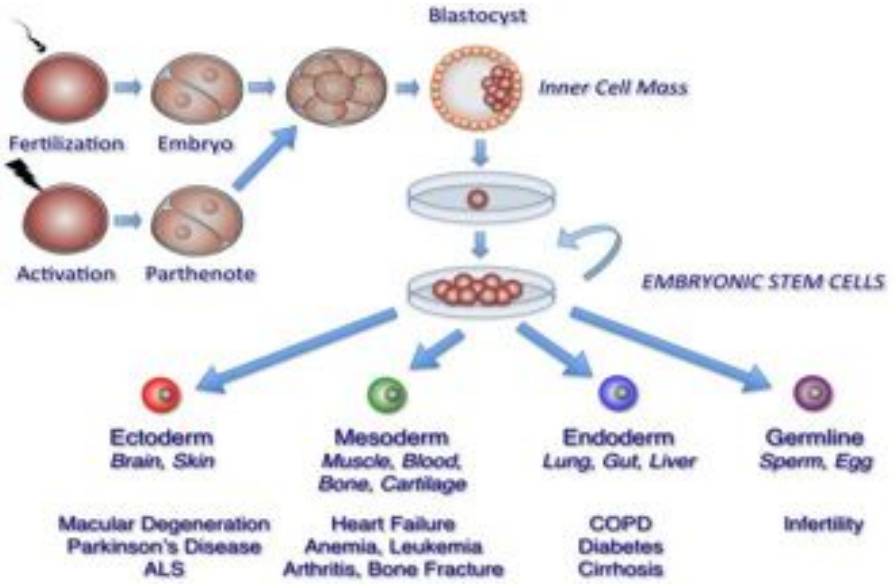

Figure 8: Generation of human embryonic stem cell lines. Donor embryos are first obtained after in vitro fertilization or by egg activation (parthenogenetic embryos), and allowed to develop in vitro. Pluripotent cells are then isolated either from the inner cell mass of pre-implantation blastocysts or from 4, 8, or 16 -cell stage morulae. Finally, isolated cells are plated in defined hESCs medium with or without feeder cell layers to propagate and select for pluripotent cell populations. These processes have resulted in hESCs lines able to generate tissues from all three embryonic germ layers and the germline. (Adopted from Yabut and Bernstein, 2011. [100] with permission).

Sox2, c-myc, and Klf4 followed by selection for activation of the Oct4 target gene Fbx15 [102]. Figure 9 explains the different steps to obtain induced pluripotent stem cells (iPSCs) lines. Current protocols allow to obtain iPSCs which are considered almost indistinguishable from ESCs [103, 104]. In Figure 10 a scheme that describes the process of reprogramming of somatic cells to a pluripotent stage is reported. Thus, scientist have now the possibility to use iPSCs instead of ESCs. However, the process to obtain iPSCs is time consuming and expensive therefore both ESCs and iPSCs are currently largely used when pluripotent stem cells lines are required.

1.4.2 *Stem cell differentiation*

Three basic methods have been developed to promote differentiation of ESCs: (i) the formation of three-dimensional aggregates known as embryoid bodies (EB), (ii) the culture of ESCs as monolayers on ex-

Figure 9: Generation of hiPSCs lines. Adult somatic cells, i.e. skin fibroblasts, are taken from patient, cultured *in vitro* and reprogrammed with specific factors (i.e. Oct4, Sox2, Klf4, Myc, Nanog, Lin28). Reprogramming can be done by viral vectors or by modified mRNAs. Pluripotent cells colonies are selected and and expanded in culture and can be differentiated to specific cell types. (Adapted from Carr et al. 2013, [105] with permission).

tracellular matrix proteins, and (iii) the culture of ESCs directly on supportive stromal layers. Each method demonstrates that ESCs can differentiate into a broad spectrum of cell types in culture [106].

1.4.2.1 *Ectoderm differentiation*

Ectoderm differentiation leads to the development of the central nervous system, hair, epidermis. The induction (i.e. the series of extrinsic and intrinsic processes that guide the cells to follow a specific developmental pathway) of ectoderm is often referred to as the "default" pathway, as neuroectoderm readily develops in cultures that contain no serum. Neuroectoderm is defined as the part of the ectoderm that give rise to the central and peripheral nervous system. Neuroectoderm induction is inhibited by the presence of bone morphogenic protein (BMP), Wnt, and activin/Nodal signaling [107, 108, 109]. Ying et al. (2003) studied development of the neuroectoderm lineage from mouse ESCs using a reporter cell line with green fluorescent protein (GFP) targeted to the neuroectoderm-specific gene Sox1. They clearly showed that induction of neuroectoderm is dependent on fibroblast growth factor (FGF) signals endogenously produced by the differentiating ESCs. Neuroectoderm generated from ESCs can

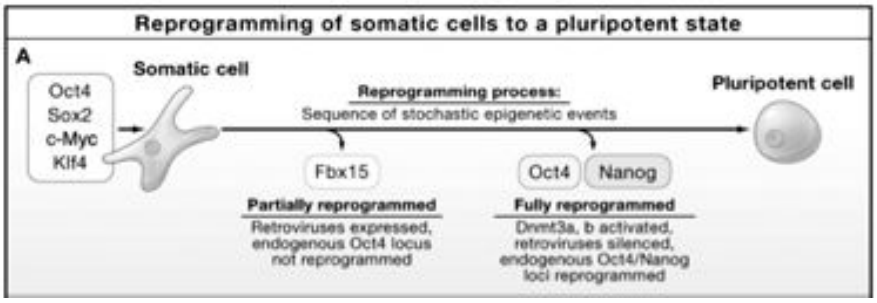

Figure 10: Reprogramming of Somatic Cells to a Pluripotent State. Transduction of the four transcription factors Oct4, Sox2, c-myc, and Klf4 into fibroblasts initiates the conversion to partially reprogrammed cells that express Fbx15 or to fully reprogrammed iPSCs cells that express Oct4 or Nanog. The process involves a sequence of stochastic epigenetic events. (Adapted from Jaenisch et al. 2008, [104] with permission).

be specified to neuronal subtypes, using factor combinations known to regulate these steps in the early embryo [106]. In addition to the neural lineages, ESC-derived ectoderm can also generate epidermal lineage cells. As observed in vivo, the BMP-signaling pathway does play a role in ectoderm specification in ESCs cultures as BMP signaling blocked neural differentiation and promoted epidermal development [110].

1.4.2.2 *Mesoderm differentiation*

Mesoderm differentiation forms the cells that represent most part of the body's internal supporting structure, including the blood, muscles, bones and heart. The early stages of mesoderm induction can be monitored by the upregulation of Flk-1 and PDGFR, receptors that are broadly expressed on subpopulations of this lineage [111]. Several studies have provided insights into the signaling pathways that regulate mesoderm induction. Park et al. [112] showed that BMP signaling is required to induce Flk-1^+ hematopoietic mesoderm from populations that express Brachyury, indicating that this pathway functions at the level of mesoderm induction. In a more recent study, Nostro et al. [113] demonstrated that the generation of hematopoietic mesoderm is dependent on a combination of Wnt, activin/Nodal, and BMP signaling, and that upregulation of Flk-1 correlated with commitment to a mesoderm fate. Concerning cardiac mesoderm, findings from several studies suggest that transient inhibition of Wnt/b-catenin signaling at this stage is essential for the generation of this population [114, 115]. Wnt/b-catenin is thus required for mesoderm induction,

whereas its inhibition is subsequently required for specification of precardiac mesoderm.

1.4.2.3 *Endoderm differentiation*

Endoderm germ layer forms many of the internal organs, including the pancreas and the liver. High levels of activin/Nodal signaling have been reported to efficiently induce definitive endoderm committment [108, 116]. Progression of the anterior cell population to definitive endoderm depends on sustained activin signaling. Increased Nodal signaling are also required for definitive endoderm formation in the early embryo [117]. Once induced, endoderm forms an epithelial sheet that undergoes specification to distinct regions known as foregut, midgut, and hindgut. This specification is controlled in part by factors secreted by surrounding mesoderm-derived tissues. By translating findings from the embryo to ESCs cultures, FGF and BMP 4 together were shown to induce a hepatic fate in activin-induced endoderm [118], whereas retinoic acid combined with inhibition of sonic hedgehog protein resulted in specification to a pancreatic fate [119].

1.4.3 *Human pluripotent stem cells microenvironment*

During embryonic development, the cell microenvironment plays a fundamental role in determining cell fate. Cells in their native tissues reside in an extremely complex environment constituted of other cell types, extracellular matrix proteins, and structural templates guiding their orientation and maintaining the three-dimensional (3D) architecture [63]. In addition, cell behavior is regulated by an intricate network of short and long range communications signals between single cells and/or tissues that occurs through a vast cascade of signaling pathways [120, 121, 122]. This dynamic environment, where cells grow and develop, is frequently called "niche". The stem cells and microenvironment may influence each other during development, and reciprocally communicate to maintain each other during adulthood. The niche protects stem cells and represents the physiological space where the signals that mediate the balanced response of stem cells to the needs of organisms are regulated [123]. In Figure 11 the elements of the local environment that participate in regulating the system of a stem cell in its tissue state are depicted.

A pluripotent stem cell can be considered naked without its own microenvironment, and may not behave as expected during pluripotency and differentiation. For this reason, during the past few years one of the biggest aims has been trying to recreate in vitro the var-

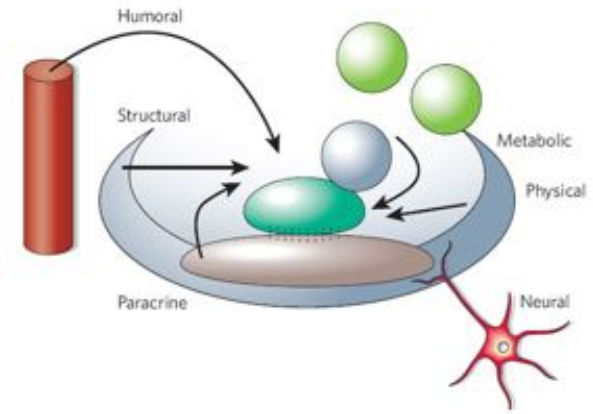

Figure 11: Components of the local microenvironment, which participate in regulating the system of a stem cell in its tissue site. These include the constraints of the architectural space, physical engagement of the cell membrane with tethering molecules on neighbouring cells or surfaces, signalling interactions at the interface of stem cells and niche or descendent cells, paracrine and endocrine signals from local or distant sources, neural input and metabolic products of tissue activity. (Adopted from Scadden, 2006 [123] with permission).

ious components of the niche found in vivo. For regenerative therapies, models and drug screening purposes, cell proliferation and differentiation must be accurately controlled. The components of the *in vitro* cell microenvironment which constitute the so-called niche are mainly given by: i) substrate, ii) soluble compounds of the environment and iii) electrical stimuli. The cells adhere to a specific substrate, which is defined by a set of chemico-physical properties, such as chemical composition, stiffness or surface topology. The cells are immersed in a aqueous environment composed by a complex ensemble of factors that can be either produced by the cells themselves, endogenous factors, or by other cells in the surroundings, exogenous factors. Finally, another important component of the stem cell niche is given by the electro-physiological stimuli which are particularly relevant for electro-excitable cells [63]. Microengineering technologies helps in reproducing cell niche conditions *in vitro*, in order to possibly reproduce some features of adult tissue types or to induce desired and controlled cell response.

1.5 CHALLENGES IN BIOLOGICAL *in vitro* STUDIES

The development of *in vitro* platforms to monitor cell response is of paramount importance for many aspects of biological research,

mainly because of the rapidity of performance, the ease of use and the lower cost of *in vitro* studies compared to the *in vivo* ones. In order to be effective, the new generation *in vitro* assays must overcome some important limitations of actual screening systems, which are mainly based on cytotoxicity measurements of cells randomly plated on a protein coated plastic surface [124]. In particular, new assays should: (i) provide information directly related to cells biology; (ii) be highthroughput for fast and low cost screening; (iii) integrate a technology able to reproduce defined physiopathological conditions or precise dosage of drugs; (iv) be user friendly [125]. Furthermore, *in vitro* models should not be based on animal cells.

While an animal cell source is very useful, for example during the troubleshooting phase in the development pipeline of a technological device or for basic science research on cell patho-physiological mechanisms, the use of human cells is irreplaceable in sight of a clinical application of the developed device or for specific studies on mechanisms involved in human pathologies. Human and animal biology can be quite different, both at the physiological and at the cellular level, and such differences can be the cause of withdrawal from the market of several approved drugs. Furthermore, the tests *in vivo* raises several ethical and economical issues and should be employed only after a decision-making process based on *in vitro* tests that reproduce in the most reliable way the condition of the physiological environment.

In this scenario, the use of human pluripotent stem cells can give scientists a new tool for studying genetic and molecular basis of cells physiology and diseases on a much relevant model. The ability of stem cells to differentiate into nearly any cell in the body gives them the potential to be the source of therapy for many currently incurable illnesses. They are important for *in vitro* studies of normal human embryogenesis, abnormal development (through the generation of cell lines with targeted gene alterations and engineered chromosomes), human gene discovery, and drug and teratogen testing and as a renewable source of cells for tissue transplantation, cell replacement, and gene therapies [126]. Nevertheless, human pluripotent stem cells (hPSCs) potential can be exploited only if reproducible and reliable *in vitro* tests are performed.

Microtechnology, by allowing organization and manipulation of cells and molecules at biologically relevant length scales, enables control of the cellular environment and assessment of cell functions with cellular resolution. This provides opportunities to create the condition necessaries to overcome the current limits of *in vitro* studies.

1.6 *in vitro* STUDIES OF NUCLEAR SHAPE AND STRUCTURE IN EUKARYOTIC CELLS.

Nuclear shape and structure in eukaryotic cells are recognized to be deeply related with cell function during developmental, physiological and pathological modifications [127, 128, 129, 130, 131, 132]. The mammalian cell nucleus is a membrane-bound organelle that contains the machinery essential for gene expression. Although early studies suggested that little organization exists within this compartment, more contemporary studies have identified an increasing number of specialized domains or subnuclear organelles within the nucleus [133, 134]. In some cases, these domains have been shown to be dynamic structures and, in addition, rapid protein exchange occurs between many of the domains and the nucleoplasm [135]. An extensive effort is currently underway by numerous laboratories to determine the biological function(s) associated with each domain. Figure 12 shows a scheme of the cell nucleus and of its different nuclear domains.

The nucleus regulates cell division and transcription processes, and it is exposed to mechanical stimuli from inside and outside the cell. Mechanical stimuli are transmitted by the cytoskeleton to the highly specialized structure nuclear membrane. The nuclear envelope connects to and interacts with the inner nucleus through the nuclear lamina, a dense protein network that is crucial for structural support of the nucleus. Lamins are also connected to chromatin strucutes and gene regulatory complexes: in particular, two types of lamins can be distinguished by whether they remain associated with the membrane vescicles during mitosis (B-type) or not (A-type). A-type lamins have a central role in defining interphase nuclear organization [129]. Mechanics of the interphase cell nucleus is of paramount importance for the biological function of healthy cells and it is related to several pathologies. A growing number of studies try to analyze nuclear mechanics behavior, and there is an emergent topic in scientific research, which investigates the possible relationship between nuclear properties and cell diseases [127, 128, 130, 136].

Nuclear stiffness has been evaluated and compared in healthy and pathological cells, and a connection between pathological behavior of the cells and nuclear stiffness was reported [130, 132, 138, 139, 140, 141]. Nuclear stiffness increases from human embryonic stem cells to differentiated cells [141] and chromatin is shown to be less condensed in the pluripotent stage [142, 143]. The most recent studies consider nuclear mechanics as a property of the nucleus that also depends on the cytoskeletal structure [144, 145, 146, 147]. It was proposed that me-

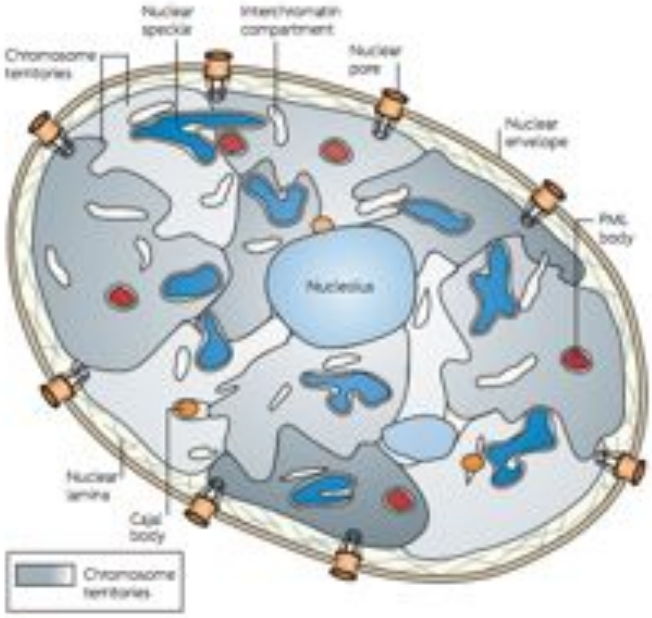

Figure 12: Organization of the mammalian cell nucleus. The nucleus is characterized by a compartmentalized distribution of functional components. The nuclear envelope contains pores and rests on a meshwork of intermediate filaments, the nuclear lamina. Nucleolar organizer regions cluster to form nucleoli. Further topographical details that are shown in this schematic nuclear section are representative for the chromosome territory-interchromatin compartment. (Adopted from Lanctot et al., 2007, [137] with permision).

chanical forces transmitted to the nucleus through the cytoskeleton can lead to modification in gene expression [148]. Therefore changes in cell shape can produce alteration of nuclear shape and function [149]. Studies on adult endothelial cells and on cancer cells reported a clear connection between cyotskeletal organization and nuclear deformability [145, 149]. In particular, the both studies show how actin filaments are essential factors in the mechanical process of nuclear remodeling. Studies on cancer cells show a strong deformability of the cell, and in particular of the nucleus, which adapts to the surrounding micro-topography [139, 145]. Despite the described large nuclear deformation, cancer cells are still capable to divide, proliferate and differentiate [139, 145]. Concomitant with these recent discoveries, significant advances have been made in terms of identifying the molecular links between the nuclear envelope and the cytoplasmic filaments [9, 141] and new insights have been gained into the mechainisms that regulate nuclear shape and stiffness. Swift et al. in a recent work re-

vealed that lamin-A plays a fundamental role in nuclear stiffness and in regulation of the process of differentiation from mesenchimal stem cells to soft or stiff tissues [150]. Lamin-A seems to be the protein of the nuclear envelope that mainly interact with the cytoskelton. Low level of lamin-A lead to differentiation in soft tissue (fat), increased levels of lamin-A leads to differentiation in stiffer tissue (bones). This same work [150] shows also that high lamin-A level impedes nuclear remodeling under stress.
In stem cells at the pluripotent stage, the cell nucleus has a poor cytoskeletal organization and a not yet developed nuclear envelope. Along the process of differentiation, the cell acquires a more and more mature organization of the cytoskeleton with the development of actin filaments and expression of nuclear proteins and lamins. Studies on stem cells can represent an effective model to evaluate transitions in nuclear stiffness from the pluripotent to the differentiated stage and to elucidate the underlying mechanisms.

1.7 *in vitro* STUDIES OF CARDIOMYOCYTES

The heart is responsible for receiving deoxygenated blood from the periphery, propelling this blood through the pulmonary circulation, and ultimately distributing the oxygenated blood to peripheral tissues. Contraction performance of heart muscle cells, called cardiomyocytes (CMs), mainly determine cardiac output [91, 151]. These cells are able to develop intense forces upon contraction thanks to their specific subcellular morphology [151]. The cardiac myocyte is a specialized muscle cell composed of bundles of myofibrils that contain myofilaments. The myofibrils have distinct, repeating microanatomical units, termed sarcomers, which represent the basic contractile units of the myocyte. In a physiological cardiac myocyte myofibrils are formed by aligned sarcomers. The sarcomer is composed of thick and thin filaments: myosin and actin, respectively. Actin and myosin filaments are anchored within a dense structure called Z-band, determining the boundaries of each sarcomer. Chemical and physical interactions between the actin and myosin cause the sarcomer length to shorten, and therefore the myocyte to contract during the process of excitation-contraction coupling (ECC) [152]. Figure 13 A shows the structure of a heart cell, with the sarcolemma, the sarcoplasmic reticulum and the sarcomeres. In Figure 13 B the mechanism of contraction through sliding of thick and thin filaments is depicted.

ECC is the process whereby an action potential triggers a myocyte to contract, and involves the following cascade of events: voltage-gated calcium channels open, intracellular calcium increases, con-

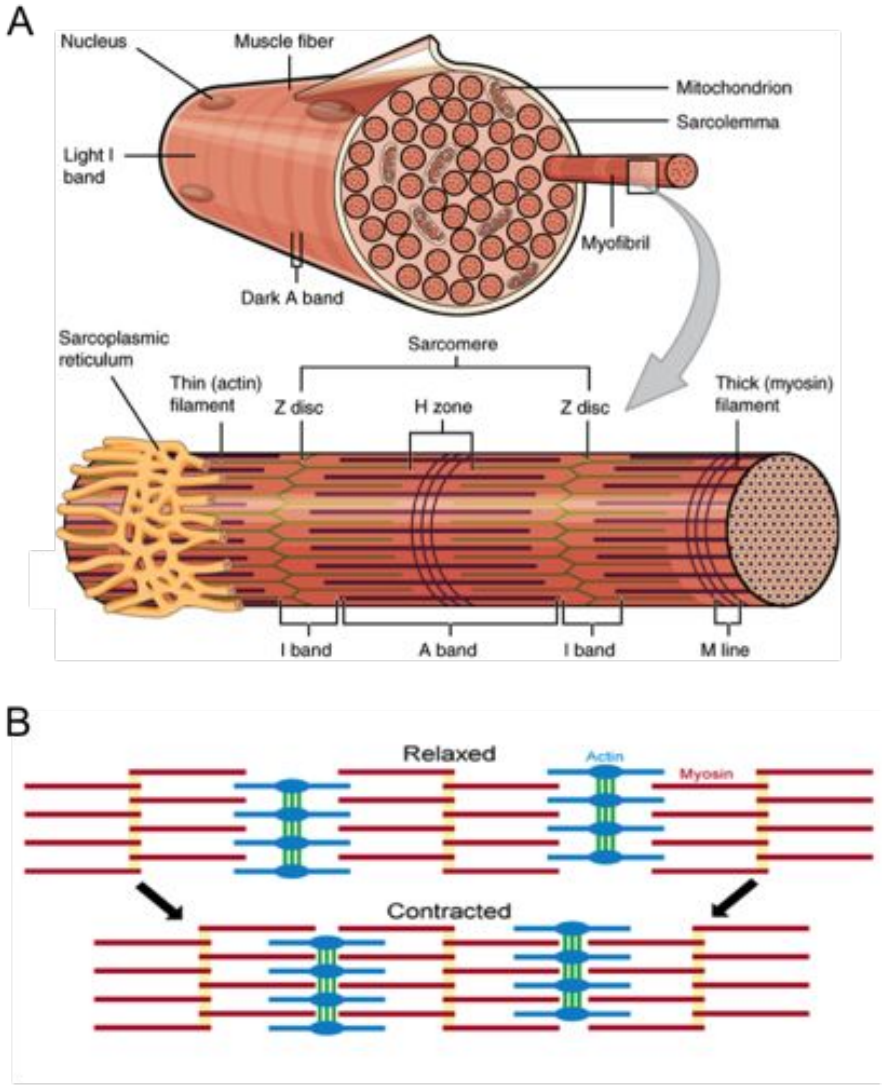

Figure 13: Structure and mechanism of contraction in human cardiomyocytes. A) Scheme of the heart muscle cell structure: sarcolemma, sarcoplasmic reticulum, and t-tubules diving down from the sarcolemma to coordinate contraction. B) Scheme of the mechanism of contraction through sliding of thick and thin filaments.(Adapted from `http://www.primepantrystuff.info/`).

tractile proteins are activated, and actin-myosin interactions shorten the contractile elements. The process of ECC is represented in Figure 14: Ca^{2+} flows into the myocyte through (voltage-activated) L-type calcium channels and, triggered by the influx, additional calcium is released from intracellular stores (sarcoplasmic reticulum; SR), via calcium-activated release channels (ryanodine receptors). Removal of calcium from the cytosol, responsible for the mechanical relaxation, is caused by rapid transportation of the same amount of

calcium from the cytoplasm by three different mechanisms: the sarcolemmal Ca^{2+} ATPase; the $\frac{Na^{+}}{Ca^{2+}}$ exchanger (NCX); and the Ca^{2+} ATPase in the SR (SERCA) [153]. In cardiac myocytes, the contraction force produced by the contractile apparatus is directly related to the momentary calcium concentration in the cytoplasm. The continuous contraction-relaxation cycle, characteristic of heart function, is created by oscillation-like increases and decreases in calcium concentration, the Ca^{2+} transients.

The deranged contraction of cardiomyocytes can cause a dysfunction of cardiac pumping and circulatory failure, which is currently the leading cause of mortality and morbidity in Western Countries. Detailed assessment of cardiac function can help to elucidate the pathophysiological mechanisms of heart failure and also facilitate development of novel therapeutic interventions. Although cardiac function is commonly evaluated through methods such echocardiography that are applied on intact hearts [154], assessing CMs response and behavior at the cellular level offers several advantages: the study of isolated cardiomyocytes enables observation of active and passive properties that can be attributed to cell autonomous mechanics, in the absence of confounding factors such as neurohormonal activities, properties of cell matrix protein and surrounding cells [155].

In this context, the development of an *in vitro* platform to monitor CMs response could be of paramount importance for many aspects of cardiology research. Several *in vitro* heart models based on artificially engineered cardiac tissue have been proposed, both at the micro- and macro- scale [156, 157, 158, 159, 160], but they are all based on animal derived cardiomyocytes. Human and animal cardiology are difficult to compare. The use of human pluripotent stem cells derived cardiomyocytes can provide scientists the solution for studying CMs physiologycal and pathophysiological mechanisms on a much relevant model. In the last few years, much effort has been put in the use of hPSC-CMs to find new possible pharmacological treatments for heart diseases [161, 162], as well as to study the developmental and pathological mechanisms at the cell level [163, 164]. Grafting of hPSC-CMs into compromised hearts of animal models has also be performed, showing their potential in regenerative medicine to treat cardiac dysfunctions [165, 166, 107]. Since these are the cells that would be effectively injected in the patient and used in the clinical practice, hPSC-CMs should be employed in order to perform relevant biological and physiological assays. However, a serious matter of concern for all applications is the early and immature phenotype displayed by CMs and, consequently, there is great interest in methods to evaluate and possibly improve their process of maturation *in vitro*. The

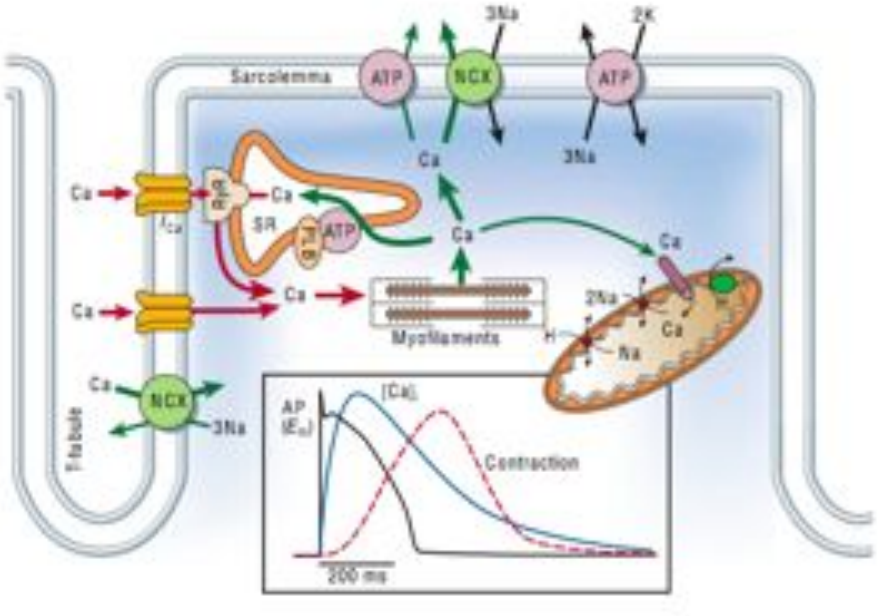

Figure 14: Scheme of excitation-contraction coupling (ECC). Ca^{2+} transport in ventricular myocytes. Inset shows the time course of an action potential, Ca^{2+} transient and cotraction measured in a rabbit ventricular myocyte at 37° C. NCX, $\frac{Na^{+}}{Ca^{2+}}$ exchange; ATP, ATPase; PLB, phospholamban; SR, sarcoplasmic reticulum. (Adopted from Bers, 2002 [152] with permission).

analysis of hPSC-CMs functional maturation shouldn't omit the evaluation of the most important outputs of heart tissue: force generation and contraction characteristics. Unfortunately, current protocols for deriving cardiomyocytes from stem cells and induced pluripotent stem cells mostly rely on staining for cardiac myocyte markers rather than on force generation because of the lack of reliable and high-throughput methods to quantify such parameter. In fact, despite that several experimental methods have been employed to quantify cellular forces, as discussed in Section 1.3.1, success has been limited. Some of these methods fail in reproducibility, other are too complex to be used in a high-throughput manner. Furthermore, most of them study isolated CMs on a flat 2D environment. The use of an elastomeric 3D environment better reproduce the mechanical environment of native heart tissue: the approaches based on the use of polydimethylsiloxane (PDMS) substrates, characterized by arrays of micropillars [78, 82, 83, 84, 90, 167] have shown that the micropost platform is a valid approach for assessing the contractile properties of various types of cardiomyocytes. The contraction force can be derived from the deflection of the elastic micropillar induced by cell shortening

[167]. However, the majority of these studies have been applied to adult or neonatal rat cardiomyocytes. More recently, measurements of contraction forces of hESC-CMs [168] and human induced pluripotent stem cell derived-cardiomyocytes (hiPSC-CMs) [169] have been reported. In particular, Rodriguez et al. [169] characterized contraction force, velocity and power of hiPSC-CMs on single cardiomyocytes spreading on dense arrays of elastic micropillars: the total force produced by a single cell was determined by summing the absolute magnitudes of the force measured at each post beneath the cell. However, the resulting sums are not equivalent to the gold standard axial measurements. Additionally, this method fails to induce an elongated shape of the cells, which corresponds to a physiological sarcomere alignment and is a typical feature of mature CMs. The alignment of the sarcomers strongly influences cell contractility. Taylor et al. [168] evaluated uni-axial contraction forces of hESC-CMs by using a thermoresponsive sacrificial support layer in conjunction with arrays of widely separated elastomeric microposts. Through this method they could prescribe elongated cell shapes. However, through their approach the only parameter that was quantified was the final contraction force exerted by the cell. Despite the mentioned works have been proposed to quantify hPSC-CMs contraction forces, none of them take into account the relevance of information on calcium dynamics combined with the study of contraction forces. Calcium dynamics, in parallel with cell morphology, is one of the critical aspects that define CMs contractility and functionality [153]. A complete and reliable analysis of the mechanism of contraction in CMs cannot omit the study of calcium dynamics.

2

AIM AND STRATEGY

2.1 AIM OF THE WORK

Cellular processes such as adhesion, migration, growth, secretion, and gene expression are triggered, controlled, or influenced by the biomolecular three-dimensional organization of cell-surface contact [61, 63]. This organization cannot be straightforwardly reproduced in the laboratory, however modern methods in microtechnology enable researchers to generate complex environments at a biologically appropriate resolution. When biological studies are performed *in vitro*, it is important to consider cell-surface interaction. In this context, the general aim of this work is:

- To fabricate substrates where mechanical, chemical and topological properties of the surface can be tuned according to the specific biological aim.
- To employ such substrates to realize an *in vitro* platform where physiological an pathophysiological parameters of the cells can be deduced and quantified.

Since human stem cells provide unique opportunities for understanding basic biology, for developing tissue models for drug testing, and for clinical applications in regenerative medicine, we focused our attention on these kind of cells. Therefore, we applied our engineered substrates to human pluripotent stem cells and to human pluripotent stem cells derived cardiomyocytes. In particular we pursued two specific biological aims:

- To investigate the physical plasticity of the nucleus on human pluripotent stem cells and its evolution along the process of differentiation.
- To quantify contraction force and simultaneously detect calcium dynamics of human pluripotent stem cells derived cardiomyocytes with an elongated shape to evaluate a possible functional maturaton of the cells due to mechanical and morphological stimuli.

2.2 STRATEGY OF THE WORK

Microfabrication technology will be employed to fabricate substrates with the desired morphology and chemical properties.

2.2.1 *Studies on human pluripotent stem cells nuclei.*

To investigate the physical plasticity of the nucleus of human pluripotent stem cells, substrates formed by a lattice of micropillars with an interaxial distance that is smaller than the average nuclear size are fabricated. The substrates are fabricated in polydimethylsiloxane (PDMS), following the protocol developed by Davidson et al. [139]. Such substrates induce a geometrical constrain to cells and cell nuclei. Deformable nuclei can penetrate among micropillar interspaces and assume an unusual branched shape, stiffer nuclei do not penetrate among micropillar interspace or, if they do, they keep a oval or round morphology. Nuclear deformability can then be quantified in a straightforward way through image analysis of the fluorescent labeled nuclei. Through this method, the capability of the nucleus to adapt to the geometry of the environment can be investigated maintainig the structure and function of the cells. On the contrary, the use of other techniques, like micropipette aspiration technique, requires the inhibition of the cytoskeleton filaments [141]. However, as discussed in Chapter 1, the cytoskeleton actively interact with the nucleus to regulate nuclear shape, therefore we prefer to evaluate nuclear behavior on intact cells. Furthermore, nuclear deformability is quantified through post- processing images acquired by confocal or fluorescent microscopy: such images can be acquired without damage of the cells, evaluating possible changes in nuclear behavior day by day on the same cells.
In our study, the physical plasticity of cell nuclei and the evolution of such physical plasticty along the process of differentation are investigated. Figure 15 reports a scheme of the studies that will be performed. As first step, (Figure 15 A), we want to quantify and compare the physical plasticty of the nuclei of cells at the pluripotent, multipotent and adult stage, to understand if and how nuclear stiffness is related to the degree of differentiation, and therefore functional specialization, of the cell. To do that, we will seed pluripotent, multipotent and adult cells on microstructured substrates and we will evaluate nuclear deformability after 48 hours.

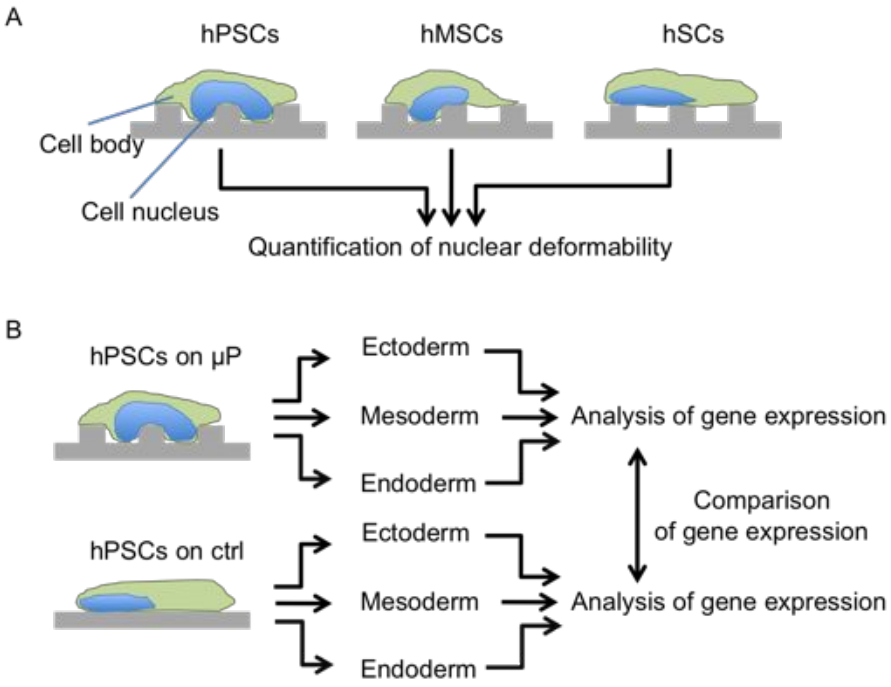

Figure 15: Analysis of nuclear behavior on microstructured substrates. A) human pluripotent stem cells (hPSCs), human multipotent stem cells (hMSCs) and human adult somatic cells (hASCs) are seeded on microstructured elastomeric substrates and nuclear deformability is quantified through image analysis of the nuclei for each cell line. B) hPSCs are seeded both on micropillared (μP) and flat (ctrl) substrates. In both cases ectoderm, mesoderm and endoderm early germ layer committment is induced. Possible differences in the expression of some specific genes between cells differentiated on μP or ctrl substrates ere evaluated through qRT-PCR.

In further experiments, (Figure 15 B), early ectoderm, mesoderm and endoderm germ layer committment will be performed directly on the microstructured substrates to evaluate:

- If ectoderm, mesdoderm and endoderm germ layers committment of hPSCs can take place by employing the standard protocols [170, 171, 172] when cells, and in particular cell nuclei, are constrained by the local morphology of the substrate.
- If cell nuclei increase their stiffness along the process of early germ layer committment also when cells and nuclei are constrained by the local morphology of the substrate.
- If there are differences in the expression of some specific genes, among cells where early germ layer specification takes place on microstructured substrates (where the process can be influ-

enced by the geometrical constrain of the substrate) and cells where early germ layer specification takes place in a standard flat substrate.

By the approach chosen, it is possible to monitor in a straightforward way the variation of nuclear shape, which can then be correlated to modification in the process of differentiation and in gene expression by immunostaining using specific marker or by quantitative real-time polymerase chain reaction (qRT-PCR). These experiments will provide further information on the effect of local geometry on the morphology of human pluripotent stem cells nuclei and on the consequence that nuclear morphological changes can have on cell function, in particular on cell differentiation. It has been reported that cell shape regulates commitment of human multipotent stem cells (hMSCs) to adipocyte or osteoblast fate [173]. We are interested in understanding if morphological reorganization of the nucleus (and therefore changes in the spatial distribution of DNA inside the nucleus) can affect the process of human pluripotent stem cells (hPSCs) early germ layer specification. To do so we want to implement a methodology that is highly reproducible, that allow the realization of several experiments in parallel, and that provides quantitative information on nuclear stiffness in intact and living cells.

2.2.2 *Studies on human pluripotent stem cells derived cardiomyocytes.*

In a second approach the micropillar technique is used to study the mechanical properties of hPSC-CMs. To this the cells are placed on the tops of flexible pillars, which are deformed upon cell contraction and expansion. Previous studies on cells in contact with micropillared surfaces were based on PDMS [78, 82, 83, 84, 90, 167]. A limit in using PDMS is related to the difficulty of permanently modify the chemistry of the surface of this elastomer. After polymerization and crosslinking, solid PDMS samples present a hydrophobic surface. This surface chemistry makes it difficult for polar solvents (such as water) to wet the PDMS surface, and may lead to non-specific adsorption of hydrophobic contaminants, which will depend rather strongly on the molecules present in the contacting and therefore might be more difficult to reproduce and understand. In addition one major problem of PDMS based systems is the potential presence of low molecular weight siloxanes, which migrate to the surface. This is evidenced by the fact that PDMS materials feel very often slippery upon touch. Such thin layers can act as lubricants and completely alter the mechanotransduction between the cells and the surface as significant dissipation within the lubricant layer or slipping at the lubricant-PDMS interface

cannot be excluded. Atmospheric air plasma and argon plasma oxidation can be used to alter the surface chemistry, adding silanol (SiOH) groups to the surface. This treatment renders the PDMS surface hydrophilic, allowing water to wet it. The oxidized surface is due to the acidity of silanol groups slightly negatively charged when exposed to water close to neutral pH and thus resists adsorption of negatively charged species. Silanol group containing surfaces can be further functionalized by reaction with functional silanes such trichlorosilanes or trialkoxysilanes for example. Nevertheless oxidized surfaces are stable for only short periods of times in air. After a short period of time hydrophobic recovery of the surface is inevitable, independently from the surrounding medium, i.e. regardless of wether the surfaces are stored in vacuum, air, or water [174]. For this reason, when a stable chemical modification of the surface is required, we will fabricate the microstructured substrates using a different substrate chemistry.
To adapt to the specific biological aim, our platform requires to be fabricated using a polymer that can be easily microstructured and micropatterned. In this way both the topological and chemical properties of the surface can be tuned. To guide cell shape, we combine a cell-adhesive photocrosslinkable elastomeric polymer with a cell-repellent polymer. The cell-adhesive photoreactive polymer P(nBA-co-%MABP) consists of n-butylacrylate (n-BA) and methacryloyl-4-oxy-benzophenone (MABP). It has been shown in previous publications [175, 176], that these copolymers can be crosslinked upon brief exposure to UV light, yielding insoluble and intractable elastomeric networks. We choose to fabricate our substrates in P(nBA-co-%MABP) for different reasons:

- Before the crosslinking process, the polymer can be diluted in toluene. This solution can easily penetrate into the very small microstructures of a stamp and be used for replica-molding fabrication processes.

- After crosslinking the prepolymer through UV light exposure, the obatined elastomer has mechanical properties similar to that of PDMS. Such mechanical properties can be tuned varying the crosslinking density of the polymer.

- After crosslinking, the polymer presents an hydrophobic surface that can be easily functionalized by a layer of proteins that are adsorbed by the surface, promoting cell adhesion.

- Thanks to the presence of the benzophenone groups, the surface of the polymer can be activated by UV light and other

polymers can be photochemically attached to the top of it, modifying the chemistry of the surface.

After fabrication of P(nBA-co-%MABP) substrates, a thin layer of a cell-repellent polymer can be photochemically attached to the surface by UV light exposure. The layer can be attached everywhere except on selected areas of the P(nBA-co-%MABP) surface that are protected from UV light exposure by a photomask and that will be therefore kept cell-adhesive. In this work, we realize substrates where cell-adhesive areas have a rectangular shape that includes two micropillars: cells are guided to adhere to these cell-adhesive areas, extending between two micropillars. As the geometry of such an arrangement is non-symmetric, it could potenially allow to force the cells into elongated shape, which has been demonstrated to be very important to fulfill cardiac myocyte function [35]. In Figure 16 a scheme of the employed substrate and of elongated CMs anchored between two elastic micropillars is depicted.
In this work we employ polyacrylamide (PAA) as cell-repellent polymer, since surface-attached layers of PAA hinder the process of protein adsorption and therefore of cell growth [49, 48, 47]. PAA is obtained adding the photoinitiator Irgacure to a solution of acrylamide and deionized water. Both BP and Irgacure are inert in absence of light, therefore when the sample is irradiated with UV light through a chrome mask, in the dark areas of the mask the crosslinking of PAA to the P(nBA-co-%MABP) surface does not take place. On the contrary, the UV light that crosses the transparent areas of the mask, hits the sample activating a process of unspecific crosslinking that binds the PAA chains to the underlying P(nBA-co-%MABP) surface.

In Figure 16 the overall experiment is represented. The hESC-CMs are seeded on the engineered substrates. Then, a group of them are kept in culture for 1 week, another group is kept in culture for 5 weeks, after which calcium dynamics and contraction force of the cells are evaluated and a comparison between the two groups is performed. We compare these two groups of cells to understand if the combination of the mechanical stimuli (cells have to "labor" to deflect the micropillars) and elongated morphology of the cell, will entail a process of functional maturation of the cells, which is of paramount importance to employ such cells both to develop new pharmacological treatments, and in regenerative medicine. In fact, hPSC-CMs have a great potential in the study and therapy of heart diseases but their use is currently limited by the early and immature phenotype they display. For this reason, the implementation of a platform that induce and simultaneously measure the process of functional matura-

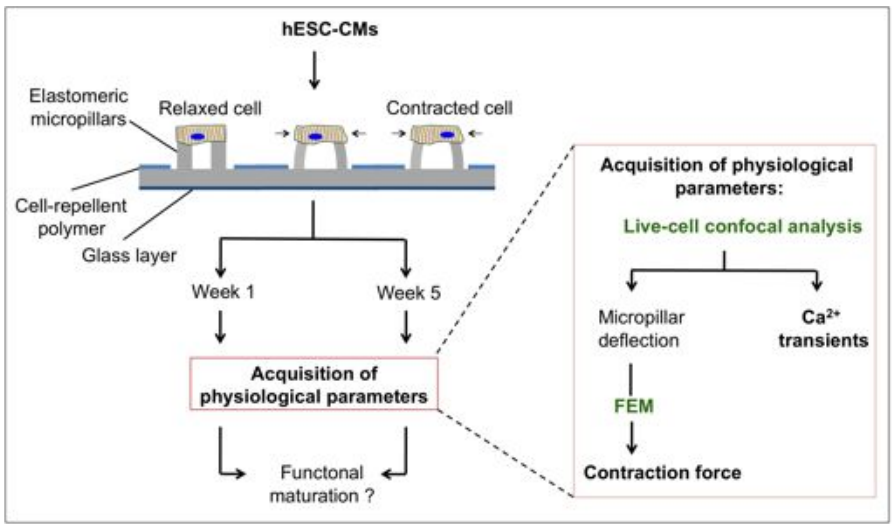

Figure 16: *In vitro* set up to simultaneously acquire contraction force and calcium dynamics on cardiomyocytes (CMs). Human embryonic stem cells- derived cardiomyocytes hESC-CMs are seeded on elastomeric microstructured P(nBA-co-%MABP) substrates that have previously been photopatterned with PAA to obtain cell-adhesive and cell-repellent areas. When cells are seeded on the substrate they adhere only to the cell-adhesive areas of the substrate and they elongate between two micropillars assuming a physiological shape. Calcium dynamics and contraction force of hESC-CMs are acquired after 1 week and after 5 weeks from seeding and compared to evaluate a possible functional maturation of the cells. Confocal analysis allows the acquisition of calcium dynamics and pillar deflection which is converted in force through the use of a proper finite element model (FEM).

tion of such cells *in vitro* is of great interest. Calcium dynamics, i.e. the oscillation-like increase and decrease in calcium concentration in the cytosol, is acquired through confocal analysis of CMs: calcium is detected by intensity changes of light emitted by the fluorescent probe fluo-4. Micropillar deflection is quantified from the analysis of confocal images and converted into contraction force values through the use of a finite element model (FEM) that describes the deflection of the micropillars when a tangential force is applied. The finite element model can be realized after characterization of the mechanical properties (Young's modulus and stress-strain curve) of P(nBA-co-%MABP). When all parameters are determined the relationship between the forces sensed by the cell and exerted by the cell on the surface and cell function is evaluated.

3

SUBSTRATE FABRICATION

3.1 POLYMERS FOR SUBSTRATE FABRICATION

3.1.1 *Polydimethylsiloxane*

Polydimethylsiloxane (Figure 17) is the most widely used silicone-based organic polymer and it is particularly known for its unusual rheological properties. Its applications range from contact lenses and medical devices to elastomers. PDMS is optically clear, and is generally considered to be inert, non-toxic and non-flammable [177, 178]. PDMS networks can be used as a substrate to grow cells. Varying the crosslink density in the polymer network allows to tune the mechanical properties in a range similar to living tissues.
PDMS samples in this work were synthesized using Sylgard 184 (Dow Corning, Midland, MI) silicone-elastomer base and Sylgard 184 (Dow Corning, Midland, MI) silicone-elastomer curing agent, with a base : curing agent proportion of 10 : 1, which means 10 parts of Sylgard 184 silicone-elastomer base with 1 part of Sylgard 184 silicone-elastomer curing agent. The mechanical properties of Sylgard 184 have been thoroughly investigated [179, 180, 181, 182, 183]: the crosslinked polymer is a material with a Young's modulus that generally ranges from 0.5 to 2 MPa depending on the mixing ratio and heating temperature [179].

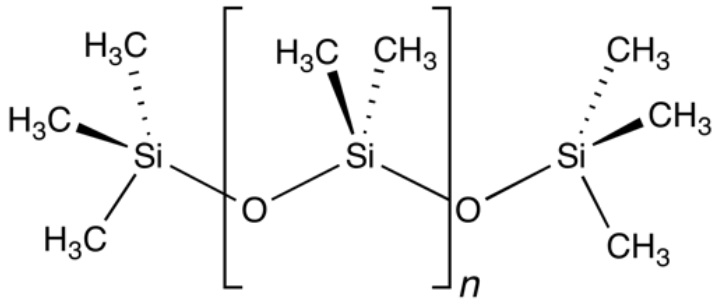

Figure 17: chemical formula of PDMS

PDMS has been employed to fabricate the microstructured substrates used in the studies concerning the physical plasticity of the nucleus of hPSCs. It has also been employed to fabricate stamps for replica molding process.

3.1.2 *Poly(nBA-co-%MABP)*

In this work, to fabricate the elastomeric microstructured substrates for cardiomyocytes culturing, we used P(nBA-co-%MABP), a cell-adhesive copolymer obtained through free radical polymerization.

3.1.2.1 *Free radical polymerization*

Free radical polymerization is a method of polymerization by which a polymer forms by the successive addition of monomers. The process consists essentially in three steps: initiation, propagation and termination [184, 185, 186]. Initiation is the first step, where an initiation molecule decomposes homolytically into two radicals:

$$I \xrightarrow{k_d} 2R \tag{2}$$

Another type of initiation is photolysis, where radiation cleaves a bond homolytically, producing two radicals. The subsequent step is propagation, during wich the polymer increases its chain length. In the propagation step, the radical attacks a monomer and creates a reactive centre. A monomer then adds to form a chain carrier.

$$R\cdot + M \xrightarrow{k_i} RM \tag{3}$$

$$RM_n\cdot + M_1 \xrightarrow{k_p} RM_{n+1} \tag{4}$$

Once a chain has been initiated, the chain propagates until termination occurs. There may be anywhere from a few to thousands of propagation steps depending on several factors such as radical and chain reactivity, the solvent, and temperature. The chain growth stops in the termination steps by combination or disproportionation. In combination two chain ends simply couple together to form one long chain. In disproportionation reactions a hydrogen atom from one chain end is abstracted to another, producing a polymer with a terminal unsaturated group and a polymer with a terminal saturated group.
Free radical polymerizations are very important for the production of polymers because high molecular weights can be obtained within short times and the polymerization conditions are mild. Furthermore, copolymers of different monomers are easily accessible [186].

3.1.2.2 *Copolymerization by free radical polymerization*

A copolymer is a polymer derived from two (or more) monomeric species, as opposed to a homopolymer where only one monomer is used. Since a copolymer consists of at least two types of constituent units, copolymers can be classified based on how these units are arranged along the chain. This classification includes alternating copolymers, block copolymers, graft copolymers and statistical copolymers. Alternating copolymers have the repeat unit sequence AB, whereas long sequences of each repeat unit are joined together in block copolymers. In graft polymers, a chain of one component is attached to the main chain of another one. In statistical copolymers, the repeat units are distributed statistically along the chain through four possible addition reactions [186]. Each reaction has a specific reaction rate where $\frac{d[A]}{d[B]}$ is the ratio of the rate of consumption of [A] and [B] and r_1 and r_2 are the relative reactivity ratios. The amount of each monomer (A and B) incorporated in the chain from a given reaction mixture can be derived from the copolymer equation:

$$\frac{d\,[A]}{d\,[B]} = \frac{[A]}{[B]}\left[\frac{r_1\,[A] + [B]}{r_2\,[B] + [A]}\right] \tag{5}$$

The relative reactivity ratios represent a measure for the reactivity of the propagating species with the other monomer. In an ideal statistical copolymer ($r_1 = r_2 = 1$), the two monomers are incorporated in the chain with the same probability. A completely alternating copolymer is formed if r_1 and r_2 approach zero. If either r_1 or r_2 is very high, a block copolymer is formed. When the reactivity of the cross-reaction is so low, that the two monomers only homopolymerize, a polymer blend is obtained. P(nBA-co-%MABP) has value of r_1 and r_2 similar to the r-parameters of P(DMAA-co-%MABP) which were found to be $r_1 = 0.30 \pm 0.05$ and $r_2 = 0.28 \pm 0.08$ [187]. P(nBA-co-%MABP) is an elastomer. Above its glass transition temperature (T_g), the networks deform easily already upon application of low forces. After releasing the force, they regain their initial shape. The mechanical properties of elastomers and in particular of P(nBA-co-%MABP) will be discussed in Chapter 4.

3.1.3 *Photocrosslinked polymer networks*

In this study, the photoactive MABP was employed as a crosslinker to prepare networks. Benzophenone is a photoreactive molecule that is activated by UV light both at the wavelength $\lambda = 365$ nm and at the wavelength $\lambda = 250$ nm. Irradiation with $\lambda = 250$ nm induces an electron transfer in the carbonyl group from the ground state S_0 to

the activated singlet state S_2 ($\pi \rightarrow \pi^*$), whereas $\lambda = 365$ nm leads to the activated single state S_1 ($n \rightarrow \pi^*$) [188, 189, 190]. The electrons return to the ground state S_0 by fluorescence or they undergo intersystem crossing to T_1 (Figure 18) [188, 189, 190].

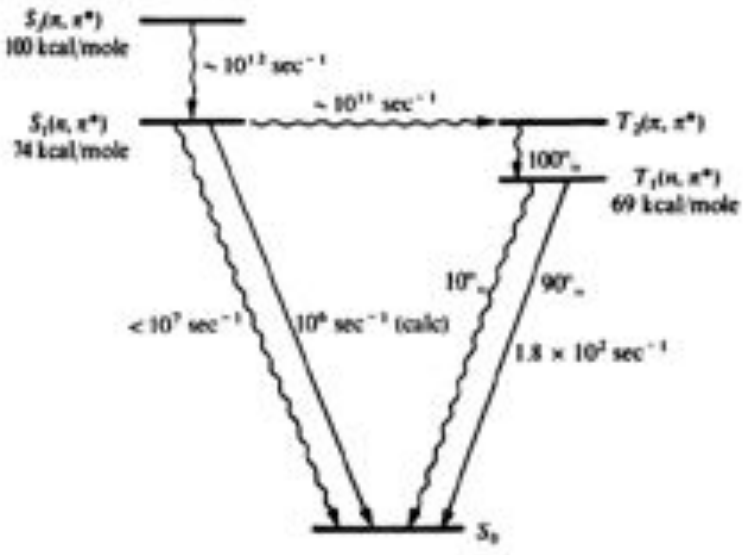

Figure 18: State diagram of benzophenone. The relaxation from S_1 can take place either by fluorescence into the ground state S_0 or by intersystem crossing (ISC) to a biradicaloid triplet state T_1 [189].

In the triplet state the BP can abstract a hydrogen atom from aliphatic C — H groups of other polymer chains, thereby forming two carbon-based radicals that combine to form a stable C — C bond (Figure 19).

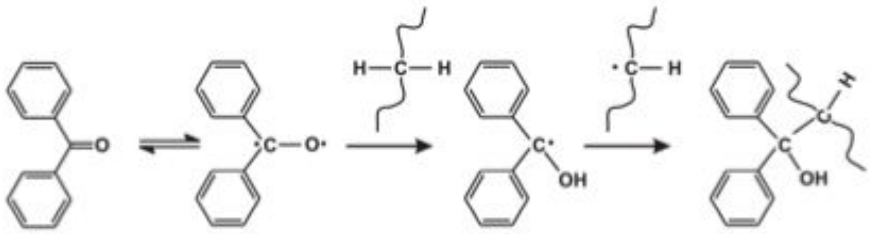

Figure 19: Mechanism of the benzophenone based crosslinking process. Upon illumination benzophenone forms biradical, which abstracts the hydrogen atom from a neighbouring C-H group of a polymer leaving a two carbon radicals, which can recombine and establish covalent bond.

Polymers containing photoreactive groups like benzophenone or its derivatives attach themselves covalently to an organic surface

upon irradiation with UV light, and simultaneously form a cross-linked polymer network (Figure 20). In this work, the photosensitive cross-linker MABP is used and incorporated in the precursor polymer.

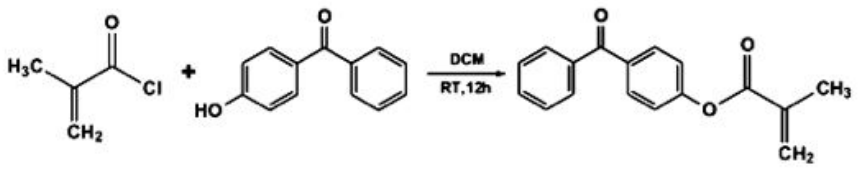

Figure 20: Reaction scheme of the synthesis of methacryloyl-4-oxybenzophenone (MABP).

3.1.3.1 *Poly(nBA-co-%MABP)*

P(nBA-co-%MABP) is a copolymer produced by free radical polymerization employing n-BA and MABP. A scheme of the reaction is reported in Figure 21. In this work three different concentrations of MABP have been tested to select the proper polymer for the biological studies: P(nBA-co-4%MABP), P(nBA-co-10%MABP) and P(nBA-co-20%MABP). The reasons why we choosed to fabricate our substrate employing this polymer are enumerated in Chapter 2. Briefly, P(nBA-co-%MABP) networks have elastic properties similar to that of PDMS, can be microstructured because the polymer is liquid before cross-linking and thanks to the use of the photosensitive cross-linker MABP can be photopatterned through UV light exposure. UV light at $\lambda = 365$ nm and $\lambda = 265$ nm can be used to cross-link the polymer or to activate specific areas of the surface.

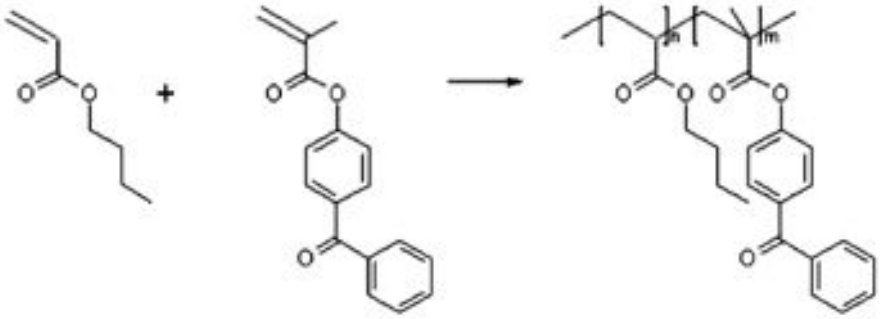

Figure 21: P(nBA-co-%MABP) synthesis through free radical polymerization.

3.1.3.2 *Silanization*

In order to modify surfaces like glass or silicon with stable polymer films, they have to be covalently bound to these surfaces. This can be achieved by using silane anchors containing benzophenone or its derivatives. In this work triethoxybenzophenone (3EBP) silane was used to modify a glass slide surface. 3EBP was spincoated on glass and then dried in oven at 120°C for 12 hours to form a thin silane layer. Through the condensation reaction the 3EBP layer become crosslinked and attached covalently to the glass surface. The thin silane layer provided the basis for the photochemical attachment of polymer with a benzophenone cross-linker. The process of silanization and polymer attachment is shown in Figure 22 .

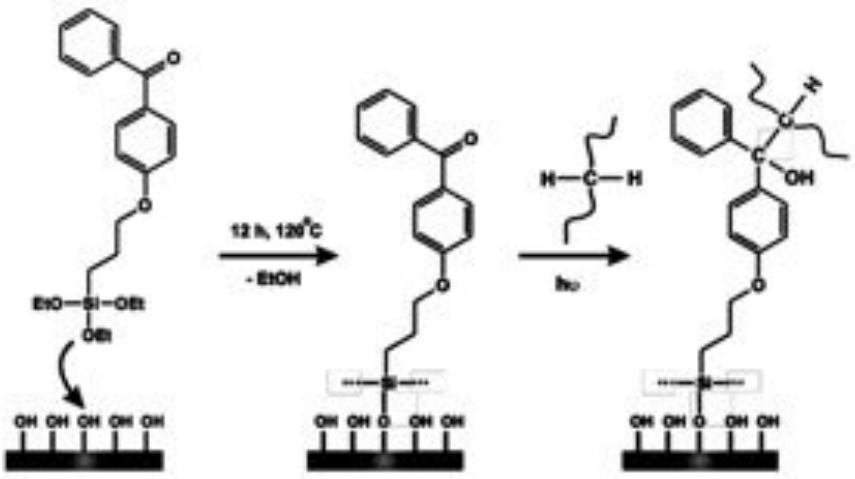

Figure 22: Silanization with triethoxybenzophenone (3EBP) silane and attachment of polymer chain through UV-irradiation

3.1.4 *PAA networks*

Polyacrylamide is a polymer formed from acrylamide subunits. Its chemical formula is $(-CH_2CHCONH_2-)$. Networks from this polymer are highly water-absorbent, and form a soft gel when hydrated accompained by a strong increase of its volume upon swelling. The most common method for catalytic initiation of acrylamide polymerization involves the generation of free oxygen radicals by ammonium persulfate. However, photo-induced methods of initiation are also available. A particularly useful method of polymerization involving photo-induced generation of free radicals, employes 1-[4-(2-hydroxyethoxy)-phenyl]-2-hy- droxy-2-methyl-1-propane-1-one (Irgacure 2959, BASF) as initiator. Polymerization is initiated through exposure to

ultraviolet light, allowing polymerization and cross-linking to be locally manipulated by varying UV light intensity or substrate exposure time [191]. By placing a light blocking mask over the gel, this method offers the opportunity to create geometric patterns across the surface of a single substrate.
In this work the acrylamide monomer subunits have been cross-linked forming polyacrylamide chains using Irgacure 2959. To this, acrylamide mixed with photoinitaitor solution was exposed to UV light ($\lambda = 365$ nm). The polymer is used to selectively photopattern cell-repellent areas on the elastomeric, cell-adhesive P(nBA-co-%MABP). The process of PAA immobilization onto the P(nBA-co-%MABP) surface, is a complex reaction of photopolymerization, crosslinking by radical abstraction and transfer and photoimmobilization. By UV light exposure, a photopolymerization and a simultaneous photoattachment reaction between PAA formed in the polymerization process and the P(nBA-co-%MABP) substrate are triggered. In particular, upon illumination benzophenone establishes covalent bonds with C- H groups of the PAA, as depicted in Figure 23. The photoattachment leads to the formation of a surface-attached monolayer of PAA chains. When now activated radicals from the added Irgacure photoinitiator abstract further hydrogen atoms from the PAA chains, this will lead to branching and eventually crosslinking. As a result this process allows the generation of a surface-attached network, which is much thicker than a simple PAA monolayer obtained in a photoattachment reaction. In that sense the Irgacure acts both as a photoinitiator and as a photocrosslinker.

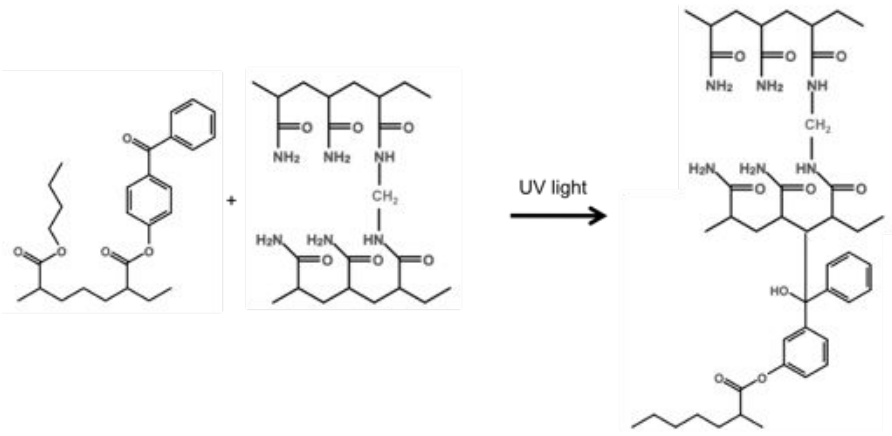

Figure 23: C-H insertion reaction between PAA and BP of P(nBA-co-%MABP). Upon illumination by UV light benzophenone establishes a covalent bond with the C- H group of PAA.

3.2 FABRICATION OF THE SUBSTRATES

3.2.1 *Fabrication of PDMS microstructured substrates*

Microstructured PDMS stamps were fabricated by replica molding from microstructured Si-wafers obtained through a standard photolithography technique. Briefly, a Si-wafer was spin coated with a thin layer of negative photoresist (AZ-1518, MicroChemicals, Germany). The photoresist was illuminated by UV-light ($\lambda = 365$ nm) through a chrome mask (Delta Mask, The Netherlands) that presented the desired pattern. Uncross-linked resist was removed rinsing the wafer in the AZ-1518 developer (MicroChemicals, Germany) for few seconds. The wafer was then etched to obtain the final micropillared stamp. The microstructured Si-wafer was subsequently silanized by exposure to the vapor of (tridecafluoro-1,1,2,2-tetrahydro octyl)-1-trichlorosilane in vacuum for 30 minutes, to facilitate PDMS removal during the replica molding step.

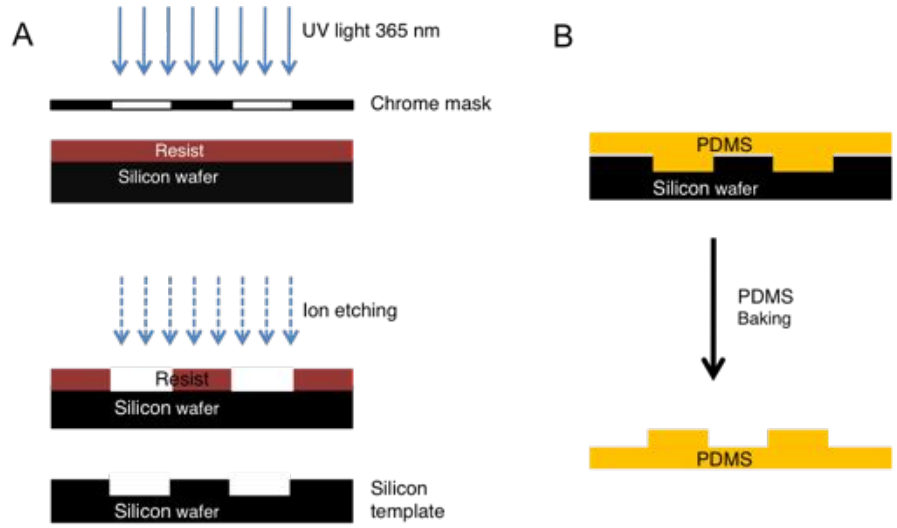

Figure 24: Fabrication of PDMS microstructured substrates. A) Photolitography step; B) Replica molding step.

PDMS elastomer was thoroughly mixed with the silicone elastomer curing agent in a 10 : 1 ratio, poured over the microstructured Si-master and kept under vacuum for 1 h to allow the complete filling of the pattern and air bubbles removal. The sample was then cured at 80^0C for 3 hours and subsequently peeled off the Si-wafers. Figure 24 shows a scheme of the process of fabrication of PDMS microstructured substrates that are obtained by fabrication of the stamps through photolitography (Figure 24 A) and subsequet repilca molding (Figure 24 B).

This process was used to fabricate microstructured samples for the investigation of the physical plasticity of the nucleus of hPSCs. The topography of the samples was characterized by scanning electron microscopy (SEM) as shown in Figure 25: the substrate was formed by a square lattice (7μm pillar width) with a distance between the pillars of 7μm (lattice constant 14μm). The height of the microstructures was fixed at around 7μm.
The same process, but using different silicon masters, was employed to fabricate the stamps used to fabricate P(nBA-co-%MABP) microstructured substrates.

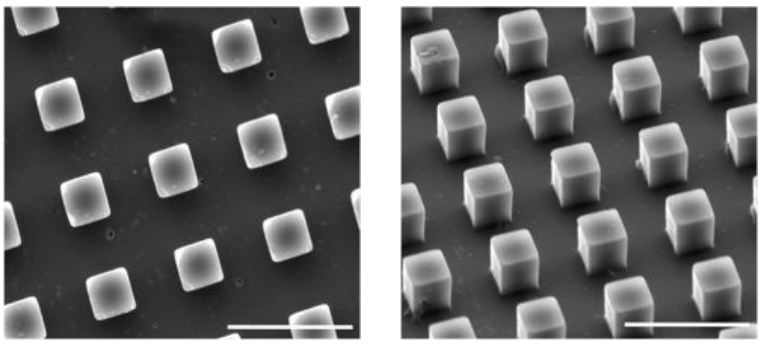

Figure 25: Scanning electron microscopy images of PDMS microstructures on silicon substrates obtained by replica molding as described in the text. Scale bar is 20μm

3.2.2 *Fabrication of P(nBA-co-%MABP) flat and microstructured substrates*

The protocol for the fabrication of P(nBA-co-%MABP) flat and microstructured substrates was developed in collaboration with Melanie Eichhorn, PhD student at Department of Microsystems Engineering (IMTEK), University of Freiburg. To fabricate flat P(nBA-co-%MABP) samples P(nBA-co-%MABP) polymer was dissolved in toluene (300 mg/ml) and 150 μl of this solution were poured on a round glass coverslip (25 mm of diameter) which was previously silanized with 3EBP silane as described in Section 3.1.3.2. The solution was spin-coated on the glass at a rotational velocity of 600 rpm for 1 minute and then irradiated by UV light ($\lambda = 365$ nm, $P = 6.5$ mW) for 20 minutes. To fabricate micostructured P(nBA-co-%MABP) samples, P(nBA-co-%MABP) polymer was dissolved in toluene (300 mg/ml) and a 60 μl drop of the resulting solution was poured on the appropriate PDMS stamp, which was previously obtained through replica molding from the appropriate silicon mask. A glass slide was then gently pressed onto the PDMS stamp filled with P(nBA-co-%MABP), allowing the

still not cross-linked polymer to completely fill the pattern of the stamp. The glass surface was previously silanized with 3EBP silane to achieve a covalent bond between the glass and the elastomer during UV light irradiation.This sandwich formed by PDMS stamp, P(nBA-co-%MABP) and silanized glass (see Figure 26) was then exposed to UV light ($\lambda = 365$ nm, $P = 6.5$ mW) for 20 minutes. The cross-linked microstructured samples covalently bonded to the glass slide were then peeled-off from the PDMS stamp. The process of fabrication of P(nBA-co-%MABP) microstructured substrates is reported in Figure 26 A.

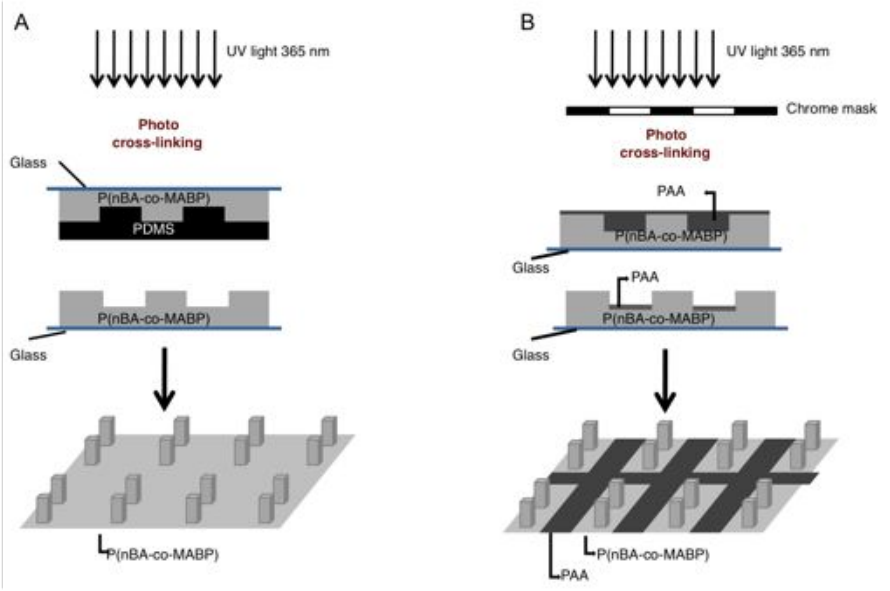

Figure 26: Fabrication of microstructured and photopatterned elastomeric substrates for cardiomyocytes culturing. A) Fabrication of P(nBA-co-%MABP) microstructured substrate; B) Photopatterning of PAA on P(nBA-co-%MABP) substrates by UV light exposure through a chrome mask.

3.2.3 *Cross-linking of PAA on P(nBA-co-%MABP) substrates*

Polyacrylamide solution was prepared by dissolving acrylamide (Sigma Aldrich, Germany) in deionized water to a final concentration of 8%. The acrylamide solution was supplemented with 30 mg/ml of photoinitiator (Irgacure, BASF, Germany) previously diluted in 100µl methanol. A 70µl drop of acrylamide+Irgacure solution was poured on a glass coverslip, the P(nBA-co-%MABP) sample was turned upside down and put in contact with the polyacrylamide solution, and a photomask consisting of dark and transparent areas was gently placed on the glass that supported the P(nBA-co-%MABP) sample. This sandwich-like sample was then irradiated for 90 s with UV light

($\lambda = 365$ nm). As a result of this process in the irradiated areas a surface-attached polymer network was generated in a rather complex mechanism, described in Section 3.1.4. After UV light exposure, the whole elastomeric sample was covered by a thin layer of cell-repellent PAA, except those areas that have not been exposed to UV light as they have been shaded by the photomask (dark areas of the photomask). The sample was rinsed with deionized water for 3 minutes to remove all the residual not cross-linked PAA. The same procedure has been applied both on flat elastomeric samples and on microstructured elastomeric samples. (Figure 26 B) reports a scheme of the process of photoimmobilization of PAA on P(nBA-co-%MABP) microstructured substrates. Figure 27 shows the surface of a flat P(nBA-co-%MABP) sample where PAA stripes have been subsequently photopatterned. A clear pattern is detected, formed by the presence and the absence of the PAA polymer layer. They are easily visible in the images as the PAA have been labeled with rhodamin. Such image prooves that PAA selectively crosslinked to the P(nBA-co-4%MABP) surface thanks to the use of a chrome mask during UV light irradiation, and that after rinsing the uncrosslinked PAA, no residual of such polymer is left on P(nBA-co-4%MABP) stripes.

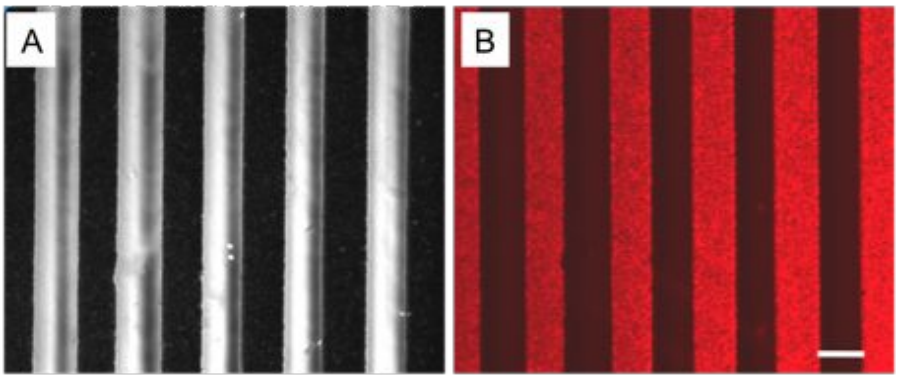

Figure 27: Image of P(nBA-co-4%MABP) photopatterned substrates with stripes of PAA. A) Phase contrast image of the substrate; B) Fluorescent microscope image of P(nBA-co-%MABP) photopatterned substrates. In black the cell-adhesive areas of P(nBA-co-%MABP) and in red the cell-repellent areas of PAA died with rhodamine. Scale bar is 100μm.

In Figure 28, a bright field image of a flat photopatterned P(nBA-co-%MABP) sample is reported. PAA has been crosslinked on P(nBA-co-%MABP) surface leaving only rectangular cell-adhesive areas measuring 30 x 15 μm that are highlighted by white dotted lines in the image. Such substrates have been employed to perform experiments

with human embryonic stem cell derived-cardiomyocytes (hESC-CMs) as described in Chapter 8.

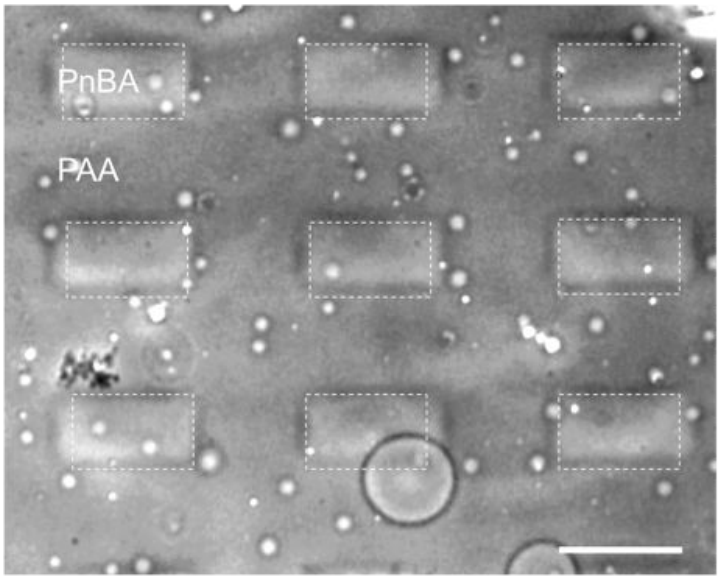

Figure 28: Bright field image of flat photopatterned P(nBA-co-%MABP) sample. White dotted lines mark the cell adhesive P(nBA-co-%MABP) areas. The rest of the surface is covered by PAA. Scale bar is 30μm.

Figure 29 shows the bright field image of a microstructured and photopatterned P(nBA-co-%MABP) sample. PAA has been immobilized everywhere except that into the rectangular areas marked by the white dotted lines. Such substrates have been employed to perform experiments with hESC-CMs as described in Chapter 8. The shape and location of the adhesive areas was planned to guide in a proper way cell adhesion and shape.

3.2.4 *Fabrication of P(nBA-co-%MABP) samples for mechanical testing*

To perform a dynamic mechanical thermal analysis (DMTA) that allows to quantify the Young's modulus of the material at the different cross-linking densities, specific samples have been fabricated: the samples needed to be at least 3 mm thick and their length had to be at least two time bigger than their width. For these reasons the samples were fabricated by casting. A solution of P(nBA-co-%MABP) in toluene (300 mg/ml) was prepared and 2 ml of this solution were poured on a rectangular teflon stamp (2x5 cm). The solution was then exposed to UV light (365 nm) for 30 minutes. The sample was peeled-off, turned upside-down, and exposed to UV light for further 30 minutes until the film was completely crosslinked. The film thickness

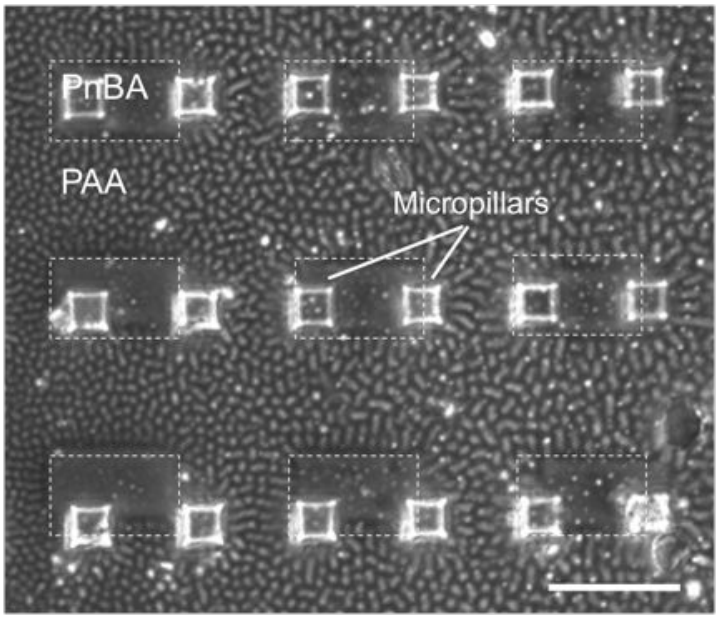

Figure 29: Bright field image of microstructured and photopatterned P(nBA-co-%MABP) sample. White dotted lines mark the cell adhesive P(nBA-co-%MABP) areas. The rest of the surface is covered by PAA. The small squares are the microstructures (micropillars in the specific case) as seen from above. Scale bar is 30μm.

ranged from 3 to 3.5 mm. An example of a sample used for the DMTA measurements is shown in Figure 30.

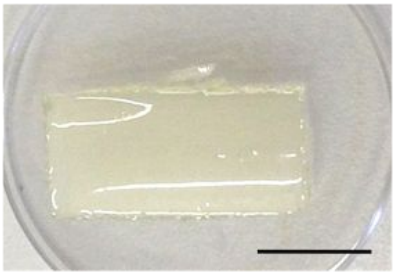

Figure 30: P(nBA-co-%MABP) sample for DMTA analysis obtained by drop casting of the precursor polymer followed by photochemical crosslinking as described in the text. Scale bar is 20 mm.

3.2.5 *Characterization of the PAA layer thickness through AFM*

The thickness of the PAA film crosslinked on top of the P(nBA-co-%MABP) surface was measured through atomic force microscopy (AFM). Figure 31 shows the scheme of a AFM measurement.

In this work, the determination of film thickness and surface topography were carried out using the AFM in tapping-mode [193, 192].

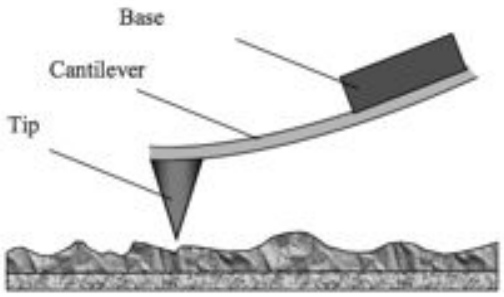

Figure 31: Scheme of AFM measurmement of a surface. (Adapted from Mironov et al, [192]).

In this mode, the cantilever oscillates while scanning over the sample surface. This causes an intermittent and very weak contact between the sample and the cantilever tip, which reduces the risk of surface damage induced by the lateral force of the tip and minimizes the tip-sample interaction. Thus, it is possible to image mechanically weak surface nanostructures such as polymers or biological samples.

3.2.5.1 *AFM results*

AFM samples were fabricated by simultaneously photoattaching and photocrosslinking PAA on a flat P(nBA-co-%MABP) substrate with UV light irradiation through a chrome mask that allowed an homogeneous crosslinking of PAA everywhere except on rectangular squares measuring 40 x 80 μm.

AFM analysis was performed on the edge of the P(nBA-co-%MABP) rectangular areas, where the boundary between the two polymers was visible. The height of the step caused by the presence of the PAA network was recorded. For all the 5 different samples tested the layer thickness was around 250 nm. This value is far less than the micropillar height (20 μm) therefore it is safe to assume that PAA layer do not influence the morphological properties of the substrate but only the chemical properties.

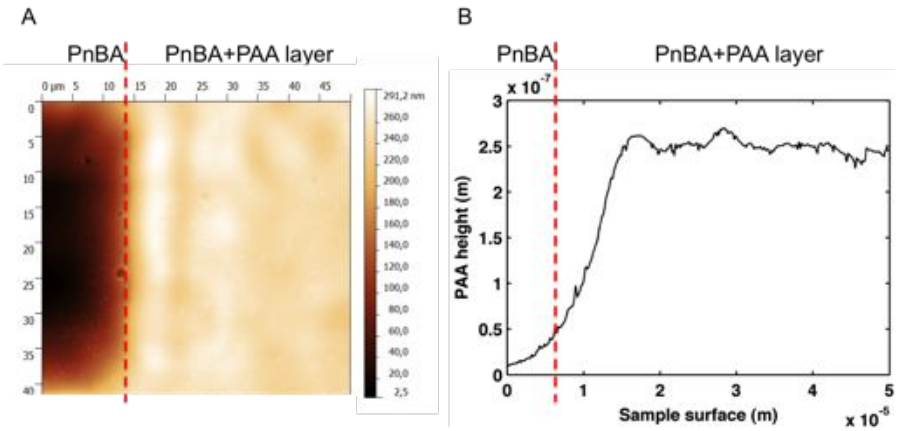

Figure 32: AFM measurement on our samples. A) AFM phase image of the substrate: the left, darker part is P(nBA-co-%MABP), the right lighter part is P(nBA-co-%MABP) covered by a layer of PAA. B) AFM profile at the edge of the P(nBA-co-%MABP) rectangular area: the lower part on the left is where there is only P(nBA-co-%MABP), the right higher part is where PAA crosslinked on P(nBA-co-%MABP).

4

MECHANICAL CHARACTERIZATION OF THE SUBSTRATE

4.1 MECHANICS OF ELASTOMERS

Elastomers are polymer networks that are weakly crosslinked and where the polymer subchains are above the glass transition temperature. They are capable of absorbing large deformations in a reversible manner. Unlike energy-elastic solids such as metals or alloys, elastomers are entropy-elastic [194, 195]. The driving forces behind the elasticity of a material are changes in the entropy of the system, i.e. the degree of disorder which is greater in the coiled disordered state of the polymer chains than in an arranged, extended, orderly state. During deformation the polymer subchains partially unfold (entropy decrease), but upon release of stress they return to their original conformations (entropy increase). This is due to the fact that the bonds can rotate freely [196, 194, 197].The crosslink prevent that during unfolding the chains translatory movements, i.e. movements of the (sub-)chains against each other, happen.

The elastic modulus increases with increasing strain as shown in Figure 33. The tensile modulus of elastomers is typically small and varies with strain, (i.e. it is non linear). However, a linear response can be assumed for small strain. This behavior comes from the elastomeric structure which is highly amorphous with twisted coiled and kinked chains: during deformation these partially straighten. but upon release of stress they return to their original conformations. In the case of suddenly applied force or large deformations [198], the recoiling of the molecules (during unloading) has a slightly different path than the uncoiling (during loading), i.e. some hysteresis occurs. The area located between the loading and unloading curves is proportional to the energy absorbed in each cycle of the loading. In this case material can be considered as partially viscoelastic.

4.1.1 *Elasticity*

Elasticity is the ability of a material to store deformational energy, and can be viewed simply as the capacity of a material to regain its original shape after being deformed [194, 197]. When the material is stretched or compressed the atoms are forced out of their equilibrium

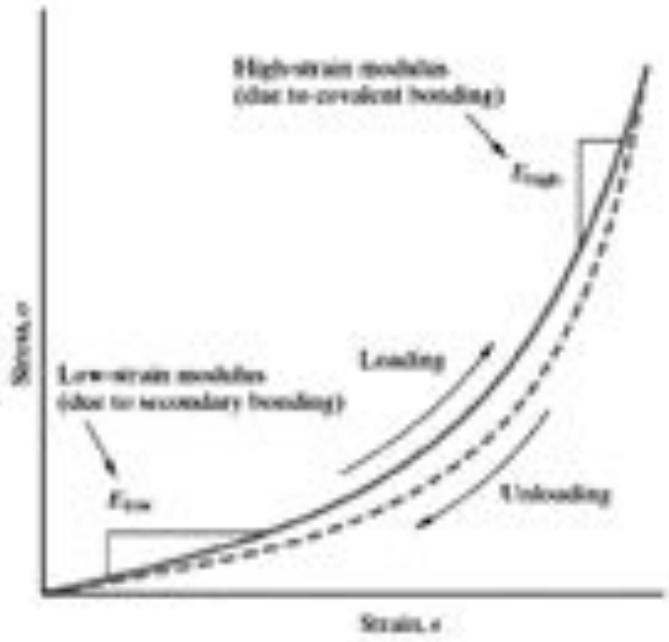

Figure 33: Stress-strain relationship of a typical elastomer. The elastic modulus increases with increasing strain. The low strain modulus has a low value because the forces needed to uncoil the molecular chains are small. The high strain modulus has a higher value because stronger forces are needed to stretch the primary (covalent) bonds.

positions and are either parted or brought together until the forces caused by the deviation from the equilibrium balance the external force. With some materials the extension or compression is limited by other factors to less than 10% of the bond length, so that the relationship between force and distance is essentially linear. When the load is removed, the interatomic forces restore the atoms to their original equilibrium positions. These kind of material can be described by Hooke's law [194]. Hooke's law describes the mechanical behavior of an ideal solid, relating the applied strain (ϵ or γ) to the resultant stress (σ or τ) through a factor called the modulus (E or G). Thus, $\sigma = E\epsilon$ (tension) or $\tau = G\gamma$ (shear). The modulus describes the material's stiffness (i.e. its ability to resist deformation). The linear region in which the modulus does not change when the strain is changed is called the Hookean region: extension and force are directly and simply proportional to each other. Strain can be expressed in a number of ways, each offering certain advantages and insights into the processes of deformation. The most commonly encountered form as-

suming small deformations is nominal or Cauchy strain, which is the increase in length per unit starting length:

$$\epsilon_c = \frac{\Delta l}{L_0} \tag{6}$$

The stress σ is expressed as the force divided by the area across which the force is acting:

$$\sigma = \frac{F}{A_0} \tag{7}$$

However, just as with strain, this simple equation is suitable only for small extensions. the ratio of stress to strain is an elastic characteristic of a material. This ratio is related to the the stiffness of the material and it is called Young's modulus, E:

$$E = \frac{\sigma}{\epsilon_c} \tag{8}$$

A typical stress-strain curve is shown in Figure 35. A different mode to apply stress is shear. The shear stress, τ, is defined as :

$$\tau = \frac{T}{A_0} \tag{9}$$

where T is the shear force, colinear to the surface A_0 where the force is acting.

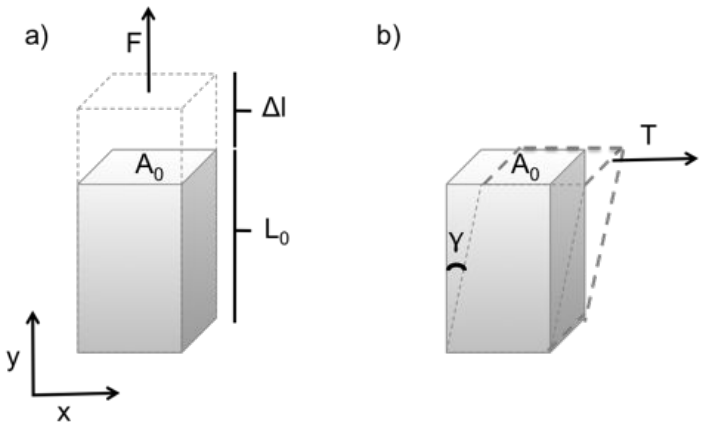

Figure 34: Scheme of elastic response of a material. A) Cauchy strain ϵ_c is calculated from the deformation Δl of the material when a force F is acting on the surface A_0 along the y axis. B) The shear stress τ is calculated dividing the force T acting along the x axis for the surface A_0 colinear to the acting force.

The shear or Coloumbs modulus is defined as

$$G = \frac{\tau}{\gamma} \tag{10}$$

where the strain γ is measured in radiants.

In an isotropic material, i.e. a material whose mechanical properties are the same in all directions, the Young's modulus and the shear modulus can be related through the expression:

$$G = \frac{E}{2(1+\nu)} \tag{11}$$

where ν is the Poisson ratio. The previous equations are valid for small strains. Elastic materials obey Hooke's law when the relationship between stress and strain is linear: this linearity is lost when large deformations take place. In materials undergoing large deformations stress-strain behavior is nonlinear and can be described by the neo-Hookean model [199]. In Figure 35 the stress-strain curve of an Hookean and neo-Hookean material are compared.

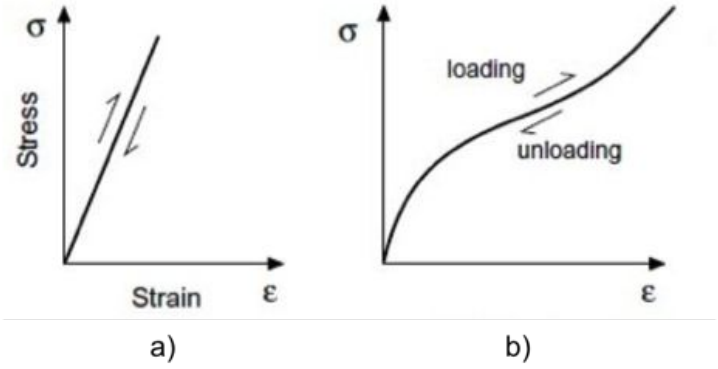

Figure 35: Stress-strain curves for elastic materials: the loading and unloading curves superpose in both cases. A) Hookean material: there is a linear relationship between stress σ and strain ϵ. B) Neo-Hookean material: There is a linear response for small deformation whereas for larger deformation the material response becomes non-linear.

4.1.2 *Viscoelasticiy*

Viscoelasticity is the property of materials that exhibit both viscous and elastic characteristics when undergoing deformation. Unlike purely elastic substances, a viscoelastic substance has an elastic component and a viscous component. The viscosity of a viscoelastic substance gives the substance a strain rate dependent on time. Purely elastic materials do not dissipate energy (heat) during a loading/unloading cycle. However, a viscoelastic substance loses energy when

a load is applied, then removed. Hysteresis is observed in the stress - strain curve, with the area of the loop being equal to the energy lost during the loading cycle. Since viscosity is the thermally activated resistance to deformation, a viscous material will lose energy through a loading cycle. Specifically, viscoelasticity is a molecular rearrangement.

Figure 36 shows a typical stress-strain curve of a viscoelastic material.

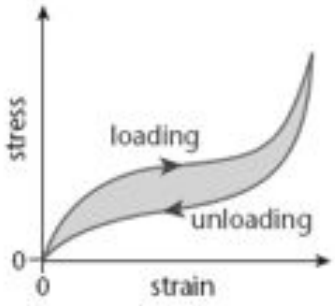

Figure 36: Stress-strain curve for viscoelastic materials: the loading and unloading curves don't superpose because there is an energy loss on the material.

An important experiment performed on viscoelastic materials is the one in which either stress or strain (usually strain) is varied cyclically (usually sinusoidally for mathematical convenience) with time, and the response is measured at various different frequencies of deformation. Dynamic mechanical thermal analysis has been applied to analyze the mechanical response of our samples.

4.2 DYNAMIC MECHANICAL THERMAL ANALYSIS

Dynamic mechanical thermal analysis DMTA is a technique where a small deformation is applied to a sample in a cyclic manner and that is widely used to characterize material's properties [196, 200]. Figure 37 shows a picture of the instrument that has been used in this work. The measurements were performed at Institut Charles Sadron of Strasbourg, with the supervision of Vincent Le Houerou. DMTA technique allows the materials response to strain, temperature, frequency and other values to be studied. The sample can be subjected by a controlled stress or a controlled strain.

For a known stress, the sample will deform to a certain extent. In DMTA, when a sinusoidal force is applied, the instrument detects an in-phase component, the storage modulus, and an out of phase com-

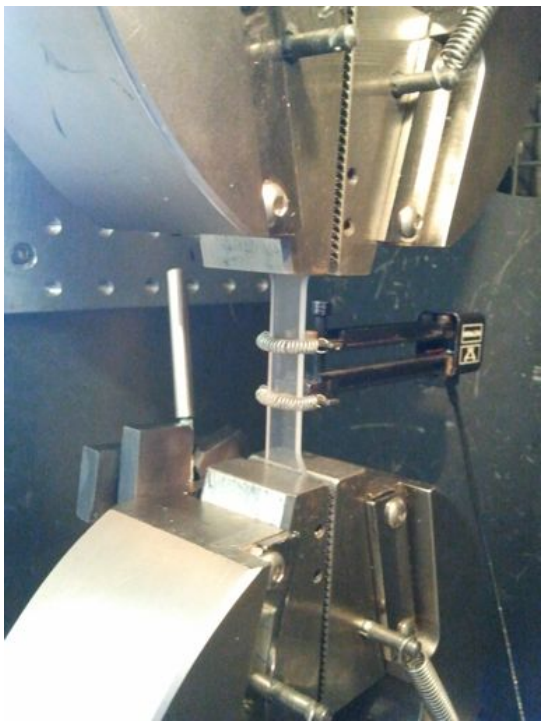

Figure 37: DMTA test on a elastomeric sample: a longitudinal cyclic load is applied while the temperature varies.

ponent, the loss modulus, which are both part of the complex modulus E^*:

$$E^* = E' + iE'' \tag{12}$$

The storage modulus, E' , is the measure of the sample's elastic response whereas the loss modulus E" is related to the energy loss due to internal motion. The ratio of the loss to the storage is the loss factor (tan delta) and is often called damping. It is a measure of the energy dissipation of a material:

$$\tan\delta = \frac{E''}{E'} \tag{13}$$

Damping is the dissipation of energy in a material under cyclic load and is reported as the tangent of the phase angle. It varies with the state of the material, its temperature, and with the frequency. While Young's modulus, which is calculated from the slope of the initial part of a stress-strain curve, is similar conceptually to the storage modulus, they are not the same. The Young's modulus E is derived from the complex modulus E^*, since it is calculated as the norm of E^*:

$$E = \sqrt{(E')^2 + (E'')^2} \tag{14}$$

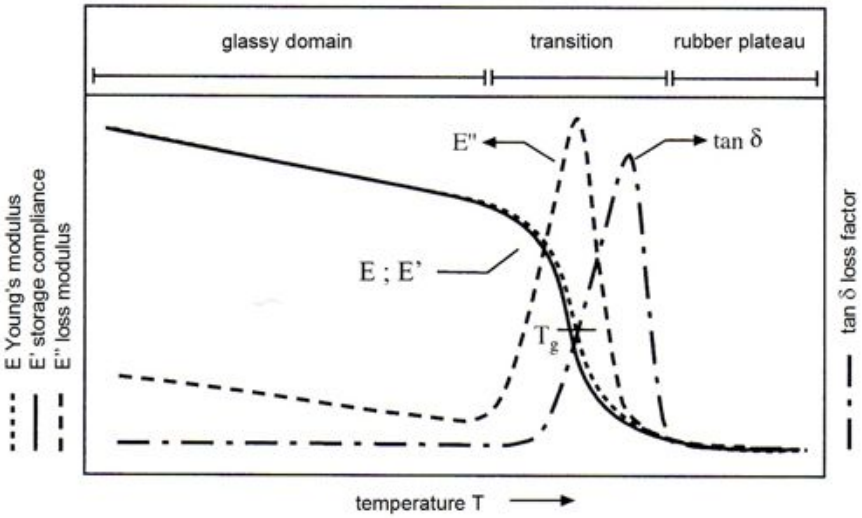

Figure 38: Typical DMTA result: while the temperature varies and the polymer goes from the glassy domain to the rubber plateau through the transition state, the storage modulus, E' , the loss modulus E", the Young's modulus E and the tan δ are measured. E' is the measure of the sample's elastic response whereas E" is related to the energy loss in internal motion. The ratio of the loss to the storage is the loss factor (tan δ).

Modulus values change with temperature and transitions in materials can be seen as changes in the E' or tan delta curves. A properly calibrated instrument requires calibration for both temperature and force. Important requirements for high quality measurements are: even thickness of the sample with parallel sides and right angles, a deflection of less than 50 µm and heating rates of 2-3 °C per minute [200]. Figure 38 shows a typical DMTA test result at a fixed frequency. The temperature varies while the polymer goes from the glassy domain to the rubber plateau and the instrument measures the values of the storage modulus, E' , the loss modulus E" and the Young's modulus E at each temperature.

4.2.1 *DMTA analysis on P(nBA-co-%MABP): evaluation of the Young's modulus*

In this work, P(nBA-co-%MABP) was used to fabricate microstructured substrates that allow the determination of cardiomyocytes contraction force: the elastomer used for this purpose has to be stiff enough to guarantee a reliable and reproducible morphology of the micropillar but soft enough to obtain structures that are displaced by cell contraction. In literature, polydimethylsiloxane (PDMS) has

been commonly used to detect cell force from pillar deflection. The Young's modulus of PDMS ranges from 0.5 to 2 MPa. In our studies on cardiomyocytes (CMs) we preferred to use P(nBA-co-%MABP) samples instead of PDMS samples for chemical properties at the surface of P(nBA-co-%MABP) which is protein-adsorbent and can easily be photopatterned to obtain substrates with cell-adhesive and cell repellent areas that direct cell growth, as described in Chapter 3. We fabricated the samples for DMTA analysis as described in Chapter 3. Briefly, rectangualar samples of P(nBA-co-%MABP) have been obtained pouring 2 ml of polymer on a 2 cm large and 5 cm long teflon stamp and exposing the liquid to 350 nm UV light for 30 minutes on one side and for further 30 minutes on the other side of the film. Then we peeled-off the samples and we measured their thickness which ranged from 3 to 3.5 mm. Through this procedure we fabricated several samples with three different cross-linking densities: P(nBA-co-4%MABP), P(nBA-co-10%MABP) and P(nBA-co-20%MABP). The elastic properties of P(nBA-co-%MABP) were tested through DMTA (Instron 4502 Tensile Machine). A small preload was applied to each sample to assure the same tensile condition for all of them at the beginning of the test and tensile loading all along the test. A sinusoidal stress with a frequency of 1 Hz was applied deforming the samples of 1% maximum, to obtain a linear elastic response from the material.

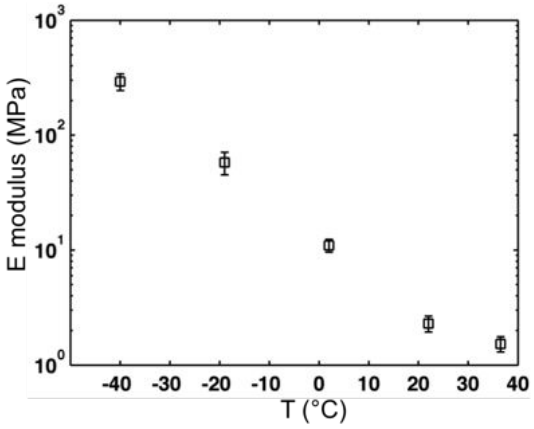

Figure 39: E modulus of P(nBA-co-4%MABP). The temperature varies while the frequency is fixed at 1 Hz.

The frequency was fixed at 1 Hz because this value is comparable to the frequency of deformation induced by the cells during their contraction. For each cross-linking density the experiment was repeated for 5 samples. Young's modulus was measured at different temperatures. In our application, it was important to determine the Young's modulus of the material at 36.5 °C which is the temperaure at which the cells that are cultured on the substrates had to be kept. The E

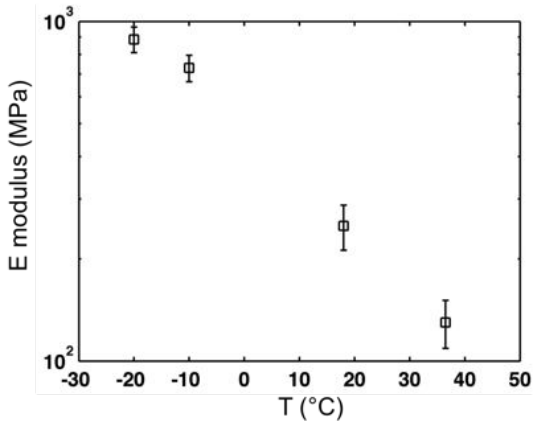

Figure 40: E modulus of P(nBA-co-10%MABP). The temperature varies while the frequency is fixed at 1 Hz.

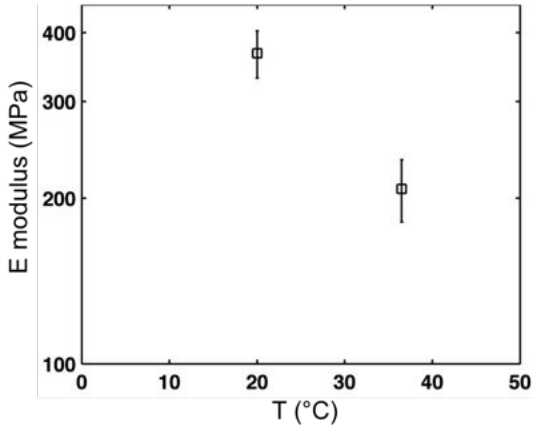

Figure 41: E modulus of P(nBA-co-20%MABP). The temperature varies while the frequency is fixed at 1 Hz.

modulus of P(nBA-co-4%MABP) has been measured from -40°C to 40°C (Figure 39) , E modulus of P(nBA-co-10%MABP) has been measured from -20°C to 40°C (Figure 40) and E modulus of P(nBA-co-20%MABP) was evaluated at 20°C and at 36.5°C (Figure 41). DMTA analysis measured a Young's modulus of 130 ± 21 MPa for P(nBA-co-10%MABP) at 36.5° and a Young's moduls of 208 ± 27 MPa for P(nBA-co-20%MABP) at 36.5°, both far too high for our purpose. In contrast to that, the Young's modulus of P(nBA-co-4%MABP) at 36.5°C was found to have a value very similar to PDMS: 1.53 ± 0.23 MPa. From these results we decided to use P(nBA-co-4%MABP) for the fabrication of our substrates.

4.3 NANOINDENTATION TEST

The nanoindentation technique allows the evaluation of the mechanical properties of very small volumes of material through the use of small probes (few μm) and a cantilever able to apply and measure normal load and tangential force in the order of μN. This instrument is commonly used to determine modulus of elasticity, hardness, fracture toughness, scratch hardness and wear properties [201]. In this work, we used the nanoindenter (Nanoindenter CSM instruments, Switzerland) to experimentally reproduce the process of bending of our micropillars when a tangential force was applied at the top of them. A picture of the instrument is reported in Figure 42. The measurements were performed at Institut Charles Sadron of Strasbourg, with the supervision of Vincent Le Houerou.

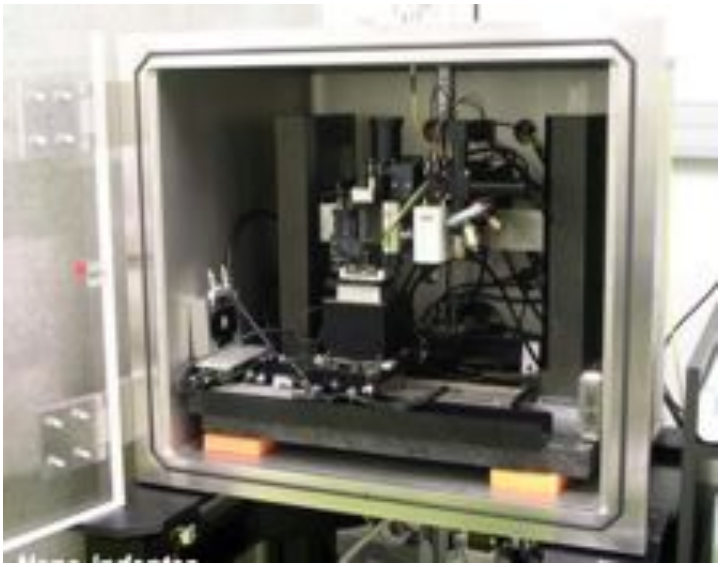

Figure 42: Nanoindenter instrument.

When a specific tangential force is applied, the deflection of the top of the micropillars depends on the material properties (i.e. Young's modulus and mechanical response) and on micropillar's morphology. From this test it was possible to simultaneously acquire the tangential force applied by the instrument and the micropillar deflection, thanks to an *in-situ* camera that recorded the contact through the transparent specimen during the test. The results obtained have been used to validate the finite element model (FEM) that we realized to quantitatively evaluate cell's contraction force from pillar deflection in the biological assays. For this tests we used P(nBA-co-4%MABP) to fabricate samples with square micropillars having a height of 10 μm, a width of 10 μm and an interaxial distance of 20 μm. In Figure 43

a scheme of the performed experiment is depicted. A round tip with a radius of 500 μm was put in contact to the top of the microstructured substrate, without applying a normal load to avoid compression of the micropillars. Then the tip was slightly moved laterally, applying a tangential force to the top of the micropillars: this forces was recorded by the instrument while the camera showed the deflection of the top of the micropillars. The glass tip was in contact with 9 micropillars. For the calculation of the force we assumed an equally distributed force among all the micropillars in contact. Therefore we calculated the tangential force f_t acting on a single pillar as the tangential force recorded by the instrument F_t divided by the number of micropillars in contact. In this case:

$$f_t = \frac{F_t}{9}; \tag{15}$$

The deflection of the micropillars were evaluated analyzing the recorded images through a MATLAB (MathWorks) algorithm. The algorithm calculates the position of the centroid of the top of each pillar in contact both in the undeformed ($c\_undeformed$) and deformed configuartion ($c\_deformed$). For each pillar the deflection Δx_i is calculated as $\Delta x_i = c\_deformed - c\_undeformed$. The final value of the deflection d is given by the mean value of the deflections calculated for each micropillar:

$$d = \sum_{i=1}^{9} \frac{\Delta x_i}{9} \tag{16}$$

The nanoindenter test allowed us to plot the relationship between tangential force and pillar deflection as reported in Figure 45 (black squares). This plot shows a linear elastic behavior for deflection of the top of the micropillars (Δx) up to 3 μm and a non linear elastic behavior for higher deflections. The elastic behavior can be assumed since no permanent deformation were recorded once removed the force.

Beam theory states that the relationship between the tangential force and the pillar deflectiont is given by Equation 17:

$$F = \left(\frac{3EI}{L^3}\right)\Delta x \tag{17}$$

From our data, the coefficient $\left(\frac{3EI}{L^3}\right)$ can be considered constatnt up to $\Delta x \sim 3$ μm, according to Hooke's law. A linear elastic behavior can be therefore assumed in this strain range: we will see further

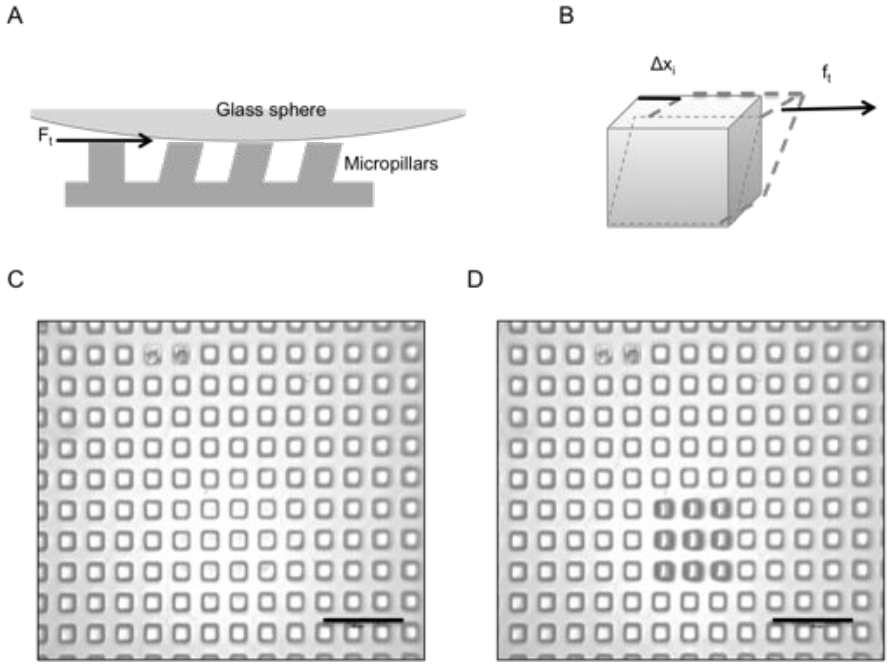

Figure 43: Bending test on P(nBA-co-4%MABP) microstructured substrates: A) Glass sphere of the nanoindenter applies a tangential force on the top of the elastomeric pillars. B) Scheme of pillar bending when a tangential force is applied. C) Sample at the underformed configuartion. Scale bar is 50μm. D) Sample during bending: deformed configuration of the micropillars. Scale bar is 50μm.

that the model calculated that it corresponds to a maximum strain of 15% (Figure 44). Beam theory is valid if the micropillar height is at least $2-2.5$ bigger than pillar width. When the microstructures have a different geometry a FEM can be used to evaluate the relationship between micropillar deflection and applied force. Since in our case the contraction forces exerted by the cells under study deforms the micropillars in a range that still corresponds to the linear-response area of the plot of Figure 45, we could assume an Hookean model for our micropillars when bended by the cells.

4.4 FINITE ELEMENT ANALYSIS

The analysis of mechanical systems have been addressed by deriving differential equations relating the variables through basic physical principles such as equilibrium, conservation of energy, conservation of mass, the laws of thermodynamics, Maxwell's equations and Newton's laws of motion. However, once formulated, solving the resulting mathematical models is often impossible, especially when the resulting models are non-linear partial differential equations. Only very

simple problems of regular geometry such as a rectangular or a circle with the simplest boundary conditions were tractable. The use of finite element analysis (FEA) allows the solution of such problems [202, 203, 204]. The way finite element analysis obtains the temperatures, stresses, flows, or other desired unknown parameters is by minimizing an energy functional [205]. An energy functional consists of all the energies associated with the particular finite element model. Based on the law of conservation of energy, the finite element energy functional must equal zero. The minimum of the functional is found by setting the derivative of the functional with respect to the unknown grid point potential for zero. Thus, the basic equation of finite element analysis is:

$$\frac{dU}{dp} = 0 \tag{18}$$

where U is the energy functional and p is the unknown grid point potential to be calculated. In mechanics, the potential is displacement, and the relationships between the stresses and the displacements developed in the structural elements can be obtained relying upon two fundamental requirements of basic structural behavior: the requirement that the structure must be in equilibrium and the requirement that the deformation must be compatible and consistent to boundary conditions. These two characteristics of structural behavior can be satisfied through a method that involves a quantity dependent both on force and displacement, namely, work. Work is the product of a force and the displacement on its point of application in the direction of the force. More generally, we define as the differential work dW done by a force F moving through a differential displacement ds as the product of F_s and ds, where F_s is the component of F in the direction ds. Thus $dW = F_s ds$ and the total work done in displacing F from some point A to some point B is, by definition:

$$W = \int_A^B F_s \, ds \tag{19}$$

In finite element analysis (FEA) the solution of mechanical problems is based on the principle of virtual work, which states that "in a body under equilibrium the sum of works of the internal and external forces for any virtual displacement field is zero"[204]. Virtual displacement are infinitesimal changes in the position coordinates of a system such that the constraints remain satisfied.

$$dW_i + dW_e = 0 \tag{20}$$

where dW_i is the variation of the work related to the internal forces and dW_e is the variation of the work related to the external forces acting on the system. In particular:

$$dW_i = \int \sigma_{ij} \epsilon_{ij} \, dV \tag{21}$$

$$dW_e = \int b_i u_i \, dV + \int t_i u_i \, dA \tag{22}$$

where the first term in Equation 22 is related to the external volumic actions and the second term to the external surface actions, while dW_i is related to the inner state of stress and strain. Further details on the principle of virtual work are provided in Appendix A. From Equation 20 it is possible to calculate the displacement u_i and therefore the strain ϵ_{ij} and stress σ_{ij}. In FEA the considered system is subdivided through a process of space sampling (mesh) into elements and the virtual work principle is used to relate the forces acting on an element to the displacements at nodes in terms of a element stiffness matrix [202]. All the element stiffness matrices are then combined together into a single stiffness matrix that is a set of equations that relate all the displacements to all the forces acting on the system, also considering the boundary conditions. This system of equations is applied to get the displacemet which are then used to find all the forces in the individual elements. Space sampling is always combined with time sampling: this time sampling considers the evolution of the loading and calculate the displacements at every time step. This space and time sampling is fundamental to find approximated solutions of the differential equation in variational form which describe the problem, because each element is small enough and each time step is short enough to consider the problem linear for that element.

4.4.1 *FEA software MARC Mentat*

There are several softwares available to solve finite element models. In this work we use the software MARC/MENTAT from MSC Softwares (USA), which is specific for the resolution of structural problems. The MARC/MENTAT program is divided into two parts: the MENTAT pre- and post- processor, and the MARC solver program. In the preprocessing step MENTAT is used to generate the finite elements model, apply boundary conditions, initial conditions, material properties, element geometry and analysis type. This information is stored in an input file, which may be further edited to generate more advanced options. In the processing step, the input file is read by the

MARC solver program, which solves the problem and write an output file, which performs the post processing step, then reads the output file.

4.4.2 *Finite element model of the elastomeric micropillar*

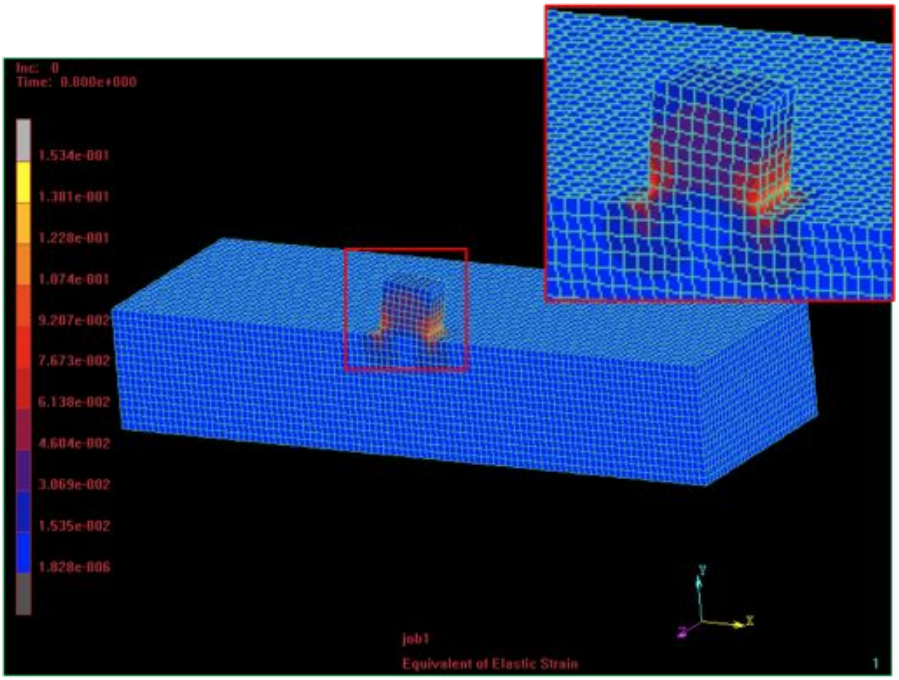

Figure 44: Finite element model of a micropillar generated as described in Chapter 3. The equivalent elastic strain for a tangential force of 2 μN (which is about 3 — 4 times bigger than the force developed by cardiomyocytes) is reported. The maximum elastic strain is on the order of 15% on a very localized area of the micropillar (marked in yellow in the image).

The finite element model of the substrate was realized according to the geometrical configuration of the samples employed to do the bending test (see Section 4.3). The substrates used for nanoindentation were made of P(nBA-4%MABP), therefore the Young's modulus of the structure modeled was fixed at 1.53 MPa. A single micropillar was modeled since all micropillars have the identical geometrical structure and mechanical properties. In the modeling process, a tangential force ranging from 0 to 4 μN was imposed to the top of the micropillar. The force was assumed to be equally distributed on the entire area of the micropillar's top. The deflection of the micropillar is due to the tangential force. The normal load in the experiments is assumed to be equal to zero. Because of the mechanical behaviour

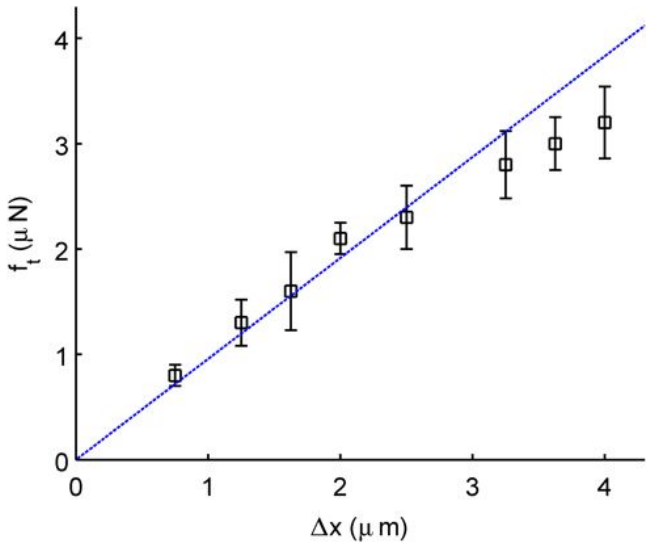

Figure 45: Comparison of the experimental result of the bending test (black squares) and the model (blue dotted line). The tangential force vs pillar displacement is reported. Experimental results and model are in a good agreement up to a deflection of the micropilarr of 3 μm,. In such range the material behavior can be assumed as linear elastic.

of P(nBa-co-4%MABP), which can be assumed to show linear elastic behavior in the range of moderate strains, an Hookean constitutive model was adopted to model the material. Figure 44 shows the modeled micropillar, when a tangential force of 2 μN is applied. We will see in Chapter 8 that such force is $3-4$ times bigger than the force applied by cardiomyocytes. In response to such force, the maximum strain was found to be on the order of 15% and only in a very localized area (base of the micropillar). The assumption of a linear elastic behaviour of the material under our condition of stress is therfeore reasonable. Figure 45 reports the relationship between tangential force and deflection calculated by the model (blue dotted line), compared with the experimental results (black squares). A good agreement between experimental data and FEM has been reported up to deflections of the micropillar of about 3 μm, which corresponds to an applied force of 2.7 μN. Beyond this value, the experimental data show a non-linear behavior of the material, which is not described by the model. However, for our application, the material can be modeled as linear elastic since cell forces do not induce strong micropillars deflections.

4.5 CONCLUSIONS

DMTA and nanoindenter analysis allowed us to determine the mechanical parameters of P(nBA-co-4%MABP). In particular, the Young's modulus E was determined to 1.53 MPa, the shear modulus G to 0.51 MPa. The Poisson's ratio ν was determined to 0.5, when it is assumed that the elastomer is an incompressible polymer. The response of a micropillared substrate fabricated in P(nBA-co-4%MABP) to a tangential force applied to the top of the micropillars has been directly measured by using a nanoindenter. The relationship between the tangential force and micropillar's top deflection has been found linear elastic in the range of moderate deflections. A good agreement between the model and the experimental data has been found up to tangential force of 2.7 μN. Thanks to this model it is possible to quantitatively evaluate the force exerted on the elastomeric micropillar by a cell, once measured experimentally the induced deflection of the pillar and the point of application of the force.

5

CELL SOURCE

5.1 HUMAN PLURIPOTENT STEM CELL SOURCE

In vitro biological assays can provide more informative notions on physiological and pathophysiological mechanisms if an high control of the microenvironment is provided: this aspect can be optimized through microtechnologies techniques as discussed in the previous chapters. Concerning the reliability and the concrete impact and applications that these studies can produce, a big limit consists in the use of cells derived from animals to study biological mechanisms that can't be then transferred to human cells. Drug response as well as physiological behaviour of animal cells can be extremely different from that of human cells. Many human diseases (metabolic, genetic, multifactorial diseases) are difficult to study in animal models.
Human stem cells can give scientists a new tool for studying genetic and molecular basis on a much relevant model. In the studies presented in this thesis, experiments have been performed on hESCs, hiPSCs and on differentiated cells derived from human pluripotent stem cells, in order to develop more relevant *in vitro* models. Figure 46 shows an example of the hESCs colonies employed in this study, while in Figure 47 the image of a colony of hiPSCs is reported. We first performed *in vitro* tests to determine the physical plasticity of the nucleus in human pluripotent stem cells with the help of microfabricated substrates. Then we focused our attention on human pluripotent stem cells derived cardiomyocytes and we developed a toolbox where topological, chemical and mechanical properties of the substrates where cells have been cultured have been tuned to obtain reliable and reproducible *in vitro* tests.

5.2 STEM CELL MAINTENANCE OF PLURIPOTENCY AND DIFFERENTIATION

Mechanisms controlling pluripotency and differentiation of pluripotent cells have been extensively studied, but many aspects remain still unknown. It has been clearly demonstrated that activin/nodal signaling maintains the pluripotent status of hPSCs [206]. Pluripotency is regulated by a combination of extrinsic and intrinsic factors, FGF signaling and a balance between transforming growth factor-beta

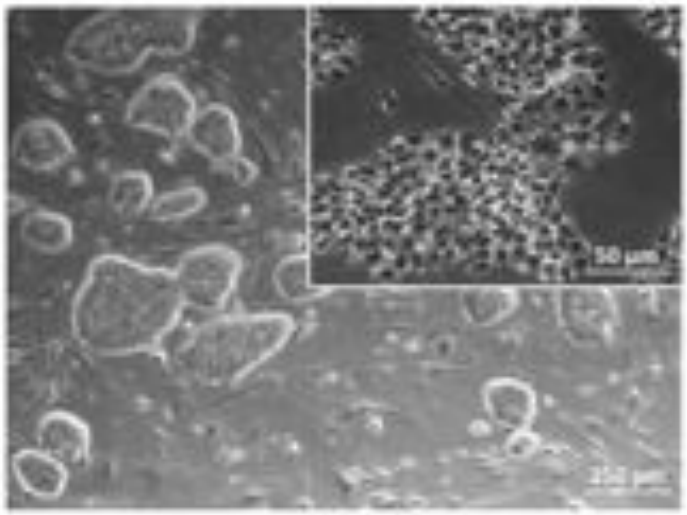

Figure 46: hESCs colonies growing on MEFs substrate, with relative enlargement of two adjacent colonies. Note the round shape and the compactness of the cells.

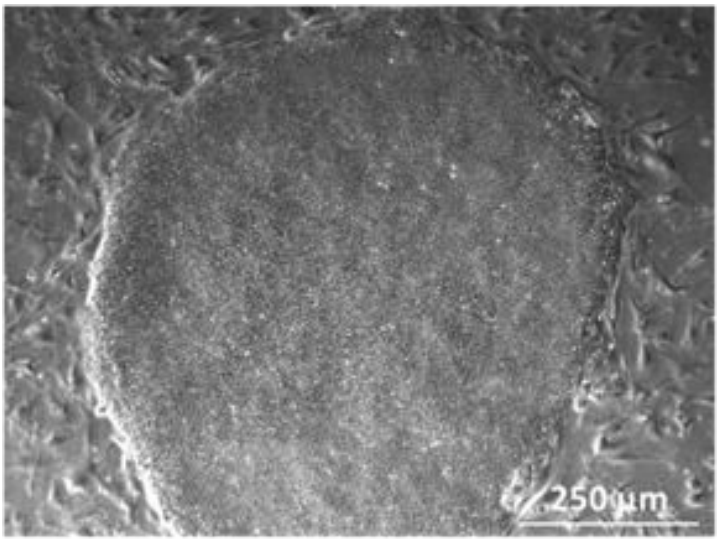

Figure 47: hiPSCs cell colony growing on MEFs substrate. Note the homogeneity and compactness of the pluripotent cells.

(TGF-beta) / Activin and bone morphogenic protein (BMP) signaling are central to hPSCs self-renewal. Intrinsic factors regulating pluripotency include transcription factors such as Nanog and octamer-binding transcription factor 4 (Oct-4) [207].
The TGF-beta ligand superfamily, plays a major role in maintaining the self-renewal capacity. TGF-beta signals through two main branches: the SMAD1/5 branch, which transduces on behalf of BMP and growth differentiation factor (GDF), and the TGF-beta/Activin/Nodal branch,

which involves the activation of SMAD2/3. There are also two inhibitory SMADs: SMAD6, which selectively inhibits SMAD1/5, and SMAD7, which inhibits both branches of TGF-beta signaling, that provide a repressive input on the pathway. Upon activation by phosphorylation and association with a common SMAD4, the receptor-activated SMADs translocates to the nucleus and, with other transcription factors, regulates gene expression. Activation of the TGF-beta/Activin/Nodal branch through SMAD2/3 is associated with pluripotency and is required for the maintenance of the undifferentiated state in hPSCs [208, 209].
FGF2 is known as a further fundamental factor promoting self-renewal in hPSCs and is capable of maintaining pluripotent cells in the absence of serum and feeder cells. FGF2 promote self-renewal of hESCs by activating the PI3K pathway [210]. Nanog is another member of the group of transcription factors whose functions are deemed essential for the process of self-renewal in hPSCs.
In contrast, BMP signaling is unable to support self-renewal and it is associated with differentiation to trophoblast or extraembryonic endoderm cells. In hPSCs, BMP_4 induces differentiation into mesoderm and ectoderm, whereas BMP2 promotes extraembryonic endoderm differentiation. Repression of BMP signaling by Noggin and FGF supports long term self-renewal.
HPSCs exhibit a number of signaling pathways involved in self-renewal and pluripotency that are interdependent and display a range of cross-talk mechanisms [211, 212]. The understanding of the exogenous and endogenous factors determining cell fate will facilitate the use of these cells in cell-based therapies and will allow further understanding of early developmental processes.

5.2.1 *Cardiac differentiation*

Directed differentiation of specific lineages from hPSCs, including human embryonic stem cells (hESCs) and human induced pluripotent stem cells (hiPSCs) is the first critical step toward constructing development or disease models, drug screening tools or cellular therapies from hPSCs.

Because postnatal cardiomyocytes have little or no regenerative capacity, very limited supplies of human cardiomyocytes are available at present. hPSCs could potentially provide an unlimited supply of cardiomyocytes from a single clonal source. In this work, human derived cardiomyocytes have been obtained adapting the protocol from Lian et al. [171]. Figure 48 shows the scheme of the protocol employed for cardiac differentiation. Efficient generation of functional human car-

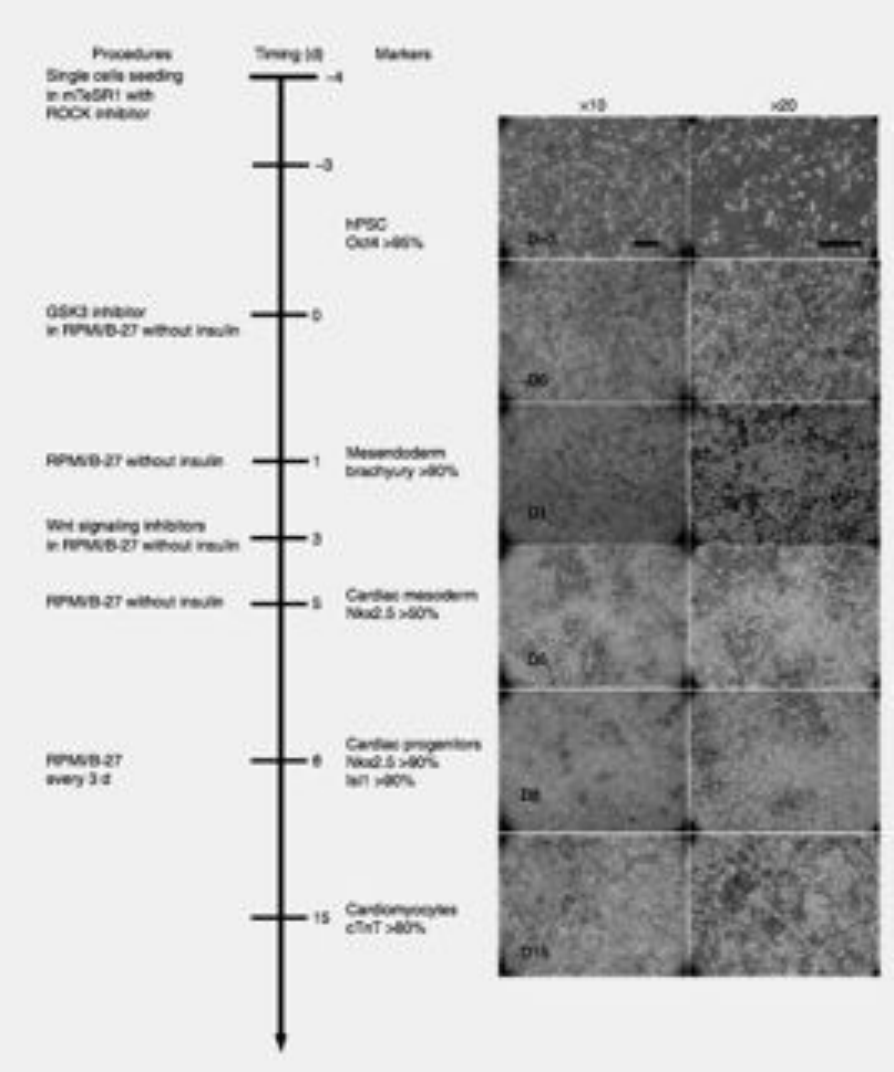

Figure 48: Schematic of the protocol for the differentiation of cardiomyocytes from hPSCs with small-molecule modulators of canonical Wnt signaling. Bright-field images of the typical morphology of day -3, day 0, day 1, day 5, day 8 and day 15. Cells are shown at x10 and x20 magnifications. Scale bar is 100 μm. (Adopted from Lian et al., 2013 [213] with permission).

diomyocytes from hPSCs is obtained using small-molecule inhibitors of canonical Wnt signaling in a growth factor-free system. Cardiogenesis is stimulated through a sequential treatment of GSK3 inhibitors and Wnt signaling inhibitors.

This approach provides robust cardiac differentiation, producing 80 — 98% cardiac cells, does not require genetic modification and is applicable to any existing hPSCs line.

The method can be performed under fully defined conditions with defined medium (RPMI/B-27 without insulin) and defined substrates

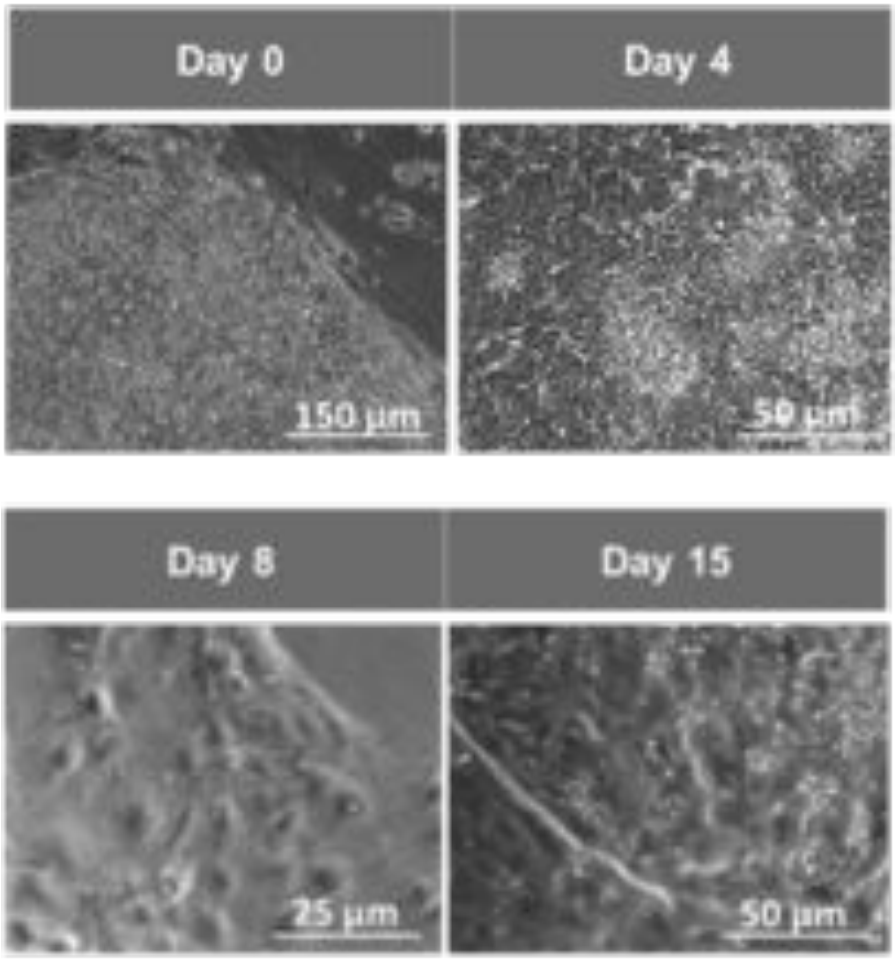

Figure 49: Sequential morphological changes from human embryonic stem cells (day 0), through mesoderm stages (days 4 and 8) to cardiomyocyte cells (day 15).

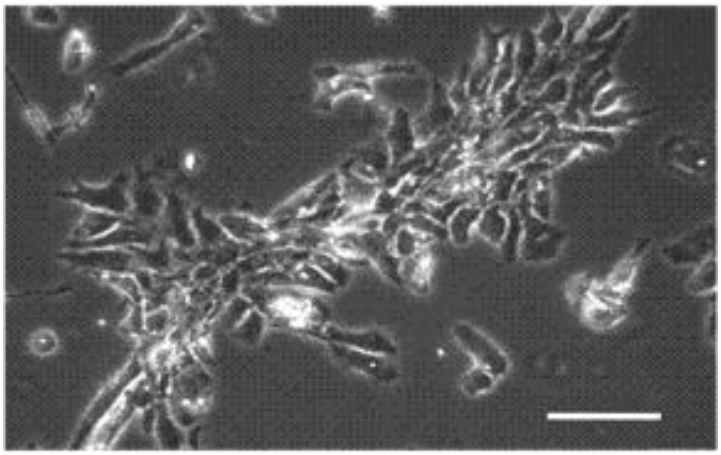

Figure 50: Cardiomyocyte cells derived from hESCs after disaggregation step. Scale bar is 60 µm.

(Matrigel coated plates). Figure 49 shows bright field images of the cells employed in this work. Cells evolve from the pluripotent stage (day 0) to the differentiated stage (day 15), through the mesoderm stage (day 4 and day 8). The subsequent step consists in disaggregation of the beating monolayer into single cells that can be seeded on the substrates. Figure 50 shows a bright field image of hESC-CMs after disaggregation step. Further details are provided in Chapter 10.

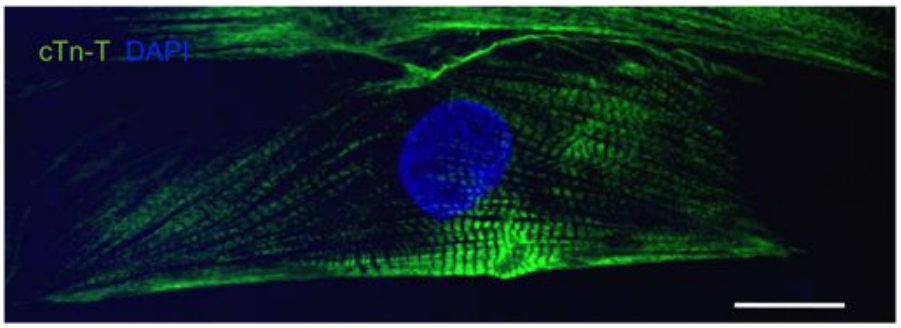

Figure 51: Immunofluorescence of cTnT in adhered hESC-CMs. Npte the clear sarcomeric organization. Nuclei are counterstained with DAPI. Scale bar is 15 μm.

A standard immunofluorescence protocol was used to stain cardiac troponin-T (cTnT) on hESC-CMs to evaluate the sarcomeric organization of the cell. Figure 51 shows a confocal image of a cardiomyocyte obtained empolying the differentiation protocol described above. Nucleus is stained in blue while cTnT in green. Immunostaining of cTnT shows a clear sarcomeric organization, represented by the well defined stripes marked in green in the image. Such sarcomeric organization is typical of heart muscle cells.

5.3 HFF CELL LINE

We used commercially available human postnatal foreskin fibroblast HFF-1 (ATCC) to text the citotoxicity of our substrate and to first evaluate the properties of cell-adhesiveness and cell-repellency of specific areas of the substrates.

6

CONFOCAL MICROSCOPY

6.1 CONFOCAL ANALYSIS

In confocal microscopy the light from the specimen that does not come from the microscope's focal plane is excluded, and the image of a thin cross-section of the sample is acquired, obtaining an image with a better contrast than that of a conventional microscope. Thus, fine details of the specimen can be observed and three-dimensional volumes of the sample can be reconstructed assembling a series of thin slices taken along the vertical axis [214]. The majority of confocal microscopes image either by reflecting light off the specimen or by stimulating fluorescence from dyes (fluorophores) applied to the specimen. In this work fluorescence confocal microscopy has been performed as it is the mode that is most commonly used in biological applications.

6.1.1 *Confocal microscopy*

In fluorescence microscopy the entire field of view of the specimen is completely illuminated. The highest intensity of the excitation light is at the focal point of the lens, but the other parts of the specimen receive also some light of lower intensity. To reduce this effect the confocal microscope pinhole is an aperture placed in front of the light source detector, so that light, which originates not from the focal volume is not allowed to pass [214, 215]. Thus, the only regions that are illuminated are a cone of light above and below the focal point, while the out-of-focus light is rejected.

As confocal microscopy is based on the creation of an image point-by-point, there are few emitted photons to collect at any given instant. Thus, each point must be illuminated for a long time to collect enough light to make an accurate measurement. This causes image acquisition to be very time consuming. The solution is to use a light source of very high intensity as a laser light source. In confocal microscopy, a computer is connected to the detector, to assemble the point-by-point images acquired by the microscope, building up the image one pixel at a time. The image created by the confocal microscope through this scanning process is of a thin planar region of the specimen. Out-of-plane unfocused light are rejected, resulting in a

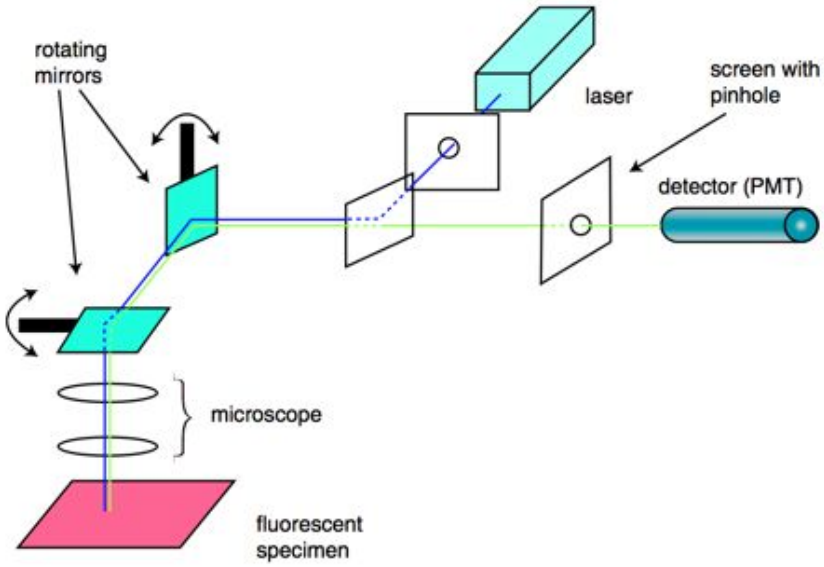

Figure 52: Basic setup of a confocal microscope. Light from the laser is scanned across the specimen by the scanning mirrors. Optical sectioning occurs as the light passes through a pinhole on its way to the detector. (Adapted from Semwogerere et al., 2005 [214] with permission).

sharper, better resolved image. In Figure 52, the scheme of a confocal microscope is depicted. The fluorescent specimen is excited by the laser light and fluoresces. The fluorescent (green) light is descanned by the same mirrors that are used to scan the excitation light (blue) from the laser and then passes through the dichroic mirror. After that, the light is focused onto the pinhole. As last step, the light that makes it through the pinhole is measured by a detector. Confocal microscopy can be employed to create images where small features such as proteins within a cell are visualized using a different fluorophores for each protein of interest. To visualize them in different colors two methods can be employed: in one method fluorophores are selected to correspond with the wavelengths of a multi-line laser and in the other fluorophores that emit at different wavelengths are selected to tag each protein [214].

6.1.2 *Confocal microscopy on living cells*

Confocal microscopy can be used effectively for the study of dynamics in living cells. However, when living specimens have to be analyzed the challenge of maintaining the normal function of the cells during the experiments must be taken into account. Cells can be damaged by the focused high intensity excitation light that has to hit the

specimen repeatedly for tracking the cellular dynamics, a problem that is worsened for 3D data collection. A further problem is that fluorophores can affect the cell behavior. Finally, oxygen molecules reacting with fluorophores in triplet excited states may generate free radicals that damage the cell. Despite the challenges, a wide variety of sophisticated fluorophores, designed to mark specific parts of the cell interior, have been developed to study different aspects of cell biology [214, 216]. The fluorophores molecules make their way into the cell and attach to the intracellular structures of interest. Fluorescent labeling is also applied to the study of dynamic processes of the cell. For example, some fluorophores have been developed for the measurement of membrane potentials and ion concentrations [217].

6.1.2.1 *Fluo-4 calcium dye*

Fluorescent calcium dyes are probes that show a strong enhancement of the fluorescence upon binding to Ca^{2+}. Fluo-3 and Fluo-4 are some of the most used calcium dyes in live-imaging. Figure 53 reports the mechanism by which a molecule of fluo-3 binds to a calcium molecule: carboxylic acid groups present in the molecules interacts with the Ca^{2+} ions. Such interaction causes a conformational change of the molecule fluo-3, that determines the fluorescent signal. Fluo-3 responds to Ca^{2+} binding with an increase of fluorescence intensity but no spectral shift [218].

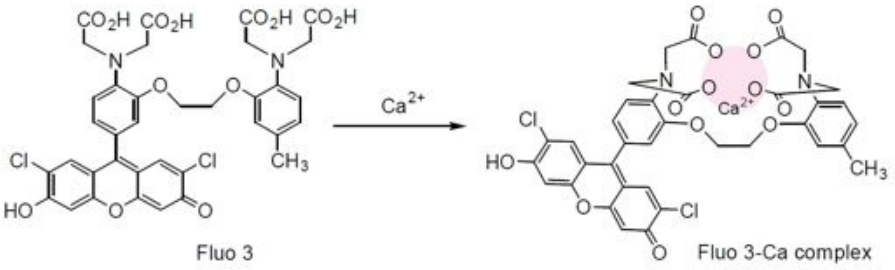

Figure 53: Mechanism of fluo3 and Ca^{2+} binding. Carboxylic acid groups present in the molecules interacts with the Ca^{2+} ions. Such interaction causes a conformational change of the molecule fluo-3, that determines the fluorescent signal.

Fluo-4 (Figure 54) is an improved version of fluo-3. Fluo-4 presents increased absorption of the exciting light at 488 nm and consequently higher fluorescence signal levels. Because it absorbs 488 nm excitation more efficiently than fluo-3, fluo-4 generates more intense fluorescence when used with an argon-ion laser sources [218]. It is commonly used as the non-fluorescent acetoxymethyl ester (Fluo-4 AM) which is cleaved inside the cell to give the free, fluorescent fluo-4.

Cell-permeant formulations can be loaded in cell media and are able to cross cell membrane. When the Ca^{2+} inside the cytosol is high, Ca^{2+} binds to fluo-4 probes that emit a fluorescent signal. As the Ca^{2+} concentration decreases, because the ion is pumped outside the cells, the free Ca^{2+} concentration inside the cell decreses, thus ions detach from the fluorofores, according to Chatelier's principle. In vitro, fluo-4 exhibits high fluorescence emission, a high rate of cell permeation, and a large dynamic range for reporting $[Ca^{2+}]$. Fluo-4 is well suited for photometric and imaging applications that make use of confocal laser scanning microscopy, flow cytometry, or spectrofluorometry, or in fluorometric high-throughput microplate screening assays. Because of its high fluorescence emission intensity, fluo-4 can be used at lower intracellular concentrations, making its use a less invasive practice [218].

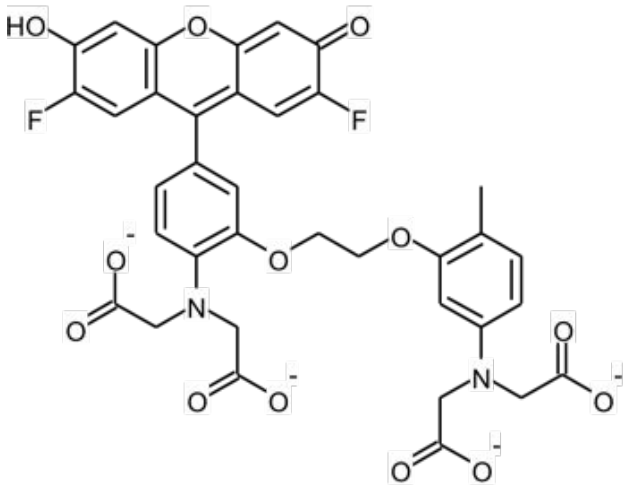

Figure 54: Chemical structure of Fluo-4.

6.1.2.2 *Di-8-ANEPPS cell membrane dye*

Substituted aminonaphthylethenylpyridinium (ANEP) dyes are molecules that fluoresce in response to electrical potential changes in their environment. These are fast-response probes that operate by means of a change in their electronic structure, and consequently their fluorescence properties, in response to a change in the surrounding electric field. Their optical response is sufficiently fast to detect transient (millisecond) potential changes in excitable cells, and they can be used to mark cell membrane as we did in this work to detect CMs membrane in particular on the area where cell anchors to the micropillars.

6.1.2.3 *Voltage sensitive dye*

A key challenge for optically monitoring the presence of an action potential is to develop sensors that can give large and fast responses to changes in transmembrane potential. To monitor cardiomyocyte's action potential we used a fluorescent sensor that has been developed by Miller et al. [219]. The sensor detect voltage changes by modulation of photo-induced electron transfer (PeT) from an electron donor through a synthetic molecular wire to a fluorophore. A molecular wire is a molecule where the charge (an electron in this case) can easily transfer between the two terminal groups of the molecule. The molecular wire minimizes the exponential distance dependence of intramolecular electron transfer and allows efficient electron transfer over a major fraction of the thickness of the plasma membrane. Figure 55 shows the functioning scheme of the probe.

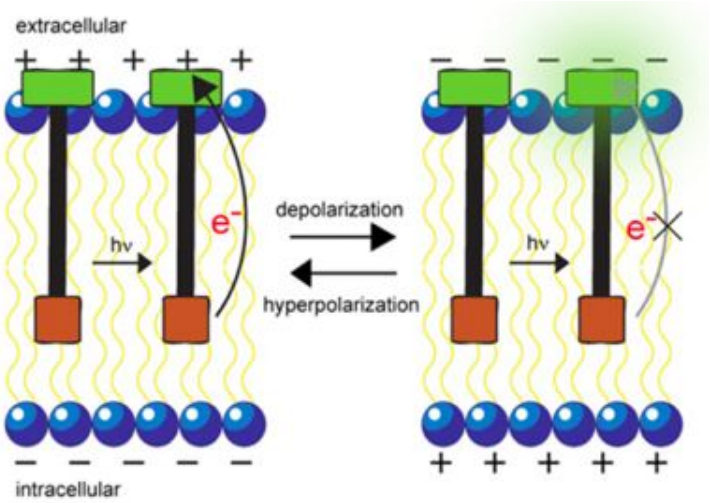

Figure 55: Mechanisms of fluorescent voltage sensing. A flux of electrons is transferred by a molecular wire (black) from an electron-rich donor (red) to a fluorescent reporter (green). At hyperpoarizing potentials, the electric field is aligned antiparallel to the direction of electron transfer, resulting in efficient photo-induced electron transfer (PeT) and quenched fluorescence (Left). Depolarization aligns the electric field in the direction of PeT, decreasing the rate of electron transfer and increasing fluorescence (Right). (Adapted from Miller et al., 2012 [219] with permission).

At hyperpolarizing potentials, there is an efficient electron transfer between the donor and the reporter, preventing fluorescent emission. Upon depolarization of cell membrane, the reverse electric field hinders the electron transfer from the donor to the reporter, resulting in fluorescence emission by the fluorphore, just as Ca^{2+} binding dequenches indicators like fuo-3 or fluo-4. Electron transfer occurs

within pico- to nanoseconds after photon absorption and returns to its initial state within a microsecond. Such timescale is suitable for biological assays.

The structural formula of the voltage sensor is reported in Figure 56. The molecule incorporates dichlorosulfofluorescein as a membrane-impermeant fluorophore, a p-phenylenevinylene molecular wire, and N,N-dimethyl- or dibutylaniline as an electron-rich quencher. The molecule also comprises 2,7-dichlorosulfofluorescein connected via one vinylene unit to dibutylaniline.

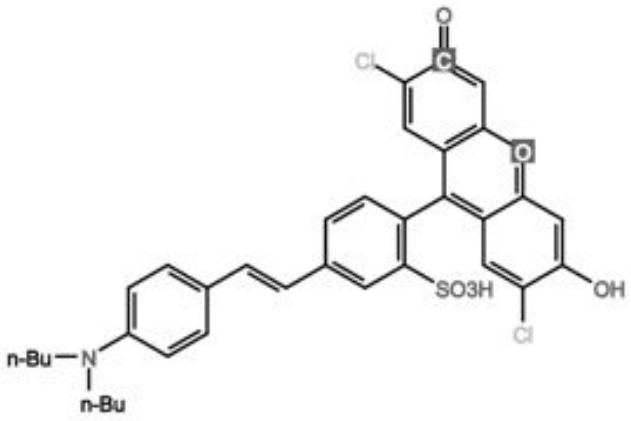

Figure 56: Chemical structure of the voltage sensitive dye.

To obtain fluorescence brightening upon depolarization the fluorophore must be located at the extracellular leaflet of the membrane. Correct positioning of the fluorophore-wire donor within the membrane is fundamental to take advantage of the vectoral nature of the transmembrane electric field and electron transfer. The longitudinal axis of the molecular wire must be normal to the plane of the plasma membrane. Furthermore, the voltage-sensitive dye molecules must all align in the same direction to avoid canceling out the electron transfer effect. The negatively charged sulfofluorescein allows an appropriate positioning of the molecule, precluding dye internalization and forcing an orientation in which the fluorophore adsorbs to the outer leaflet of the plasma membrane, with the lipophilic molecular wire and alkyl aniline dangling into the lipid bilayer.

7

PHYSICAL PLASTICITY OF THE NUCLEUS IN HUMAN PLURIPOTENT STEM CELLS

7.1 PHYSICAL PLASTICITY OF THE NUCLEUS OF HPSCS SEEDED ON MICROSTRUCTURED ELASTOMERIC SUBSTRATES

Nuclei of osteosarcoma cells have been reported to be highly deformable when seeded on microstrucutred substrates [139]. Despite the nuclear deformation they keep a degree of viability and capacity to proliferate similar to osteosarcoma cells seeded on flat substrates where nuclei keep a round shape.

In this work we were interested in evaluating physical plasticity of human pluripotent stem cells, using the same approach of Davidson et al. [139] and Badique et al. [145] to induce a morphological constrain to cell nuclei: cells were seeded on matrigel-coated microstructured polymeric substrates characterized by square micropillars with a width of 7 micrometers, an interaxial distance of 14 micrometers and a height of 7 micrometers. The geometrical structure of the substrates has been designed in order to impose a geometrical constrain to cell body and nucleus: the available space among micropillars is smaller than the average diameter both of cells and cell nuclei. The substrates were fabricated in polydimethylsiloxane (PDMS) as described in Chapter 3. Hoechst or 4',6-diamidino-2-phenylindole (DAPI) stain was used to mark cell nuclei of all cell lines and observed through fluorescent or confocal microscope. Figure 57 reports an image of the substrate used for this cell study (left) and an image of cell nuclei of human embryonic stem cells (hESCs) seeded on the substrate (right). Nuclei clearly deform to adapt to the substrate morphology. In Figure 58 a further example of the nuclear response of hESCs seeded on microstructured substrates is reported: nuclei assume an highly deformed shape, penetrating into the micropillar interspaces. Nuclei are able to assume very unusual, branched shapes, to adapt to the morphological environment.

To understand if this physical plasticity of the nucleus could be related to the degree of differentiation of the cells, we decided to compare the deformability of the nucleus of cell lines at different degree of differentiation: human embryonic stem cells (hESCs) and human induced pluripotent stem cells (hiPSCs), cord blood mesenchimal stem cells (CBMSCs), and human epithelial renal cells (hERCs). The behav-

ior of such cell line in response to geometrical constrain of the substrate was also compared to the results obtained by Davidson et al. on osteosarcoma cells (SaOs-2).

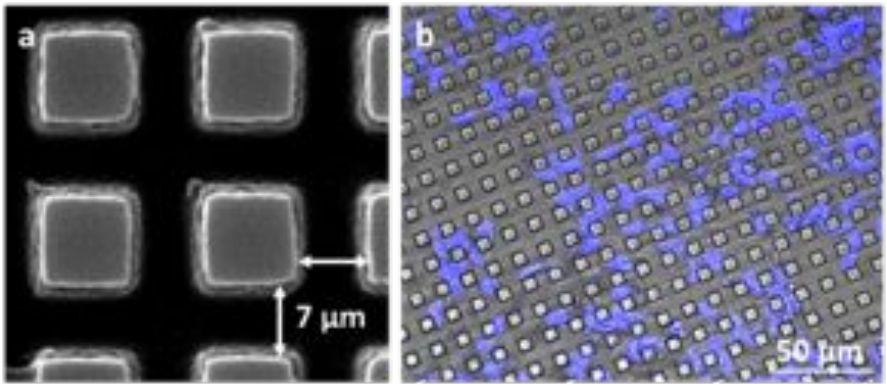

Figure 57: Image of the substrate used for the study on nuclear deformability. A) PDMS micropillars obtained from a square lattice of 7x7 µm. B) hESCs adhering to the micropillar substrate. Note the evident nuclei deformation (stained in blue with DAPI) of the stem cells adapting to the microstructured geometry.

In Figure 59 images of fluorescent labeled nuclei of different cell lines seeded on microstructured substrates are shown. SaOs-2, hESCs and hiPSCs nuclei are highly deformable. Most of the nuclei of hERCs keep a round shape, while CBMSCs are characterized by an intermediate behavior, with some nuclei more and some other less deformable. Qualitative results suggest that nuclear capability to deform adapting to the substrate morphology is related to the degree of differentiation of the cell: the more differentiated and therefore specialized is the cell, the less deformable is the nucleus. To quantitatively evaluate nuclear deformation, we calculated two parameters, which are related respectively to nuclear penetration among micropillar interspaces and to nuclear shape: nuclear deformability (N_D) and nuclear concavity (N_C), based on image analysis methods described in Chapter 10 and in Appendix B.

Briefly, N_D has been calculated as the percentage of the nuclear volume that lies below pillar height: we named V_b (volume below) the part of the nucleus which penetrates among pillar interspaces and V_a (volume above) the part of the nucleus which stays above the pillar heads. Nuclear deformability (N_D) is defined here as $N_D = \left(\frac{V_b}{(V_a+V_b)}\right) * 100$. Figure 60 shows a confocal image of a fluorescent labeled deformed nucleus which volume lies in part above the head of the micropillars and in part below this height. In Figure 61 the nuclear deformability values calculated respectively for SaOs-2, hESCs,

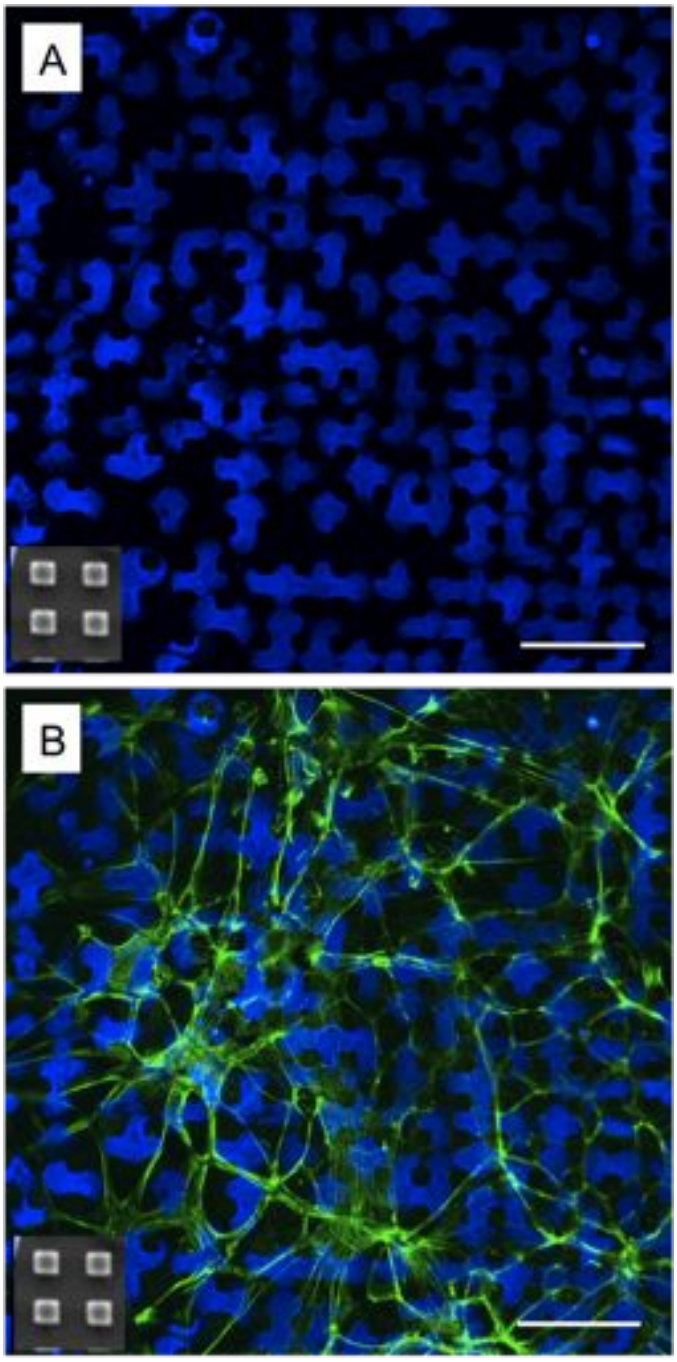

Figure 58: hESCs seeded on microstructured PDMS substrate after 48 hours from seeding. Cell nuclei penetrate among micropillar interspaces assuming very unusual deformed shapes. A) Immunostaining of nuclei with DAPI. B) Immunostaining of nuclei (blue) with DAPI and actin filaments (green) with phalloidin. Scale bar is 30 μm.

hiPSCs, CBMSCs and hERCs after fixing the cells at day 2 are plotted. Pluripotent stem cells present an high nuclear deformability (above

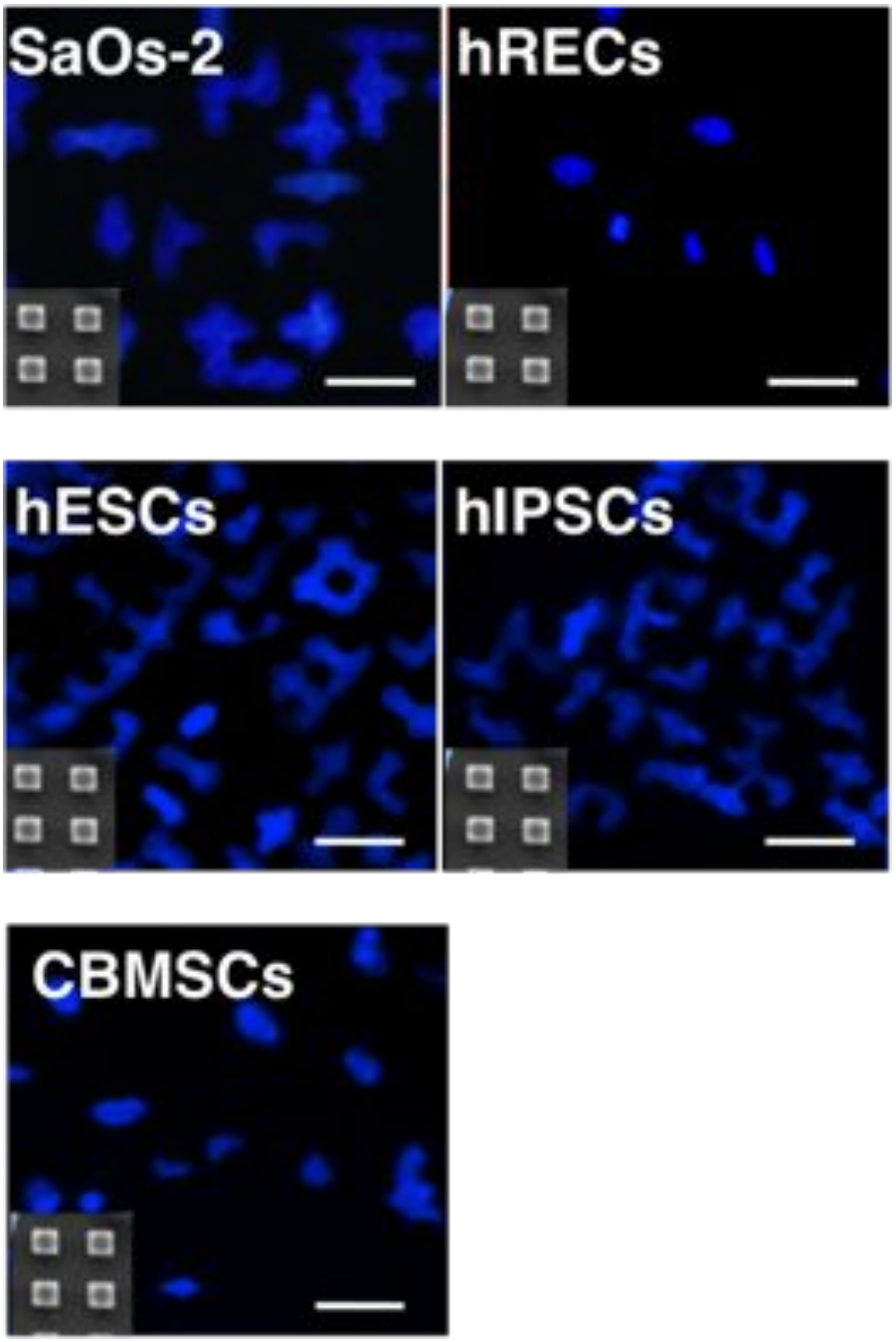

Figure 59: Evaluation of nuclear deformability for different cell lines. DAPI stained nuclei of SaOs-2, hiPSCs, hESCs, and CBMSCs acquired through fluorescent microscopy at day 2. Images show very deformed nuclei that assume unusual concave and sometimes branched shapes in hESCs, hiPSCs and SaOs-2. hERCs keep a round shape and CBMSCs show an intermediate behavior. Scale bar is 20 μm.

50%) which progressively decreases in the case of partially (CBMSCs,

$N_D = 23\% \pm 12\%$) and completely (hERCs, $N_D = 11\% \pm 4\%$) differentiated cells. SaOs-2 present values of N_D which are higher than the values calculated for human pluripotent stem cells lines ($N_D = 85\% \pm 12.6\%$).
Along with nuclear deformability (N_D), nuclear concavity (N_C) was quantified to evaluate the physical plasticity of the nucleus of different cell lines seeded on microstructured substrates. This is an interesting parameter as any concave structural element has been caused by substrate perturbation as the native cells (i.e. cells not in contact with a microstructured substrate) do not exhibit any concave structures. N_C is the percentage of nuclei that present at least one concave element. Figure 62 shows five images of fluorescent labeled nuclei that present respectively 0, 1, 2, 3 and 4 concave elements. For each cell line the distribution of the number of concavities (N_C) was also evaluated: cell lines where the majority of the cells present none or only one concavity can be considered less deformable than cells where high number of nuclei show three or four concavities. Figure 63 reports the value of nuclear concavity calculated for each cell line and the corresponding distribution of the amount of concavities (1, 2, 3 or more) for each cell line. Hardly deformable cells such as CBMSCs and hERCs are characterized by nuclei that never present three or four concavities. Concave shapes appear only in deformable nuclei to adapt to pillar interspaces. SaOs-2, hESCs and hiPSCs have value of N_D above 60%, i.e. more than a half of the analyzed cell nuclei presented one or more concave structure due to the adaptation of the nucleus to the microstructures of the surface. In contrast to that, CBMSCs and hERCs have value of N_C below 25%. Furthermore nuclei of CBMSCs and hERCs were found to never present 3 or more concavities. The quantification of N_C reported in Figure 63 shows that pluripotent cells present higher capability to adapt to the substrate morphology than multipotent and adult cells. Such results confirm that the process of cell differentiation leads to an increase in nuclear stiffness.

7.2 MAINTENANCE OF PLURIPOTENCY

After assessing how hESCs have a highly deformable nucleus, we investigated if maintenance of pluripotency in hESCs is affected by the strong variation in nuclear shape due to the geometrical constrain imposed by microstructured substrates.

Human embryonic stem cells were seeded both on flat (Ctrl) and microstructured (μP) matrigel-coated PDMS substrates, and cultured in expansion medium. After 6 days cells were fixed and immunofluorescence analysis of pluripotency markers Oct-4, Nanog and SSEA4

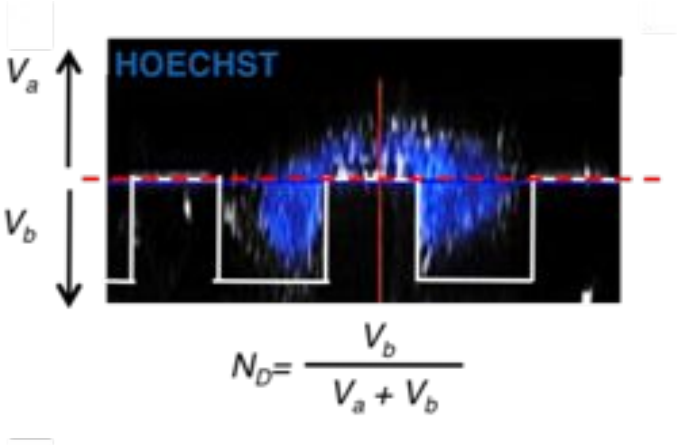

Figure 60: Definition of nuclear deformability. Confocal image of a fluorescent labeled deformed nucleus: V_b (volume below) is the part of the nucleus which penetrates among pillar interspaces; V_a (volume above) is the part of the nucleus which stays above pillar height. Nuclear deformability (N_D) is defined as $N_D = \left(\frac{V_b}{(V_a+V_b)}\right) * 100$.

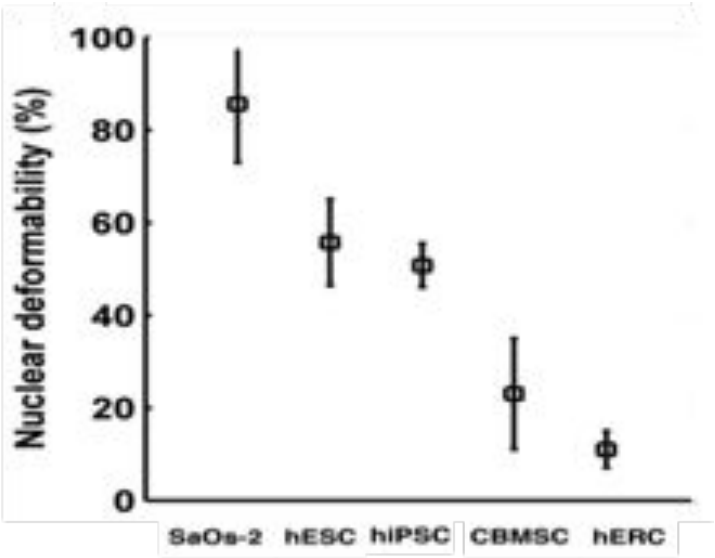

Figure 61: Quantification of nuclear deformability for different cell lines. Nuclear deformability values were calculated respectively for SaOs-2, hESCs, hiPSCs, CBMSCs and hERCs after fixing the cells at day 2. hESCs , hiPSCs and SaOs-2 present a nuclear deformability above 50%.

was performed, as reported in Figure 64. Cells expanded in Ctrl and μP substrates show a qualitatively comparable expression of the pluripotency markers. In order to confirm these data, we performed quantitative real-time polymerase chain reaction (qRT-PCR) on the two mRNA

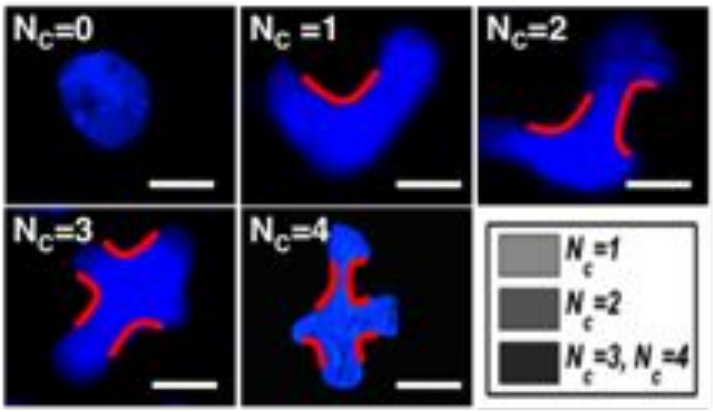

Figure 62: Concave structures of the nuclei. Confocal images of fluorescent labeled nuclei. The concave structures of the nuclei, due to cell adaptation to the geometry of the substrate, are marked in red. Examples of nuclei with 0 concavities (Number of concavities = N_c = 0), 1 concavity (N_c = 1), 2 concavities (N_c = 2), 3 concavities (N_c = 3) and 4 concavities (N_c = 4) are shown. The presence of such concavities in the nucleus is related to nuclear capability to deform.

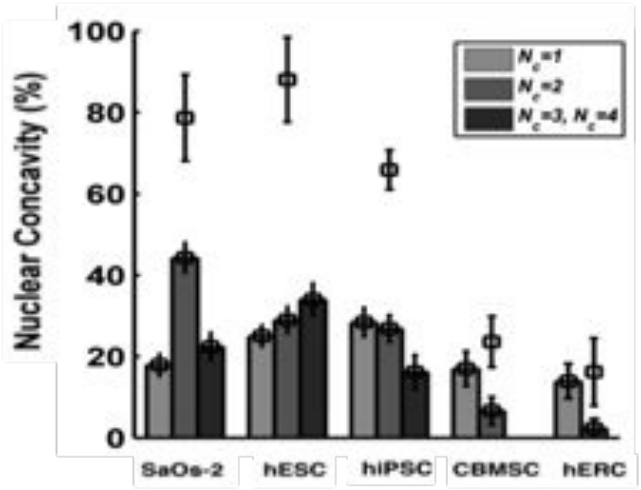

Figure 63: Nuclear concavity (N_C), meant as the percentage of cell nuclei having at least one concave structure when seeded on microstructured substrates, has been evaluated on different cell lines. hESCs, hiPSCs and SaOs-2 have high values of N_C (above 50%). In contrast to that, CBMSCs and hERCs have low values of N_C (below 25%). Furhtermore CBMSCs and hERCs do not present highly branched nuclei, (i.e. nuclei where 3 or more concave structures are not present), as reported by the histograms.

transcripts OCT4 and NANOG, encoded by pluripotency genes POU5F1

and NANOG, respectively. The results of the qRT-PCR, shown in Figure 65, report that the quantity of mRNA transcripts OCT4 and NANOG found in cells expanded on Ctrl are comparable to that found in cells expanded on μP. Pluripotency is maintained by hPSCs also when the expansion is performed in μP substrates, where cell nuclei present very deformed shapes. Consequently, alteration of nuclear shape does not affect maintenance of pluripotency.

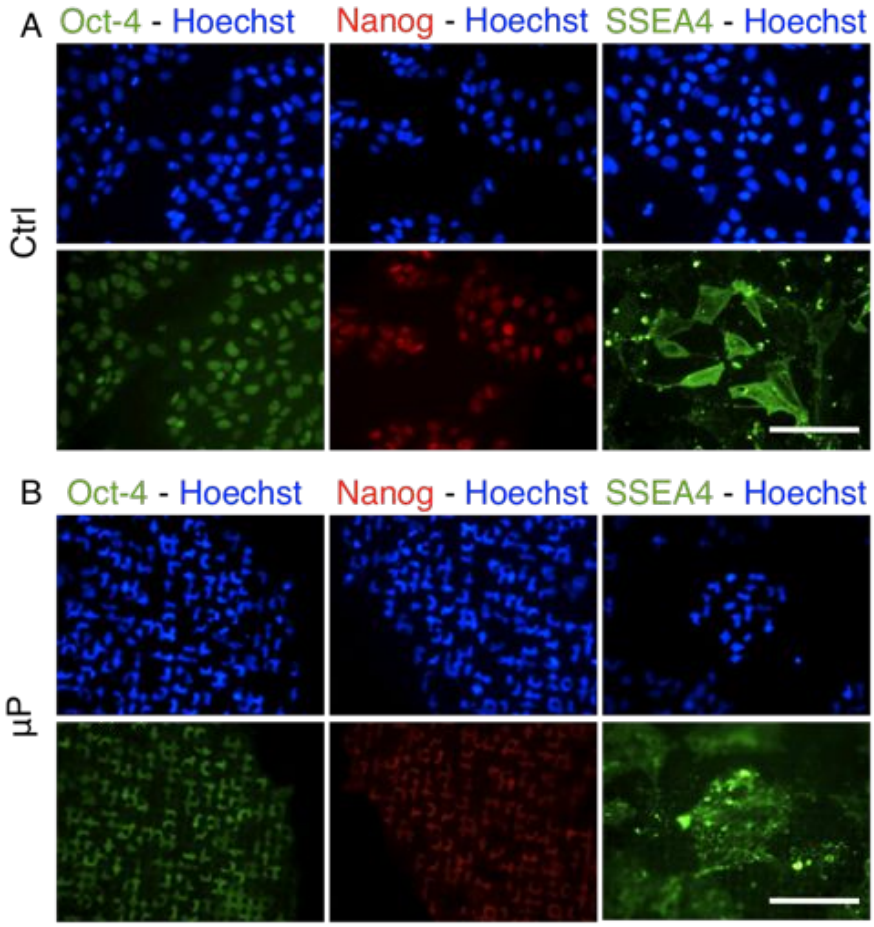

Figure 64: hESCs pluripotency maintenance on microstructured substrates. A) Immunofluorescence panel of cells cultured on flat PDMS substrates (Ctrl), showing cell nuclei and pluripotency marker expression of Oct-4, Nanog and SSEA4. B) Immunofluorescence panel of cells cultured on PDMS microstructured substrates (μP), showing cell nuclei and pluripotency marker expression of Oct-4, Nanog and SSEA4. Marker expression between Ctrl and μP is similar. These panels show how nuclear deformation seems to have no effect on pluripotency maintenance. Scale bar is 50 μm.

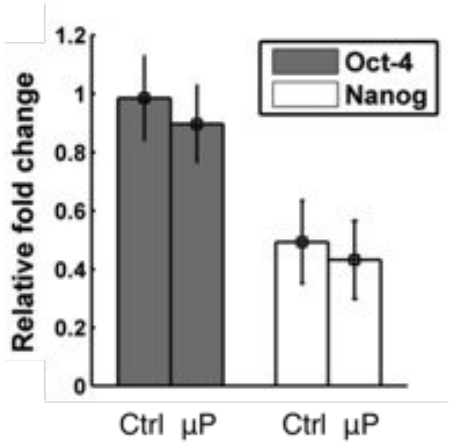

Figure 65: qRT-PCR on OCT-4 and NANOG mRNA transcripts of hESCs cultured on flat PDMS (Ctrl) and micropillared PDMS substrates (µP) shows comparable expression of pluripotency transcripts between the two conditions. Relative fold expression normalized on GAPDH ($n = 3$).

7.3 NUCLEAR DEFORMATION AND EARLY GERM LAYER SPECIFICATION

As next step, we analyzed if the alteration of nuclear shape induced by the substrate morphology can influence the process of early germ layer committment into the three germ layers (ectoderm, endoderm, mesoderm). Again, we seeded hESCs both on flat (Ctrl) and microstructured (µP) matrigel-coated PDMS substrates. The scheme in Figure 66 shows the different steps of the experiment: from cell seeding on microstructured substrates, to cell specification into the three early germ layers, to quantification of the nuclear deformation for each germ layer. Cells were first expanded for two days in expansion medium to achieve $70 - 80\%$ cell confluence. Early germ layer specification was induced for 5 days, after which the nuclei, which had been fluorescently labeled, were observed through fluorescent or confocal microscopy. To understand if early germ layer specification took place, we immunolabeled a specific marker for each germ layer: Beta-III tubulin (Beta-III Tub) for ectoderm, brachyury-T (Bra-T) for mesoderm and alpha fetoprotein (AFP) for endoderm. Figure 67 shows fluorescent microscope images of immunostained cells seeded on flat substrates (panel above) and on microstructured substrates (panel below). Interestingly, when seeded on microstructured substrates, nuclei from ectoderm germ layer tend to escape from pillar interspaces and assume a round shape, whereas nuclei from mesoderm and endoderm germ layers still lie among the microstructures and keep a

deformed shape. Immunofluorescence analysis of ectoderm, mesoderm and endoderm markers seems normally expressed in cells on μP, compared to flat controls, and both in cells with a deformed nucleus (mesoderm, endoderm) and in cells with an undeformed nucleus (ectoderm). However, immunofluorescence analysis does not provide quantitative information on the expression of the above mentioned markers.

To quantitatively assess possible changes in gene expression of the cells due to the variation of nuclear shape in response to the microstructured environment, qRT-PCR was performed to evaluate the expression of Beta-III Tub, Bra-T and AFP for each germ layer, both for ctrl reference (flat) and μP substrates.

In Figure 68, qRT-PCR results are reported. AFP, which is the marker of endoderm committment, is significantly higher expressed in endoderm differentiating cells both on flat and μP substrates. Beta-III Tub, which is the marker of ectoderm specification, is significantly higher expressed in ectoderm differentiating cells both on flat and microstructured substrates. Bra-T, which is the marker of mesoderm, is significantly higher expressed in mesoderm differentiating cells both on flat and microstructured substrates. Interestingly, Bra-T results also significantly more expressed in endoderm differentiating cells cultured on μP than in endoderm differentiating cells cultured on flat (Ctrl) substrates.

Our data suggest that when ectoderm or mesoderm early germ layer committment was performed, the morphology of the substrate, which lead to a reorganization of the nuclear shape, did not influence the process of cell specification. In contrast to that, when endoderm early germ layer committment was performed, we found an unusually high expression of the mesoderm marker Bra-T on cells cultured on microstructured substrate. From such data it seems that changes in nuclear morphology influence the process of endoderm early germ layer committment. On the other hand, the processes of ectoderm and mesoderm early germ layer specification seem to evolve despite the variation in nuclear shape. The reasons why the effect of variation in nuclear morphology influences only the process of endoderm early germ layer committment are still under investigation.

The qualitative analysis of the nuclear morphology along the process of differentiation into the three germ layers, revealed that when cells were induced into ectoderm specification on microstructured substrates, their nuclei raised up from micropillar's interspaces assuming a round shape. Cell nuclei respond in a different way to the morphological environment along the process of differentiation, in the case of ectoderm committment. Initially when cells are in the

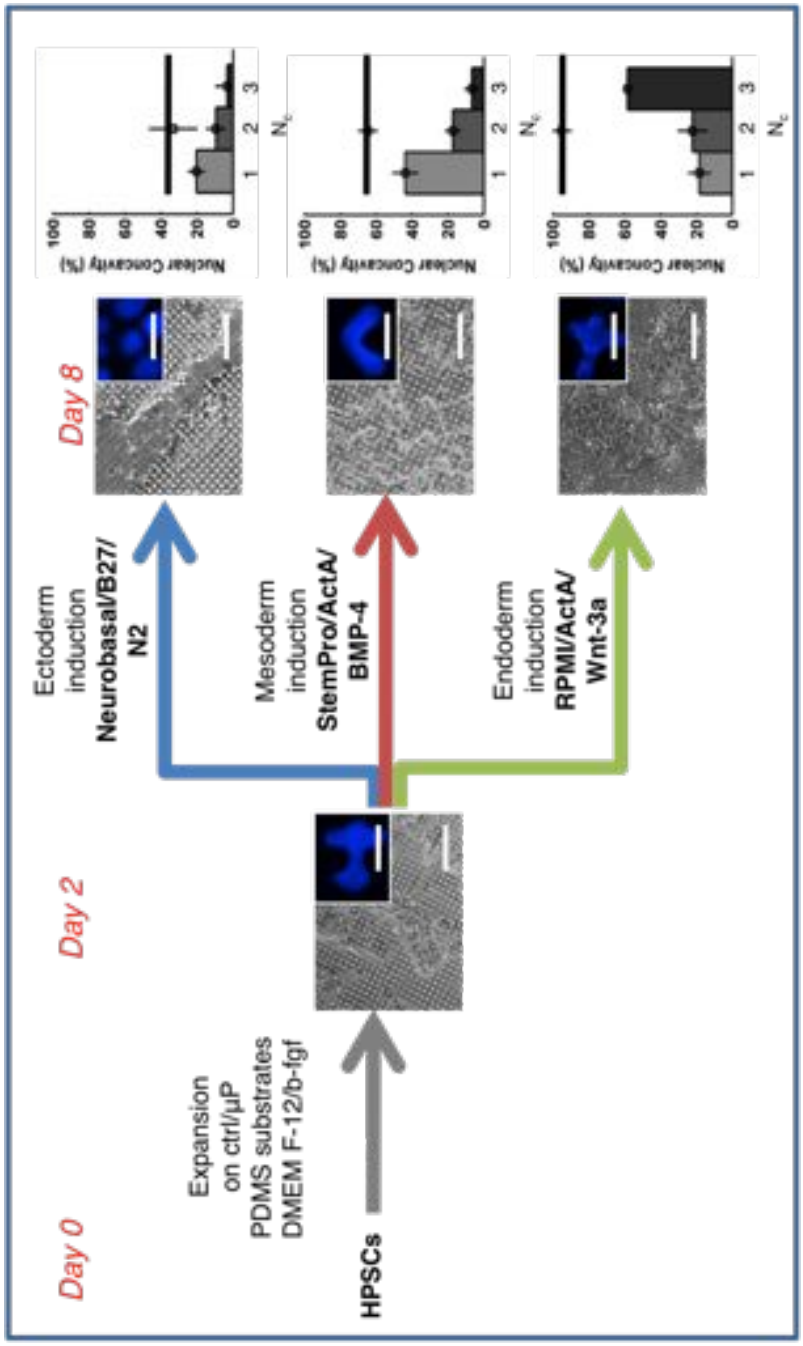

Figure 66: Schematic experimental procedure of early germ layer commitment in hESCs with self-deformed nuclei. Cell are passaged on microstuctured PDMS substrates and expanded for 2 days. Different replicates are then induced with specific media into 3 germ layers for 5 days. Nuclear concavity is then calculated in the three different conditions (ectoderm, mesoderm, endoderm early germ layer specification).

pluripotent stage, nuclei strongly adapt to the geometry of the sub-

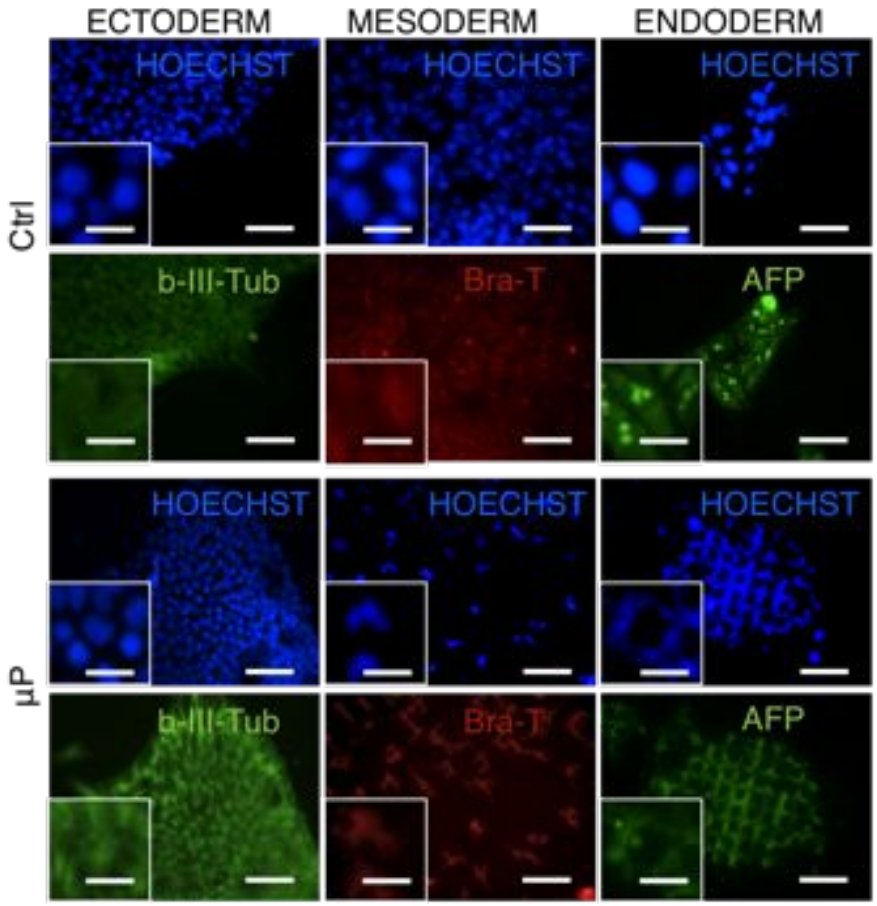

Figure 67: Immunofluorescence panel showing hESCs after early germ layer specification performed both on flat PDMS substrates (Ctrl) and on PDMS substrates (μP). Cells are marked with Beta-III Tub for ectoderm, Bra-T for mesoderm and AFP for endoderm. Notably, ectoderm cell nuclei tend to homogeneously emerge from the pillars and gain round shape. Mesoderm and endoderm cells tend to differentiate while maintaining highly deformed nuclei.

strate. Then, as long as the process of early germ layer specification takes place, cell nuclei are not capable to squeeze in between micropillar interspaces, and gain a round or oval shape.

In Figure 69 a time-course of live-stained hESCs nuclei from pluripotent state at day 1, with highly deformed shapes, to early ectodermal commitment at day 3, with almost entirely round-shaped nuclei, is shown. In Figure 70 the quantification of the nuclear concavity parameter, calculated day by day, is plotted. Notably, major shape changes happen between day 1 and day 2 - 3 of early germ layer committment, with a big part of cells losing self-deformation capacity.

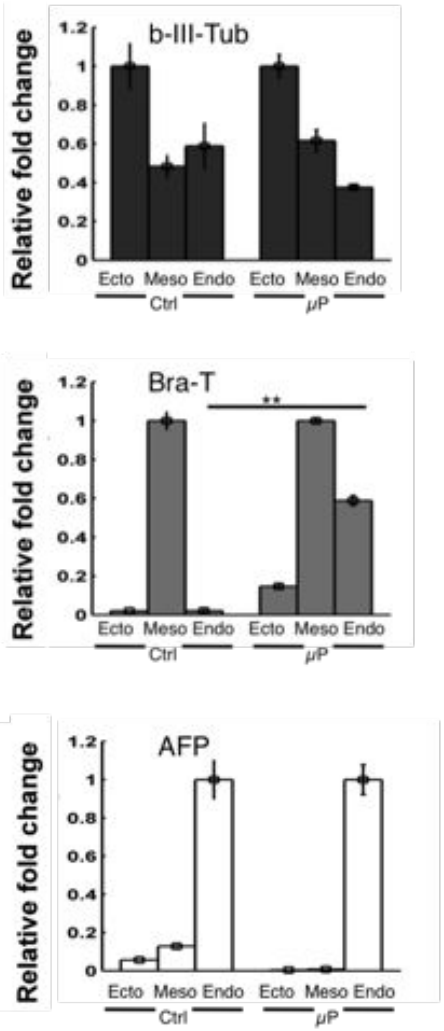

Figure 68: qRT-PCR of Beta-III Tub, Bra-T and AFP performed on cell committed to early germ layers both on flat (Ctrl) and on microstructured substrates (μP). Beta-III Tub, which is the marker of ectoderm, is significantly higher expressed in ectoderm differentiating cells both on flat and μP substrates. Bra-T, which is the marker of mesoderm, is significantly higher expressed in mesoderm differentiating cells both on flat and μP substrates. Interestingly, Bra-T results significantly more expressed in endoderm differentiating cells cultured on μP than in cells cultured on flat (Ctrl) substrates. AFP, which is the marker of endoderm, is significantly higher expressed in endoderm differentiating cells both on flat and μP substrates. Relative fold expression normalized on GAPDH ($n = 3$). Student t test p-values $P \leqslant 0.01$ (**).

The investigation of nuclear membrane protein expression along the process of ectoderm specification, and in particular the analysis of the differences in protein expression between day 1 and day 3 of

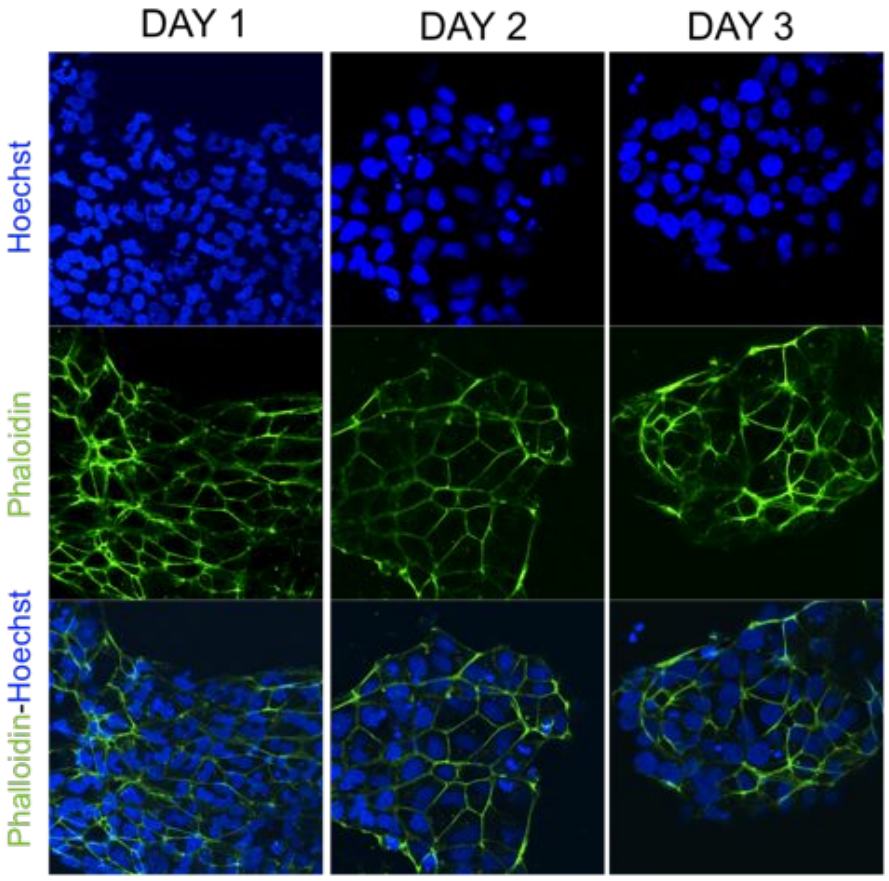

Figure 69: Immunostaining of actin and nuclei on hESCs along ectodermal committment on micropillared surfaces. Nuclear morphology at day 1 of the specification process is still very deformed. From day 2 nuclei assume a less and less deformed shape and raise up from the micropillars.

early germ layer committment is currently in progress and will help in uderstanding which proteins play a major role in the process of nuclear stiffening, typical of differentiated cells.

7.4 DISCUSSION

One of the most fundamental problem in tissue morphogenesis is the question of how changes in cell shape produce alteration of nuclear form and function [148, 149]. Nuclear structural properties strictly depend on the composition and organization of both lamina and chromatin and physical malleability or rigidity of the nucleus is fundamental to assure a specific cell function.
Maniotis et al. proposed that cell shape information are transduced into gene expression through mechancial forces transmitted by the

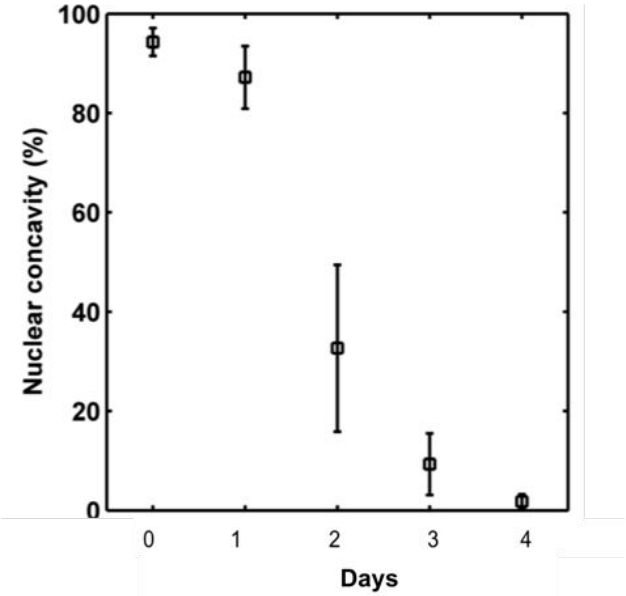

Figure 70: Nuclear concavity time-course of pluripotent cells (day 0) induced to ectoderm commitment (Day 4). Major drop of N_C is in between day 1 and day 2 of ectodermal committment process.

cytoskeleton [148]. The importance of the mutual connection between nucleus and cytoskeleton is also reported by Khatau et al., who showed the presence of a dome-like actin structure, called actin cap, that covers the top of the nucleus. Their results suggest that this structure is partially involved in the process of nuclear shape adjustment [147, 132]. Varsaevel et al. reported studies on the connection betwen cell and nuclear shape on endothelial cells, showing how in adult cells actin filament are essential factors in the mechanical process of nuclear remodeling [149]. In particular, they assessed that intermediate filaments provide resistance to nuclear deformation and thus help to maintain the mechanical integrity of the nucleus, whereas the mechanism governing nuclear elongation and orientation relies on actomyosin activity and actin filament organization. Badique at al. described a strong connection between nuclear deformability and cytoskeletal organization also on different cancerous cell lines. In his work it is shown how actin filaments play a fundamental role in the process of nuclear deformation [145].
Concomitant with these recent discoveries, significant advances have been made in terms of identifying the molecular links between the nuclear envelope and the cytoplasmic filaments (as discussed in Chapter 1), and new insights have been gained into the mechanistic maintenance of the nucleus [140, 141, 150]. However, despite the proofs of the involvement of cytoskeletal actin filament interplaying with the proteins of the nuclear enevelope in the alteration of the intracellu-

lar force balance, the mechanical and biological explanations of the adaptive remodelling of the nucleus are still unclear.

In this scenario, the study of the physical plasticity of human pluripotent stem cell nuclei and its modification along the process of differentiation can represent a powerful model to assess how, when and through which mechanisms, nuclear shape is regulated in differentiated cells.

Swift et al. in a recent work revealed that lamin-A plays a fundamental role in defining nuclear stiffness and in regulation of the process of differentiation from mesenchimal stem cells to soft or stiff tissues [150]. According to their work, lamin-A seems to be the protein of the nuclear envelope that regulates cyotoskeletal response. Low level of lamin-A lead to differentiation in soft tissue (fat), increased levels of lamin-A leads to differentiation in stiffer tissue (bones). This same work shows also that high lamin-A level impedes nuclear remodeling under stress.

Pajerowski et al. [141] measured the nuclear stiffness of pluripotent stem cells which is shown to progressively increase along the process of differentiation. Such results are in agreement with our experiments on hPSCs, CBMSCs and hERCs seeded on microstructured substrates: our analysis shows that nuclei of cells at the pluripotent stage alter their shape to adapt to the geometry of the substrate and this peculiarity is progressively lost for more differentiated cells. This process can be related to the expression of lamin A/C in the nuclear envelope that connect and interact with cytoskeletal filaments to maintain the nuclear integrity in differentiated cells, as proposed by Pajerowski [141] and Swift [150]. However, several other complexes link the nuclear membrane to the cytoskeleton, as described in Chapter 1, and they can play a role in the process of nuclear remodeling.

In this work, we were interested in understanding if the alteration of nuclear shape typical of hPSCs seeded on microstructured substrates, would affect cell function, since this strong change on the morphology of cell nucleus can imply a reorganization of chromatin and a rearrangement of chromatin-lamina interaction. A relationship between morphological organization of cell nuclei and gene expression would support the hypothesis of a high correlation and cooperation among the different specific areas of cell nucleus called nuclear domains [133] which final function could be related also to their spatial location in the nucleus.

The immunofluorescence and qRT-PCR analyses on hPSCs expanded for 6 days both on flat and micrsotructured substrates revealed that the maintenance of pluripotency is not influenced by nuclear morphological reorganization induced by micropillars. Immunofluorescence

anlaysis of pluripotency markers Oct-4, Nanog and SSEA4 showed similar marker expression on flat and microstructured substrates. A further quantitative analysis of OCT-4 and NANOG performed by qRT-PCR confirmed that there is not a significative difference in the expression of important pluripotency markers when cells are expanded on flat (not deformed nuclei) or on microstructured (deformed nuclei) substrates. Such data demonstrated that at the pluripotent stage a clear morphological organization of the nucleus and of the cytoskeleton is still not developed and not necessary. In contrast to that, a precise control of the nuclei and cytoskeleton interplay to regulate cell and nuclear integrity will be required in most differentiated cells. Pluripotency was kept despite the high nuclear deformation of hPSCs when seeded on microstructured substrates. However, the process of early germ layer commitment in endoderm, mesoderm and ectoderm did not always evolve in the same way when cells were differentiated on flat or on microstructured substrates. After 5 days of committment into the three germ layers both on flat and on microstructured substrates, we observed that nuclei from ectoderm germ layer tend to escape from micropillar interspaces and assume a round shape, whereas nuclei from mesoderm and endoderm germ layers still lie among the microstructures, keeping deformed shapes. The change in nuclear shape typical of ectoderm early germ layer committment took place in particular between day 1 and day 2 - 3 of differentiation, when nuclear concavity decreased from a value of 87% to a value of 30%. Such increase in nuclear stiffness could be related to variation in protein expression and function at the level of nuclear envelope, in good agreement with previously reported evidences that during differentiation there is a stiffening of cell nuclei regulated by the development of lamins and cytoskeletal filaments typical of the process of differentiation. According to our results, such development occurs between day 1 and day 3 of early germ layer committment, therefore further experiments will focus on the analysis of differences in proteins expression during this time lapse.

When we quantified gene expression of three markers specific for each germ layer (Beta-III Tub for ectoderm, Bra-T for mesoderm and AFP for endoderm), we discovered that the expression of Beta-III Tub (normally higher in ectoderm germ layer) and AFP (normally higher in endoderm germ layer) were not significatively different between ctrl and μP, whereas the level of expression of Bra-T (typical of mesoderm commitment) was unusually high in cells committed to endoderm on microstructured substrates. Such result suggests that the process of differentiation in endoderm was hindered when cells presented deformed nuclei during differentiation. Further experiments

will be addressed to confirm such hypothesis and to clarify which mechainisms, that impede a normal process of endoderm early germ layer committment, are involved.

7.5 CONCLUSIONS

In summary, our study showed that:

- Maintenance of pluripotency of hPSCs is not affected by alteration in nuclear shape.
- The process of early germ layer committment into mesoderm and ectoderm takes place also when cells are differentiated on microstructured substrates.
- Along the process of ectoderm committment, a stiffening of cell nuclei is reported;
- The process of endoderm germ layer committment seems to be hindered by the alteration of nuclear shape, reported on hPSCs seeded on microstructured substrates. In fact, alteration in nuclear shape affects the expression of Bra-T.

All together, these results revealed that the physiological process of specification from human pluripotent stem cells to early germ layer committment can be influenced by nuclear shape. Further experiments are in progress, to elucidate which proteins of the nuclear envelope and of the cytoskeleton are involved in the process of nuclear stiffening reported between day 1 and day 2 - 3 of early germ layer committment. Additionally, further quantitative comparison between gene expression of cells differentiated on flat and on μP substrates will be developed. New results will help to understand how important nuclear shape is in the process of cell differentiation, which role nuclear morphology plays in gene expression and which are the key proteins and molecules in the nuclear envelope and cytoskeleton that play a fundamental role in defining nuclear shape along the process of cell differentiation.

8

CALCIUM DYNAMICS AND CONTRACTION FORCE QUANTIFICATION ON HUMAN PLURIPOTENT STEM CELLS DERIVED CARDIOMYOCYTES

8.1 CELL-SUBSTRATE INTEGRATION

We evaluated the contraction force of hESC-CMs by placing cells on micropillared elastomeric substrates: from micropillar deflection it was possile to quantify the force of contraction applied by the cells according to the finite element model (FEM) described in Chapter 4. The elastomeric microstructured substrates where formed by micropillars having a width of 10 μm, a heigth of 20 μm and a interaxial distance of 25 μm. We also evaluated the duration of hESC-CMs calcium transients both on flat and on microstructured substrates, to understand if the mechanical stimuli provided by micropillar deflection could influence the process of functional maturation of the cells. In both cases (flat and microstructured substrates), the surface was photopatterned to guide cell adhesion and tune cell shape.
The fabrication protocols are described in more detail in Chapter 3. Briefly, flat P(nBA-co-4%MABP) substrates were obtained by spin-coating the polymer on a previously silanized glass slide and crosslinking it by UV light exposure. Microstructured P(nBA-co-4%MABP) substrates were obtained by pouring a drop of polymer into the appropriate PDMS stamp and crosslinking it by UV light exposure. In both cases polyacrylamide (PAA) was selectively crosslinked to the top of the P(nBA-co-4%MABP) surface by UV light exposure through a chrome mask.
We first tested the cell response to our engineered substrates using human foreskin fibroblasts (HFF) cells. HFF were seeded on flat P(nBA-co-4%MABP) substrates photopatterned with PAA in such a way that stripes of cell-adhesive areas and stripes of cell-repellent areas were obtained. Hydropilic PAA stripes are protein-repellent so they do not adsorb the proteins present in the cell medium. In contrast to that, hydrophobic P(nBA-co-4%MABP) stripes adsorb such proteins. Since cell adhesion is mediated by transmembrane receptors that interact with the proteins present in the environment, HFF adhered to the protein-adsorbent P(nBA-co-4%MABP) stripes, whereas adhesion of HFF to PAA stripes was prevented. In response to surface chemistry and topography, a strong cellular alignment was observed in the di-

rection of the patterns. Figure 71 shows HFF after seeding on substrates having cell-adhesive stripes with a width of 100 μm (images above) or 50 μm (images below). The images show how HFF selectively grew and aligned on the cell-adhesive areas. The capability to guide cell-adhesion through the described approach was therefore demonstrated.

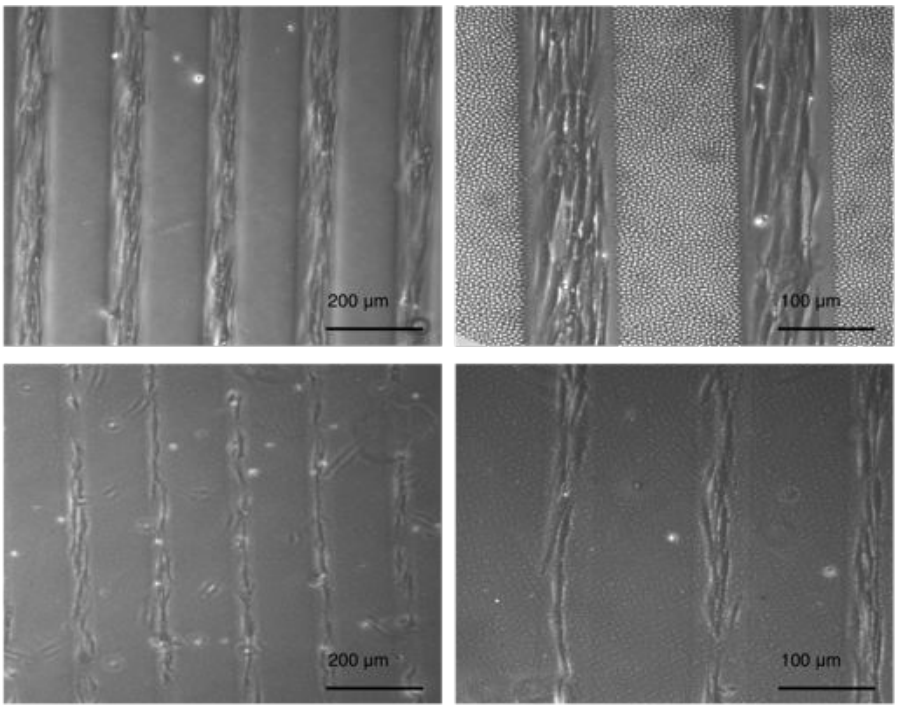

Figure 71: Bright field image of HFF growing on P(nBA-co-4%MABP) photopatterned substrates. Cell-adhesive areas have a width of 100 μm (images above) or of 50 μm (images below). In both cases cells grow only onto cell-adhesive stripes and tend to align in the direction of such stripes.

We then evaluated human embryonic stem cell derived-cardiomyocytes (hESC-CMs) response to our substrates. First, we seeded hESC-CMs on flat P(nBA-co-4%MABP) where a thin PAA network was attached by the photochemical process described above everywhere except that on rectangular areas measuring 30 x 15 μm. Such substrates were exposed to laminin solution before cell seeding. During this exposure to the laminin solution, a thin laminin layer was adsorbed to the hydrophobic P(nBA-co-%MABP) areas. After 3 - 4 days cells were contracting. Figure 72 shows a bright field image of hESC-CMs seeded on such substrates: cells selectively grew on cell-adhesive areas and assumed a rectangular shape to adapt to the morphology of the cell-adhesive areas.

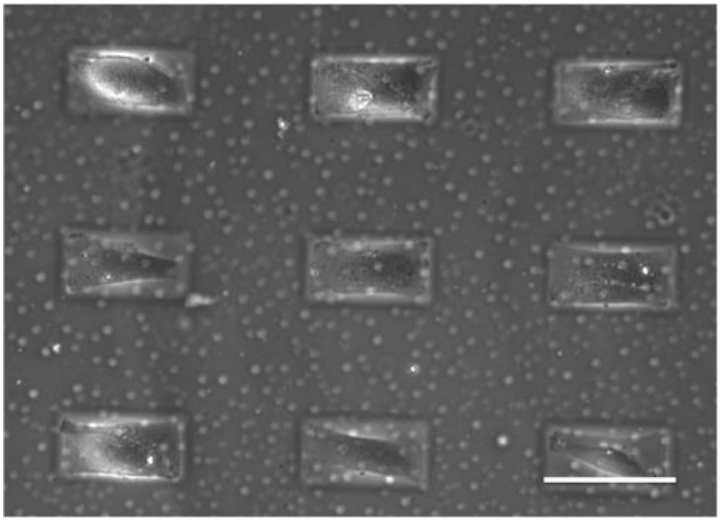

Figure 72: Bright field image of hESC-CMs seeded on photopatterned substrates: the rectangular areas are the cell-adhesive areas of P(nBA-co-4%MABP). Cell growth is clearly visible on the cell-adhesive areas: cells elongate and assume a rectangular shape to fill all the available space. Scale bar is 30 μm.

In the following step, we fabricated P(nBA-co-4%MABP) microstructured substrates and we then attached PAA on the surface everywhere except that on rectangular areas that extended from one pillar to another pillar. Cell-adhesive areas had a rectangular shape measuring 30 x 15 μm. Substrates were exposed to laminin solution before hESC-CMs seeding. After 3 - 4 days cells were contracting on such substrates. Figure 73 shows a cardiomyocyte that adheres to the rectangular cell-adhesive area and elongates between two micropillars (above): the cell anchor to the micropillars and bend them upon contraction (below). The displacement of the top of the micropillars (Δx) is clearly visible.

From these tests, we confirmed that hESC-CMs were guided to grow only onto the cell adhesive areas of the surface. Cells maintained their contractility and could be analyzed also several days after seeding (up to 8 weeks).

8.2 HESC-CMS IMMUNOHISTOCHEMISTRY

To evaluate cell phenotype and structural organization and to localize the points of adhesion of the cells to the micropillars, immunofluorescence analysis on hESC-CMs seeded both on flat and on microstructured substrates was performed.

To evaluate the sarcomeric organization of hESC-CMs, cardiac troponin-

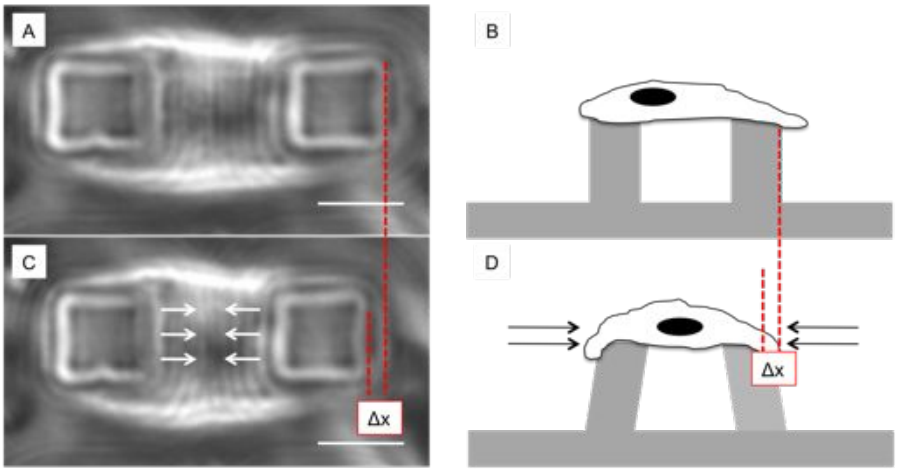

Figure 73: Bright field image of a cardiomyocyte seeded on a microstructured and photopatterned substrate. A) Cell adheres to the cell-adhesive areas elongating between two micropillars. B) Scheme of the cell at rest. C) Micropillars top is displaced by the cell upon contraction. D) Scheme of the cell bending the micropillars upon contraction. the displacement of the micropillar top (Δx) is marked by red dotted lines. Scale bar is 10 μm.

T (cTnT) protein was marked through immunofluorescence staining. Troponin-T is one of the three troponins (along with troponin-C and troponin-I) that are component of the thin filament of the sarcomere of striated muscle and that allow the physiological process of relaxation and contraction of the cell. Because they are components of the sarcomeres, immunohistochemistry of cTnT allows to identify the sarcomeric organization of the cell [220]. To confirm cell phenotype we also immunostained sarcoendoplasmic reticulum calcium-ATPase (SERCA-2a). SERCA-2a is the main responsable of the removal of cytosolic Ca^{2+} from the cytosol, that results in muscle relaxation [221]. To localize the focal adhesion points of the cells anchored to the micropillars, we immunostained vinculin. Vinculin is a cytoskeletal protein involved in the linkage of integrins to actin. Along with other proteins, it can form the focal complexes of the cell, i.e. the adhesion sites of the cell to the surrounding surface or ECM [3]. Immunostaining protocols are descripted in Chapter 10.
In Figure 74, immunostaining of cTnT on hESC-CMs seeded on flat photopatterned substrates is reported. Cell-adhesive areas are rectangular areas measuring 30 x 15 μm. Cells adhere and spread to the cell-adhesive areas. The stripe-like structure of cTnT (highlighted by the white circles in the image), corresponds to a sarcomeric organization of the cell typical of cardiomyocytes [222].

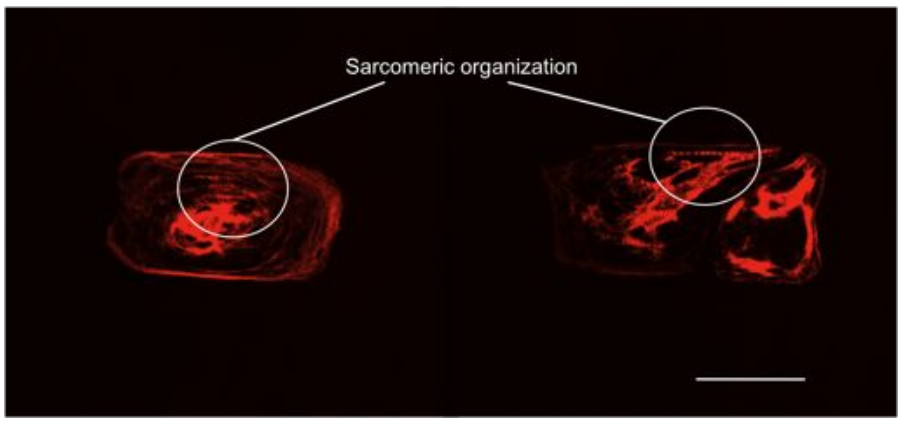

Figure 74: Immunostaining of cTnT on hESC-CMs seeded on flat photopatterned substrate. Cell adhere an spread to the rectangular cell-adhesive areas. Immunostaining of cTnT (red) shows a clear sarcomeric organization, typical of cardiac muscle cells, as highlighted by the white circles in the image. Scale bar is 15 μm.

In Figure 75 immunostaining of cTnT on hESC-CMs seeded on microstructured and photopatterned substrates is reported. Cells adhere to the cell-adhesive areas and assume an elongated shape, anchoring their extremities to two different micropillars. A clear sarcomeric organization was detected by immunostaining of cTnT (red signal), perpendicular to the direction of elongation of the cell, as displaced in physiological cardiomyocytes [222].

Figure 76 shows the SERCA-2a immunofluorescence analysis of a cardiomyocyte seeded on microstructured and photopatterned substrate. Cell elongate between two elastic micropillars. The presence of SERCA-2a is typical of cardiac muscle cells phenotype [221]. The image shows the presence of SERCA-2a (red signal) all along the cell.

When cells shorten due to the contraction mechanism, the micropillars to which they are attached is bended. In this work, we determined the force of contraction exerted basing on an indirect method. Cell force was evaluated basing on micropllar deflection. In the circumstance of the same exerted force, the higher are the cell adhesion points to the micropillars (i.e. the points of application of the force), the higher are the micropillar deflection. Therefore, it is of paramount importance to know at which height of the micropillar the cell is anchored. For this reason, immunofluorescence analysis of focal adhesion points has been performed on hESC-CMs seeeded on microstructured and photopatterned substrates. Figure 77 shows confocal images of 4 different cardiomyocytes where vinculin has been immunostained. During the acquisition of the images by confocal microscopy, the z-scan of the micropillar (from micropillar base

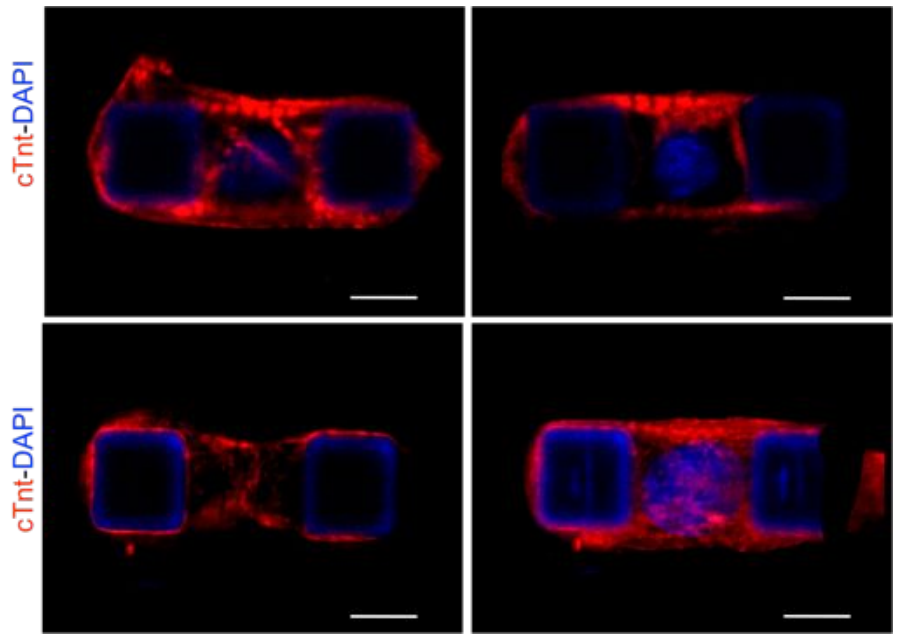

Figure 75: Immunostaining of cTnT on hESC-CMs seeded on microstructured and photopatterned substrates. Confocal images of four different hESC-CMs anchored between two μ-pillars: cTnT is stained in red and a clear sarcomeric organization perpendicular to the direction of elongation of the cell is visible. Nuclei are stained in blue. μ-pillars walls are visible in blue due to some emission of the benzophenone of P(nBA-co-%MABP). Scale bar is 10 μm in all images.

to micropillar head) was performed and the location of the cell-to-micropillars adhesion sites was determined.

8.3 CALCIUM DYNAMICS AND μ-PILLAR DEFLECTION DETECTED THROUGH CONFOCAL ANALYSIS

Before fixing the cells and immunostaining them, live imaging was performed by confocal analysis. From such measurements we were able to record simultaneously the calcium dynamics of the cells (release and uptake of calcium from the sarcoplasmic reticulum (SR) and from outside the cell to the citosol) and micropillar bending due to cell contraction.
Calcium dynamics was recorded following the variation of the intensity of the fluorescent signal emitted by the fluorescent probe fluo-4 (described in Chapter 6) along time. Such variation is related to the changes of calcium concentration in the citosol. Figure 78 describes how calcium dynamics was acquired. Figure 78 A shows a CM anchored between two micropillars, where calcium signal is marked in

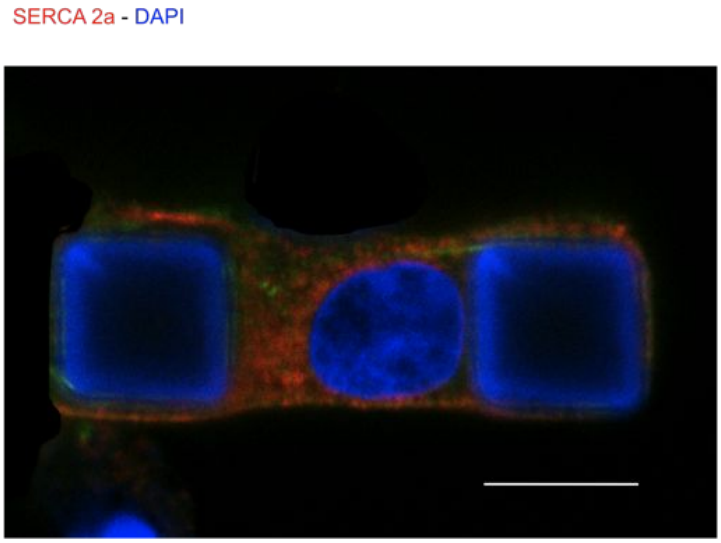

Figure 76: Immunostaining of SERCA-2a on hESC-CMs seeded on microstructured an photopatterned substrates. SERCA-2a (red signal) is visible all along the cell. The presence of SERCA-2a is typical of cardiac muscle cells phenotype. Nuclei are stained in blue. μ-pillars walls are also visible in blue due to some emission of the benzophenone of P(nBA-co-4%MABP). Scale bar is 10 μm.

green. When calcium concentration increases inside the cell, fluo-4 molecules bind to the ion and emitt a fluorescent signal. The increasing (calcium release phase) and decreasing (calcium reuptake phase) fluorescent signal emitted by the analyzed cell was recorded for few seconds. Figure 78 B shows the variation of the intensity of the signal emitted by fluo-4 along time. The plot of the variation of the intensity signal along time provides the shape of the calcium transient curve, as reported in Figure 78 C. From such curve, it was possible to determine different parameters: calcium release phase (Ca^{2+} Rel), calcium reuptake phase (Ca^{2+} Up) and the duration of the calcium transient. Ca^{2+} Rel was defined as the time from baseline to 95% of the peak, Ca^{2+} Up was defined as the time from 95% to 50% relaxation curve. The total duration of the calcium transient (Ca^{2+} Tot) was defined as:

$$Ca^{2+}Tot = Ca^{2+}Rel + 2 * (Ca^{2+}Up) \tag{23}$$

Further information concerning the calculation of such parameters are provided in Chapter 10.
The acquired calcium transients are slower than that registered in adult CMs, in agreement with other studies [223, 224, 225]. Therefor, in adult CMs calcium release from the SR contributes almost 70% of

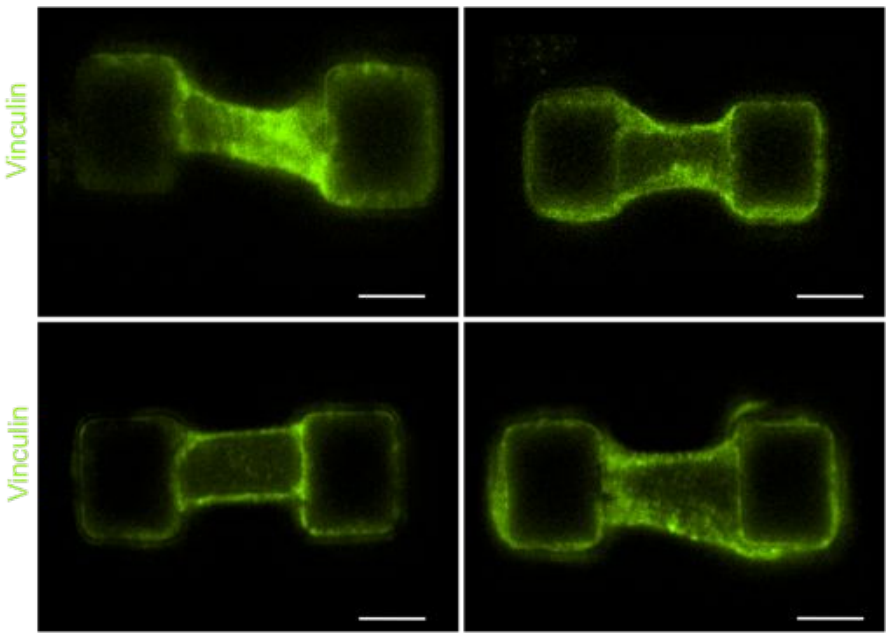

Figure 77: Immunostaining of vinculin of hESC-CMs seeded on microstructured and photopatterned substrates. Confocal images of four different hESC-CMs anchored between two μ-pillars are reported: vinculin is stained in green and thanks to confocal analysis the height of the micropillar at which cell anchor can be detected. Scale bar is 10 μm in all images.

the total calcium release. On the contrary, hPSC-CMs have very little SR function in the early phase, and most cation influx is through the cell membrane. This is the reason of slower and usually smaller calcium transients. Such calcium transients reveal an immature phenotype of hPSC-CMs [225].

Micropillar deflection was evaluated recording the variation of micropillar walls position along time, due to cell contraction and therefore shortening. Confocal analysis revealed such deflections due to di-8-ANEPPS fluorescent dye adsorbed to micropillar walls. The recorded deflection coincide to the displacement of the micropillars at the height at which the cell adhere to the pillar through focal adhesion points. When cells adhere to the micropillar top, the deflection of micropillar head is recorded. When cells adhere to lower parts of the micropillar, the deflection of the micropillar at that height is recorded. Figure 79 shows how micropillar deflection was detected. In Figure 79 A, a CM embracing two micropillars is visible. Micropillar edges are visualized in red. Figure 79 B shows a live-scan acquisition where a variation of micropillar edges (red lines) position along time is detectable. Such variation is then converted into μm as plotted in Figure 79 C. The

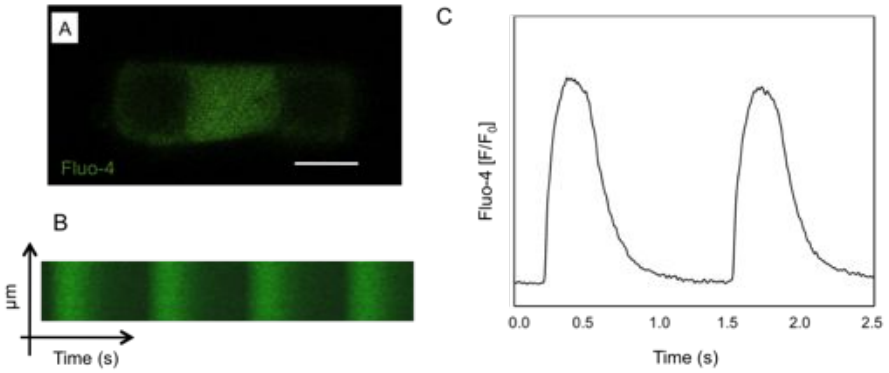

Figure 78: Calcium dynamics of hESC-CMs detected through confocal analysis. A) Image of a CM anchored between two µ-pillars acquired while calcium is released inside the citosol and can be detected thanks to fluo-4 fluorescent dye. Scale bar is 10 µm. B) Line scan acquisiton of the variation of fluo-4 intensity due to cell contraction and relaxation along time. C) Plot of the variation of the intensity of fluo-4, due to calcium release and uptake along time. From such curves it is possible to evaluate biological parameters.

peak of such curve was the value employed to evaluate the contraction force exerted by the cells.

Since fluo-4 and di-8-ANEPPS emit at two different wavelengths (490 to 550 nm for fluo-4 and 600 to 700 nm for di-8-ANEPPS) it was possible to record simultaneously the calcium dynamics and the consequent micropillar deflection from which cell contraction force could be quantified. Figure 80 shows an example of simultaneous acquisition of calcium dynamics and micropillar deflection. In Figure 80 A a CM embracing two micropillars is shown. Calcium signal is visible in green, micropillar shape and position are detectable in red. Figure 80 B shows a live-scan recording of a calcium transient (green signal which intensity increases and then decreases), and the corresponding micropillar deflection (red line). In Figure 80 C the plots of the acquired calcium transient (green) and micropillar deflection (red) are reported.

8.4 QUANTIFICATION OF CONTRACTION FORCE THROUGH FINITE ELEMENT MODELING

Contraction force exerted by the cells has been quantified combining the information regarding the location of the focal adhesion points, detected by immunostaining of vinculin as described in Section 8.2, with the data of micropillar deflection. Micropillar deflection was quantified at the micropillar height where focal cell adhesion sites

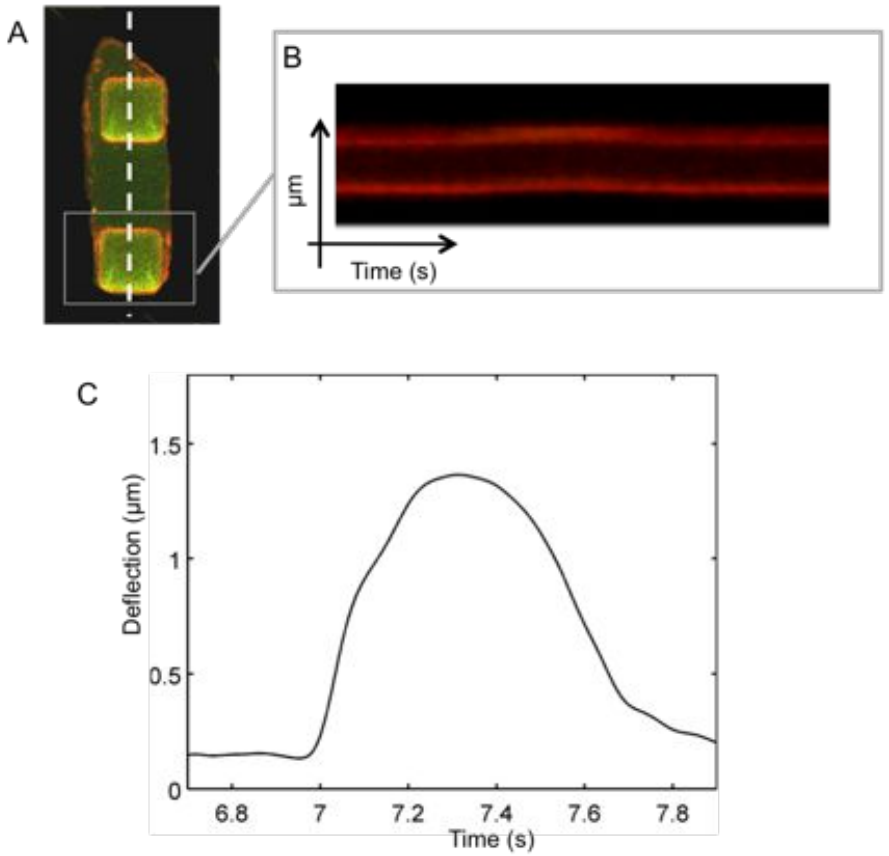

Figure 79: Micropillar deflection detected through confocal analysis. A) Image of a CM anchored between two µ-pillars: di-8-ANEPPS adsorbed to µ-pillar walls allows to visualize pillar shape and position. B) Line scan acquisiton of di-8-ANEPPS adsorbed to µ-pillar walls: it is possible to visualize µ-pillar deflection due to cell contraction. C) Plot of µ-pillar deflection. The peak of the curve is the value employed to quantify cell force.

were detected, as discussed in Section 8.3. Since the evaluated cardiomyocytes act between single couples of pillars, it was possible to estimate contractile forces of cells through an indirect method, by applying assigned values of deflection to the pillars and estimating the corresponding forces. Deflections of the pillar were applied as imposed displacement in the FEM. Figure 81 shows an example of imposed deflection and consequent developed force according to our model. Figure 81 A shows the modeled micropillars upon deflection. Such deflection is due to a tangential force applied at a height of 16 µm. Such tangential force is visualized in the model of Figure 81 B. The area of action of the force is highlighted in the model by the red and yellow colors.

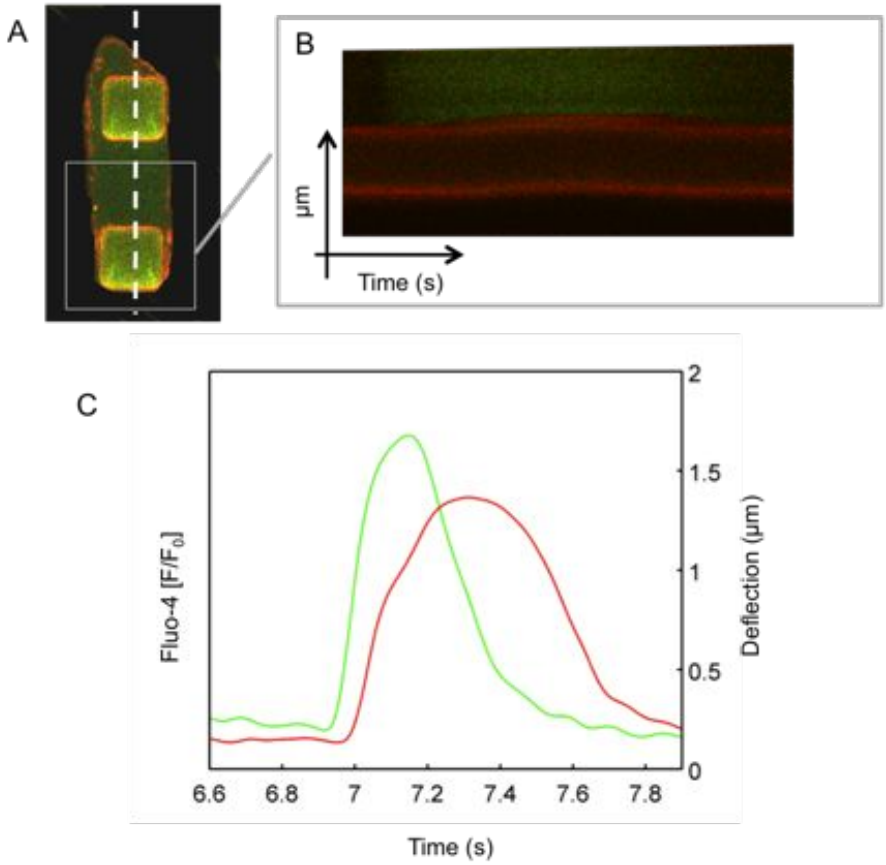

Figure 80: Simultaneous acquistion of hESC-CMs calcium dynamics and micropillar deflection through live-imaging confocal analysis. A) Image of a CM anchored between two µ-pillars. Calcium is marked by Fluo-4 (green signal), micropillar walls are marked by di-8-ANEPPS (red signal). B) Live-scan image of the process of contraction of a CM along time: the variation of fluo-4 intensity is marked in green, while micropillar deflection is visible in red. C) Plot of the simultaneous acquisition of calcium dynamics (green) and micropillar deflection (red).

8.5 CASE STUDY: EVALUATION OF HESC-CMS FUNCTIONAL MATURATION.

Current protocols for the derivation of human cardiomyocytes from pluripotent stem cells recapitulate the events of early embryogenesis through chronologically defined sequences of cytokine stimulation. Although large amounts of contracting cardiomyocytes can be obtained, their application is limited by their early and immature phenotype. hPSC-CMs can differ from adult cardiomyocytes with respect to structure, proliferation, metabolism and electrophysiology, better approximating fetal cardiomyocytes [225]. However, time in culture

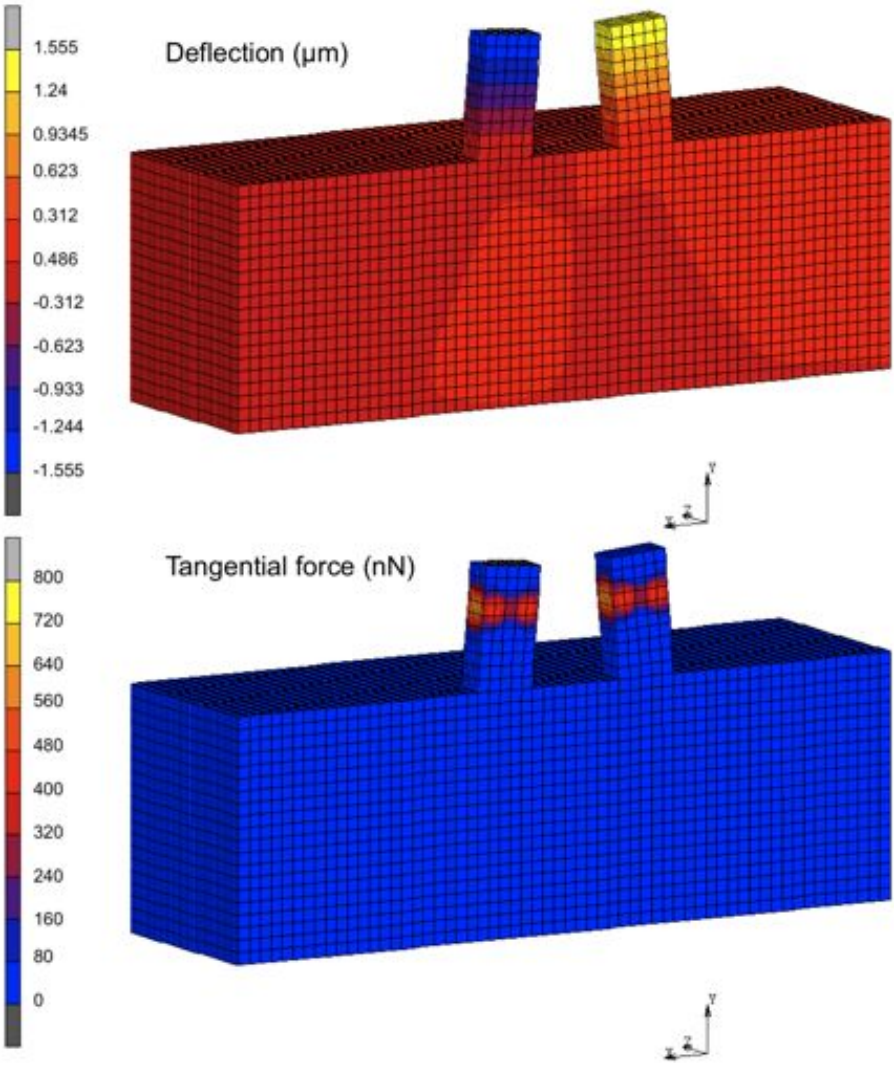

Figure 81: Examples of FEM to quantify hESC-CMs contraction force. In this case the force is applied at a height of 16 μm. The displacement recorded at the height of 16 μm is 0.99 μm (A) and the corresponding tangential force is 720 nN (B).

appears to significantly impact phenotype, affecting action potential characteristics as well as expression of key ion channels [225].
We hypothesize that an integration of the time in culture with mechanical and morphological cues would probably better mimic the cardiac development, which involves a proper electrical/mechanical environment. Therefor, it has been reported that elastic boundary of the cells can enhance the development of the sarcoplasmic reticulum (SR) [226], and that the elongated structure typical of adult CMs is an important feature to fulfill cardiac muscle cell function [35].
In our experiments, the chemistry of the surface was tuned to guide cell adhesion into rectangular areas, where cells attached and spread,

hCMs on flat substrates - Week 1			
	Ca^{2+} Rel	Ca^{2+} Up	Ca^{2+} Tot
Mean (s)	0.38	0.50	1.38
Sd (s)	0.05	0.09	0.17

Table 1: Calcium transient of hESC-CMs on flat substrates, week 1.

assuming an elongated shape. The mechanical stimuli was provided by the presence of the elastomeric micropillars: cells contract repeatedly displacing such micropillars that oppose a mechanical force.
To validate our hypothesis, calcium dynamics of hESC-CMs seeded both on flat and on microstructured photopatterned substrates has been measured and compared on cells after 1 week from seeding and on cells after 5 weeks from seeding. Additionally, contraction force of hESC-CMs seeded on microstructured and photopatterned substrates, was quantified after 1 week and after 5 weeks from seeding. The aim was to evaluate if the combination of morphological and mechanical stimuli to the cells, would lead to variations of the calcium transients characteristics and of the developed forces.
Our results on hESC-CMs seeded on flat substrates, showed that the total duration of the calcium transients (Ca^{2+} Tot) decreased from a value of 1.38 ± 0.17 s to a value of 1.07 ± 0.09 s, as reported in Table 1 and Table 2. Such decrease was mostly releated to a variation of the calcium reuptake phase, as described by the graphs in Figure 82. The graph on the left shows the variation of calcium release phase from week 1 to week 5 of culture, both for cells seeded on flat and on microstructured substrates. When cells were seeded on flat substrates, there was no a significant variation of the duration of calcium release in the cell. The graph on the right shows the results concerning the calcium reuptake phase, both for cells seeded on flat as well as on microstructured substrates. In this case, there was a statistically significative decrease in the calcium reuptake phase from week 1 to week 5 of culture on flat substrates. In the same figure, the results concering calcium dynamics of hESC-CMs seeded on microstructured substrates are reported. Such experimental condition lead to a decrease in both calcium release (Figure 82 A) and calcium reuptake phase (Figure 82 B) between cells analyzed after 1 week and after 5 weeks of culture. The total duration of the calcium transients varied from a value of 1.17 ± 0.13 s to a value of 0.5 ± 0.08 s, as reported in Table 3 and Table 4.

hCMs on flat substrates - Week 5			
	Ca^{2+} Rel	Ca^{2+} Up	Ca^{2+} Tot
Mean (s)	0.31	0.38	1.07
Sd (s)	0.03	0.05	0.92

Table 2: Calcium transient of hESC-CMs on flat substrates, week 5.

hCMs on µP substrates - Week 1			
	Ca^{2+} Rel	Ca^{2+} Up	Ca^{2+} Tot
Mean (s)	0.35	0.36	1.17
Sd (s)	0.03	0.07	0.13

Table 3: Calcium transient of hESC-CMs on microstructured substrates, week 1.

hCMs on µP substrates - Week 5			
	Ca^{2+} Rel	Ca^{2+} Up	Ca^{2+} Tot
Mean (s)	0.19	0.16	0.50
Sd (s)	0.02	0.02	0.08

Table 4: Calcium transient of hESC-CMs on microstructured substrates, week 5.

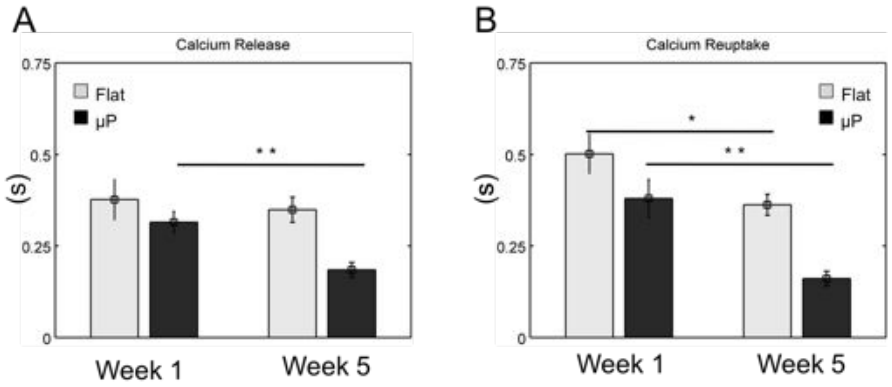

Figure 82: Comparison of calcium dynamics parameters of hESC-CMs after 1 week and after 5 weeks of culture on flat (light gray) and microstructured (black) substrates. A) Calcium release phase (Ca^{2+} Rel) does not significatively decrease from week 1 to week 5 of culture when cells are seeded on flat substrates. On the contrary, there is a consistent decrease in Ca^{2+} Rel when cells are cultured on microstructured substrates. In particular, Ca^{2+} Rel goes from a value of 0.35 ± 0.03 s to a value of 0.19 ± 0.02 s. B) Calcium reuptake phase (Ca^{2+} Up) significatively decreases from week 1 to week 5 of culture when cells are seeded both on flat (from 0.5 ± 0.09 to 0.38 ± 0.05) and on microstructured substrates (from 0.36 ± 0.07 to 0.16 ± 0.02). When cells are cultured on microstructured substrates such decrease is more pronounced. Student t-test p-values, $P \leqslant 0.001$ (**), $P \leqslant 0.001$ (*).

Contraction force of hESC-CMs seeded on microstructured substrates has also been measured both at week 1 and week 5 of culture, in concomitance with the acquisition of calcium transients. Figure 83 A shows two examples of cells where calcium transient and corresponding developed force were acquired simultaneously. The image on the left shows an example of calcium transient and contraction force of a hESC-CM after 1 week of culture. The image on the right shows an example of calcium transient and developed contraction force of a hESC-CM after 5 weeks of culture. During the cardiac action potential, Ca^{2+} enters the cell and triggers Ca^{2+} release from the sarcoplasmic reticulum. The combination of Ca^{2+} influx and release raises the free intracellular Ca^{2+} concentration (raising part of the calcium transient curve), allowing Ca^{2+} to bind to the myofilament protein troponin C. The contraction process is therefore triggered (raising part of the contraction force curve). For relaxation to occur (descending part of the contraction force curve) cytosolic Ca^{2+} must decline (descending part of the calcium transient curve), allowing Ca^{2+} to dissociate from troponin. The evaluated calcium transient and contraction

force curves present a shape that is qualitatively comparable with the transient of calcium and contraction process curves descripted by Bers in his work on excitation-contraction coupling [152]. Figure 83 B displays the relationship between calcium transients duration and consequent developed contraction force. Interstingly, cells characterized by shorter transients of calcium, tend to develop stronger forces. In general, cells analyzed after 1 week of culture present longer transients of calcium and develop weaker forces than cells analyzed after 5 weeks of culture.

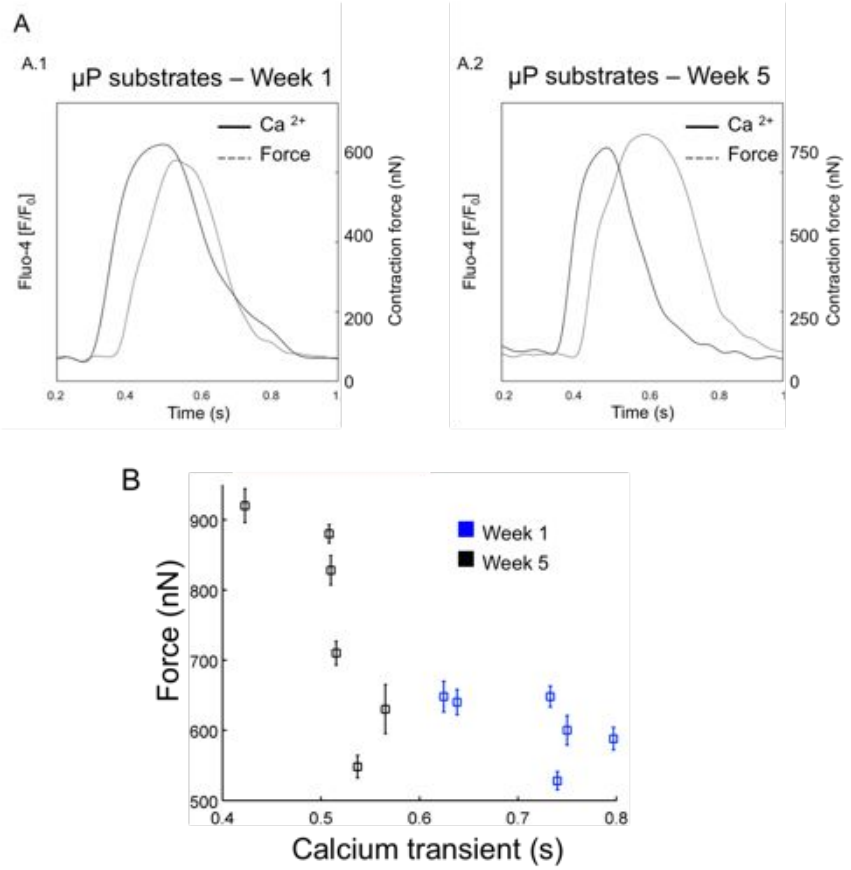

Figure 83: Examples of simultaneous acquistion of calcium dynamics and contraction force on hESC-CMs. A) Plots of the calcium transient and consequent developed force of hESC-CMs analyzed after 1 week (A.1) and 5 weeks (A.2) of culture. B) Plot of contraction force vs duration of calcium transients of hESC-CMs analyzed after 1 week (blue squares) and after 5 weeks (black squares) of culture. Shorter transients are often associated with higher developed forces.

Our results showed that there was an increase of the developed force when cells were kept in culture for several days and that our system is sensitive enough to detect variation of contraction force

of few nN. The final force values calculated at week 1 and week 5 of culture are reported in Figure 84. Contraction force varied from a value of 502 ± 122 nN at week 1 to a value of 719 ± 101 nN at week 5 of culture. These results, combined with the data on calcium transients, support the concept that hPSC-CMs require cell-substrate interaction for activation of mechanotransduction pathways promoting functional cardiac maturation, as in physiological cardiomyocyte development.

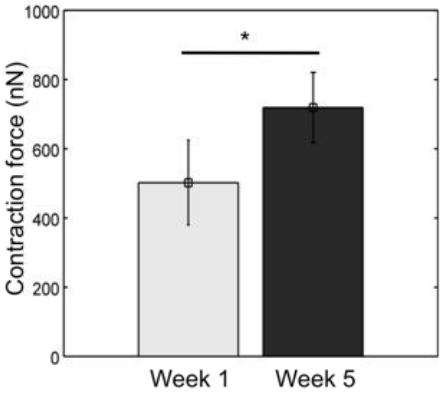

Figure 84: Comparison of contraction force of hESC-CMs after 1 week (light gray) and after 5 weeks (black) of culture on microstructured substrates. The developed force increases from 502 ± 122 nN on cells analyzed at week 1 to 719 ± 101 nN on cells analyzed at week 5.

8.6 CORRELATION OF HESC-CMS ACTION POTENTIAL TO CALCIUM DYNAMICS AND CONTRACTION FORCE

Calcium is the most important ion regulating the mechanism of contraction in CMs and its release and uptake from and into the SR is directly responsible of the contraction process in the cell and of the force developed. Recording calcium dynamics and contraction force provides significant information on the physiological or pathological condition of the cells, on drug response, or on the process of maturation of human pluripotent stem cells derived cardiomyocytes (hPSC-CMs). Nevertheless, one could be interested in obtaining information on the dynamics of another fundamental parameter: the action potential of the cells. The action potential is the first event that triggers the entire mechanism of contraction: cell membrane depolarization caused by the action potential allows the opening of mebrane Ca^{2+} channels. The increase of calcium inside the cells triggers the release of Ca^{2+} from the SR and the consequent cell contraction. Using the fluorescent dye presented in Chapter 6, the voltage sensitive

dye (VSD), it is possible to record the action potential of the cells through confocal analysis. Figure 85 shows an example of acquisition of the action potential by confocal analysis. In Figure 85 A the variation of the intensity of the fluorescent probe along time, related to the process of depolarization and repolarization of cell membrane, is shown. Figure 85 B reports the plot of the variations of the intensity signal, which directly represents the shape of the action potentials. The presented method allows to record the shape, the duration and the frequency of the action potential of hESC-CMs by simply performing live-cell confocal analysis. The employed voltage sensitive dye has an emission spectra (500 to 600 nm) that superposes to that of fluo-4, therefore the two fluorescent probe can not be recorded with the same sample. However, the use of a calcium sensitive dye with a different emission spectra will allow the simultaneous acquisition of calcium dynamics, contraction force and action potential. Once acquired simultaneously, the three parameters could be correlated to gain physiological and pathophysiological information of the investigated cells.

8.7 DISCUSSION

We presented here an *in vitro* platform based on human pluripotent stem cells derived cardiomyocytes and *ad hoc* micro-fabrication technologies for studies of the physiology of such cells. In particular, calcium dynamics and contraction force of single hESC-CMs could be simultaneously detected on hESC-CMs after 1 week and after 5 weeks of culture to evaluate the relevance of cell-substrate interaction in the process of cell maturation. Substrate chemistry and geometry have been tuned to guide cell adhesion and shape: axial contractile properties and calcium dynamics could be detected on single hESC-CMs with an elongated shape.

Recent studies reported that the key modulators of heart output are not only the cell composition, differentiation, and orientation [227, 228, 114], but also the embedding matrix composition [157] and the external stimuli such as cyclic stretching or electrical stimulation [156, 228, 229, 230]. Rodriguez et al. [231] and Jacot et al. [232] reported how the variation of substrate stiffness influence cell development on neonatal rat hESC-CMs. In response to these inputs, the most important outputs of heart tissue are force generation and contraction characteristics. Unfortunately, current protocols for deriving cardiomyocytes from stem cells and induced pluripotent stem cells rely on staining for cardiac myocyte markers [233, 234, 235] rather than on force generation. Few methods are available to measure contrac-

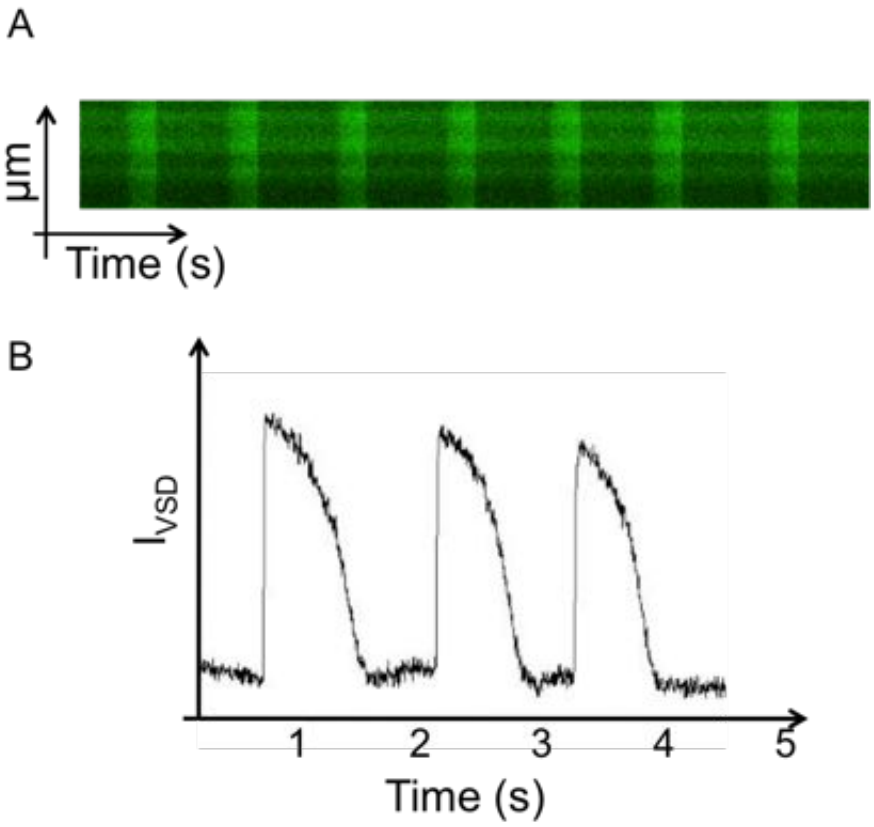

Figure 85: Detection of hESC-CMs action potential through confocal analysis. A) Line scan acquisiton of the variation of the voltage sensitive dye (VSD) intensity due to the action potentials. C) Plot of the variation of the intensity of the VSD, due to the depolarization of cell membrane during the action potential.

tion performance of hESC-CMs in a reproducible and high-trhoughput manner. The use of elastic micropost platforms can be considered a valid approach for assessing the contractile properties of various types of cardiomyocytes [82, 93, 85, 94, 95, 167, 231, 226]. The contraction force can be derived from the deflection of the elastic micropillars induced by cell shortening [78]. However, up to now the majority of these studies have been applied to adult or neonatal rat cardiomyocytes. Recently, Rodriguez et al. [169] characterized contraction force, velocity and power of hiPSC-CMs on single cardiomyocytes spreading on dense arrays of elastic micropillars: through this method cells adhere to a large number of microposts. The limits of this work are that the force is measured as the sum of the forces applied to each micropost and cells don't assume an elongated (more physiological) shape. Since hESC-CMs shape is one of the regulators of functionally fundamental myocyte features, such as assembly and organization of sarcomeric structure, proper calcium handling abil-

ity and modulation of cardiac ion channel properties [236, 237, 238], meaningful in vitro studies should be carry out on cells that resemble as more as possible a physiological morphology. Taylor et al. [168] achieved to measure the uni-axial contractile properties of single hESC-CMs modifying a traditional force post assay [85] by enlarging the posts and lattice constants and by filling the volume between the posts with a sacrificial layer. Through this platform they quantified only the contraction force of the cells, but in cardiac myocytes, the contraction force produced by the contractile apparatus is directly related to the momentary calcium concentration in the cytoplasm. For this reason, we realized a platform which combines the measurement of the uni-axial contractile force of hESC-CMs with the detection of the corresponding calcium transients while cell adhesion and shape were guided by substrate chemistry and geometry.

In our experiments we compared calcium dynamics and contraction force of hESC-CMs seeded on flat and microstructured substrates after 1 week and after 5 weeks of culture, to verify if and how the environment in which cells have been cultured could influence their performance and eventually contribute to their functional maturation. In particular, cell seeded on our engineered substrates have an elongated shape and at each contraction they deform the elastomeric micropillars which acts as springs. Our results support the hypothesis that morphological and mechanical stimuli influence the process of functional maturation of the cells. When cells were seeded on microstructured substrates, the transients of calcium shortened from cells analyzed after 1 week of culture and cells analyzed after 5 weeks of culture. Concerning the contraction force, this could be measured only on cells seeded on microstructured substrates, since we needed information on micropillar deflections to deduce the force. Contraction force was found to increase from a value of 502 ± 122 nN at week 1 to a value of 719 ± 101 nN at week 5 of culture.

Previous experiments with adult cardiomyocytes and carbon fibers demonstrated peak isometric forces ranging from 2.42μ N [87] to 5.7μ N [239]. Per post measurements of 39 nN have been reported by Kim et al. on neonatal rat cardiomyocytes, using elastomeric force post arrays [78] and of 13.3 to 17.6 nN on human induced pluripotent stem cells cardiomyocytes by Rodriguez et al. [169]. It is difficult to compare such measurements with our results because in the mentioned works the cells had spread out into shapes that are not physiologically realistic. Using micropost arrays, uni-axial measurements of both neonatal rat cardiomyocytes and human embryonic stem cells derived cardiomyocytes have been performed by Taylor et al. [168]. They found twitch forces around 150 nN on neonatal rat

cardiomyocytes and from 50 to 100 nN on human embryonic stem cells derived cardiomyocytes. In this work they used arrays of microposts with an interaxial distance of 80μm, about three times bigger than the interaxial distance of our arrays, hence a comparison with our measurements is again difficult to make. Kajzar et al. [167] measured forces of around 400 nN on neonatal rat cardiomyocytes using micropost arrays with an interaxial distance of 30μm, comparable to that of our platform. Our measurements have values in between the minimum reported value of 13 nN and the maximum reported value of 5.7μN. A direct comparison with the forces calculated in the previously mentioned works is not straightforward since the final value is influenced by several factors such as cell type, cell shape, substrate geometry and method of calculation of the force.

Our results show an increase of the force developed by the cells from week 1 to week 5 of culture, which could be related to an improvement in organization of cardiac cell structural features. Simultaneous analysis of calcium transients and consequent developed forces, suggest that cells with a faster calcium dynamics develop stronger forces. The combination of a microstructured and photopatterned substrate and the use of confocal images to detect both micropillar deflection and calcium dynamics in the cells, overcomes some of the limits of the current *in vitro* studies of isolated cardiac muscle cells: (i) thanks to chemical and morphological patterning cells assume an elongated, more physiological shape; (ii) contraction force is combined with information on calcium dynamics which are acquired simultaneously; (iii) hPSC-CMs instead of animal derived CMs are used in this work.

All together, our results support the concept that cell-substrate interaction is necessary for the maturation of human pluripotent stem cells derived cardiomyocytes and further validate the studies which proved how CMs shape along with mechanical stimulation of the cell, contribute in regulating cardiac myocyte function [236, 238]. This platform can be used not only to monitor the process of differentiation and maturation of hESC-CMs but possibly to induce functional maturation of the cells. Cardiac differentiation protocols from pluripotent stem cells are, to date, the best promise for a human cardiac *in vitro* model feasible for drug screening and disease modeling, but the immature phenotype of the derived cardiomyocytes is still a matter of concern for these applications. Therefore, understanding the processes behind *in vitro* maturation is of great interest. Furthermore, since both calcium dynamics and micropillar displacement are detected through confocal analysis, this technique is also suitable for high-throughput monitoring of drug-induced changes in spontaneous frequency or contractility of hPSC-CMs. Additionally, collecting infor-

mation about the functional properties of hPSC-CMs could give a clearer scenario about pathological effects on hPSC-CMs.

8.8 CONCLUSIONS

Our platform is suitable to perform quantitative *in vitro* studies on hPSC-CMs: the platform allows the simultaneous detection of the uniaxial contraction force and calcium dynamics of hPSC-CMs with an elongated morphology. To guide cell shape, we combined a cell-adhesive photopolymerizable elastomeric polymer with a cell-repellent polymer. The final substrate consisted of elastomeric micropillars and presented rectangular areas of cell-adhesive polymer where CMs selectively grew extending between two micropillars and assuming an elongated shape. Calcium dynamics was acquired through confocal analysis of CMs where calcium was detected by using the fluorescent probe fluo-4. Micropillar deflection was also detected by confocal images and converted into contraction force values employing a FEM that describes the deflection of the micropillars when a tangential force is applied. We reported that the duration of the transient of calcium decreases when cells are kept in culture on our substrate for several weeks and the contraction force developed by the cells increases. The platform can be suitable for physiological and pathophysiological in vitro assays as well as for monitoring functional maturation of hPSC-CMs.

9

SUMMARY

Stem cells are currently considered fundamental for understanding basic biology, for developing tissue models for drug testing, and for clinical applications in regenerative medicine because of their unlimited self-renewal capacity and high multilineage differentiation potential. However, stem cell studies face significant challenges in identifying stem cell populations, controlling their fate, and characterizing their phenotype because such cells are ultimately functionally defined, and thus can often be identified only retrospectively [240].
To overcome these limits the use of *in vitro* assays represents a crucial strategy: the ability to culture cells *in vitro* has revolutionized hypothesis testing in basic cell and molecular biology research and has become a standard methodology in drug screening. However, the traditional cell culture methodology consisting of the immersion of a large population of cells in a homogeneous fluid medium has become limiting. First of all, such *in vitro* assays do not correctly represent the complex cell *in vivo* microenvironment. Additionally, they are not suitable for a high number of parallel *in vitro* studies, which would result too expensive and time consuming. In contrast to that, microfabrication technologies have facilitated the implementation of *in vitro* assays where the biochemical composition and topology of the substrate, as well as the medium composition surrounding the cells, could be controlled with micrometer resolution. Such assays are well suited for the development of fast, low-cost *in vitro* systems that allow for high-throughput culturing and analysis of cells under large numbers of conditions [61].
Innovative microtechnologies can contribute to the quantitative understanding of how phenomena at the microscale can determine stem cell behavior basing on the increasing ability to control culture conditions and the throughput of data while reducing times and costs. In particular, microtechnologies must be designed and developed to capture the complexity of cell-substrate, cell-cell, and cell-soluble environment interactions considering the characteristic time and length scales of biological phenomena [63].
In this work, we focused our effort on tuning cell environment through microfabrication technologies. Microfabrication technology, has an inherent potential for the development of fast, inexpensive cell culture systems that produce results at high throughput, i.e. probing

large numbers of single cells under a large set of different conditions. Furthermore, it enables to design, with micrometer control, the biochemical composition and topology of the substrates employed for biological studies, that influences cellular processes such as adhesion, migration, growth, secretion, and gene expression.
The aim of this work was to use microfabrication technique, to tune morphological, chemical and mechanical properties of the substrate in order to reproduce a cell environment that induce specific cell responses and/or through which physiological parameters of the investigated cells could be deduced.

9.1 EFFECTS OF GEOMETRIC CONSTRAINTS ON HPSCS EARLY GERM LAYER COMMITTMENT.

We investigated the physical plasticity of human pluripotent stem cells (hPSCs) nuclei and its variation along the process of specification to the three early germ layers (ectoderm, mesoderm and endoderm). Nuclear shape and structure in eukaryotic cells are recognized to be deeply related with cell function during developmental, physiological and pathological modifications [127, 128, 129, 130, 131, 132] and a growing number of studies try to analyze nuclear mechanics behavior to investigates the possible relationship between nuclear properties and cell diseases [127, 128, 130, 136], since one of the most fundamental problem in tissue morphogenesis is the question of how changes in cell shape produce alteration of nuclear form and function [148, 149]. In this context, we aimed at evaluating possible effects of geometric constraints, which influences nuclear shape, in the process of early germ layer committment and therefore gene expression.
To address this aim we investigated hPSCs nuclear capacity to self-deform under defined geometrical constraints, or in other words the spontaneous response of the cell adhesion and nuclear deformation to the topography of the environment. The geometrical constraints have been induced by the use of microstructured polymeric substrates. Microfabrication techniques based on photolithography (to realize the silicon template) and soft lithography (to obtain the final substrate) were applied to fabricate microstructured PDMS substrates. The substrates were formed by a lattice of micropillars with a pillar to pillar distance (7μm) that was smaller than the average nuclear size. Deformable nuclei could penetrate among micropillar interspaces and assume an unusual branched shape. Stiffer nuclei did not penetrate among micropillar interspaces or, if they did, they kept an oval or round morphology. The use of a simple microfabrication technique,

allowed us to quantify in a straightforward way the spontaneous nuclear deformability of the cells under study and to follow the evolution of cell deformability along the process of early germ layer committment through image analysis methods.
Our results showed a substantial difference in nuclear deformability among pluripotent stem cells (hiPSCs, hESCs), multipotent stem cells (CBMSCs) and somatic epithelial cells (hERCs), in agreement with previously reported results that attribute an high deformability to pluripotent stem cells which is progressively lost along the process of differentiation [141]. This process could be related to the expression of lamin A/C in the nuclear envelope that connect and interact with cytoskeletal filaments to maintain the nuclear integrity in differentiated cells. The immunofluorescence and qRT-PCR analyses on hPSCs expanded for 6 days both on flat and microstructured substrates showed that the maintenance of pluripotency is not influenced by nuclear morphological reorganization induced by micropillars. On the other hand the process of early germ layer commitment in endoderm, mesoderm and ectoderm did not always evolve in the same way when cells were diferentiated on flat or microstructured substrates. Early ectoderm, endoderm and mesoderm specification was induced both on microstructured and flat PDMS substrates. We then performed qRT-PCR to detect gene expression of β-III tubulin (ectoderm marker), Brachyury-T (mesoderm marker) and α-fetoprotein (endoderm marker) . Our results showed that gene expression of mesoderm marker Bra-T was significatively higher in cells differentiated to endoderm early germ layer on micrsotructured substrates, compared to the differentiated on flat PDMS substrates. Such data reveal that the physiological process of differentiation from human pluripotent stem cells to early endoderm committment can be influenced by nuclear shape. Future work will address in further investigating the possible differences in gene and therefore protein expression of cells differentiated on flat or on μP substrates.
We also observed that early ectoderm specification on microstructured substrates took place while nuclei raised up from pillar interspaces and assumed a round shape. This process happened in particular between day 1 and day 2-3 of ectoderm committment. Such data reveal that the process of nuclear stiffening, due by structural and functional modification of citoskeletal and nuclear envelope proteins, takes place during the first 2-3 days of ectoderm committment. Further experiments on ectoderm will be adressed to define which proteins are expressed in the nuclear envelope and in the cytoskeleton between day 1 and day 2-3 of differentiation, that are the responsible of nuclear stiffening and nuclear morphological reorganization.

New results will help to understand how important nuclear deformation is during differentiation, which role plays nuclear morphology in gene expression and which are the key mechanisms related to nuclear organization and protein expression in the nuclear envelope and cytoskeleton that play a fundamental role in cell differentiation.
The advantage of our method, compared to other studies in which nuclear stiffness was evaluated after inhibition of cytoskeletal structure [141, 129], is that nuclear behavior can be evaluated investigating live and intact cells. Furthermore, it is a simple method, thus several experiments can be perfomed in parallel. Additionally, nuclear deformability, which is directly related to nuclear shape, can be straightforwardly quantified by fluorescent or confocal microscope images analysis.
Since we demonstrated a correlation between the degree of cell differentiation and nuclear deformability, a possible application of this methodology could be the evaluation of the stage of differentiation of the cells from the physical plasticty of the nucleui on microstructured substrates. This approach could be also employed to evaluate the percentage of obtained induced pluripotent stem cells from a cell reprogramming protocol, in order to establish its efficiency.

9.2 DETECTION OF HESC-CMS FUNCTIONAL PARAMETERS TO INVESTIGATE THE EFFECT OF CELL SHAPE AND MECHANICAL STIMULI ON CELL MATURATION.

Microfabrication techniques have been applied in this work to assess a further biological aim concerning the study of human pluripotent stem cells derived cardiomyocytes (hPSC-CMs). Because heart disease is a major public health concern, much effort has been devoted to study heart cells, namely cardiomyocytes. In this scenario, the microscaled, high throughput approach and the use of human samples can represent the most effective way to produce new generation and effective cardiac human *in vitro* models, which would be representative of the human biology and physiology.
In this work we developed an *in vitro* model based on human cardiomyocytes and *ad hoc* micro-technologies for physio-pathological studies. Microfabrication techniques played a crucial role to obtain substrates where chemical, mechanical and morphological properties have been tuned to guide cell growth in specific cell-adhesive areas. This way, cells assumed an elongated physiological shape and could anchor their extremities to elastomeric micropillars thanks to which part of the biological assay could be performed.

The aim of this part of the work, has been to realize an *in vitro* platform where calcium dynamics and contraction force of single hESC-CMs with an elongated shape could be simultaneously detected. Such platform was then employed to evaluate the effect of morphological an mechanical stimuli in the process of hESC-CMs *in vitro* maturation.
Microstructured substrates have been fabricated through replica molding using the photocrosslinkable and cell-adhesive material P(nBA-4%MABP). The substrate surface presented elastomeric square micropillar with a width of 10 μm and a height of 20 μm. The mechanical properties of the polymer and of the micropillared surface have been thoroughly investigated through DMTA analysis and nanoindenter tests, to evaluate the Young's modulus of the material and the mechanical response of the micropillars when bended by the application of a tangential force. A finite element model (FEM) of the substrate has been developed according to the effective geometry of the surface and the mechanical behavior of the material. A thin layer of cell-repulsive crosslinked PAA was photochemically attached to the rubber substrates by exposing it to UV light through a chrome mask. The mask allowed local control of the surface chemistry. In the exposed areas cell repellent PAA was attached, in the non-exposed areas the rubber remained unmodified, which allowed protein adsorption. Cells seeded on these substrates could grow only on the rectangular areas where no cell-repellent PAA was attached to the rubber. Cells anchored between two micropillars assumed an elongated shape. A clear sarcomeric organization perpendicular to the direction of contraction of the cell was evidenced through cardiac troponin-T (cTnT) immunostaining. Spontaneous contraction of the cells displaced the top of the micropillars. Thanks to confocal analysis we could simultaneously detect calcium dynamics of the cells (through Fluo-4 live imaging staining) and the consequent micropillar deflection due to the fluorescence of di-8-ANEPPS adsorbed to the micropillar walls. The location of the cell adhesion points to the micropillar walls - which correspond to the point of application of the force by the cell to the substrate - were determined by confocal analysis of the cells after immunostaining of vinculin. The recorded deflection was then applied to the finite element model (FEM) who provided the quantitaive value of the contraction force exerted by the cell. Contraction force increased from a value of 502 ± 122 nN at week 1 to a value of 719 ± 101 nN at week 5 of culture. In the literature, contraction force measurements range from a minimum value of 13 nN by Rodriguez et al. [169] of human induced pluripotent stem cells CMs seeded on dense arrays of elastomeric micropillars and a maximum value of 5.7μN by

Nishimura et al. [239] of adult rat CMs analyzed by carbon fiber technique. A direct comparison with the forces calculated in other works is not straightforward since the final value is influenced by several factors such as cell type, cell shape and strength of cell adhesion and in some cases also substrate geometry and method of calculation of the force.
Calcium dynamics measurements revealed that the duration of the calcium transients decreases on cells cultured for 5 weeks compared to that of cells cultured for 1 week regardless of whether cells were cultured on flat or on microstructured substrates. This was probably due to the "time in culture" maturation effect. However, cells seeded on microstructured substrates displayed a much more consistent decrease in the duration of the calcium transients from week 1 to week 5 of culture. Such decrease was probably related to the mechanical stimuli provided to the cells by the micropillar opposition to bending.
This study demonstrated the feasibility of developing an *in vitro* based test for hESC-CMs, able to give insight on both viability and functionality of hESC-CMs. In particular, we could monitor the variation of physiological parameters as calcium transient and contraction force on hESC-CMs seeded on flat and microstructured substrates at different days of culture. Our results showed how functional and structural maturation of hESC-CMs is strictly related not only to the endogenous and exogenous factors but also to the mechanical stimuli of the environment and to cell shape (as described and discussed in Chapter 8), which can influence the mechanotransduction pathways responsible of cell maturation. This platform can be used not only to monitor the process of differentiation and maturation of hESC-CMs, but possibly to induce functional maturation of the cells. Furthermore, since both calcium dynamics and micropillar deflection are detected through confocal analysis, this technique is also suitable for high-throughput monitoring of drug-induced changes in spontaneous frequency or contractility of CMs.

9.3 CONCLUSIONS

Microfabrication techniques offer the potential to modulate, on a cellular and subcellular level, the biochemical composition as well as the topography of the substrate, the type of cell neighboring each cell, and the medium surrounding each cell. In this work, we examined examples of the unique applications of microfabrication in addressing biological questions. Topographical contact guidance of hPSCs and their nuclear behavior along the process of differentiation

has been studied with microfabricated substrates. Some effects of cell shape and cell-substrate interactions on cell proliferation, differentiation, and communication have been reported. Controlled organization of human derived heart cells have been achieved by surface photopatterning, while microfabrication has also enabled precise measurements on live cells, such as mechanical forces. Compared to traditional cell culture techniques, microfabrication techniques, in combination with surface chemistry methods, have the intrinsic ability to precisely control and separate the effects of many of the parameters that affect cellular and subcellular events and signaling pathways. However, most current *in vitro* studies using microfabrication techniques have been conducted in an artificial 2D environment (2D cell patterns and/or constant flow conditions) that still cannot reproduce the complex 3D organization found *in vivo*. Therefore, as in any cell culture study, results must be interpreted with caution and, whenever possible, be validated later with *in situ* and *in vivo* studies. However, an added benefit of microtechnology is that microsystems are most often amenable to high-throughput studies either because microdevices cost less to operate, produce, or buy, or simply because they are smaller and faster. In cell biology applications, "high-throughput benefit" combined with "small-scale benefit" represent the key to realize *in vitro* studies in which hundreds or thousands of cells will be cultured, controlled, and monitored in parallel on a small area and/or volume, precisely tuning cell environment. This approach can allow a consistent reduction of expensive, time consuming and ethically debated *in vivo* tests. Furthermore, the use of human stem cells will provide more reliable physiological and pathophysiological models.

10 EXPERIMENTAL SECTION

10.1 MATERIALS

10.1.1 *Chemical reagents*

3EBP and n-butylacrylate (n-BA) were purified as described by Belardi et al., [175]. All other chemicals and solvents used throughout this work were used as received from standard suppliers without further purification.

Table 5: List of chemicals, solvents and reagents

Substance	Supplier
Acetone	Roth or Sigma Aldrich
Acrylamide	Sigma Aldrich
AZ-1518 photoresist	MicroChemicals, Germany
AZ-1518 developer	MicroChemicals, Germany
α,α-azobisisobutyronitrile	Fluka
Dichloromethane	Roth or Sigma Aldrich
Ethanol	Roth or Sigma Aldrich
Ethyl acetate	Roth
Irgacure	BASF
Isopropanol	Sigma Aldrich
Methanol	Sigma Aldrich
Sylgard 184	Dow Corning
Toluene	Sigma Aldrich
(tridecafluoro-1,1,2,2-tetrahysrooctyl) -1-trichlorosilane	Sigma Aldrich

Table 6: List of substrates

Substrate	Supplier
Glass substrates, 25mm diameter	Menzel-Gläser, Germany
Silicon wafer, diameter 150 mm, thickness 650µm	Si-Mat, Kaufering, Germany

10.2 POLYMER SYNTHESIS

10.2.1 *Synthesis of methacryloyl-4-oxy-benzophenone (MABP)*

In a typical run, 11.5 g of methacryloyl chloride in 40 ml of dichloromethane (DCM) was added to a solution containing 19.8 g of 4-hydroxybenzophenone and 11.12 g of triethylamine in 200 ml of DCM, while the reaction mixture was cooled in an ice bath. The mixture was allowed to warm to room temperature and stirred overnight. After completion of reaction, the mixture was thoroughly washed with 5% HCl, $NaHCO_3$ solution and water (three times each). Then, the solution (organic phase) was added into a beaker containing cold n-hexane (1 : 10) and kept in a freezer at -20°C overnight to complete precipitation: Subsequently, the precipitate was filtered off at 0°C, dried in vacuum and re-crystallized from 10% ethyl acetate-hexane mixture (1 : 9) [241].

10.2.2 *Polymerization of P(nBA-co-MABP)*

The copolymer P(n-BA-co-4% MABP) was produced by free radical polymerization, employing 2.7 ml n-BA (19.2mmol), 208 mg MABP (0.8 mmol) and 3.3 mg azobisiobutyronitrile (AIBN) (0.1 mmol%) in 50 mL ethyl acetate. The reaction vessel was degassed by four freeze-thaw cycles and then placed in a preheated water bath at 60°C for 16 hours. Afterwards, the polymers were precipitated by drop wise adding a solution to a large excess of methanol/water 1 : 1 as precipitation agent and subsequently filtered off. At last, the polymers were dried in the vacuum oven at 100°C with a pressure of 300 mbar for 3 hours. The yield was 58%. P(nBA-co-10%MABP) and P(n-BA-co-20%MABP) have been fabricated emplying hte same protocol, but different quantities of n-BA and MABP. For P(nBA-co-10%MABP) 2.6 ml n-BA (18 mmol) and 533 mg MABP (2.0 mmol) have been employed. For P(nBA-co-20%MABP) 2.28 ml n-BA (16 mmol) and 1.07 g MABP (4.0 mmol) have been employed

Table 7: Material for cell culture

Material	Supplier
Multiwell plates	Starstedt, Germany
Dulbecco's MEM F-12	Invitrogen
KnockOut (KO) Serum	Invitrogen
basic-fibroblast growth factor (b-FGF)	Invitrogen
Penicillin Streptomycin (Pen-Strep)	Invitrogen
Matrigel, Basement Membrane Matrix	BD Bioscience
B27 Supplement	Invitrogen
Neurobasal medium	Invitrogen
N2 Supplement	Invitrogen
StemPro 34	Invitrogen
L-glutamine	Invitrogen
Ascorbic acid	Sigma Aldrich
Activin A	R&D Systems
BMP-4 Protein	R&D Systems
RPMI 1640 Medium	Invitrogen
Sodium butyrate	Sigma Aldrich
Wnt-3a recombinant	R&D
mTeSR1 medium	Invitrogen
Trypsin	Invitrogen
Norepinephrine	Sigma ldrich
Dimethyl sulfoxide (DMS)	Invitrogen
CHIR99021 inhibitor	Invitrogen
Laminin protein	BD Biosscience
Claycom Medium	JRH Bioscience
Dulbecco's phosphate buffered saline w/o Ca^{2+} and Mg^{2+} (PBS)	Invitrogen

Table 8: Material for biological assays

Material	Supplier
Fetal Bovine Serum (FBS)	Sigma Aldrich
Paraformaldheyde	Sigma Aldrich
Triton-X 100	Sigma Aldrich
Mouse monoclonal anti-cTnT	Sigma Aldrich
Mouse monoclonal anti-α-actinin	Sigma Aldrich
Mouse monoclonal anti-Cx43	Millipore
Goat polyclonal anti-SERCA2a	Santa Cruz
Goat polyclonal anti-GATA4	Santa Cruz
Mouse monoclonal anti-vinculin	Sigma Aldrich
Mouse monoclonal anti-Oct4	Invitrogen
Mouse monoclonal anti-SSEA4	Invitrogen
Mouse monoclonal ant-Nanog	invitrogen
Mouse monoclonal anti-brachyury T	Invitrogen
Mouse monoclonal anti-alpha fetoprotein	Invitrogen
Mouse monoclonal anti-beta III Tubulin	Invitrogen
Secondary antibody goat anti-mouse	Invitrogen
Secondary antibody goat anti-rabbit	Invitrogen
4',6-diamidino-2-phenylindole (DAPI)	Sigma Aldrich
Hoechst	Invitrogen
4-(2-hydroxyethyl)-1-piperazineethane-sulfonic acid (HEPES)	Invitrogen
Fluo-4 AM	Invitrogen
Pluronic F-127	Invitrogen
Sulfinpyrazone	Sigma Aldrich
di-8-ANEPPS	Invitrogen

Table 9: List of instruments

Method	Supplier
AFM	Digital Instruments Multimode
Optical microscope	Leica DMI6000 B, Leica Mycsrosystem
Fluorescent microscope	Leica DMI6000 B, Leica Micorsystems
Confocal microscope	Leica TCS SP5, Leica Microsystems
DMTA	Instron 4502 Tensile Machine
Nanoindenter	Nanoindenter CSM Instrument
Spin coater	Laurell WS-400b-6npp/lLITEHOR)
ImageJ	National Institutes of Health, USA
Matlab	MathWorks

10.2.3 *Polyacylamide solution*

Acrylamide solution was prepared diluting acrylamide (Sigma Aldrich, Germany) in deionized water obtaining a final concentration of 8%. The solution was obtained mixing 2 ml of 40% acrylamide solution (Sigma Aldrich) with 110µl 4-(2-hydroxyethyl)-1-piperazineethanesulfonic acid)HEPES, and 7.525 ml Milli-Q water. PAA was supplemented with 30 mg of photoinitiator (Irgacure, BASF, Germany) previously diluted in 100µl methanol.

10.3 SUBSTRATE FABRICATION METHODS

10.3.1 *Photolithography*

Silicon wafers were pre-baked at 100° C for ten minutes and slowly cooled down at room temperature for dehydration and subsequently spin coated with a 2µm thick layer of AZ-1518 photoresist (Micro-Chemicals, Germany) for 30 s at 2000 rpm. After spin coating, a soft-baking step of 1 minute at 100° C was performed. The photoresist was illuminated with UV light ($\lambda = 365$ nm, $P = 6.5$ mW) through a chrome mask (Delta Mask, The Netherlands) that consisted of square and rectangular lattice of different sizes and distance. Uncross-linked resist was removed rinsing the wafer in an AZ-1518 developer (Micro-Chemicals, Germany) for 20 s. The developing process was stopped by immersion in isopropanol. The silicon wafers with resist structure were then etched through reactive ion etching (RIE) in order to fabricate the microstructures at the desired depth. After the process of etching the 2µm layer of resist was removed and final mi-

crostructured wafers purely in silicon were obtained. The obtained microstructurated Si-wafers were subsequently silanized by exposure to the vapor of (tridecafluoro-1,1,2,2-tetrahysrooctyl)-1-trichlorosilane in vacuum for 30 minutes.

10.3.2 *Fabrication of polydimethylsiloxane (PDMS) microstructured substrates*

PDMS (Sylgard 184, Dow-Corning, Midland, MI) elastomer was thoroughly mixed with the silicone elastomer curing agent in a 10 : 1 ratio, poured over the microstructured Si-master and kept under vacuum for 1 h to allow the complete filling of the patterns and air bubbles removal. The sample was then cured at 80°C for 2 hours and subsequently peeled off the Si-wafers. These samples were used for cell culture or as stamp for the subsequent fabrication of P(nBA-co-%MABP) elastomeric and microstructured substrates.

10.3.3 *Silanization*

In order to provide organic groups for the following process, the glass slides were covered with a solution of 3EBP silane 20 mg/mL toluene. The solution was spincoated on the glass at a rotation speed of 800 rpm for 60 s. The silane was cured for 12 h at 120°C on a preheated hotplate.

10.3.4 *Fabrication of P(nBA-co-%MABP) microstructured substrates*

P(nBA-co-4%MABP) microstructured substrates were frabicateed by replica molding. 300 mg of P(nBA-co-4%MABP) were dissolved in 1 ml toluene and a 60µl drop of the resulting solution was poured on the appropriate PDMS stamp. A glass coverslip was then gently pressed on the top of this drop, allowing the still not crosslinked polymer to completely fill the pattern of the stamp. The glass surface was previously silanized (using 3EBP silane) to achieve a covalent bond between the glass slide and the elastomer during UV light irradiation.This sandwich formed by PDMS stamp, P(nBA-co-4%MABP) and silanized glass was then exposed at UV light ($\lambda = 365$ nm, 6.5 mW power) for 20 minutes. The cross-linked microstructured samples covalently bonded to the glass slide were then peeled off from the PDMS stamp.

10.3.5 *Polyacrylamide cross-linking on P(nBA-co-%MABP) microstructured substrates*

A 70µl drop of PAA and Irgacure solution was poured on a glass coverslip, the microstructured P(nBA-co-%MABP) sample was turned upside down and put in contact with the acrylamide solution, and a black and transparent mask characterized by the desired micropattern was gently lean on the top of the glass that supported the elastomeric sample. This sandwich-like sample was then irradiated for 90 s through UV light($\lambda = 365$ nm, 6.5 mW power) . As a result of this process in the irradiated areas a surface-attached polymer network was generated in a rather complex mechanism, described. After UV light exposure, all the microstructured elastomeric sample is covered by a thin layer ($\sim$ 200 nm) of cell-repellent PAA, except the areas that have not been exposed to UV light thanks to the use of the mask. The sample was rinsed with dionized water for 3 minutes to remove all the not cross-linked PAA residual.

10.3.6 *Fabrication of P(nBA-co-%MABP) bulk material for mechanical tests*

The bulk material for DMTA analysis was fabricated by casting. A solution of P(nBA-co-%MABP) in toluen (300 mg/ml) was prepared and 1 ml of this solution was poured on a rectangular teflon stamp (2x5 cm). The solution was then exposed at UV light (365 nm) for 30 minutes. The sample was peeled-off, turned upside-down, and exposed to UV light to further 30 minutes until the film was completely crosslinked. The film thickness ranged from 3 to 3.5 mm.

10.4 MECHANICAL TESTS

10.4.1 *DMTA test*

dynamic mechanical thermal analysis (DMTA) was performed on P(nBA-co-%MABP) samples to evaluate the influence of cross-linking density on the polymer mechanical properties. Rectangular samples of P(nBA-co-4%MABP), P(nBA-co-10%MABP) and P(nBA-co-20%MABP) were fabricated, a preload of -0.02 MPa was applied to assure that the rectangular samples were in tension at the beginning of the test and a sinusoidal stress was applied with an amplitude a that was chosen in order to keep the strain $\epsilon \sim 1\%$. The frequency of the sinusoidal stress was fixed at 1 Hz whereas the temperature changed. The E modulus of P(nBA-co-4%MABP) has been measured from -40°C to

40°C , the E modulus of P(nBA-co-10%MABP) has been measured from -20°C to 40°C and the E modulus of P(nBA-co-20%MABP) was evaluated at 20°C and at 36.5 °C .

10.4.2 *Bending test*

The bending test was performed through a nonaindenter (Nano-indenter CSM instruments, Switzerland). The instrument has a cantilever with a diamond or glass tip (depending on the shape and diameter of the tip) at its end through wich it is possible to apply and record normal and tangential forces on samples that can be also very small (few hundreds μm). The presence of an *in-situ* camera allows to record the modification of the sample surface during the test. In this work P(nBA-co-4%MABP) microstructured samples have been tested. The samples consisted of a lattice of square micropillars having a height o 10 μm, a width of 10 μm and an interaxial distance of 20 μm. A round glass tip with a radius of 500 μm was put in contact to the top of the microstructured substrate, without applying a normal load to avoid compression of the micropillar. Then the tip was slightly moved laterally, and the tangential force produced between the tip and the bended top of the elastomeric micropillars was recorded by the instrument while the camera showed the deflection of the top of the micropillars. The glass tip was in contact with 9 micropillars: we assumed an equally distributed force among all the micropillars in contact since the radius of the glass tip is muh biggr than the micropillar width, and we calculated the tangentail force f_t acting on a single pillar as the tangential force recorded by the instrument F_t divided by the number of micropillars in contact. In this case:

$$f_t = \frac{F_t}{9}; \tag{24}$$

The deflections of the micropillars were evaluated analyzing the recorded images through a MATLAB (MathWorks) algorithm. The algorithm calculates the position of the centroid of the top of each pillar in contact both in the undeformed ($c\_undeformed$) and deformed configuartion ($c\_deformed$). For each pillar the deflection Δx_i is calculated as $\Delta x_i = c\_deformed - c\_undeformed$. The final value of the deflection d is given by the mean value of the deflections calculated for each micropillar.

$$d = \sum_{i=1}^{9} \frac{\Delta x_i}{9} \tag{25}$$

10.5 CELL CULTURE

10.5.1 *Human ESCs and human iPSCs lines culture and expansion*

HESCs line (hES2, from National Stem Cell Bank, Madison, WI) were expanded in gelatin-coated Petri dishes, in co-culture with mouse embryonic fibroblasts (MEF, Chemicon) mitomycin C-inactivated, for various passages. Expansion medium is composed of DMEM F-12 (Invitrogen), 20% KO serum (Invitrogen), 10% MEF conditioned medium, 20 ng/mL basic fibroblast growth factor (b-FGF, Invitrogen), 0.1 mM β-mercaptoethanol (Invitrogen), 1% non-essential amino acid (Invitrogen) and 1% Pen/Strep (Invitrogen). HESCs were passaged to new feeder using trypsin 0.25% (Invitrogen) and disaggregating to single cell solution. For MEFs depletion and cell expansion and differentiation, cells were passaged on matrigel-coated (MRF 50%, BD Biosciences) microchannels. HiPSC lines ADHF#1 (from Center for iPS Cell Research and Application, iCeMS, Kyoto University) , Send#1 (generated with Sendai viruses), mRNA#1- #2 (generated with mmRNA technology) were cultured and expanded during this PhD work. Human iPS reprogramming using modified mRNA (mmRNA) was performed according to Warren et al. [242]. Cells were cultured in gelatin-coated multiwells with mitomycin c-treated MEFs co-culture, in expansion medium DMEM F-12, 20% KO serum, 10 ng/mL b-FGF, 0.1 mM β-mercaptoethanol, 1% non-essential amino acids and 1% Pen/Strep. HiPSCs were passaged to new feeder using CTK solution (trypsin 0.25% - collagenase 4 - Ca^{2+}) and manually detached by pick to keep technique, under stereoscopic microscope inside biological safety cabinet.

10.5.2 *Human ESCs early germ layer committment*

For early germ layer induction and analysis, we used proper cell seeding concentration to achieve 70 — 80% cell confluence after 2 days. Ectoderm differentiation was induced with DMEM F-12 and Neurobasal medium (both from Invitrogen), 1 : 1 ratio, supplemented with B27 1% (Invitrogen), N2 1% (Invitrogen) and β-met 0.1 mM. Medium was changed every 2 days. Mesoderm differentiation was induced with StemPro-34 (Invitrogen) supplemented with 2 mM L-glutamine (Invitrogen), transferrin 200 ng/mL, 0.5 mM ascorbic acid (Sigma), activin A 0.3 ng/mL (R&D), BMP-4 3 ng/mL (R&D). Medium was changed every 2 days. Endoderm differentiation was induced with RPMI1640 containing 1X B27 (both from Invitrogen), 1mM sodium butyrate (Sigma), 100 ng/ml activin A (R&D) and 50 ng/mL Wnt3a

(R&D) for the first 2 days. The second endoderm medium was KO DMEM with KO serum 20%, L-glutamine 1 mM, NEAA 1%, DMSO 1%,β-met 0.1 mM, P/S 1% for other 3 days. HPSCs specification was induced for 5 days in all three germ layers.

10.5.3 *Cardiac differentiation and disaggregation*

Cardiomyocyte differentiation protocol has been adapted from Lian et al., [171]. The hPSCs are initially cultured on Matrigel-coated (0.05% solution) plates on mTeSR1 medium (Invitrogen) until they are fully confluent. Differentiation is initiated by removing the mTeSR1 medium and adding RPMI/B-27 medium lacking insulin (Invitrogen) and containing a GSK3 inhibitor, such as CHIR99021 and 1% Pen/Strep. After 24 h, the medium is changed to RPMI with 1% B27 supplement w/o insulin, and 1% Pen/Strep for another 2 days. The medium is then changed to RPMI with B27 supplement w/o insulin and IWP4. At day 5, the culture is switched to RPMI-B27 and maintained for the entire culture time. Medium is changed every week. For disaggregation, a digestion mix solution is prepared with collagenase I.(2mg/ml), collagenase IV (1mg/ml), DNase I (2µl/ml) and 10µM Y-27632 in PBS with Ca^{2+} and Mg^{2+}. Cells are incubated for 5 minutes at 37°C in this solution, then everything is removed, centrifuged and risospended in RPMI-B27 before seeding on the appropriate substrates.

10.5.4 *hCMs seeding on microstructured substrates*

Single cell suspensions were plated on the substrates after incubation for 1 hour with 20µg/ml laminin (BD, Bioscience, USA) at a 4000 cells/mm^2 density. A 100µl drop of cell and medium solution was plated over the substrate and left over night. The following day 2 ml of medium are added.

10.6 IMAGE ANALYSIS

10.6.1 *Nuclear deformability*

Nuclear deformability is defined here as the capability of the nuclei to penetrate among pillar inter-spaces and it was quantitatively evaluated as the percentage of the nuclear volume which lies below pillar height. The quantification was performed through the use of a Matlab (MathWorks) algorithm that analyzes a set of z-stack confocal images of fluorescent labeled nuclei (DAPI or Hoechst). The algorithm counts

the number of blue pixels in each image and sum all of the pixel from each z-stack image above pillar height: this sum represents an approximation of the nuclear volume above pillar height (V_a). Subsequently the algorithms evaluate through the same method the volume below pillar height (V_b). As final step, nuclear deformability (ND) is evaluated as:

$$N_D = \left(\frac{V_b}{V_a + V_b}\right) * 100 \tag{26}$$

N_D was evaluated for at least 50 nuclei for each cell line. Mean and standard deviation have been evaluated for each cell line.

10.6.2 *Nuclear concavity*

Nuclear concavity (N_C) is defined as the capability of cell nucleus to assume unusual concave shapes when it penetrates among pillar interspaces in order to adapt to the available area, and it was quantitatively evaluated as the percentage of nuclei having at least one concavity. A set of confocal images of DAPI or Hoechst stained nuclei (5 to 8 images for each cell line) which were acquired at a height of 4μm have been analyzed by a suite of Matlab (MathWorks) algorithms. Nuclear images are first of all turned into black and white, then the contour of the nuclei is found. In the following step a function that calculates the convex area surrounding the nucleus is applied ("convex hull"). Afterwards, the area defined by the nuclear contour is subtracted to the area defined by the convex hull.In presence of nuclear concavities the result of this subtraction is not zero because the convex hull includes also one or more zones that don't belong to the nucleus. In order to avoid to consider as concavity some very small curvatures in the nucleus or some artifacts due to image acquisition, we considered as concavities only the areas with a size equal or bigger than the 10% of the nuclear area. The algorithm also displays were these concave areas are located and it was possible to make a statistics of how many nuclei have just one concavity, two concavities or three or more concavities for each cell line. N_C was evaluated for at least 120 nuclei for each cell line. The final value is given by the mean and the error bars are the standard deviation among all the analyzed nuclei.

10.6.3 *Calcium and pillar deflection acquistion through confocal analysis*

HESC-CMs were loaded in serum-free Dulbecco's modified Eagle medium containing 4-(2-hydroxyethyl)-1-piperazineethanesulfonic acid) (HEPES) 25 mmol/l (Invitrogen) and supplemented with 2.5 mmol/l of fluorescent calcium dye Fluo-4 AM (Invitrogen) for 20 minutes at 37° C in the presence of 2 mmol/l of Pluronic F-127 (Invitrogen) and 20 mmol/l of sulfinpyrazone (Sigma-Aldrich), then incubated for additional 10 minutes at 37° C without Fluo-4 AM, and added with 0.2 mmol/l of di-8-ANEPPS (Invitrogen). Cell dynamics were obtained in recording solution: NaCl, 125 mmol/l; KCl, 5 mmol/l; Na_3PO_4, 1 mmol/l; $MgSO_4$, 1 mmol/l; 4-(2-hydroxyethyl)-1-piperazine-ethanesulfonic acid, 20 mmol/l; $CaCl_2$, 2 mmol/l; and glucose, 5.5 mmol/l, to pH 7.4 with NaOH. Line scans were acquired with a Leica TCS SP5 fluorescence confocal microscope using a 63x oil immersion objective, with 488 nm Ar laser line as an excitation source and 400 Hz acquisition frequency. Line scans were then analyzed using Matlab (MathWorks) software to obtain calcium transient profile and quantify micropillar displacement. Figure 86 reports an explanation of how the two parameters considered in tis thesis to evaluate calcium dynamics have been calculated. In particular, calcium release (Ca^{2+} Rel) was calculated as the time that it takes to the transient to go from the baseline to 95% of the peak value of the recorded signal. For evaluating the calcium reuptake rate (Ca^{2+} Up), the half time of the calcium decay was considered, calculated here as the time necessary to go from the 95% of the peak value of the intensity of the signal, to the 50%.

Micropillar's deflection was recorded thanks to di-8-ANEPPS fluorescence from cell membrane embracing micropillars. Since fluo-4 and di-8-ANEPPS emit at two different wavelengths (490 to 550 nm for fluo-4 and 600 to 700 nm for di-8- ANEPPS) it was possible to record simultaneously the calcium dynamics following the variation of intensity of fluo-4 and the consequent micropillar's deflection from which cell contraction force has been quantified. Through image analysis it was possible to plot the transient of calcium as the variation of the fluo-4 intensity (green signal) of the line scan along time; the deflection has been evaluated following the variation of micropillar edges position along time. The points of the micropillars where cells anchored were detected by immunostaining of the focal adhesion points through vinculin: in this way it was possible to determine the exerted force through the FEM according to the measured micropillar deflection and the effective localization of the applied force.

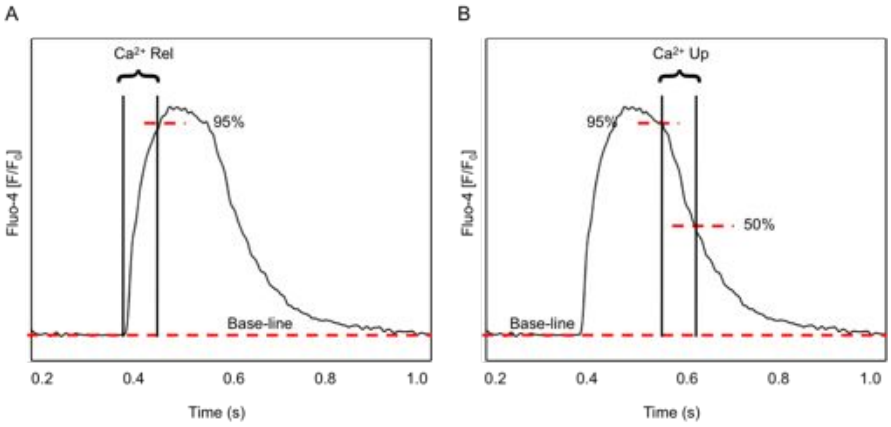

Figure 86: Quantification of the parameters that define calcium dynamics. A) Calculation of Ca^{2+} Rel: this parameter is the time that takes the transient to go from the base-line value to the 95% of the maximum value, registered by the confocal microscope as the peak of fluorescent intensity. B) Calculation of Ca^{2+} Up: this value is calculated as the time that takes the descending part of the transient to go from a value of 95% of the peak to a value of 50% of the peak.

10.7 BIOLOGICAL ASSAYS

10.7.1 *Immunofluorescence analysis*

10.7.1.1 *Immunostaining on pluripotent and early germ layer differentiated stem cells*

Immunofluorescence analyses were performed after fixing cells on paraformaldehyde 4% for 15 min. Blocking and permeabilization was performed with heat inactivated serum 5%, TritonX-100 (Sigma Aldrich) 0.1% for 1h. Cells were stained using primary antibodies in blocking buffer 1 h room temperature for pluripotency markers, or overnight 4°C for differentiation markers, depending on the antibody. Immunostaining was done with secondary antibodies Alexa Fluor 488, 594 (Invitrogen) and DAPI or Hoechst nuclear staining incubation for 1 h at 37°C.

10.7.1.2 *Immunostaining of hPSC-CMs*

Cells were fixed with PBS containing 2% paraformaldehyde (Sigma-Aldrich) for 7 minutes, permeabilized with PBS containing 0.5% Triton X-100 (Sigma-Aldrich), and blocked in PBS containing 2% horse serum for 45 minutes, at room temperature. Primary antibodies were applied for 1 hour at 37°C. Cells were washed in PBS (Invitrogen) and

incubated with fluorescence-conjugated secondary antibodies against mouse, rabbit, or goat, depending on primary antibody used, for 45 minutes at 37° C. Finally, nuclei were counterstained with DAPI (Sigma Aldrich), and samples were mounted viewed under Leica TCS SP5 fluorescence confocal microscope (Leica Microsystems, Wetzlar, Germany). Primary antibodies used were the following: mouse monoclonal anti-cTnT (Sigma Aldrich; 1:100 dilution), mouse monoclonal anti-α-actinin (Sigma-Aldrich; 1:100 dilution), mouse monoclonal anti-Cx43 (Millipore; 1:100 dilution), goat polyclonal anti-SERCA2a (Santa Cruz; 1:200 dilution), and goat polyclonal anti-GATA4 (Santa Cruz; 1:200 dilution), a mouse monoclonal anti-vinculin (Sigma-Aldrich; 1:100 dilution). Secondary antibodies used were the following: goat anti-mouse (Invitrogen; 1:200 dilution), goat anti-rabbit (Invitrogen; 1:200 dilution), and donkey anti-goat (Jackson ImmunoLab; 1:300 dilution). All antibodies were diluted in 3% bovine serum albumin (Sigma Aldrich).

10.7.2 *Quantitative real time PCR*

The qRT-PCR was performed with TaqMan gene expression assay probes (Invitrogen) according to manufactures instructions, using glyceraldehyde 3-phosphate dehydrogenase GAPDH, POU-5F1 (oct4), NANOG (Nanog), TUBB3 (beta-III tubulin), AFP (alpha-fetoprotein), T (brachyury) probe sets (all from TaqMan Invitrogen). Reaction was done on ABI Prism 7000 machine and results were analyzed with ABI Prism 7000 SDS software. glyceraldehyde 3-phosphate dehydrogenase (GAPDH) expression was used to normalize values of gene expression, and data are shown as relative fold change, with a minimum replicates of $n = 3$ for each experimental condition.

10.8 STATISTICAL ANALYSIS

Data are presented as means +/- standard deviation. Data pairs were compared by non-directional Student's t-test- All data manipulation and computation was performed with Matlab software.

APPENDIX A

A.1 PRINCIPLE OF VIRTUAL WORK AND FEM

In mechanics the relationships between the stresses and the displacements developed in the structural elements can be obtained relying upon two fundamental requirements of basic structural behavior: the requirement that the structure must be in equilibrium and the requirement that the deformation must be compatible and consistent to boundary conditions. These two characteristics of structural behavior can be satisfied through a method that involves a quantity dependent both on force and displacement, namely, work. Work is the product of a force and the displacement on its point of application in the direction of the force. If we consider a deformable body both the external and the internal forces may do virtual work.The virtual work is the work of a force on a particle along a virtual displacement. Virtual displacement are infinitesimal changes in the position coordinates of a system such that the constraints remain satisfied. The surface of the body can be subdivided in two parts: one part where displacement are prescribed but the reactive force in this area are not prescribed (S_u), and the remaining part where displacement are not prescribed but reactive surface force are prescribed (S_f), Figure 87 . If we consider a body of an elastic material, the following equations

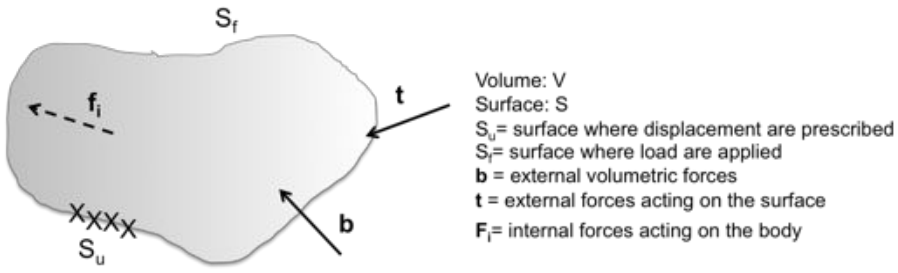

Figure 87: External and internal forces acting on an element. S_u correspond to the area of the surface where displacements are prescribed.

hold in the body:

- Force balance

$$\frac{d\sigma_{ij}}{dx_j} + b_i = 0; \tag{27}$$

- Strain-displacement relations

$$\epsilon_{ij} = \frac{1}{2}\left(\frac{du_i}{dx_j} + \frac{du_j}{dx_i}\right); \tag{28}$$

- Stress-strain relations

$$\sigma_{ij} = C_{ijpq}\epsilon_{pq}. \tag{29}$$

In S_f, the traction vector $\mathbf{t}$ defined as:

$$\sigma_{ij}n_j = t_i \tag{30}$$

is prescribed. n_i is the unit vector normal to the surface. Now, we define $\mathbf{u}$ as virtual displacement field in the body. $\mathbf{u}$ is unrelated to the real displacement field in the body. The field is arbitrary, except that it vanishes on the part of the boundary S_u, where the actual displacement field is prescribed, i.e. $\mathbf{u} = \mathbf{0}$. We define the external virtual work as:

$$dW_e = \int b_i u_i \, dV + \int t_i u_i \, dA \tag{31}$$

The first integral extends over the volume of the body, and the second integral extends on the surface of the body. Note that the traction is known on S_f. Associated with the virtual displacement field is a virtual strain field ϵ_{ij}, defined by:

$$\epsilon_{ij} = \frac{1}{2}\left(\frac{du_i}{dx_j}\frac{du_j}{dx_i}\right) \tag{32}$$

We define the internal virtual work as:

$$dW_i = \int \sigma_{ij}\epsilon_{ij} \, dV \tag{33}$$

The integral extends over the volume of the body. The principle of virtual work (PVW) states that the stress, body force and traction are in equilibrium if and only if dW_i equals the dW_e for every virtual displacement field.

A.1.1 *Principle of virtual work applied to finite element analysis (FEA)*

To maintain $dW_i = dW_e$ for every virtual displacement field is a very complex task. Instead, in FEA $dW_i = dW_e$ is maintained for a subset of virtual displacement fields. This leads to an approximate solution of the actual displacement field. The finite element method is a particular way to construct this subset of virtual displacement fields, as outlined below:

- The body is divided into elements. The basic variables are the displacement vectors at all the nodes, called the nodal displacements.
- The displacement field is interpolated by the nodal displacements and the virtual displacement field is interpolated by the virtual nodal displacements.
- The strain-displacement relations are used to express the strain field in terms of the nodal displacements.The same procedure is used to express the virtual strain field in terms of the virtual nodal displacements
- The stress-strain relations are used to express the stress field in terms of the nodal displacements.
- The relationship $dW_i = dW_e$ is required for every set of virtual nodal displacements. This leads to a set of algebraic equations for the nodal displacements.

When the elements become very small, the nodal displacements approach the actual displacement field. In practice, the element sizes are finite, not infinitesimal; hence the name finite element method.

B

APPENDIX B

B.1 NUCLEAR DEFORMABILITY - MATLAB CODE

Nuclear deformability is defined here as the capability of the nuclei to penetrate among pillar inter-spaces and it was quantitatively evaluated as the percentage of the nuclear volume which lies below pillar height through the Matlab code reported in Figure 88.

B.2 NUCLEAR CONCAVITY - MATLAB CODE

A set of confocal images of DAPI or Hoechst stained nuclei (5 to 8 images for each experimental condition) which were acquired at a height of 4 μm have been analyzed.Figure 89 shows how two different images (the first of a round nucleus, the second of a nucleus presenting 4 concavities) are elaborated by the algorithm. Nuclear images are first of all turned into black and white, then the contour of the nuclei is found. In the following step a function that calculates the convex area surrounding the nucleus is applied ("convex hull"). Afterwards, the area defined by the nuclear contour is subtracted to the area defined by the convex hull. In presence of nuclear concavities the result of this subtraction is not zero because the convex hull includes also one or more zones that don't belong to the nucleus. In order to avoid to consider as concavity some very small curvatures in the nucleus or some artifacts due to image acquisition, we considered as concavities only the areas with a size equal or bigger than the 10% of the nuclear area.

Figure 90 and Figure 91 show the Matlab code that allows the detection of nuclear concavities.

```
clear all
close all
clc

n_image_above=19;
Pixel_volume_above=0;
White_pixel_volume_above=0;
n_inizio=0;

% insert set of confocal images

cd('/Users/eleonora/Documents/MATLAB/deformation_nuclei/HIPS_images/HIPS_11')

% consider all the images above pillar height and sum the white pixels
% (which correspond to pixels of the nucleus)

for i = n_inizio:n_image_above-1

    if i<10
    str = strcat('Image150', int2str(i),'.jpg');
    eval('img=imread(str);');
    else
      str = strcat('Image15', int2str(i),'.jpg');
    eval('img=imread(str);');
    end %if

    img=img(:,:,3);

 % threshold image
    imbw=img>30;

    size_im=size(imbw);

    N=size_im(1)*size_im(2)  % total of pixel in the image
    n=length(find(imbw)); % total of white pixel in the image
    Pixel_volume_above=Pixel_volume_above+N;
    White_pixel_volume_above=White_pixel_volume_above+(n*2.83);

end %for


n_image_below=11;
Pixel_volume_below=0;
White_pixel_volume_below=0;

% consider all the images below pillar height and sum the white pixels
% (which correspond to pixels of the nucleus)

for i = n_image_above:n_image_above+n_image_below-1

    if i<10
    str = strcat('Image150', int2str(i),'.jpg');
    eval('img=imread(str);');
    else
        if i<100
            str=strcat('Image15', int2str(i),'.jpg');
    eval('img=imread(str);');
        else
            str = strcat('Image', int2str(i),'.jpg');
    eval('img=imread(str);');
    end %if
    end %if

    %threshold image
    imbw=img>30;
    size_im=size(imbw);

    N=size_im(1)*size_im(2);  % total of pixel in the image
    n=length(find(imbw)); % total of white pixel in the image
    Pixel_volume_below=Pixel_volume_below+N;
    White_pixel_volume_below=White_pixel_volume_below+(n*2.83);

end %for


Volume_nuclei=(White_pixel_volume_above+White_pixel_volume_below)
percentage_nuclei_above=(White_pixel_volume_above/2*100)/Volume_nuclei


percentage_nuclei_below=(White_pixel_volume_below*100)/Volume_nuclei

cd('/Users/eleonora/Documents/MATLAB/deformation_nuclei')


deformability_cancer_cell_5=percentage_nuclei_below;
```

Figure 88: Matlab code to calculate nuclear defomability.

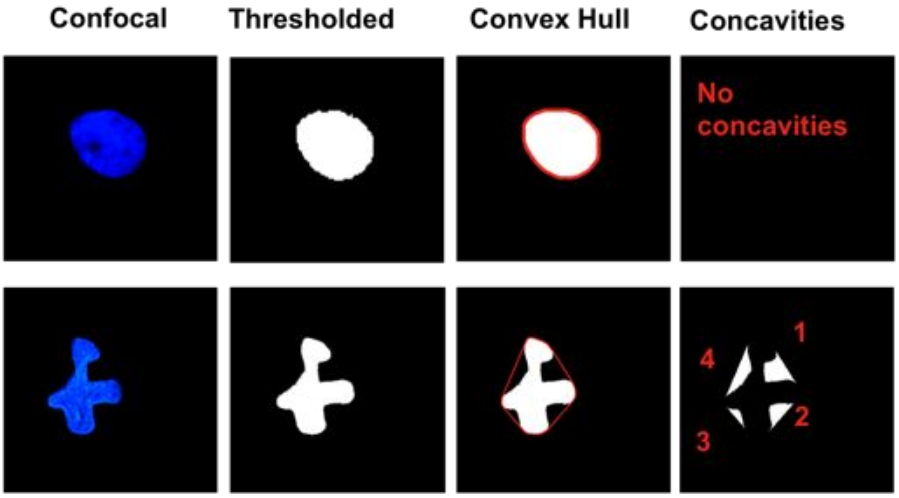

Figure 89: Subsequent steps of the Matlab algorithm that calculates the number of nuclear concavities from the nucleus confocal image. The row above shows the consecutive steps starting from a round nucleus: the last image of the sequence shows that no concavities have been found. The row below shows the consecutive steps of the algorithm starting from a deformed nucleus: the last image of the sequence shows that 4 concavities have been found.

```
clc;
clear all;
close all;
workspace;

% Open up an image .
filename = '/Users/Documents/MATLAB/concavity_MATLAB/concave_cancer.jpg';
originalImage = imread(filename);

figure(1)
imshow(originalImage, []);
title('Original Image');
Image=originalImage(:,:,3);

% Threshold the image.
binaryImage = Image > 70;
binaryImage=bwareaopen(binaryImage, 140);
figure(2)
imshow(binaryImage, []);
title('Thresholded Image');

% Take the convex hull
[convexHullImage hullVerticesX hullVerticesY] =imConvexHull(binaryImage);


% Show original image with convex hull outline plotted over it.
figure(3)
imshow(binaryImage, []);
hold on;
plot(hullVerticesX, hullVerticesY, 'r','LineWidth',2);
title('Convex Hull');

% Calculate the Euclidean Distance Map.
edmImage = bwdist(binaryImage);%
figure(4)
imshow(edmImage, []);
title('Original EDM Image - note high values in corners');


% Mask it by the convex hull.
edmImage2 = edmImage .* single(convexHullImage);
figure(5)
imshow(edmImage2, []);
title('Concavity Areas');

'
```

Figure 90: Matlab algorithm to calculate nuclear concavity.

```
function [convexHullImage hullVerticesX hullVerticesY] =imConvexHull(binaryImage)
[rows columns] = size(binaryImage);
boundaries = bwboundaries(binaryImage);
numberOfBlobs = size(boundaries, 1);
blobVertices = [];
for k = 1 : numberOfBlobs
thisBoundary = boundaries{k};
blobVertices = [blobVertices; thisBoundary];
end
hullIndexes = convhull(blobVertices(:,2), blobVertices(:,1));
hullVerticesX = blobVertices(hullIndexes,2);
hullVerticesY = blobVertices(hullIndexes,1);
convexHullImage = poly2mask(hullVerticesX, hullVerticesY, rows,columns);
return;
```

Figure 91: Matlab function to calculate the convex area surrounding the nucleus, named "convex hull".

C

REFERRED CONFERENCE PROCEEDINGS

POSTERS

1. E.Grespan, E. Serena, V. Le Houerou. J. Ruehe and N. Elvassore, "Probing functional maturation of single human pluripotent stem cells-derived cardiomyocyte". ISSCR 2015 24/06/2015-27/06/2015, Stockholm, Sweden.

2. E. Grespan, G. Giobbe, F. Badique4, K. Anselme, J. Rühe and N. Elvassore, "Nuclear plasticity in human pluripotentstem cells investigated by micropatterned polymeric substrates". ESB 2013 08/09/2013-12/09/2013, Madrid, Spain.

3. E. Grespan, G. Giobbe, F, Badique, K. Anselme, J. Rühe and N. Elvassore, "Nuclear self-deformability in human pluripotwent stem cells under geometrical constrain". IRTG summer school 2013, 7/07/2013-12/07/2013, Mittelwhir, France.

4. E. Grespan, G. Giobbe, F, Badique, K. Anselme, J. Rühe and N. Elvassore, "Evolution of human pluripotent stem cells nuclear plasticity induced by geometrical constrain". ISSCR 2013, 12/06/2013-15/06/2013, Boston, USA.

5. E. Grespan, N. Elvassore, J. Rhüe, "Myoblast proliferation and alignment induced by surface-engineered polymeric substrates". Discussion meeting on challenges and prospects of polymers at interface, 24/04/2013-26/04/2013, Schluchsee, Germany.

6. E. Grespan, S. Martewicz, O. Prucker, V. Le Houerou, N. Elvassore and J. Rühe, "Analysis of single cardiomyocyte contration-forces and calcium dynamics through elastic microstructurated substrates". IRTG summer school 2012 ,08/07/2012-13/07/2012, Mittelwhir, France.

7. E.Grespan, S. Martewicz, P.G. Pavan, J. Rühe and N. Elvassore, "Analysis of single cardiomyocyte contraction-forces through elastic microstructured substrates". GNB 2012 26/06/2012-29/06/2012, Rome, Italy.

8. E.Grespan, S. Martewicz, N.Elvassoere and J. Rühe, "Micropatterned elastic substrates as a tool to study cardiomyocyte phys-

iology and pathophysiology". Discussiom meeting on " Challenges and prospects on polymer chemistry". 02/05/2012-05/05/2012, Schluchsee, Freiburg , Germany.

9. E. Grespan, V. Le Houerou, G. Reiter, "Characterization of the friction in differently micropatterned Poly-L-lactic acid films". IRTG summer school 2011, 09/07/2011-14/07/2011, Mittelwhir, France.

ORAL PRESENTATIONS AT SCIENTIFIC CONFERENCES

1. E. Grespan, S. Martewicz, P. Pavan, V. Le Houerou, O. Prucker, J. Rühe and N. Elvassore, "Simultaneous study of calcium dynamics and contraction force in single-cardiomyocytes using polymeric micropatterned substrates". ESB 2013, Madrid, Spain.

2. E. Grespan, S. Martewicz, P.Pavan, V. Le Houerou, J. Rühe and N. Elvassore, "Contraction force of single-cardiomyocyte evaluated through the use of microstructurated elastic substrates combined with the study of calcium dynamics". GRICU 2012 ,16/09/2012-19/09/2012, Pescara, Italy.

D

ACKNOWLEDGEMENTS

First of all, I would like to sincerely thank Prof. Jürgen Rühe for his careful supervision, and for all the time he dedicated to the frutiful discussion that improved and guided my work. In these years he has represented for me an excellent scientific supervisor and also a mentor. Through his constructive critics as well as his encouragements and positive opinions, I could grow both as researcher and as person. He represented for me an example of authority and integrity.

Many thanks go to Prof. Nicola Elvassore, who welcomed me in his group with open arms, and represented a reference point for discussing and solving the biological issues of my work. He tought me to think about "big questions to answer" and to go to the objective step by step, but never forgetting the aim. He represented for me the visionary supervisor, with the typical Italian inventiveness.

I would like to thank Vincent Le Houerou, who supervised me during the weeks I spent in Strasbourg and who was always ready to answer my questions regarding the mechanical properties of the polymers under study. He represented the person who showed me which are the proper way to behave in all occasions, with the typical French "savoir-faire".

I also thank Prof. Günter Reiter, who gave me the opportunity to be a member of the IRTG Soft Matter Science and who always motivated me to take initiatives to create a scientific network during the PhD. I thank him for scientific discussion and for supporting me all along the IRTG experience.

Thanks to Dr. Oswald Prucker, better known as "Ossi" for scientific discussion regarding the process of fabrication of the substrates, for the suggestions he gave me all along the PhD, for the time he had to dedicate in solving problems I created involuntarely, and for always being very nice with me.

A huge thank goes to the IRTG coordinators Christelle Vergnat, Amandine Henckel and Birgitta Zovko and to Mrs. Gudrun Conrad, Mrs. Petra Hettich and Mrs. Zahra Dandani who were always very kind

with me. Without their help and support I would have not be able to solve several burocratic issues. Thank you all a lot for the time you had to dedicate to me.

Thanks to Melanie Eichhorn, who was for me a wonderful colleague, who helped me everytime I had a problem, who shared with me scientific ideas, who worked with me in the lab, who lost much time in translating documents from German to Italian for helping me and who is now for me a great friend. I will never forget the wonderful times we spent both inside and outside the University.

Thanks to all the IRTG members, in particular Carina Gillig and Marcel Rothfelder who always made me feel at home when I was in Freiburg and who were always ready to help me for any reason. Thanks also to Tristan Bourrel who was my reference point in Strasbourg and to all the people I shared unforgettable moments with: Patrycja Polinska, Joseph Lejeune, Chunyan Yao, Kim Tremel, Maximilian Vielhauer, Andreas Weinberger, Andy Kiessling, Alexey Shvets. For me having the possibility to develop my PhD in such an international environment was a unique opportunity.

Thanks to Vitaly Kondrashov, Gregor Osterwinter (i.e. PasquaInverno) and Samar Kazan, who always welcomed me in their office, who always made me feel at home and who always made me laugh a lot. I was always looking forward to seeing you when I came to Freiburg!

I really want to thank all members of CPI, you all have been wonderful with me everytime I was around! Especially I would like to thank Nils Korf because he was always very kind and helpful with me. Many thanks also to Natalia Schatz who synthesized the polymer I employed in this work.

I take this opportunity to thank the members of BIOERA lab, in particular Onelia Gagliano, who is first of all a great friend, Alessandro Zambon and Francesco Lamberti for the time we spent together working in the lab and chatting during the coffee breaks. I would like to thank Sebastian Martewicz for all the thing he tought me and Elena Serena for the afternoon we spent at the confocal microscope. I thank you all for the wonderful work environment.

And last but not least I want to thank the people I love the most. My husband Mario, who always supported me and who tought me what really matters in life. My sisters and brother, who I admire and

love in such a way that can not be described by words. My mother and my father, who represent for me an exemplary woman and an exemplary man, an exemplary couple, exemplary parents, with a touch of enthusiasm and hilarity that I always bring with me.

Finally, I want to thank my wonderful little son Jacopo, just for existing.

BIBLIOGRAPHY

[1] Dupont S., Morsut L., Aragona M., Enzo E., Giulitti S., Cordenonsi M., Zanconato F., Le Digabel J., Forcato M., Bicciato S., Elvassore N., and Piccolo S. Role of yap/taz in mechanotransduction. *Nature*, 474(7350):179–183, Jun 2011.

[2] Ingber D.E. Cellular mechanotransduction: putting all the pieces together again. *FASEB J*, 20(7):811–827, May 2006.

[3] Anselme K., Ploux L., and Ponche A. Cell/material interfaces: Influence of surface chemistry and surface topography on cell adhesion. *Journal of Adhesion Science and Technology*, 24(5):831–852, 2010.

[4] Bershadsky A., Kozlov M., and Geiger B. Adhesion-mediated mechanosensitivity: a time to experiment, and a time to theorize. *Current Opinion in Cell Biology*, 18(5):472–481, 10 2006.

[5] Baker J.P. and Titus M.A. Myosins: matching functions with motors. *Current Opinion in Cell Biology*, 10(1):80 – 86, Feb 1998.

[6] Fujita S., Ohshima M., and Iwata H. Time-lapse observation of cell alignment on nanogrooved patterns. *Journal of The Royal Society Interface*, 6(Suppl 3):S269–S277, Apr 2009.

[7] Ezratty E. J, Partridge M.A., and Gundersen G.G. Microtubule-induced focal adhesion disassembly is mediated by dynamin and focal adhesion kinase. *Nat Cell Biol*, 7(6):581–590, Jun 2005.

[8] Wang N., Tytell J.D., and Ingber D.E. Mechanotransduction at a distance: mechanically coupling the extracellular matrix with the nucleus. *Nat Rev Mol Cell Biol*, 10(1):75–82, 01 2009.

[9] Davidson P. *The interaction of healthy and cancerous cells with nano- and microtopography*. PhD thesis, Institut de Science des Materiaux de Mulhouse, Universite de Haute Alsace, 2011.

[10] Cukierman E., Pankov R., Stevens D.R., and Yamada K.M. Taking cell-matrix adhesions to the third dimension. *Science*, 294(5547):1708–1712, 2001.

[11] Katz B.Z., Zamir E., Bershadsky A., Kam Z., Yamada K.M., and Geiger B. Physical state of the extracellular matrix regulates

the structure and molecular composition of cell-matrix adhesions. *Mol Biol Cell*, 11(3):1047–1060, Mar 2000.

[12] Vogel V. Mechanotransduction involving multimodular proteins: converting force into biochemical signals. *Annu Rev Biophys Biomol Struct*, 35:459–488, 2006.

[13] Wada K.I., Itoga K., Okano T., Yonemura S., and Sasaki H. Hippo pathway regulation by cell morphology and stress fibers. *Development*, 138(18):3907–3914, Sep 2011.

[14] Badouel C. and McNeill H. Snapshot: The hippo signaling pathway. *Cell*, 145(3):484—484.e1, Apr 2011.

[15] Piccolo S., Cordenonsi M., and Dupont S. Molecular pathways: Yap and taz take center stage in organ growth and tumorigenesis. *Clin Cancer Res*, 19(18):4925–4930, Sep 2013.

[16] Vogel V. and Sheetz M. Local force and geometry sensing regulate cell functions. *Nat Rev Mol Cell Biol*, 7(4):265–275, Apr 2006.

[17] Khan S. and Sheetz M.P. Force effects on biochemical kinetics. *Annual Review of Biochemistry*, 66(1):785–805, 1997.

[18] Faisal K.M., Laurie G.W., McCaffrey T.A, and Falcone D.J. Exposure of cryptic domains in the alpha 1-chain of laminin-1 by elastase stimulates macrophages urokinase and matrix metalloproteinase-9 expression. *J Biol Chem*, 277(16):13778–13786, Apr 2002.

[19] Orr A.W., Helmke B.P., Brett R. Blackman, and Schwartz M.A. Mechanisms of mechanotransduction. *Dev Cell*, 10(1):11–20, Jan 2006.

[20] Brancaccio M., Fratta L., Notte A., Hirsch E., Poulet R., Guazzone S., De Acetis M., Vecchione C., Marino G., Altruda F., Silengo L., Tarone G., and Lembo G. Melusin, a muscle-specific integrin beta1-interacting protein, is required to prevent cardiac failure in response to chronic pressure overload. *Nat Med*, 9(1):68–75, 01 2003.

[21] Guvendiren M. and Burdick J.A. Stem cell response to spatially and temporally displayed and reversible surface topography. *Advanced Healthcare Materials*, 2(1):155–164, 2013.

[22] Baker B.M., Nathan A.S., Gee A.O., and Mauck R.L. The influence of an aligned nanofibrous topography on human mesenchymal stem cell fibrochondrogenesis. *Biomaterials*, 31(24):6190–6200, Aug 2010.

[23] Tan J. and Saltzman M. Biomaterials with hierarchically defined micro- and nanoscale structure. *Biomaterials*, 25(17):3593 – 3601, 2004.

[24] Teixeira A.I., Abrams G.A., Bertics P.J., Murphy C.J., and Nealey P.F. Epithelial contact guidance on well-defined micro- and nanostructured substrates. *J Cell Sci*, 116(Pt 10):1881–1892, May 2003.

[25] Curtis A. and Wilkinson C. Topographical control of cells. *Biomaterials*, 18(24):1573–1583, Dec 1997.

[26] Walboomers X.F., Croes H.J.E., Ginsel L.A., and Jansen J.A. Contact guidance of rat fibroblasts on various implant materials. *Journal of Biomedical Materials Research*, 47(2):204–212, 1999.

[27] Walboomers X.F., Ginsel L. A., and Jansen J.A. Early spreading events of fibroblasts on microgrooved substrates. *J Biomed Mater Res*, 51(3):529–534, Sep 2000.

[28] Loesberg W.A., Walboomers X.F., van Loon J.J.W.A., and Jansen J.A. The effect of combined cyclic mechanical stretching and microgrooved surface topography on the behavior of fibroblasts. *J Biomed Mater Res A*, 75(3):723–732, Dec 2005.

[29] Dalby M.J. Cellular response to low adhesion nanotopographies. *International Journal of Nanomedicine*, 2(3):373–381, 09 2007.

[30] Dalby M.J., Gadegaard N., Tare R., Andar A., Riehle M.O., Herzyk P., Wilkinson C.D.W., and Oreffo R.O.C. The control of human mesenchymal cell differentiation using nanoscale symmetry and disorder. *Nat Mater*, 6(12):997–1003, Dec 2007.

[31] Kunzler T.P., Drobek T., Schuler M., and Spencer N.D. Systematic study of osteoblast and fibroblast response to roughness by means of surface-morphology gradients. *Biomaterials*, 28(13):2175–2182, Apr 2007.

[32] Riboldi S.A., Sadr N., Pigini L., Neuenschwander P., Simonet M., Mognol P., Sampaolesi M., Cossu G., and Mantero S. Skeletal myogenesis on highly orientated microfibrous

polyesterurethane scaffolds. *J Biomed Mater Res A*, 84(4):1094–1101, Mar 2008.

[33] Lam M.T., Sim S., Zhu X., and Takayama S. The effect of continuous wavy micropatterns on silicone substrates on the alignment of skeletal muscle myoblasts and myotubes. *Biomaterials*, 27(24):4340–4347, Aug 2006.

[34] Streeter D.D.Jr, Spotnitz H.M., Patel D.P., Ross J.Jr, and Sonnenblick E.H. Fiber orientation in the canine left ventricle during diastole and systole. *Circ Res*, 24(3):339–347, Mar 1969.

[35] Chien K.R., Domian I.J., and Parker K.K. Cardiogenesis and the complex biology of regenerative cardiovascular medicine. *Science*, 322(5907):1494–1497, Dec 2008.

[36] Feinberg A.W., Wilkerson W.R., C.A. Seegert, Gibson A.L., Hoipkemeier-Wilson L., and Brennan A.B. Systematic variation of microtopography, surface chemistry and elastic modulus and the state dependent effect on endothelial cell alignment. *J Biomed Mater Res A*, 86(2):522–534, Aug 2008.

[37] Roach P., Parker T., Gadegaard N., and Alexander M.R. Surface strategies for control of neuronal cell adhesion: A review. *Surface Science Reports*, 65(6):145 – 173, 2010.

[38] Baier R.E., Meyer A.E., Natiella J.R., Natiella R.R., and Carter J.M. Surface properties determine bioadhesive outcomes: methods and results. *J Biomed Mater Res*, 18(4):337–355, Apr 1984.

[39] Keselowsky B.G., Collard D.M., and Garcia A.J. Integrin binding specificity regulates biomaterial surface chemistry effects on cell differentiation. *Proceedings of the National Academy of Sciences*, 102(17):5953–5957, 2005.

[40] Yanagisawa I., Sakuma H., Shimura M., Wakamatsu Y., Yanagisawa S., and Sairenji E. Effects of wettability of biomaterials on culture cells. *J Oral Implantol*, 15(3):168–177, 1989.

[41] Lim J.Y.l, Liu X., Vogler E.A., and Donahue H.J. Systematic variation in osteoblast adhesion and phenotype with substratum surface characteristics. *Journal of Biomedical Materials Research Part A*, 68A(3):504–512, 2004.

[42] Lee J.H., Khang G., Lee J.W., and Lee H.B. Interaction of different types of cells on polymer surfaces with wettability gradient. *J Colloid Interface Sci*, 205(2):323–330, Sep 1998.

[43] Faucheux N., Schweiss R., Lutzow K., Werner C., and Groth T. Self-assembled monolayers with different terminating groups as model substrates for cell adhesion studies. *Biomaterials*, 25(14):2721–2730, Jun 2004.

[44] Rodrigues S.N., Goncalves I.C., Martins M.C.L., Barbosa M.A., and Ratner B.D. Fibrinogen adsorption, platelet adhesion and activation on mixed hydroxyl-methyl-terminated self-assembled monolayers. *Biomaterials*, 27(31):5357–5367, Nov 2006.

[45] Roach P., Farrar D., and Perry C.C. Interpretation of protein adsorption: surface-induced conformational changes. *J Am Chem Soc*, 127(22):8168–8173, Jun 2005.

[46] Wörz A., Berchtold B., Moosmann K., Prucker O., and Rühe J. Protein-resistant polymer surfaces. *J. Mater. Chem.*, 22:19547–19561, 2012.

[47] Pandiyarajan C.K., Prucker O., Zieger B., and Rühe J. Influence of the molecular structure of surface-attached poly(n-alkyl acrylamide) coatings on the interaction of surfaces with proteins, cells and blood platelets. *Macromol Biosci*, 13(7):873–884, Jul 2013.

[48] Baghai M., Tamura N., Beyersdorf F., Henze M., Prucker O., Rühe J., Goto S., Zieger B., and Heilmann C. Platelet repellent properties of hydrogel coatings on polyurethane-coated glass surfaces. *ASAIO J*, 60(5):587–593, Oct 2014.

[49] Scherag F.D., Brandstetter T., and Rühe J. Raising the shields: Pcr in the presence of metallic surfaces protected by tailor-made coatings. *Colloids and Surfaces B: Biointerfaces*, 122(0):576 – 582, oct 2014.

[50] Chen C.S., Mrksich M., Huang S., Whitesides G.M., and Ingber D.E. Geometric control of cell life and death. *Science*, 276(5317):1425–1428, May 1997.

[51] Gawain Thomas, Nancy A Burnham, Terri Anne Camesano, and Qi Wen. Measuring the mechanical properties of living cells using atomic force microscopy. *J Vis Exp*, 27(76), Jun 2013.

[52] Pelham R.J. and Wang Y-l. Cell locomotion and focal adhesions are regulated by substrate?flexibility. *Proceedings of the National Academy of Sciences*, 94(25):13661–13665, 1997.

[53] Tee S.Y., Fu J., Chen C.S., and Janmey P.A. Cell shape and substrate rigidity both regulate cell stiffness. *Biophysical Journal*, 100(5):L25–L27, 2015/01/25 2010.

[54] Nemir S. and West J.L. Synthetic materials in the study of cell response to substrate rigidity. *Ann Biomed Eng*, 38(1):2–20, Jan 2010.

[55] Silver F.H., Kato Y.P., Ohno M., and Wasserman A.J. Analysis of mammalian connective tissue: relationship between hierarchical structures and mechanical properties. *J Long Term Eff Med Implants*, 2(2-3):165–198, 1992.

[56] Yu X. and Bellamkonda R.V. Dorsal root ganglia neurite extension is inhibited by mechanical and chondroitin sulfate-rich interfaces. *J Neurosci Res*, 66(2):303–310, Oct 2001.

[57] Engler A.J., Carag-Krieger C., Johnson C.P., Raab M., Tang H.Y., Speicher D.W., Sanger J.W., Sanger J.M., and Discher D.E. Embryonic cardiomyocytes beat best on a matrix with heart-like elasticity: scar-like rigidity inhibits beating. *J Cell Sci*, 121(Pt 22):3794–3802, Nov 2008.

[58] Jacot J.G., McCulloch A.D., and Omens J.H. Substrate stiffness affects the functional maturation of neonatal rat ventricular myocytes. *Biophys J*, 95(7):3479–3487, Oct 2008.

[59] Discher D.E., Janmey P., and Wang Y-I. Tissue cells feel and respond to the stiffness of their substrate. *Science*, 310(5751):1139–1143, Nov 2005.

[60] Folch A. and Toner M. Microengineering of cellular interactions. *Annual Review of Biomedical Engineering*, 2(1):227–256, 2000.

[61] Li N., Tourovskaia A., and Folch A. Biology on a chip: Microfabrication for studying the behavior of cultured cells. *Critical Reviews in Biomedical Engineering*, 31(5):423–488, 2003.

[62] Toh Y.C., Blagovic K., and Voldman J. Advancing stem cell research with microtechnologies: opportunities and challenges. *Integrative Biology*, 2:305–325, Aug 2010.

[63] Serena E., Cimetta E., Luni C., and Elvassore N. Microtechnology for stem cell culture. In Krishnarao Appasani and Raghu K. Appasani, editors, *Stem Cells and Regenerative Medicine*, pages 465–482. Humana Press, 2011.

[64] Nguyen K.T. and West J.L. Photopolymerizable hydrogels for tissue engineering applications. *Biomaterials*, 23(22):4307 – 4314, 2002.

[65] Koegler P., Clayton A., Thissen H., Santos G.N.C., and Kingshott P. The influence of nanostructured materials on biointerfacial interactions. *Adv Drug Deliv Rev*, 64(15):1820–1839, Dec 2012.

[66] Rogers J.A., Kateri P.E., Rebecca J.J., and Whitesides G.M. Generating 90 nanometer features using near-field contact-mode photolithography with an elastomeric phase mask. *Journal of Vacuum Science and Technology*, 16:59–68, 1998.

[67] Abbott N.L., Kumar A., and G.M. Whitesides. Using micromachining, molecular self-assembly, and wet etching to fabricate 0.1-1-pm-scale structures of gold and silicon. *Chemistry of Materials*, 1994.

[68] Abbott N.L., Folkers J.P., and Whitesides G.M. Manipulation of the wettability of surfaces on the 0.1 to 1-micrometer scale through micromatching and molecular self-assembly. *Science*, 257(5075):1380–1382, 1992.

[69] Kumar A. and Whitesides G.M. Features of gold having micrometer to centimeter dimensions can be formed through a combination of stamping with an elastomeric stamp and an alkanethiol 'ink' followed by chemical etching. *Applied Physics Letters*, 63(14):2002–2004, 1993.

[70] Ghibaudo M.and Saez A., Trichet L., Xayaphoummine A., Browaeys J., Silberzan P., Buguin A., and Ladoux B. Traction forces and rigidity sensing regulate cell functions. *Soft Matter*, 4, Jul 2008.

[71] Zaidel-Bar R., Ballestrem C., Kam Z., and Geiger B. Early molecular events in the assembly of matrix adhesions at the leading edge of migrating cells. *Journal of Cell Science*, 116:4605–4613, Nov 2003.

[72] Levental K.R., Yu H., Kass L., J.N. Lakins, Egeblad M., Erler J.T., Fong S.F.T., Csiszar K., Giaccia A., Weninger W., Yamauchi M., Gasser D.L., and Weaver V.M. Matrix crosslinking forces tumor progression by enhancing integrin signaling. *Cell*, 139(5):891–906, Nov 2009.

[73] Legate K., Wickström S., and Fässler R. Genetic and cell biological analysis of integrin outside-in signaling. *Genes & Development*, 23(4), Feb 2009.

[74] Sawada Y., Tamada M., Dubin-Thaler B.J., Cherniavskaya O., Sakai R., Tanaka S., and Sheetz M.P. Force sensing by mechanical extension of the src family kinase substrate p130cas. *Cell*, 127(5):1015 – 1026, 2006.

[75] Brunner C.A., Ehrlicher A., Kohlstrunk B., Knebel D., Käs J.A.., and Goegler M. Cell migration through small gaps. *European Biophysics Journal*, 35(8):713–719, Oct 2006.

[76] Kress H., Stelzer E.H.K., Holzer D., Buss F., Griffiths G., and Rohrbach A. Filopodia act as phagocytic tentacles and pull with discrete steps and a load-dependent velocity. *PNAS*, 104(28):11633–11638, Jul 2007.

[77] Prass M., Jacobson K., Mogilner A., and Radmacher M. Direct measurement of the lamellipodial protrusive force in a migrating cell. *The Journal of Cell Biology*, 174(6):767–772, Sep 2006.

[78] Kim K., Taylor R., Sim J.Y., Park S.-J., Norman J., Fajardo G., Bernstein D., and Pruitt B.L. Calibrated micropost arrays for biomechanical characterisation of cardiomyocytes. *Micro Nano Letters, IET*, 6(5):317–322, May 2011.

[79] Brady A.J., Tan S.T., and Ricchiuti N.V. Contractile force measured in unskinned isolated adult rat heart fibres. *Nature*, 282(728-729), Dec 1979.

[80] Das T., Maiti T.K., and Chakraborty S. Traction force microscopy on-chip: shear deformation of fibroblast cells. *Lab Chip*, 8:1308–1318, Jun 2008.

[81] Merkel R., Kirchgessner N., Cesa C.M., and Hoffmann B. Cell force microscopy on elastic layers of finite thickness. *Biophysical Journal*, 93:3314–3323, Nov 2007.

[82] Balaban N.Q., Scwarz U.S., Riveline D., Goichberg P., Tzur G., Sabanay I., Mahalu D., Safran S., Bershadsky A., Addadi L., and Geiger B. Force and focal adhesion assembly: a close relationship studied using elastic micropatterned substrates. *Nature Cell Biology*, 3(5):466–472, May 2001.

[83] Cesa C.M., Kirchgebner N., Mayer D., Schwarz U.S., Hoffmann B., and Merkel R. Micropatterned silicone elastomer substrates

for high resolution analysis of cellular force patterns. *Review of Scientific Instruments*, 78(3):034301–034301–10, Mar 2007.

[84] Digabel J., Ghibaudo M., Trichet L., Richert A., and Ladoux B. Microfabricated substrates as a tool to study cell mechanotransduction. *Medical and Biological Engineering and Computing*, 48(10):965–976, Oct 2010.

[85] Tan J.L., Tien J., Pirone D.M., Gray D.S., Bhadriraju K., and Chen C.S. Cells lying on a bed of microneedles: An approach to isolate mechanical force. *PNAS*, 100(4):1484–1489, Jan 2003.

[86] Fabiato A. Myoplasmic free calcium concentration reached during the twitch of an intact isolated cardiac cell and during calcium-induced release of calcium from the sarcoplasmic reticulum of a skinned cardiac cell from the adult rat or rabbit ventricle. *The Journal of general physiology*, 78(5):457–497, 11 1981.

[87] Yasuda S-I, Sugiura S., Kobayakawa N., Fujita H., Yamashita H., Katoh K., Saeki Y., Kaneko H., Suda Y., Nagai R., and Sugi H. A novel method to study contraction characteristics of a single cardiac myocyte using carbon fibers. *American Journal of Physiology - Heart and Circulatory Physiology*, 281(3):H1442–H1446, 2001.

[88] Garcia-Webb M.G., Taberner A.J., Hogan N.C., and Hunter I.W. A modular instrument for exploring the mechanics of cardiac myocytes. *American Journal of Physiology - Heart and Circulatory Physiology*, 293(1):H866–H874, 2007.

[89] Harris A.K., Wild P., and Stopak D. Silicone rubber substrata: a new wrinkle in the study of cell locomotion. *Science*, 208(4440):177–179, 1980.

[90] Barentin C., Sawada Y., and Rieu J-P. An iterative method to calculate forces exerted by single cells and multicellular assemblies from the detection of deformations of flexible substrates. *European Biophysics Journal*, 35(4):328–339, 2006.

[91] Yin S., Zhang X., Zhan C., Wu J., Xu J., and Cheung J. Measuring single cardiac myocyte contractile force via moving a magnetic bead. *Biophysical Journal*, 88:1489–1495, Feb 2005.

[92] Polio S.R., Rothenberg K.E., Stamenovic D., and Smith M.L. A micropatterning and image processing approach to simplify

measurement of cellular traction forces. *Acta Biomaterialia*, 8(1):82 – 88, 2012.

[93] Fu J., Wang Y-K., Yang M.T., Desai R.A., Yu X., Liu Z., and Chen C.S. Mechanical regulation of cell function with geometrically modulated elastomeric substrates. *Nature Methods*, 7(9):733–736, Sept 2010.

[94] Klein F., Striebel T., Fischer J., Jiang Z., Franz C.M., von Freymann G., Wegener M., and Bastmeyer M. Elastic fully three-dimensional microstructure scaffolds for cell force measurements. *Advanced Materials*, 22(8):868–871, 2010.

[95] Cohen D.M., Yang M.T., and Chen C.S. Measuring cell-cell tugging forces using bowtie-patterned mpads (microarray post detectors). In Troy A. Baudino, editor, *Cell-Cell Interactions*, volume 1066 of *Methods in Molecular Biology*, pages 157–168. Human Press, 2013.

[96] Potten C.S. and Loeffler M. Stem cells: attributes, cycles, spirals, pitfalls and uncertainties. lessons for and from the crypt. *Development*, 110(4):1001–1020, Dec 1990.

[97] Orkin S.H. and Zon LI. Hematopoiesis and stem cells: plasticity versus developmental heterogeneity. *Nature Immunology*, 3(4):323–328, Apr 2002.

[98] Thomson J.A., Itskovitz-Eldor J, Shapiro S, Waknitzn M.A., Swiergiel J.J., Marshall V.S., and Jones J.M. Embryonic stem cell lines derived from human blastocysts. *Science*, 282(5391):1145–1147, 1998.

[99] Reubinoff B.E., Pera M., Fong C., Trounson A., and Bongso A. Embryonic stem cell lines from human blastocysts: somatic differentiation in vitro. *Nature biotechnology*, 18(4):399–404, Apr 2000.

[100] Yabut O. and Bernstein H.S. The promise of human embryonic stem cells in aging-associated diseases. *Aging (Albany NY)*, 3(5):494 – 508, May 2011.

[101] Hochedlinger K. and Jaenisch R. Nuclear reprogramming and pluripotency. *Nature*, 441:1061–1067, June 2006.

[102] Takahashi K. andTanabe K., Ohnuki M., Narita M., Ichisaka T., Tomoda K., and Yamanaka S. Induction of pluripotent stem cells from adult human fibroblasts by defined factors. *Cell*, 131(5):861–872, Nov 2007.

[103] Wernig M., Meissner A., Foreman R., Brambrink T., Ku M., Hochedlinger K., Bernstein B.E., and Jaenisch R. In vitro reprogramming of fibroblasts into a pluripotent es-cell-like state. *Nature*, 448:318–324, July 2007.

[104] Jaenisch R. and Young R. Stem cells, the molecular circuitry of pluripotency and nuclear reprogramming. *Cell*, 4:567–582, 2 2008.

[105] Carr A-J.F., Smart M.J.K., Ramsden C.M., Powner M.B., da Cruz L., and Coffey P.J. Development of human embryonic stem cell therapies for age-related macular degeneration. *Trends in Neurosciences*, 3(7):385–395, Jun 2013.

[106] Murry C.E. and Keller G. Differentiation of embryonic stem cells to clinically relevant populations: Lessons from embryonic development. *Cell*, 132(4):661–680, Jun 2008.

[107] Masumoto H., Matsuo T., Yamamizu K., Uosaki H., Narazaki G., Katayama S., Marui A., Shimizu T., Ikeda T., Okano T., Sakata R., and Yamashita J.K. Pluripotent stem cell-engineered cell sheets reassembled with defined cardiovascular populations ameliorate reduction in infarct heart function through cardiomyocyte-mediated neovascularization. *Stem Cells*, 30:1196–1205, Jun 2012.

[108] Kubo A., Shinozaki K., Shannon J.M., Kouskoff V., Kennedy M., Woo S., Fehling H.J., and Keller G. Development of definitive endoderm from embryonic stem cells in culture. *Development*, 131(7):1651–1662, Apr 2004.

[109] Ying Q.L., Stavridis M., Griffiths D., Li M., and Smith A. Conversion of embryonic stem cells into neuroectodermal precursors in adherent monoculture. *Nat Biotechnol*, 21(2), Feb 2003.

[110] H Kawasaki, K Mizuseki, S Nishikawa, S Kaneko, Y Kuwana, S Nakanishi, S I Nishikawa, and Y Sasai. Induction of midbrain dopaminergic neurons from es cells by stromal cell-derived inducing activity. *Neuron*, 28(1):31–40, Oct 2000.

[111] Ema M., Takahashi S., and Rossant J. Deletion of the selection cassette, but not cis-acting elements, in targeted flk1-lacz allele reveals flk1 expression in multipotent mesodermal progenitors. *Blood*, 107:111–117, Jan 2006.

[112] Park C., Afrikanova I., Chung Y.S., Zhang W.J., Arentson E., Fong Gh G., Rosendahl A., and Choi K. A hierarchical order of

factors in the generation of flk1- and scl-expressing hematopoietic and endothelial progenitors from embryonic stem cells. *Development*, 131(11):2749–2762, Jun 2004.

[113] M Cristina Nostro, Xin Cheng, Gordon M Keller, and Paul Gadue. Wnt, activin, and bmp signaling regulate distinct stages in the developmental pathway from embryonic stem cells to blood. *Cell Stem Cell*, 2:60–71, Jan 2008.

[114] Naito H., Melnychenko I., Didié M., Schneiderbanger K., Schubert P., Rosenkranz S., Eschenhagen T., and Zimmermann W-H. Optimizing engineered heart tissue for therapeutic applications as surrogate heart muscle. *Circulation*, 114(1):I72–8, 2006.

[115] Ueno S., Weidinger G., Osugi T., Kohn A.D., Golob J.L., Pabon L., Reinecke H., Moon R.T., and Murry C.E. Biphasic role for wnt/beta-catenin signaling in cardiac specification in zebrafish and embryonic stem cells. *Proc Natl Acad Sci U S A*, 104(23):9685–9690, Jun 2007.

[116] Yasunaga M., Tada S., Torikai-Nishikawa S., Nakano Y., Mitsuhiro Okada, Lars Martin Jakt, Satomi Nishikawa, Tsutomu Chiba, Takumi Era, and Shin-Ichi Nishikawa. Induction and monitoring of definitive and visceral endoderm differentiation of mouse es cells. *Nat Biotechnol*, 23(12):1542–1550, Dec 2005.

[117] Schier A.F. Nodal signaling in vertebrate development. *Annu Rev Cell Dev Biol*, 19:589–621, 2003.

[118] Gouon-Evans V., Boussemart L., Gadue P., Nierhoff D., Koehler C.I., Kubo A., Shafritz D.A., and Keller G. Bmp-4 is required for hepatic specification of mouse embryonic stem cell-derived definitive endoderm. *Nat Biotechnol*, 24(11):1402–1411, Nov 2006.

[119] D'Amour K.A., Bang A.G., Eliazer S., Kelly O.G., Agulnick A.D., Smart N.G., Moorman M.A., Kroon E., Carpenter M.K., and Baetge E.E. Production of pancreatic hormone-expressing endocrine cells from human embryonic stem cells. *Nat Biotechnol*, 24(11):1392–1401, Nov 2006.

[120] Barabasi A-L. and Oltvai Z.N. Network biology: understanding the cell's functional organization. *Nat Rev Genet*, 5(2):101–113, Feb 2004.

[121] Metallo C.M., Mohr J.C., Detzel C.J., de Pablo J.J., Van Wie B.J., and Palecek S.P. Engineering the stem cell microenvironment. *Biotechnol Prog*, 23(1):18–23, Jan-Feb 2007.

[122] Discher D.E., Mooney D.J., and Zandstra P.W. Growth factors, matrices, and forces combine and control stem cells. *Science*, 324(5935):1673–1677, 2009.

[123] Scadden D.T. The stem-cell niche as an entity of action. *Nature*, 441:1075–1079, Jun 2006.

[124] Möller C. and Slack M. Impact of new technologies for cellular screening along the drug value chain. *Drug Discovery Today*, 15(9):384 – 390, 2010.

[125] Serena E., Cimetta E., Zatti S., Zaglia T., Zagallo M., Keller G., and Elvassore N. Micro-arrayed human embryonic stem cells-derived cardiomyocytes for *In Vitro*functional assay. *PLoS ONE*, 7(11):e48483, 11 2012.

[126] Gearhart J. New potential for human embryonic stem cells. *Science*, 282(5391):1061–1062, 1998.

[127] Lombardi M.L. and Lammerding J. Chapter 6 - altered mechanical properties of the nucleus in disease. In G.V. Shivashankar", editor, *Nuclear Mechanics and amp; Genome Regulation*, volume 98 of *Methods in Cell Biology*, pages 21 – 141. Academic Press, 2010.

[128] Rowat A.C., Lammerding J., and Ipsen J.H. Mechanical properties of the cell nucleus and the effect of emerin deficiency. *Biophysical Journal*, 91(12):4649 – 4664, 2006.

[129] Dahl K.N., Ribeiro A.J.S., and Lammerding J. Nuclear shape, mechanics, and mechanotransduction. *Circulation Research*, 102(11):1307–1318, 2008.

[130] Lee J.S.H., Hale C.M., Panorchan P., Khatau S.B., George J.P., Tseng Y., Stewart C.L., Hodzic D., and Wirtz D. Nuclear lamin a/c deficiency induces defects in cell mechanics, polarization, and migration. *Biophysical Journal*, 93(7):2542 – 2552, 2007.

[131] Caille N., Thoumine O., Tardy Y., and Meister J.J. Contribution of the nucleus to the mechanical properties of endothelial cells. *Journal of Biomechanics*, 35(2):177 – 187, Feb 2002.

[132] Khatau S.B., Kim D.H., Hale C.M., Bloom R.J., and Wirtz D. The perinuclear actin cap in health and disease. *Nucleus*, 1(4):337–342, Aug 2010.

[133] Lamond A.I. and Earnshaw W.C. Structure and function in the nucleus. *Science*, 280(5363):547–553, Apr 1998.

[134] Spector D L. Macromolecular domains within the cell nucleus. *Annual Review of Cell Biology*, 9(1):265–315, Nov 1993.

[135] Misteli T. The concept of self-organization in cellular architecture. *The Journal of Cell Biology*, 155(2):181–186, Oct 2001.

[136] De Vos W.H., Houben F., Hoebe R.A., Hennekam R., Van Engelen B., Manders E.M.M., Ramaekers F.C.S., Broers J.L.V., and Van Oostveld P. Increased plasticity of the nuclear envelope and hypermobility of telomeres due to the loss of a-type lamins. *Biochimica et Biophysica Acta (BBA) - General Subjects*, 1800(4):448 – 458, Apr 2010.

[137] Lanctot C., Cheutin T., Cremer M., Cavalli G., and Cremer T. Dynamic genome architecture in the nuclear space: regulation of gene expression in three dimensions. *Nat Rev Genet*, 8(2):104–115, Feb 2007.

[138] Zink D., Fischer A.H., and Nickerson J.A. Nuclear structure in cancer cells. *Nature Reviews Cancer*, 4:677–687, Sep 2004.

[139] Davidson P.M., Hayriye Ö., Hasirci V., Reiter G., and Anselme K. Microstructured surfaces cause severe but non-detrimental deformation of the cell nucleus. *Advanced Materials*, 21(35), Jun 2009.

[140] Tamiello C., Kamps M.A.F., Van Den Wijngaard A., Verstraeten V.L.R.M., Baaijens F.P.T., Broers J.L.V., and Bouten C.C.V. Soft substrates normalize nuclear morphology and prevent nuclear rupture in fibroblasts from a laminopathy patient with compound heterozygous lmna mutations. *Nucleus*, 4(1), 2013.

[141] Pajerowski J.D., Dahl K.N., Zhong F.L., Sammak P.J., and Discher D.E. Physical plasticity of the nucleus in stem cell differentiation. *PNAS*, 104(40):15619–15624, Sep 2007.

[142] Chalut K.J., Markus H., Lautenschläger F., Boyde L., Chan C.J., Ekpenyong A., Martinez-Arias A., and Guck J. Chromatin decondensation and nuclear softening accompany nanog downregulation in embryonic stem cells. *Biophysical Journal*, 103(10):2060 – 2070, Nov 2012.

[143] Chalut K.J., Kulangara K., Giacomelli M.G., Wax A., and Leong K.W. Deformation of stem cell nuclei by nanotopographical cues. *Soft Matter*, 6(8), 2010.

[144] Dahl K.D., Booth-Gauthier E.A., and Ladoux B. In the middle of it all: Mutual mechanical regulation between the nucleus and the cytoskeleton. *Journal of Biomechanics*, 43(1):2 – 8, Jan 2010.

[145] Badique F., Stamov D.R., Davidson P.M., Veuillet M., Reiter G., Freund J-N, Franz C.M., and Anselme K. Directing nuclear deformation on micropillared surfaces by substrate geometry and cytoskeleton organization. *Biomaterials*, 34(12):2991 – 3001, 2013.

[146] Crisp M., Liu Q., Roux K., Rattner J.B., Shanahan C., Burke B., Stahl P.D., and Hodzic D. Coupling of the nucleus and cytoplasm: role of the linc complex. *The Journal of Cell Biology*, 172(1):41–53, Dec 2006.

[147] Khatau S.B., Hale C.M., Stewart-Hutchinson P.J., Patel M.S., Stewart C.L., Searson P.C., Hodzic D., and Wirtz D. A perinuclear actin cap regulates nuclear shape. *PNAS*, Oct 2009.

[148] Maniotis A.J., Chen C.S., and Ingber D.E. Demonstration of mechanical connections between integrins, cytoskeletal filaments, and nucleoplasm that stabilize nuclear structure. *PNAS*, 94(3):849–854, 1997.

[149] Versaevel M., Grevesse T., and Gabriele S. Spatial coordination between cell and nuclear shape within micropatterned endothelial cells. *Nature Communications*, 3:671–682, Feb 2012.

[150] Swift J., Ivanovska I.L., Buxboim A., Harada T., Dingal P.C. Dave P., Pinter J., Pajerowski J.D., Spinler K. R., Shin J-W, Tewari M., Rehfeldt F., Speicher D.W., and Discher D.E. Nuclear lamin-a scales with tissue stiffness and enhances matrix-directed differentiation. *Science*, 341(6149), 2013.

[151] Walker C.A. and Spinale F.G. The structure and function of the cardiac myocyte: a review of fundamental concepts. *J Thorac Cardiovasc Surg*, 118(2):375–382, Aug 1999.

[152] Bers D.M. Cardiac excitation-contraction coupling. *Nature*, 415:198–205, Oct 2002.

[153] Jussi T Koivumaki, Jouni Takalo, Topi Korhonen, Pasi Tavi, and Matti Weckstrom. Modelling sarcoplasmic reticulum calcium

atpase and its regulation in cardiac myocytes. *Philos Trans A Math Phys Eng Sci*, 367(1896):2181–2202, Jun 2009.

[154] Chang W-T., Yu D., Lai Y-C., Lin K-Y., and Liau I. Characterization of the mechanodynamic response of cardiomyocytes with atomic force microscopy. *Anal Chem*, 85(3):1395–1400, Feb 2013.

[155] Iribe G., Helmes M., and Kohl P. Force-length relations in isolated intact cardiomyocytes subjected to dynamic changes in mechanical load. *Am J Physiol Heart Circ Physiol*, 292(3):H1487–97, Mar 2007.

[156] M. Radisic, Park H., Shing H., Consi T., Schoen F.J., Langer R., Freed L.E., and Vunjak-Novakovic G. Functional assembly of engineered myocardium by electrical stimulation of cardiac myocytes cultured on scaffolds. *Proceedings of the National Academy of Sciences*, 101(52):18129–18134, 2004.

[157] Hansen A., Eder A., Bönstrup M., Flato M., Mewe M., Schaaf S., Aksehirlioglu B., Schwoerer A.P., Schwörer A., Uebeler J., and Eschenhagen T. Development of a drug screening platform based on engineered heart tissue. *Circulation research*, 107(1), July 2010.

[158] Katare R.G., Ando M.i, Kakinuma Y., and Sato T. Engineered heart tissue: A novel tool to study the ischemic changes of the heart <italic>in vitro</italic>. *PLoS ONE*, 5(2):e9275, 02 2010.

[159] Kim S.B., Cropek D.M., United States Army. Corps of Engineers, Engineer Research, Development Center (U.S.), and Construction Engineering Research Laboratory (U.S.). *A Cell-based Biosensor for Real-time Detection of Cardiotoxicity Using Lens-free Imaging*. Royal Society of Chemistry, 2011.

[160] Grosberg A., Alford P.W., McCain M.L., and Parker K.K. Ensembles of engineered cardiac tissues for physiological and pharmacological study: heart on a chip. *Lab Chip*, 11(24):4165–73, 2011.

[161] Pawani H. and Bhartiya D. Pluripotent stem cells for cardiac regeneration: overview of recent advances & emerging trends. *Indian J Med Res*, 137(2):270–282, Feb 2013.

[162] Chani Hodonsky, Kaihong Wu, Lakshmi Mundada, and Ming-Sing Si. Generation of human cardiomyocytes for cardiac

regenerative therapies: differentiation and direct reprogramming. *Curr Pharm Des*, 20(12):2012–2022, 2014.

[163] Wei Eric Wang, Xiongwen Chen, Steven R Houser, and Chunyu Zeng. Potential of cardiac stem/progenitor cells and induced pluripotent stem cells for cardiac repair in ischaemic heart disease. *Clin Sci (Lond)*, 125(7):319–327, Oct 2013.

[164] Yang X., Pabon L., and Murry C.E. Engineering adolescence: maturation of human pluripotent stem cell-derived cardiomyocytes. *Circ Res*, 114(3):511–523, Jan 2014.

[165] Laflamme M.A., Chen K.Y., Naumova A.V., Muskheli V., Fugate J.A., Dupras S.K., Reinecke H., Xu C., Hassanipour M., Police S., O'Sullivan C., Collins L., Chen Y., Minami E., Gill E.A., Ueno S., Yuan C., Gold J., and Murry C.E. Cardiomyocytes derived from human embryonic stem cells in pro-survival factors enhance function of infarcted rat hearts. *Nat Biotech*, 25(9):1015–1024, 09 2007.

[166] Shiba Y., Fernandes S., Zhu W-Z., Filice D., Muskheli V., Kim J., Palpant N.J., Gantz J., Moyes K.W., Reinecke H., Van Biber B., Dardas T., Mignone J.L., Izawa A., Hanna R., Viswanathan M., Gold J.D., Kotlikoff M.I., Sarvazyan N., Kay M.W., Murry C.E., and Laflamme M.A. Human es-cell-derived cardiomyocytes electrically couple and suppress arrhythmias in injured hearts. *Nature*, 489(7415):322–325, Sep 2012.

[167] Kajzar A., Cesa C. M., Kirchgeßner N., Hoffmann B., and Merkel R. Toward physiological conditions for cell analyses: Forces of heart muscle cells suspended between elastic micropillars. *Biophysical Journal*, 94(5):1854–1866, March 2008.

[168] Taylor R.E., Kim K., Sun N., Park S-J., Sim J.Y., Fajardo G., Bernstein D., Wu J.C., and Pruitt B.L. Sacrificial layer technique for axial force post assay of immature cardiomyocytes. *Biomed Microdevices*, 15(1):171–181, Feb 2013.

[169] Rodriguez M.L., Graham B.T., Pabon L.M., Han S.J., Murry C.E., and Sniadecki N.J. Measuring the contractile forces of human induced pluripotent stem cell-derived cardiomyocytes with arrays of microposts. *J Biomech Eng*, 136(5):051005, May 2014.

[170] Hay D.C., Fletcher J., Payne C., Terrace J.D., Gallagher R.C. J., Snoeys J., Black J.R.., Wojtacha D., Samuel K.and Hannoun Z., Pryde A., Filippi C., Currie I.S., Forbes S.J., Ross J.A., Newsome

P.N., and Iredale J.P. Highly efficient differentiation of hescs to functional hepatic endoderm requires activina and wnt3a signaling. *PNAS*, 105(34):12301–12306, Jul 2008.

[171] Lian X., Hsiao C. andWilson G., Zhu K., Hazeltine L.B., Azarine S.M., Raval K.K., Zhang J., Kamp T.J., and Palecek S.P. Robust cardiomyocyte differentiation from human pluripotent stem cells via temporal modulation of canonical wnt signaling. *PNAS*, 109(27):1848–1857, July 2012.

[172] Camnasio S., Delli Carri A., Lombardo A., Grad I., Mariotti C., Castucci A., Rozell B., Lo Riso P., V. Castiglioni, C. Zuccato, C. Rochon, Y. Takashima, G. Diaferia, I. Biunno, C. Gellera, M. Jaconi, A. Smith, Hovatta O., Naldini L., Di Donato S., Feki A., and Cattaneo E. The first reported generation of several induced pluripotent stem cell lines from homozygous and heterozygous huntington's disease patients demonstrates mutation related enhanced lysosomal activity. *Neurobiology of Disease*, 46(1):41 – 51, 2012.

[173] McBeath R., Pirone D.M., Nelson C.M., Bhadriraju K., and Chen C.S. Cell shape, cytoskeletal tension, and rhoa regulate stem cell lineage commitment. *Developmental Cell*, 6(4):483 – 495, 2004.

[174] Whitesides G.M., Ostuni E., Takayama S., Jiang X., and Ingber D.E. Soft litography in biology and biochemistry. *Annual Review of Biomedical Engineering*, 3(1):335–373, 2001.

[175] Belardi J., Schorr N., Prucker O., and Ruehe J. Artificial cilia: Generation of magnetic actuators in microfluidic systems. *Advanced Functional Materials*, 21(17), Jul 2011.

[176] Eichhorn M., Stannard C., Anselme K., and Rühe J. Nucleus deformation of saos-2 cells on rhombic micro-pillars. *J Mater Sci Mater Med*, 26(2), Feb 2015.

[177] Whitesides G.M. The origins and the future of microfluidics. *Nature*, 442:368–373, Jul 2006.

[178] Schneider F., Fellner T., Wilde J., and Wallrabe U. Mechanical properties of silicones for mems. *Journal of Micromechanics and Microengineering*, 18(6):065008, 2008.

[179] Liu M., Sun J., and Chen Q. Influences of heating temperature on mechanical properties of polydimethylsiloxane. *Sensors and Actuators, A: Physical*, 151(1):42–45, 2009.

[180] Schneider F., J. Draheim, Kamberger R., and Wallrabe U. Process and material properties of polydimethylsiloxane (pdms) for optical mems. *Sensors and Actuators, A: Physical*, 151(2):95–99, 2009.

[181] Unger M.A., Chou H-P., Thorsen T., Scherer A., and Quake S.R. Monolithic microfabricated valves and pumps by multilayer soft lithography. *Science*, 288(5463):113–116, 2000.

[182] Kim T.K., Kim J.K., and Jeong O.C. Measurement of nonlinear mechanical properties of pdms elastomer. *Microelectronic Engineering*, 88(8):1982 – 1985, 2011.

[183] Johnston I.D., McCluskey D.K., Tan C.K.L., and Tracey M.C. Mechanical characterization of bulk sylgard 184 for microfluidics and microengineering. *Journal of Micromechanics and Microengineering*, 24(3):1 – 7, Feb 2014.

[184] Cowie J.M.G. *Polymers: chemistry and physics of modern materials.* Thornes, 2000.

[185] Hiemenz P.C. and Lodge T. *Polymer chemistry.* CRC Press, 2007.

[186] Matyjaszewski K. and Davis T.P. *Handbook of Radical Polymerization.* John Wiley and Sons., 2002.

[187] Hartleb W. *Fabrication and Characterization of Magnetically Actuated Rubber Cilia.* Department of Microsystems Engineering (IMTEK) at the University of Freiburg, 2011.

[188] Toomey R., Freidank D., and Rühe J. Swelling behaviour of thin, surface-attached polymer networks. *Macromolecules*, 37:882–887, 2004.

[189] Turro N.J. *Modern molecular photochemistry.* Univ. Science Books, 2001.

[190] Prucker O., Naumann C.A., Ruehe J., Wolfgang K., and Curtis F.W. Photochemical attachment of polymer films to solid surfaces via monolayers of benzophenone derivatives. *Journal of the American Chemical Society*, 121(38):8766–8770, 1999.

[191] Kandow C.E., Georges P.C., Janmey P.A., and Beningo K.A. Polyacrylamide hydrogels for cell mechanics: Steps toward optimization and alternative uses. In Yu-Li Wang and Dennis E. Discher, editors, *Cell Mechanics*, volume 83 of *Methods in Cell Biology*, pages 29 – 46. Academic Press, 2007.

[192] Mironov V.L. Fundamentals of scanning probe microscopy. *The Russian academy of science*, 2004.

[193] Meyer E. Atomic force microscopy. *Progress in Surface Science*, 41(1):3 – 49, 1992.

[194] Ward I.M. *Mechanical properties of solid polymers*. John Wiley and Sons, New York, 1983.

[195] Nagdi K. *Rubber as an engineering material: guideline for users*. Hanser Publisher, New York, 1992.

[196] Ferry J.D. *Viscoelastic properties of polymers*. John Wiley and Sons, New York, 1980.

[197] Treloar L.R.G. *The physics of rubber elasticity*. Clarendon Press, Oxford, 1975.

[198] Spathis G. and Kontou E. Viscoelastic response of elastomers in large deformations. *Polymer Gels and Networks*, 3(2):209 – 220, 1995.

[199] Ogden R.W. *Non linear elastic deformations*. Ellis Horwood Limited, Chichester, 1984.

[200] Menard K.P. *Dynamic Mechanical Analysis: a practical introduction*. CRC Press, 1999.

[201] Fischer-Cripps A.C. *Nanoindentation*. Springer, New York, 2004.

[202] Zienkiewicz O.C., Taylor R.L., and Zhu J.Z. *The finite element method: its basis and fundamentals*. Elsevier Butterworth Heinemann, Oxford, 2005.

[203] Rao S. *The finite element method in engineering*. Butterworth-Heinemann, 2005.

[204] Bathe K-J. *Finite element procedures*. Prentice Hall, 1996.

[205] Reddy J.N. *Energy principle and variational methods in applied mechanics*. John Wiley and Sons, New York, 2002.

[206] Vallier L., Touboul T., Brown S., Cho C., Bilican B., Alexander M., Cedervall J., Chandran S., Ahrlund-Richter L., Weber A., and Pedersen R.A. Signaling pathways controlling pluripotency and early cell fate decisions of human induced pluripotent stem cells. *Stem Cells*, 27(11):2655–2666, Nov 2009.

[207] Biswas A. and Hutchins R. Embryonic stem cells. *Stem Cells Dev.*, 16(2):213–222, Apr 2007.

[208] Xiao L., Yuan X., and Sharkis S.J. Activin a maintains self-renewal and regulates fibroblast growth factor, wnt, and bone morphogenic protein pathways in human embryonic stem cells. *Stem Cells*, 24(6):1478–1486, Jun 2006.

[209] James D., Levine A.J., Besser D., and Hemmati-Brivanlou A. Tgfbeta/activin/nodal signaling is necessary for the maintenance of pluripotency in human embryonic stem cells. *Development*, 132(6):1273–1282, Mar 2005.

[210] Xu R.H., Peck R.M., Li D.S., Feng X., Ludwig T., and Thomson J.A. Basic fgf and suppression of bmp signaling sustain undifferentiated proliferation of human es cells. *Nature Methods*, 2(3):185–190, Mar 2005.

[211] Boyer L.A., Lee T.I., Cole M.F., Johnstone S.E., Levine S.S., Zucker J.P. Guenther M.G. Kumar R.M., Murray H.L., Jenner R.G., Gifford D.K., Melton D.A., Jaenisch R., and Young R.A. Core transcriptional regulatory circuitry in human embryonic stem cells. *Cell*, 122(6):947–956, Sep 2005.

[212] Pan G. and Thomson J.A. Nanog and transcriptional networks in embryonic stem cell pluripotency. *Cell Res.*, 17(1):42–49, Jan 2007.

[213] Lian X., Zhang J., Azarin S.M., Zhu K., Hazeltine L.B., Bao X., Hsiao C., Kamp T.J., and Palecek S.P. Directed cardiomyocyte differentiation from human pluripotent stem cells by modulating wnt/beta-catenin signaling under fully defined conditions. *Nature Protocols*, 8:162–175, Jan 2013.

[214] Semwogerere D. and Weeks E.R. *Confocal Microscopy*, chapter 58, pages 1–10. Taylor and Francis, 2005.

[215] Sheppard C.J.R. *Scanning Confocal Microscopy*, chapter 218, pages 2525–2544. CRC Press, 2007.

[216] Teraski M. and Dailey M.E. *Handbook of Biological Con- focal Microscopy, 2nd Ed.* Plenum Press, New York, 1995.

[217] Atkins P. *Physical Chemistry, 5th Ed.* W. H. Freeman and Company, New York., 1994.

[218] Gee K.R., Brown K.A., Chen W-N.U., Bishop-Stewart J., Gray D., and Johnson I. Chemical and physiological characterization of fluo-4 ca^{2+} -indicator dyes. *Cell calcium*, 27(2):97–106, Feb 2000.

[219] Miller E.W., Lin J.Y., Frady E.P., Steinbach P.A., Kristan W.B., and Tsien R.Y. Optically monitoring voltage in neurons by photo-induced electron transfer through molecular wires. *Proceedings of the National Academy of Sciences*, 109:2114Ð2119, 2012.

[220] Mueller M., Vafaie M., Biener M., Giannitsis E., and Katus H.A. Cardiac troponin t. *Circulation Journal*, 77(7):1653–1661, 2013.

[221] Periasamy M., Bhupathy P., and Babu G.J. Regulation of sarcoplasmic reticulum ca^{2+} atpase pump expression and its relevance to cardiac muscle physiology and pathology. *Cardiovasc Res*, 77(2):265–273, Jan 2008.

[222] Guan K., Furst D.O., and Wobus A.M. Modulation of sarcomere organization during embryonic stem cell-derived cardiomyocyte differentiation. *Eur J Cell Biol*, 78(11):813–823, Nov 1999.

[223] Itzhaki I., Rapoport S., Huber I., Mizrahi I., Zwi-Dantsis L.AND Arbel G., Schiller J., and Gepstein L. Calcium handling in human induced pluripotent stem cell derived cardiomyocytes. *PLoS ONE*, 6(4):e18037, 04 2011.

[224] Xi J., Khalil M., Shishechian N., Hannes T., Pfannkuche K., Liang H., Fatima A., Haustein M., Suhr F., Bloch W., Reppel M., Saric T., Wernig M., Janisch R., Brockmeier K., Hescheler J., and Pillekamp F. Comparison of contractile behavior of native murine ventricular tissue and cardiomyocytes derived from embryonic or induced pluripotent stem cells. *FASEB J*, 24(8):2739–2751, Aug 2010.

[225] Robertson C., Tran D.D., and George S.C. Concise review: Maturation phases of human pluripotent stem cell-derived cardiomyocytes. *Stem cells (Dayton, Ohio)*, 31(5):10.1002/stem.1331, 05 2013.

[226] Boudou T., Legant W.R., Mu A., Borochin M.A., Thavandiran N., Radisic M., Zandstra P.W., Epstein J.A., Margulies K.B., and Chen C.S. A microfabricated platform to measure and manipulate the mechanics of engineered cardiac microtissues. *Tissue engineering. Part A*, 18(9-10), May 2012.

[227] Carrier R.L., Papadaki M., Rupnick M., Schoen F.J., Bursac N., Langer R., Freed L.E., and Vunjak-Novakovic G. Cardiac tissue engineering: Cell seeding, cultivation parameters, and tissue construct characterization. *Biotechnology and Bioengineering*, 64(5):580–589, 1999. cited By (since 1996)314.

[228] Zimmermann W-H, Schneiderbanger K., Schubert P., Didié M., Münzel F., Heubach J.F., Kostin S., Neuhuber W. L., and Eschenhagen T. Tissue engineering of a differentiated cardiac muscle construct. *Circ Res*, 90(2):223–30, 2002.

[229] Samuel J.L. and Vandenburgh H.H. Mechanically induced orientation of adult rat cardiac myocytes in vitro. *In Vitro Cell Dev Biol*, 26(9):905–14, 1990.

[230] Eschenhagen T., Fink C., Remmers U., Scholz H., Wattchow J., Weil J., Zimmermann W., Dohmen H.H., Schäfer .H., Bishopric N., Wakatsuki T, and Elson E.L. Three-dimensional reconstitution of embryonic cardiomyocytes in a collagen matrix: a new heart muscle model system. *FASEB J*, 11(8):683–94, 1997.

[231] Rodriguez A.G., Han S.J., Regnier M., and Sniadecki N.J. Substrate stiffness increases twitch power of neonatal cardiomyocytes in correlation with changes in myofibril structure and intracellular calcium. *Biophysical Journal*, 101(10):2455 – 2464, 2011.

[232] Jacot J.G., Kita-Matsuo H., Wei K.A., Vincent Chen H.S., Omens J.H., Mercola M., and McCulloch A.D. Cardiac myocyte force development during differentiation and maturation. *Annals of the New York Academy of Sciences*, 1188(1):121–127, 2010.

[233] Kehat I., Kenyagin-Karsenti D., Snir M., Segev H., Amit M., Gepstein A., Livne E., Binah O., Itskovitz-Eldor J., and Gepstein L. Human embryonic stem cells can differentiate into myocytes with structural and functional properties of cardiomyocytes. *The Journal of Clinical Investigation*, 108:407–414, Aug 2001.

[234] Kattman S.J., Witty A.D., Gagliardi M, Dubois N.C., Niapour M., Hotta A., Ellis J., and Keller G. Stage-specific optimization of activin/nodal and bmp signaling promotes cardiac differentiation of mouse and human pluripotent stem cell lines. *Cell Stem Cell*, 8(2):228–240, 2011.

[235] Zhang J., Wilson G.F., Soerens A.G., Koonce C.H., Yu J., Palecek S.P., Thomson J.A., and Kamp T.J. Functional cardiomyocytes derived from human induced pluripotent stem cells. *Circ Res*, 104(4):e30–41, Feb 2011.

[236] Kuo P-L, Lee H., Bray M-A, Geisse N.A.., Huang Y-T, Adams W.J., Sheehy S.P., and Parker K.K. Myocyte shape regulates lateral registry of sarcomeres and contractility. *The American journal of pathology*, 181(6):2030–2037, 12 2012.

[237] Yin L., Bien H., and Entcheva E. Scaffold topography alters intracellular calcium dynamics in cultured cardiomyocyte networks. *Am J Physiol Heart Circ Physiol*, 287(3), Sep 2004.

[238] Walsh K.B. and Parks G.E. Changes in cardiac myocyte morphology alter the properties of voltage-gated ion channels. *Cardiovasc Res*, 55(1):64 – 75, Jul 2002.

[239] Nishimura S., Yasuda S-I., Katoh M., Yamada K.P., Yamashita H., Saeki Y., Sunagawa K., Nagai R., Hisada T., and Sugiura S. Single cell mechanics of rat cardiomyocytes under isometric, unloaded, and physiologically loaded conditions. *Am J Physiol Heart Circ Physiol*, 287(1):H196–202, Jul 2004.

[240] Caspi O., Lesman A.t, Basevitch Y., Gepstein A., Arbel G., Habib I.H.M., Gepstein L., and Levenberg S. Tissue engineering of vascularized cardiac muscle from human embryonic stem cells. *Circ Res*, 100(2):263–272, Feb 2007.

[241] Pandiyarajan C.K. *The interaction of blood proteins and platelets on surface-attached poly(alkylacrylamide) networks.* PhD thesis, Department of Microsystems Engineering (IMTEK) at the University of Freiburg, 2013.

[242] Warren L., Bryder D., Weissman I.L., and Quake S.R. Transcription factor profiling in individual hematopoietic progenitors by digital rt-pcr. *Proceedings of the National Academy of Science*, 103(47):17807–17812, Jul 2006.